Investigative Application of the Intrinsic Extended Finite Element Method for the Computational Characterization of Composite Materials

Sebastian P. Favè

Thesis submitted to the Faculty of the
Virginia Polytechnic Institute and State University
in partial fulfillment of the requirements for the degree of

Master of Science
in
Aerospace Engineering

Gary D. Seidel, Chair
Alan J. Brown
Rakesh K. Kapania

Aug 15, 2014
Blacksburg, Virginia

Keywords: Intrinsic XFEM, Moving Least Squares, Level-Set Method, Effective Material Properties, Composite Materials

Investigative Application of the Intrinsic Extended Finite Element Method for the Computational Characterization of Composite Materials

Sebastian P. Favè

(ABSTRACT)

Computational micromechanics analysis of carbon nanotube-epoxy nanocomposites, containing aligned nanotubes, is performed using the mesh independent intrinsic extended finite element method (IXFEM). The IXFEM employs a localized intrinsic enrichment strategy to treat arbitrary discontinuities defined through the level-set method separate from the problem domain discretization, i.e. the finite element (FE) mesh. A global domain decomposition identifies local subdomains for building distinct partition of unities that appropriately suit the approximation. Specialized inherently enriched shape functions, constructed using the moving least square method, enhance the approximation space in the vicinity of discontinuity interfaces, maintaining accuracy of the solution, while standard FE shape functions are used elsewhere. Comparison of the IXFEM in solving validation problems with strong and weak discontinuities against a standard finite element method (FEM) and analytic solutions validates the enriched intrinsic bases, and shows anticipated trends in the error convergence rates. Applying the IXFEM to model composite materials, through a representative volume element (RVE), the filler agents are defined as individual weak bimaterial interfaces. Though a series of RVE studies, calculating the effective elastic material properties of carbon nanotube-epoxy nanocomposite systems, the benefits in substituting the conventional mesh dependent FEM with the mesh independent IXFEM when completing micromechanics analysis, investigating effects of high filler count or an evolving microstructure, are demonstrated.

This work received support from the Society of Naval Architects and Marine Engineers (SNAME) and the American Society of Naval Engineers (ASNE).

Elements of this work were run on the advanced research computing (ARC) resources of Virginia Tech.

Acknowledgments

Foremost, I would like to express my gratitude to Dr. Gary Seidel, my thesis advisor and chair of my master's advisory committee, for his guidance and support throughout my graduate education. Invitation to join his research team, as an undergraduate student, has played an enormous role in leading me to the success I have found for myself moving forward, and for that I am most appreciative. Participating in undergraduate research heavily influenced my decision to pursue a graduate education and motivated my career search for opportunities with continued learning and technology development well integrated into the position responsibilities. I am especially grateful to have been introduced to the XFEM during a discussion with Dr. Seidel when considering possibilities for my master's research topic. Exploration of the novel FEM as the crucial tool for my research ignited my interest in computational programming and simulation. Moreover, though I encountered numerous occasions of frustration while learning and implementing the numerical method my forward progress and ultimate success yielded far more memorable moments of triumph.

I also wish to thank my graduate advisory committee members, Dr. Alan Brown and Dr. Rakesh Kapania, for their service in my education and the engineering community at large. Their contributions in reviewing this work will certainly benefit the final submission of this thesis. Undergraduate course with Dr. Brown reaffirmed my interest in the Naval Architecture and Marine Engineering industry and lead to my initial consideration towards earning a graduate degree. Graduate courses with Dr. Kapania fed my passion for learning from exemplary practiced teachers and further solidified my decision to continue my education in the field of materials and structures. All together it has been a pleasure to learn from and interact with the faculty members of the Aerospace and Ocean Engineering Department at Virginia Tech

In special mention I would also like to acknowledge my research colleagues Adarsh Chaurasia who was always willing to share insight of relevance to my work and regular helped me clarify minor issues as well as Xiang Ren for his assistance in creating the randomly dispersed CNT fiber configurations. Along similar lines I recognize Josh Burton, Skylar Stephens, and Yumeng Li for their continuous faith in my abilities. Additionally I would like to thank Dr. Roger Chang. He has has served as an invaluable ally in supporting my educational pursuits at Virginia Tech, predominately during my undergraduate education. In doing so he has provided unique guidance, insight, and anecdotes in regards to numerous manners of life during my stay in Blacksburg. He has become a renowned resource to a large portion of the engineering student body at Tech and a friend to those who regularly sought his company. I consider myself fortunate to count myself

among those ranks.

I would also like to make mention and acknowledge the support of the Society of Naval Architects and Marine Engineers (SNAME) and the American Society of Naval Engineers (ASNE). Their recognition and rewarding of academic success and future potential in the naval architecture and marine engineering industry through scholarship awards has been a great benefit in furthering my education. I was honored to receive scholarships from both professional organizations, designated *The Alan C. McClure Scholar* from SNAME and a graduate student scholar from ASNE during my final year of study. Participation as a student member has presented great insight into the maritime industry and excellent networking opportunities. I look forward to further involvement with both societies in entering the workforce.

Lastly, I wish to extent my appreciation to my parents, Dominique and Carl-Philipp Favè. Their love and support has been instrumental in bringing about so many accomplishments in my life. Thank you for encouraging me to create my own path to my interests and for sharing in my enthusiasm with each decision. Along those same lines I have been extremely fortunate to have the best siblings and friends I could imagine, who routinely provided honest and almost more importantly comedic encouragement in the moments of my exaggerated pessimism towards a succesful completion. I would never wish for an alternate path, in which I would have had to have done it without any one of you.

Contents

List of Figures

List of Tables

1 Introduction

Incentivized by their tailorable mechanical, electrical, and thermal properties, advanced composite materials are increasing being turned to as substitutes for the more traditional metallic materials used in the aircraft and ship building industries. Driven at both ends, by the U.S. defense department and commercial sector, such composites have witnessed expansive emergence in large scale applications within the past decade. As new businesses and strategies continue to pursue the capabilities afforded by these materials, development of modeling tools for the proficient design and testing of composites become vitally important to alleviate the burden associated with the cost and time of experimental studies. In this context, design is interpreted to focus on the manufacturing of a composite material to satisfy selected effective material properties, whereas testing implies evaluation of the macro- to composite filler length-scale response of the material system to expected stimulus. While inclusive simulation based design, testing, and certification of composites remains a future endeavor, new techniques can serve to provide efficient preliminary analysis leading to a founding direction for material design and subsequent testing. It is in regards to both exploratory design and investigative testing which this research is intended to contribute, through demonstration of a mesh independent finite element (FE) method (FEM)[1].

With the growing utilization of composites, nanocomposites (i.e. composites having at least one constituent phase with a characteristic length on the scale of nanometers) have become of unique interest. Observation of these nanocomposites to serve as multifunctional materials, where the nanoscale additive or filler provides simultaneous improvements to multiple characteristics of the material system, has been a significant factor influencing the development and research of composite materials. Of particular interest, as nano-filler material, are single walled carbon nanotubes (SWCNT)s, typically dispersed within a polymer matrix, referred to herein as a CNT-polymer nanocomposite. Numerous studies have proposed and shown SWCNTs to be contributors to enhanced mechanical, electrical, and thermal properties in CNT-polymer nanocomposites relative to pure polymer matrix materials, generally used with structural carbon fiber composites [17, 54, 74, 79]. In an effort to best apply these multifunctional nanocomposites to progress the utility of advanced or smart structures in the aerospace and marine industries reliable and comprehensive quantification and understanding of their properties is essential.

[1] In the context of this thesis "mesh independent" methods are to be distinguished from meshless methods, based on the following definitions: Mesh independent methods operate based on a discrete problem domain representation using finite elements, but does not require a conforming mesh to define discontinuities, hence terminology of *mesh independence*. Meshless methods operate based on a discrete problem domain representation using scattered material points with no element connectivity.

To this end, multiscale models (in which analysis occurs at multiple length scales characteristic of the problem in consideration, and relevant information is passed between scales) have been developed to explore the design space of multifunctional nanocomposites [104, 110]. Recent work focused on CNT-polymer nanocomposites for investigating effects of distribution, orientation, interphase regions, and clustering on effective elastic, electrical, and thermal properties using both analytic and computational micromechanics can be found in References [47, 88, 89, 90, 95]. Additional investigations into the multifunctional effects of CNTs leading to macroscale piezoresistivite response due to inherent CNT piezorestivity and electron hopping phenomenon can be found in References [20, 21, 83]. In a number of these studies computational micromechanics techniques are used to consider complexities not so readily accountable with analytic techniques, particularly with the multifunctional effects. For instance, independent and combined effects of interphase regions and clustering on effective elastic properties are examined in Ref. [47]. A similar study of effects on effective coefficient of thermal expansion are investigated in Ref. [95], where computational methods are used to obtain results at CNT volume fractions with interphase percolation. The intricacies of changing inhomogeneous nanoscale electrostatic behavior is captured with a computational model in Ref. [20], and further extended with the incorporation of coupled electromechanical cohesive zones in Ref. [21] to include damage effects.

In all these studies the standard FEM is utilized as the computational tool within a continuum micromechanics model. The FEM provides the robust numerical power to consider various attributes associated with the nanoscale filler material including size, orientation, clustering, and dispersion in simultaneous analysis. However, drawbacks to the FEM in terms of efficiency and ease of use can be identified if investigating the design space through a parametric study of certain nanocomposite attributes, specifically when they involve changes to the representative problem geometry. In such cases each new geometry must be meshed individually to capture its unique considerations. In exploration of a small set of variables this may be tolerable, but if intending to investigate the influence of a large number of variables in multiple combinations the time and effort required to build each representative geometric model for meshing can be expensive. The proposition of this thesis seeks to alleviate these concerns by demonstrating the performance of a mesh independent enriched FEM as an effective replacement for the standard FEM in such studies. In particular this work proves the locally enriched intrinsic extended finite element method (IXFEM) [38, 39] as a viable choice within the spectrum of mesh independent FEMs.

The advantage in switching to a mesh independent enriched FEM is that description of the problem mor-

phology is separated from the FE mesh, i.e. a mesh conforming to discontinuity interfaces is no longer necessary. For the studies described above this is a major gain to reduce initial overhead with constructing individual representative geometries, and to consider variations on a problem configuration for multiple analyses. "Enrichment" in these methods then refers to the enhancement, through modification, of the standard polynomial approximation function of the FEM, as achieved with the addition of extra (enrichment) functions, for the purposed of incorporating expected behavior in the approximation space characteristic of the discontinuity to be modeled. Suitable enrichment functions are selected based on *a priori* knowledge of the variable field response expected to occur at a discontinuity interface, generally taken from analytic solutions or empirical observation. In the physical world these responses are identified as rapid changes in the field variable or its gradient, and are aptly treated as discontinuities in the approximation function or its derivatives respectively [39]. Discontinuities are most broadly categorized as strong or weak, where strong indicate discontinuous behavior in the primary variable field to be solved, and weak indicate discontinuous behavior in the gradient of the primary variable (secondary variables). Typical examples in material mechanics include cracks and internal void interfaces as strong discontinuities and distinct material interfaces for weak discontinuities. Definitions for enrichment of the approximation space can thus be considered in two senses: theoretically it is the principle of increasing the order of completeness achievable in the approximation, computationally it is the ability to achieve higher accuracy of the expected solution by introducing information from an analogous analytic solution into the approximation [69]. In examining the mathematics of implementation, introduced in Section 1.2 and presented in detail for the IXFEM in Chapters 2 and 3, the computational definition is more fitting.

The underlying foundation for development of enriched FEMs has been the partition of unity method (PUM) [4, 5], for enriching FE or meshfree approximations [13]. It was first applied by Melenk and Babuška [64] in creating the globally enriched partition of unity FEM (PUFEM). Two subsequent particularizations of the PUM include the generalized FEM (GFEM) [97, 99], again using a global enrichment, and the extended FEM (XFEM) [30, 67], proposing a local enrichment scheme. In conception each method utilized a extrinsic enrichment approach, with a later variant of the standard XFEM (i.e. the extrinsic XFEM, EXFEM) established using an intrinsic enrichment [38, 39]. This is the IXFEM, as discussed and utilized in the work that follows. The IXFEM, being a variant of the EXFEM, employs a local enrichment strategy, based on a global decomposition of the problem domain into overlapping subdomains. Within each subdomain a distinct partitions of unity is constructed from either standard FE or specialized enriched shape functions, the

enriched shape functions being generated using the moving least squares (MLS) method through minimization of a weighted error functional. Given selection of an intrinsic basis vector in the MLS computation, a set of functions result which is capable of representing any linear combination of the functions in the intrinsic basis exactly [39]. In contrast to extrinsically enriched FEMs, where the enrichment functions are added to the approximation function through the PUM concept, in the IXFEM the enrichment functions are added to the intrinsic basis producing inherently enriched shape functions through the MLS method which are used directly in defining the approximation function. As with most recent developments of the EXFEM, the IXFEM uses the level-set method (LSM) [76, 93] to describe all discontinuities independent of the domain discretization (i.e. the FE mesh). As implied before, this dramatically facilitates mesh generation as a regular structured grid can quickly be constructed, of simple repeating triangular or rectangular elements. As another advantage, this mesh can easily be repurposed for variations of a problem since it contains minimal specific geometric information, besides overall external boundary dimensions and shape. The unique internal configuration of the problem domain, to be modeled, is instead realized using the LSM to represent existence of all internal discontinuity interfaces. Descriptions of the individual interfaces is achieved using a special class of scalar functions known as level-set functions (LSFs).

An outline of the thesis is as follows: The remainder of Chapter 1 first reviews development of the XFEM and various applications to which it has been applied for analysis during its evolution. Subsequent discussion moves on to the mathematics of the XFEM. Initial focus is given towards the "enrichments" made to the approximation functions, for various FEM formulations employing mesh based enrichment strategies, in this setting the difference of the XFEM to similar computational methods is established. In closing the chapter, differences in the two variants of the XFEM (extrinsic versus intrinsic enrichment) are laid out, and reason for selecting to work with the IXFEM are provided. Chapter 2 introduces the methodologies and numerical techniques that work in combination to create the IXFEM. Highlights of discussion include the domain decomposition strategy to achieve local enrichment, the MLS method to create the enriched shape functions, and the LSM to define internal discontinuity interfaces. In following, Chapter 3 reviews application of the IXFEM for plane linear elastic mechanics, and additional particulars in regards to numerical implementation of the methods described in Chapter 2. Chapter 4 presents the results of this thesis research with corresponding discussion of the findings. Two validation problems precede investigation of the IXFEM for computational characterization of composite materials. A summary of the work done and results obtained is given in Chapter 5, followed by discussion of directions for future work to extend this research and its

results in Chapter 6. In addition a number of appendices are provided at the end providing extended details of specific aspects of the IXFEM, demonstration of the LSM to model discontinuity interfaces and ensuing enriched shape functions, and certain data for the inputs of the results shown in Chapter 4.

1.1 Development and Applications of the XFEM

Since the development of the finite element method, one of the most influenced areas of study has been the simulation and analysis of crack initiation and propagation. Fundamentally founded in the concepts of linear elastic fracture mechanics (LEFM), refer to Ref. [35], the study of cracks and other defects was delivered an indispensable tool with the introduction and rapid development of the FEM. Previous restraints to working with complex geometries and loading cases were nearly all but removed as the power of finite element analysis (FEA) was directed at LEFM. With continuing development the FEM was extended to work with elastic-plastic fracture mechanics (EPFM), and is now applied in almost all computational studies of crack behavior. However, limitations with the FEM still exist to freely model arbitrary cracks, namely the mesh dependency inherent in the conventional FEM, i.e. the constraint that FE mesh element boundaries must define discontinuity interfaces. In the analysis of crack growth this leads to mesh dependence of the solution [62, 71, 111] or requires consistent remeshing between load- or time-steps to resolve [14, 16]. With the introduction of the XFEM these issues were eliminated, through a novel approach exploiting the fundamental idea of partition of unity, allowing cracks (and discontinuity interfaces in general) to be represented and modeled fully independent of the FE mesh.

Development of the XFEM, to be discussed next, was largely an outcome of the extensive research into meshfree methods [13], hence a number of similar techniques first established in such methods are applied in the XFEM, refer to References [5, 11] for an comprehensive overview of meshless methods. Underpinning the enriched local approximations made in the XFEM, over finite elements, or meshfree approximations in the case of meshless methods, is the partition of unity method (PUM) [4, 5] permitting modifications to the FE approximation function, and is considered to be first implemented in a finite element sense for enrichment of the solution space in the work of Melenk and Babuška [64], where it was termed the partition of unity finite element method (PUFEM). The PUFEM is largely considered as the precursor to the well established enriched FEMs of current use, e.g. the GFEM and XFEM. Introduction of the PUM concept in meshless methods can be found in the work of Duarte and Oden [33].

Given the interest by those in the LEFM field to model crack behavior impartial from a FE mesh it is natural that the earliest work in developing the XFEM focused on modeling fracture phenomenon. A description introducing the XFEM for modeling cracks can be found in Ref. [13]. Origins for the application of a local PUM concept to model fracture can be found in Belytschko and Black [8], where crack tip enrichment functions are used for modeling the whole crack, with a mapping to consider small deviations from a straight line crack. For the case of substantially curved cracks remeshing at the crack root was done, hence this formulation was termed a minimal remeshing FEM for fracture. It is in the paper by Moës et al. [67], improving the method of Ref. [8], that a FEM requiring no remeshing for modeling crack propagation is first presented, along with the name extended finite element method (XFEM). Introducing the notion of combining the Heaviside function, to model the crack length, with crack tip enrichment functions, for the singular tip, the works of [67, 30, 31] enabled arbitrarily curved cracks to be fully modeled independent from a FE mesh. Numerous subsequent work continued to expand the capabilities of the XFEM. Branching and intersection of cracks, through superimposing of Heaviside functions, is demonstrated in Ref. [28], expansion to three-dimensions is discussed in Ref. [102] using polar forms of the crack tip enrichment functions in the plane normal to the crack front, more recent improvements to a three-dimensional implementation can be found in References [3, 42]. Enrichment functions including higher order terms in the asymptotic expansion for the crack tip field in two-dimensions are explored in the work of Liu et al. [61], Xiao et al. [108]. A radius of influence for determining the crack tip enrichment domain was investigated in References [6, 56, 105] and showed an improvement in convergence results with mesh refinement. The effect of transition regions, those between non-enriched and enriched domains, in impacting convergence was studied by Laborde et al. [56], these tests were reexamined by Chahine et al. [19] using cutoff weight functions for the enrichment. Stress intensity factors were mostly computed in the early works using the domain form of the J-integral [28, 46, 67, 72], a direct evaluation using enrichment functions defined in terms of stress intensity factors was proposed in Ref. [61], and robust techniques for the J-integral calculation are given in Ref. [59]. Comparisons of the performance of the contour integral, J-integral, and cutoff functions can be found in Ref. [80]. Contact and cohesion of cracks have also be considered, with Dolbow et al. [32] looking at frictional contact for crack growth, and Wells and Sluys [107] using the step function enrichment to solve delamination problems in composites. In Ref. [114] new crack tip enrichment functions for cohesive cracks are proposed using a generalized Heaviside function (or a sign function), further cohesive models in enriched FEMs are described in References [15, 29, 66].

Another area in which the XFEM was rapidly adopted for development was the modeling of materials with granular structures. The ability to define and model the grain boundaries separate from a mesh is a significant advantage in reducing the complex mesh geometries required previously. Work by Belytschko et al. [12] first approximated multibody problems with sliding interfaces using the Heaviside function for the analogous problem of a jointed rock. Several enrichment techniques have been developed, with most only permitting either normal displacements or tangential slip, at grain boundary junctions the techniques discussed in Ref. [33] are needed to handle the intersection of interfaces. Similar to the study of cracks, cohesive laws were added to the XFEM to model normal separation [109], with the subsequent addition of penalty parameters in effort to avoid interpenetration of grains [32].

Representation of discontinuity interfaces using the LSM [76, 93] has become a major component of the XFEM, allowing complicated geometries to be described as simple functions. Curves and surfaces in two- and three-dimensional space respectively are reduce to scalar values stored at the nodes and interpolated elsewhere using FE shape functions, this has further served to facilitate the evaluation of enrichment functions. In the case of moving or growing discontinuities, evolution of the interface is realized by solving a hyperbolic evolution equation governing the level sets [13]. This typically requires projection of the velocity field of the discontinuity interface throughout the problem domain, the fast marching method (FMM) [91, 92] has been found to be particularly effective at this computation in three-dimensions. Specific applications of the XFEM introducing the LSM for crack growth in two dimensions are presented in References [96, 12], with corresponding extension to three-dimensions in References [68, 46]. Treatment for updating the level sets of cracks using the FMM in three-dimensions can be found in the work of Sukumar et al. [100]. Further work with the LSM to modeling multiple branching and intersecting cracks is described in References [18, 63, 115].

Additional areas of study for the XFEM have been dislocations and phase interfaces. Dislocations are treated in a manner similar to cracks, based on the Volterra concept of dislocation [13]. Mesoscale analysis of dislocations are included in References [43, 44, 105] for two-dimensions, References [44, 78] for three-dimension, and in Ref. [78] for thin shells. Phase interface problems are typically paired with the LSM for tracking interfaces. In contrast to the bulk of the work mentioned previously, concentrated on cracks, where the primary variable (often displacement) is discontinuous, in this case it is the gradient of the primary variable (strains and stresses) that may show discontinuities, i.e. weak disconitnuity interfaces. The simplest enrichment function to incorporate this discontinuity in the derivatives is the absolute value function (also refereed to as the ridge or tent function in the literature) [13]. Discontinuous gradients were

first modeled in meshless methods by Krongauz and Belytschko [55], then extended to FEMs through the LSM in References [12, 103]. Initial issues arising in the transition elements, wherein parasitic behavior was introduced in the approximations, was later resolved through various special techniques. Some solutions switched back to using discontinuous enrichment functions and constrained the continuity of the primary variable using Lagrange multiples or a Nitsche's method [51, 70]. This idea was first proposed by Hansbo and Hansbo [48]. One-dimensional thermal and phase change problems using this method are solved in Ref. [65]. Evolving phase boundaries were considered in References [22, 25] through a pairing of the XFEM with the LSM, a combination of the XFEM with the FMM can be found in Ref. [52].

Important issues related to the implementation of the XFEM concern quadrature rules for integration of enriched approximation functions and the impact of transition elements in influencing solution accuracy and convergence rates. Low order Gauss quadrature routines usually applied in the FEM where polynomial approximations are used exclusively are fine, but when the approximation space includes enrichments with singular or discontinuous functions improved strategies are necessary to avoid inaccuracies or poor convergence [8, 67, 97, 98]. Various approaches have been sought. Higher order Gauss quadrature was shown to provide little improvement, while adaptive routines worked for singular functions [97]. Subdomain quadrature has been most popular, wherein enriched elements are subdivided based on the discontinuity path through the element, and a fixed order Gauss rule is used inside each subelement [8, 67]. The works of Béchet et al. [6], Laborde et al. [56] introduced a polar mapping of the quadrature rules to best capture the singular behavior of the crack tip enrichment functions. A transformation to a line or surface integral for two- or three-dimensional problems respectively is also presented in Ref. [106]. Errors in the transition elements were studied by Sukumar et al. [103] and shown to adversely impact convergence rate of problems using the ridge enrichment function, a modified ridge enrichment function was proposed that returned a superior convergence rate. Additional investigation by Chessa et al. [26] found the error to exist due to parasitic terms in the approximation space of transition elements, an assumed strain method was devised eliminating the issue. Other resolutions employed interior penalty methods [45]. The recent approach introduced by Fries [36] uses a ramp function to weigh the contribution of enriched shape functions in transition regions providing a conforming approximation throughout the problem domain satisfying the PUM everywhere, eliminating the partially enriched elements existing in the originally formulation of the XFEM.

Variations on the XFEM for incorporating enrichments have likewise been developed. The work of Hansbo and Hansbo [48] proposed a different form for representation of displacement discontinuities where a new

element is superimposed on top of enriched elements. A conversion of the Heaviside enrichment function using a polynomial B-spline in Ref. [50] permitted traditional Gauss quadrature routines to be used again. The largest modification in implementation would come with the intrinsic enrichment variant of the XFEM developed in References [38, 39]. In this formulation no additional unknowns are introduced in the approximation, instead the approximation space is composed of directly enriched shape functions achieved through minimization of a MLS computation. This approach has been demonstrated for modeling weak and strong discontinuities in materials and fluids in References [37, 38]. A locally enriched space-time XFEM was developed in References [23, 24] to solve hyperbolic problems with discontinuities.

Comprehensive synopses of the history of the XFEM and how it relates to meshless methods and other enriched FEMs can be found in References [13, 40, 69]. From the review provided here it is evident that modeling of stationary and propagating cracks in homogeneous materials has been the main concentration for application and development of the XFEM. Applications of the XFEM for study of composite materials has largely been considered with interface cracks between dissimilar materials [72, 101]. Minimal work has focused on modeling representative composite systems, using the LSM to define the filler material as a weak internal discontinuity, and limited work has set out to prove the XFEM as viable means for computational material characterization analysis. In addition most work continues to develop on the EXFEM, so far the IXFEM has only been introduced as an alternative and proven for a small number of mechanics and fluids problems [38, 39, 37].

1.2 Enrichment of Approximation in Finite Element Methods

The finite element method [81, 82] is a well recognized and proven numerical technique for approximating the solution to a boundary value problem of differential equations. However as described in the motivation the FEM still has its restriction, particularly in the modeling of arbitrary and complex discontinuities. Development of meshless and enriched FEMs aim to eliminate these issues by removing the mesh geometry definition of their interfaces. Enriched FEMs are of particular interest as they exploit the extensive body of knowledge already established for finite element technology and software tools. Herein the enrichment approach developed for various FEMs is discussed beginning from the underlying foundation of the PUM concept utilized to bring in alterations to the approximation functions.

Before presenting the enriched approximations, that of the conventional FEM is presented for comparison.

The FEM is based on an approximation function $u^h(\boldsymbol{x})$, for the desired solution field $u(\boldsymbol{x})$, of the form shown in Eqn. 1.2.1,

$$u(\boldsymbol{x}) \approx u^h_{\mathrm{FE}}(\boldsymbol{x}) = \sum_{n_i \in \mathcal{N}} N_i(\boldsymbol{x}) u_i = \{\boldsymbol{N}(\boldsymbol{x})\}^{\mathrm{T}} \boldsymbol{u} \tag{1.2.1}$$

where summation occurs over the complete nodal set $\mathcal{N}$ discretizing the global domain Ω, $N_i(\boldsymbol{x})$ are standard FE shape functions (denoted as $N_i^{\mathrm{FE}}(\boldsymbol{x})$) having a compact support $\tilde{\Omega}_i$, and u_i are the primary variable values to be determined at corresponding nodes n_i. Expressions for the shape functions are polynomials specific to the element geometry (e.g. triangular or quadrilateral elements) and element order (e.g. linear, bilinear, or quadratic), and can be found in nearly all introductory texts to the FEM. Alternately the expression for the approximation function can be given as shown in Eqn. 1.2.2,

$$u(\boldsymbol{x}) \approx u^h(\boldsymbol{x}) = \sum_{i=1}^{k} p_i(\boldsymbol{x}) a_i = \boldsymbol{p}^{\mathrm{T}}(\boldsymbol{x}) \boldsymbol{a} \tag{1.2.2}$$

where $\boldsymbol{p}(\boldsymbol{x})$ is a column vector of dimension k containing the basis functions of the approximation space (denoted by superscript T to be transposed in Eqn. 1.2.2) and $\boldsymbol{a}$ are unknowns determined from the approximation at the nodes[2]. This form of the approximation will help to identify the difference between extrinsic and intrinsic enrichment schemes as discussed in Section 1.3. Foundation for expansion of the FEM approximation to incorporate enrichment is the partition of unity (PU) concept. A PU is defined for domain Ω_{PU} as a set of n^{f} functions $f_g^{\mathrm{PU}}(\boldsymbol{x}),\ g \in \{1, \ldots, n^{\mathrm{f}}\}$ such that

$$\sum_{f_g \in \Omega_{PU}} f_g^{\mathrm{PU}}(\boldsymbol{x}) = 1 \quad \forall \boldsymbol{x} \in \Omega_{\mathrm{PU}} \tag{1.2.3}$$

The property then exploited in enriched FEMs, is that any function $\zeta(\boldsymbol{x})$ can be reproduced as a product of the PU functions $f_g(\boldsymbol{x})$ with $\zeta(\boldsymbol{x})$ [13, 69], this is demonstrated in Eqn. 1.2.4.

$$\sum_{f_g \in \Omega_{PU}} f_g^{\mathrm{PU}}(\boldsymbol{x}) \zeta(\boldsymbol{x}) = \zeta(\boldsymbol{x}) \tag{1.2.4}$$

By design the FE shape functions satisfy a PU, i.e.

[2]In this formulation it is important to realize the unknowns $\boldsymbol{a}$ are not directly tied to the primary variable(s) $\boldsymbol{u}$ as in the approximation function form of Eqn. 1.2.1.

$$\sum_{n_i \in \mathcal{N}_k^{\mathrm{el}}} N_i(\boldsymbol{x}) = 1 \quad \forall \boldsymbol{x} \in \Omega_k^{\mathrm{el}} \tag{1.2.5}$$

where $\mathcal{N}_k^{\mathrm{el}}$ is the set of p element nodes for an element e_k, with corresponding domain Ω_k^{el}. The PU concept then provides a mathematical framework for enriching the approximation *extrinsically* through the addition of enrichment functions to a standard FEM approximation [39], to be shown next.

Using the PU concept, an extrinsic basis, column vector $\boldsymbol{q}(\boldsymbol{x})$, containing n^{ef} enrichment functions $f_g^{\mathrm{enr}}(\boldsymbol{x}),\ g \in \{1, \ldots, n^{\mathrm{ef}}\}$ as defined in Eqn. 1.2.6, can be added to the FEM approximation to increase the order of completeness as shown in Eqn. 1.2.7.

$$\boldsymbol{q}(\boldsymbol{x}) = \{f_1^{\mathrm{enr}}(\boldsymbol{x}), f_2^{\mathrm{enr}}(\boldsymbol{x}), \ldots, f_{n^{\mathrm{ef}}}^{\mathrm{enr}}(\boldsymbol{x})\}^{\mathrm{T}} \tag{1.2.6}$$

$$u_{\mathrm{PU}}^h(\boldsymbol{x}) = \sum_{n_i \in \mathcal{N}} N_i(\boldsymbol{x}) u_i + \sum_{f_g \in \Omega_{PU}} f_g^{\mathrm{PU}}(\boldsymbol{x}) \boldsymbol{q}^{\mathrm{T}}(\boldsymbol{x}) \boldsymbol{b}_g \tag{1.2.7}$$

The first part of the approximation function is that of the standard FEM u_{FE}^h, equivalent to Eqn. 1.2.1, the second is the PU enrichment $\tilde{u}_{\mathrm{PU}}^h$, where $\boldsymbol{b}_g$ are additional unknowns (extra degrees of freedom) that regulate the enrichment functions $f_g^{\mathrm{enr}}(\boldsymbol{x})$, of vector $\boldsymbol{q}(\boldsymbol{x})$, to best approximate the associated enriched solution. Functions f_g^{PU} are defined to satisfy a PU over the enriched support domain $\Omega_{\mathrm{PU}}^{\mathrm{enr}}$, and ensure a local support region for the enrichment functions. This formulation is considered the partition of unity method of References [4, 5].

First to implement the PUM concept, the partition of unity finite element method [64] uses classical FE shape functions $N_i(\boldsymbol{x})$ for the PU functions $f_g^{\mathrm{PU}}(\boldsymbol{x})$ in Eqn. 1.2.7, and enriches the global solution at every node n_i as defined in the second summation term of Eqns. 1.2.8.

$$u_{\mathrm{PUFE}}^h(\boldsymbol{x}) = \sum_{n_i \in \mathcal{N}} N_i(\boldsymbol{x}) u_i + \sum_{n_i \in \mathcal{N}} N_i(\boldsymbol{x}) \boldsymbol{q}^{\mathrm{T}}(\boldsymbol{x}) \boldsymbol{b}_i \tag{1.2.8a}$$

$$u_{\mathrm{PUFE}}^h(\boldsymbol{x}) = \sum_{n_i \in \mathcal{N}} N_i(\boldsymbol{x}) u_i + \sum_{n_i \in \mathcal{N}} N_i(\boldsymbol{x}) \sum_t q_t(\boldsymbol{x}) b_{it} \tag{1.2.8b}$$

In these expressions all variables are as defined previously, where u_i and b_{it} are the unknown primary variables and extra coefficients to be solved respectively, and in Eqn. 1.2.8b $t = \{1, \ldots, n^{\mathrm{ef}}\}$, such that

$n^{\text{ef}} = \dim(\boldsymbol{q}(\boldsymbol{x}))$.

The generalized finite element method [97, 99] follows very closely to that of the PUFEM, except different interpolation functions are used for the FE u^h_{FE} and enriched $\tilde{u}^h_{\text{GFE}}$ portions of the approximation function, as indicated in Eqn. 1.2.9.

$$u^h_{\text{GFE}}(\boldsymbol{x}) = \sum_{n_i \in \mathcal{N}} N_i(\boldsymbol{x}) u_i + \sum_{n_i \in \mathcal{N}} \tilde{N}_i(\boldsymbol{x}) \boldsymbol{q}^{\text{T}}(\boldsymbol{x}) \boldsymbol{b}_i \tag{1.2.9}$$

Standard FE functions $N_i(\boldsymbol{x})$ are used for the FE approximation portion, while various other functions satisfying a PU can be used for $\tilde{N}_i(\boldsymbol{x})$ in the enriched approximation portion. In first introduction the GFEM, like the PUFEM, employed a global enrichment of the nodes, but as these methods have matured in development they have also seen changes in formulation, and like the XFEM have implemented localized enrichment. Thus the distinction between the PUFEM, GFEM, and XFEM has become less distinct in recent years [40].

As pioneered by Belytschko and colleagues the *extrinsic* extended finite element method [30, 67] was first to introduce a local enrichment strategy, based on proximity of elements to discontinuity interfaces, in the approximation function, for the purposes of reducing the added computational cost of the extra unknowns. Like the GFEM different interpolation functions can be used with the FE and enriched portions of the approximation, but generally they are taken to be equivalent [13], i.e. $\tilde{N}(\boldsymbol{x}) = N(\boldsymbol{x})$ in Eqns. 1.2.10.

$$u^h_{\text{EXFE}}(\boldsymbol{x}) = \sum_{n_i \in \mathcal{N}} N_i(\boldsymbol{x}) u_i + \sum_{n_i \in \tilde{\mathcal{N}}'} \tilde{N}_i(\boldsymbol{x}) \boldsymbol{q}^{\text{T}}(\boldsymbol{x}) \boldsymbol{b}_i \tag{1.2.10a}$$

$$u^h_{\text{EXFE}}(\boldsymbol{x}) = \sum_{n_i \in \mathcal{N}} N_i(\boldsymbol{x}) u_i + \sum_{n_i \in \tilde{\mathcal{N}}'} \tilde{N}_i(\boldsymbol{x}) \sum_t q_t(\boldsymbol{x}) b_{it} \tag{1.2.10b}$$

As indicated by the approximation function, a FE approximation exists over the entire global nodal set $\mathcal{N}$ while the enrichment is computed for a specific nodal subset $\tilde{\mathcal{N}}'$. These particular nodes would be those that define elements containing segments of the discontinuity interface approximation Γ^h_{disc} described through the LSM, i.e. elements "cut" by the discontinuity. In general there can exist $\tilde{n}^\Omega$ nodal subsets $\tilde{\mathcal{N}}'$ such that the global approximation of the EXFEM takes the form,

$$u^h_{\text{EXFE}}(\boldsymbol{x}) = \sum_{n_i \in \mathcal{N}} N_i(\boldsymbol{x}) u_i + \sum_{n_i \in \tilde{\mathcal{N}}'_1} \tilde{N}_i(\boldsymbol{x}) \boldsymbol{q}_1^{\mathrm{T}}(\boldsymbol{x}) \boldsymbol{b}_i + \ \ldots \ + \sum_{n_i \in \tilde{\mathcal{N}}'_m} \tilde{N}_i(\boldsymbol{x}) \boldsymbol{q}_m^{\mathrm{T}}(\boldsymbol{x}) \boldsymbol{b}_i \tag{1.2.11}$$

where a distinct enrichment of the approximation function occurs for each discontinuity enclosing nodal subset $\tilde{\mathcal{N}}'_m,\ m \in \{1, \ldots, \tilde{n}^{\Omega}\}$.

For all the enriched FEMs defined thus far (PUFEM, GFEM, EXFEM) the enrichment is brought into the approximation function by adding an extrinsic enrichment set of functions $\boldsymbol{q}(\boldsymbol{x})$ to the original standard FE approximation. In contrast, development of the *intrinsic* extended finite element method [38, 39] introduced an enriched FEM without additional unknowns, as the enrichment is instead directly built into the shape functions where appropriate, through utilization of the MLS method. The approximation function for the IXFEM is then expressed as,

$$u^h_{\text{IXFE}}(\boldsymbol{x}) = \sum_{n_i \in \mathcal{N}} \hat{N}_i(\boldsymbol{x}) u_i \tag{1.2.12}$$

where the "hat" on the shape functions $\hat{N}_i(\boldsymbol{x})$ emphasizes the variability and difference of the shape functions in the approximation of the IXFEM compared to the standard FEM of Eqn. 1.2.1[3]. In regions free of discontinuities, shape functions $\hat{N}_i(\boldsymbol{x})$ are set equivalent to standard FE interpolation functions, as the polynomial approximation afforded by $N_i^{\text{FE}}(\boldsymbol{x})$ are sufficient to capture the response away from discontinuities. However in the vicinity of discontinuities special enriched shape functions are constructed based on a intrinsic basis $\boldsymbol{p}(\boldsymbol{x})$, in contrast to the extrinsic basis $\boldsymbol{q}(\boldsymbol{x})$ used with the EXFEM, supplemented with the same enrichment functions $f_g^{\text{enr}}(\boldsymbol{x})$ as would be used in an EXFEM formulation through $\boldsymbol{q}(\boldsymbol{x})$. Lastly in transition regions, a superposition of FE and enriched shape functions is defined using ramp functions, ensuring a conforming approximation over the global domain Ω. Given the similarity of Eqn. 1.2.12 for the approximation function in the IXFEM, where enrichment is completely contained within the shape functions, to that of Eqn. 1.2.1 for the FEM, numerical operation of the IXFEM can be considered to operate in a manner most similar to the standard FEM.

[3]Hidden in Eqn. 1.2.12 is the logic to identify distinct regions in which different approximations are built, this will be covered in reviewing the domain decomposition strategy.

1.3 Realization of Enrichment - Extrinsic versus Intrinsic in the XFEM

In the previous section several approaches for modifying the approximation function in enriched FEMs were presented. The PUFEM, GFEM, and EXFEM can all be considered particularizations of the PUM, as they all implement approximations of the form,

$$u^h(\boldsymbol{x}) = \sum_{n_i} N_i(\boldsymbol{x}) u_i + \text{enrichment terms} \tag{1.3.1}$$

where specialized enrichment functions are added in extension to the standard FE approximation space. This is recognized as an extrinsic enrichment. Looking at the EXFEM in particular the approximation function Eqn. 1.2.10 can rewritten concisely as,

$$u^h_{\text{EXFE}}(\boldsymbol{x}) = u^h_{\text{FE}}(\boldsymbol{x}) + \tilde{u}^h_{\text{EXFE}}(\boldsymbol{x}) \tag{1.3.2a}$$

$$u^h_{\text{EXFE}}(\boldsymbol{x}) = \boldsymbol{p}^{\text{T}}(\boldsymbol{x})\boldsymbol{a} + \tilde{\boldsymbol{q}}^{\text{T}}(\boldsymbol{x})\boldsymbol{b} \tag{1.3.2b}$$

where the FE and extrinsically enriched portion of the approximation are denoted by u^h_{FE} and $\tilde{u}^h_{\text{EXFE}}$ accordingly, in Eqn. 1.3.2a. In the second form, Eqn. 1.3.2b, these components of the approximation are defined in terms of basis vectors $\boldsymbol{p}(\boldsymbol{x})$ and $\tilde{\boldsymbol{q}}(\boldsymbol{x})$, specifying the polynomial functions for the standard FE and the n^{ef} localized enrichment functions f^{enr}_g for the enriched approximation respectively ($\tilde{\boldsymbol{q}}(\boldsymbol{x})$ here indicates the multiplication between interpolation functions $\tilde{N}_i(\boldsymbol{x})$ and extrinsic basis $\boldsymbol{q}(\boldsymbol{x})$ in Eqn. 1.2.10). The unknowns $\boldsymbol{a}$ are associated with the primary variables to be determined at nodes n_i while unknowns $\boldsymbol{b}$ are associated with the extra degrees of freedom at the nodes coming from addition of the enrichment functions. This is the major contributor to the added computational cost in the EXFEM, as adaptive expansion of the global system of equations is required to introduce these new unknowns, culminating in an enlarged matrix expression $\mathbf{Ku} = \mathbf{F}$ which must be solved for $\mathbf{u}$. This representation of the algebraic systems of equations is referred to as the FE model in this work and is comprised of stiffness matrix $\mathbf{K}$, force vector $\mathbf{F}$, and unknowns vector $\mathbf{u}$, refer to Ref. [69, chap. 3] to see directly how these matrix and vector variables are expanded in the global sense to account for the extra unknowns.

As mentioned previously, the IXFEM removes the extrinsic enrichment portion in the approximation function in favor of a direct intrinsic enrichment of the shape functions. In the same sense as done above the

approximation function Eqn. 1.2.12 can be rewritten concisely as,

$$u^h_{\mathrm{IXFE}}(\boldsymbol{x}) = \hat{u}^h_{\mathrm{IXFE}}(\boldsymbol{x}) \tag{1.3.3a}$$

$$u^h_{\mathrm{IXFE}}(\boldsymbol{x}) = \hat{\boldsymbol{p}}^{\mathrm{T}}(\boldsymbol{x})\hat{\boldsymbol{a}} \tag{1.3.3b}$$

where the "hat" again emphasizes the variability of the shape functions, as essential to operation of the IXFEM. Alternatively defined based on intrinsic basis vector $\hat{\boldsymbol{p}}(\boldsymbol{x})$, in Eqn. 1.3.3b, it is the selection of functions in $\hat{\boldsymbol{p}}(\boldsymbol{x})$ which dictate the form that the shape functions $\hat{N}_i(\boldsymbol{x})$ take in the approximation. In regions devoid of discontinuities a strictly polynomial basis $\boldsymbol{p}^{\mathrm{poly}}$ (corresponding to the problem domain dimensions and element order) can be used to recreate standard polynomial FE shape functions in MLS method. However in regions including a discontinuity the polynomial basis functions are supplemented with enrichment functions $f^{\mathrm{enr}}_g(\boldsymbol{x})$ contained in basis $\tilde{\boldsymbol{p}}^{\mathrm{enr}}$, see Eqn. 1.3.4. Together they form the intrinsic enriched basis $\boldsymbol{p}^{\mathrm{enr}}$, as defined in Eqn. 1.3.5, which when used in the MLS method generates inherently enriched shape functions [38].

$$\tilde{\boldsymbol{p}}^{\mathrm{enr}}(\boldsymbol{x}) = \{f^{\mathrm{enr}}_1(\boldsymbol{x}), f^{\mathrm{enr}}_2(\boldsymbol{x}), \ldots, f^{\mathrm{enr}}_{n^{\mathrm{ef}}}(\boldsymbol{x})\}^{\mathrm{T}} \tag{1.3.4}$$

$$\boldsymbol{p}^{\mathrm{enr}}(\boldsymbol{x}) = \{\boldsymbol{p}^{\mathrm{poly}}(\boldsymbol{x}), \tilde{\boldsymbol{p}}^{\mathrm{enr}}(\boldsymbol{x})\}^{\mathrm{T}} \tag{1.3.5}$$

Comparing Eqns. 1.3.4 to 1.2.6 it is shown that the same functions which are added extrinsically in the EXFEM are instead added intrinsically in the IXFEM. This eliminates the extra unknowns and their associated computational cost in solving the FE model when using the IXFEM, however the increase in cost comes from constructing the enriched MLS shape functions as it requires a matrix inversion for all points of evaluation, this will be discussed in further detail in Section 2.2.

In summary from comparing the newly developed IXFEM, from References [38, 39], to the EXFEM, from References [8, 67], the following features are discerned (it is because of features 2 and 3 the IXFEM was designated the *intrinsic* XFEM):

1. Both methods implement their approximation enrichment locally, i.e. only where needed, effectively minimizing the increase in computational work that comes with utilizing "extended" FEM approaches.

2. The supplementary enrichment functions $\tilde{\boldsymbol{p}}^{\text{enr}}(\boldsymbol{x})$ incorporated into the enriched intrinsic basis $\boldsymbol{p}^{\text{enr}}(\boldsymbol{x})$ for the IXFEM are consistent with those of $\boldsymbol{q}(\boldsymbol{x})$ added extrinsically in the EXFEM approximation function.

3. In the IXFEM, enrichment is realized intrinsic to specialized shape functions, in doing so no additional unknowns are introduced in the approximation. This is the distinguishing feature of the IXFEM from the EXFEM.

4. No inconsistencies appear in partially enriched (transition) elements, coming out of the local enrichment strategy, in native implementation of the IXFEM. This is in contrast to the native EXFEM where systematic errors are prevalent in transition elements, hindering optimal convergence for some applications, as shown in References [26, 56]. A proposed *corrected* EXFEM has since been introduced to resolve this issue [36]

5. Extending the viable approximation by enrichment, both methods introduce added complexity and greater computational expense compared to conventional FE approximations. In the IXFEM increased work lies in evaluating the enriched MLS shape functions. Whereas in the EXFEM extra work lies with the additional unknowns involved in the approximation. For either method the increased computational cost is directly related to the number of enrichment functions added to the underlying standard FE approximation. Realized as the extra functions $\tilde{\boldsymbol{p}}^{\text{enr}}(\boldsymbol{x})$ included in the IXFEM enriched intrinsic basis, or the extra functions $\boldsymbol{q}(\boldsymbol{x})$ included in the EXFEM approximation. Furthermore, as the enrichment information culminates in the approximation function $u^h(\boldsymbol{x})$ for the two methods more involved integration and differentiation techniques are necessary for processing the weak form and post-processing the solution respectively.

6. Post-processing for the IXFEM is more straight forward in its implementation because Eqn. 1.2.12 is easier to work with then Eqn. 1.2.10.

Given these differences between the two variants of the XFEM, reasons for selecting to work with the IXFEM were based on three key factors. Primarily its avoidance of introducing extra unknowns is a substantial advantage in this study[4] where high numbers of discontinuities will be considered in the ultimate analysis of randomly aligned CNT-polymer nanocomposites. Secondly, even though Ref. [13] cites the IXFEM as

[4] A comparative analysis of the computational cost, in terms of time or number of operations, of the EXFEM versus IXFEM for equivalent problems is not reported in this work as it was not a research objective to compare the two methods.

being more complex in method than the standard XFEM (referring to the EXFEM) for enrichment of discontinuities, it is the author's opinion that the similarity of the approximation function form to that of the FEM significantly facilities integration of the methodology of the IXFEM in the framework of the standard FEM. Lastly, given the limited amount of work done using the IXFEM in current literature, it was a secondary objective of this research to contribute and advance the body of knowledge and resources associated with the IXFEM.

2 Description of Numerical Methods

The methodologies and numerical techniques discussed and implemented herein are those establishing the intrinsic extended finite element method, as developed by Fries and Belytschko [38, 39], purposefully designed and selected to formulate a mesh based, locally enriched FEM without additional unknowns. Together their application leads to an intrinsic enrichment approach centered in the construction of special *enriched* shape functions which enhance the approximation in the vicinity of discontinuities. Designated subdomains for assembling differing PUs are realized through an initial global domain decomposition, based on definition of discontinuity interfaces by the LSM. Those regions containing discontinuities are suitably accounted for by appropriate selection of an enriched intrinsic basis to be used in the MLS method for evaluation of the enriched shape functions. Standard FE shape functions are utilized elsewhere as polynomial approximations remain adequate in capturing the system response faraway from discontinuities. Transition regions, those connecting non-enriched and enriched subdomains, use a linear superposition of standard FE and enriched MLS shape functions to ensure continuity of the approximation. With the approximation enrichment contained solely in the special shape functions the procedure can in a straight forward fashion be implemented in the well-established and developed finite element framework of knowledge.

This chapter reviews the tactics and numerical methods implemented in the IXFEM and introduces their integration in the finite element framework. Details of the domain decomposition strategy are presented first in Section 2.1, for realization of localized enrichment. With subsequent description on the involvement of ramp functions to achieve coupling of resulting subdomains through transition, or blending, regions. The utility of the MLS method to generate enriched shape functions is explained in Section 2.2, with further notes on the implications to the MLS method based on the enriched intrinsic basis discussed afterward. Definition of specialized mesh-based weight functions are also provided to guarantee stability in evaluation of the enriched MLS shape functions. Lastly the LSM is described in Section 2.3, for defining and tracking of discontinuity interfaces independent from the FE mesh.

2.1 Mesh Based Enrichment

2.1.1 Domain Decomposition for Local Enrichment

Designed as a variable approximating FE technique, through a PUM-concept, the IXFEM operates within the conventional FEM framework [38], thus domain discretization follows directly from FE mesh principles. The global domain $\Omega \in \mathbb{R}^d$ is taken to be partitioned into n^{el} elements $e_k, k \in \{1, \ldots, n^{\text{el}}\}$ each with corresponding element domain Ω_k^{el}. The union ($\bigcup$) of all elements and element domains is the element set $\mathcal{E}$ and the global domain Ω respectively.

$$\mathcal{E} = \bigcup_{k=1}^{n^{\text{el}}} e_k = \{e_1, \ldots, e_{n^{\text{el}}}\} \tag{2.1.1}$$

$$\Omega = \bigcup_{k=1}^{n^{\text{el}}} \Omega_k^{\text{el}} = \{\Omega_1^{\text{el}}, \ldots, \Omega_{n^{\text{el}}}^{\text{el}}\} \tag{2.1.2}$$

With each element e_k having p element nodes indicated by $\mathcal{N}_k^{\text{el}} \in (\mathbb{N}^+)^p$ collectively totaling n^{nd} nodes $n_i, i \in \{1, \ldots, n^{\text{nd}}\}$ in Ω. The union of all element nodes, or all nodes considered individually, is the complete nodal set $\mathcal{N}$.

$$\mathcal{N} = \bigcup_{k=1}^{n^{\text{el}}} \mathcal{N}_k^{\text{el}} = \bigcup_{i=1}^{n^{\text{nd}}} n_i = \{n_1, \ldots, n_{n^{\text{nd}}}\} \tag{2.1.3}$$

To perform, as needed, local enrichment distinct to the discontinuities present in the problem domain necessitates division of its entirety into categorized regions which are properly managed. Identification of these assorted regions is determined through evaluation of the LSM function(s), to be described further in Section 2.3, at the discrete nodes. Based on the resulting values the global domain is decomposed into subsets of elements, or equivalently element subdomains, and corresponding subsets of nodes. Within these subdomains, to be defined subsequently, appropriate shape functions are used to construct different PUs. Where the solution behavior is expected to behave in a manner suitably approximated by a continuous polynomial (far enough away from discontinuities) standard FE shape functions are used. However, in the vicinity of discontinuities the solution will show pronounced non-polynomial behavior which the enriched shape functions are designed to accommodate [39]. In transition subdomains a weighted linear superposition of standard and enriched shape functions is created, through the use of ramp functions, to obtain a single

shape function per node to build the overall PU.

Presentation of the domain decomposition methodology and nomenclature discussed here follows closely from References [38, 39]. Deviation in the procedure, as described herein, pertains to the initial information used in partitioning the domain, i.e. node based information versus element based information to delineate subdivisions of the global domain. In the paper by Fries and Belytschko [38], introducing the IXFEM, domain decomposition starts from a predetermined global division of the total nodal set $\mathcal{N}$, from which element subdomains and further nodal subsets are derived. Whereas in this thesis decomposition starts from a predetermined global division of the total element set $\mathcal{E}$, from which nodal subsets and further element subdomains are derived. The reason for this change in approach is to promote an element first based classification philosophy for domain decomposition, with all nodal information being inferred from the element class (non-enriched, enriched, or transition). In the author's view, this manner of thinking, keeping element identity foremost in mind, meshes best to link the concept of a locally enriched approximation to its local domain of influence, i.e. an enriched element domain, which is paramount when developing an IXFEM code. Explanation on how the preliminary element subsets are first identified is provided in Section 3.2.2. Recalling Eqns. 2.1.1 and 2.1.2, it is observed that the complete element set $\mathcal{E}$ and global domain Ω are analogous, therefore identification of element subsets are interchangeable with element subdomains. Moving forward the domain decomposition will be considered in terms of element subdomains and nodal subsets, this keeps inline with Ref. [38].

For a global domain as shown in Figure 2.1 the element domain set Ω is taken to be decomposed into n^{Ω} non-complementary element subdomains $\Omega'_m, m \in \{1, \ldots, n^{\Omega}\}$, indicated as the shaded element regions in the figure. By "non-complementary" it is meant that the union of all subdomains Ω'_m does not equate to the global domain, i.e. $\Omega \neq \bigcup_{m=1}^{n^{\Omega}} \Omega'_m$, this property is demonstrated in Figure 2.1. Paired nodal subsets $\mathcal{N}'_m$, for subdomains Ω'_m, are composed from the union of all nodes on the elements in Ω'_m,

$$\mathcal{N}'_m = \bigcup_{e_k \in \Omega'_m} \mathcal{N}^{\mathrm{el}}_k, \quad \{k = 1, \ldots, n^{\mathrm{el}}\} \tag{2.1.4}$$

such that the n^{Ω} corresponding nodal subsets $\mathcal{N}'_m$ are complementary. In this sense, "complementary" indicates that the union of all nodal subsets is equivalent to the global nodal set $\mathcal{N}$, defined earlier in Eqn. 2.1.3, and that the intersection ($\bigcap$) of distinct subsets is an empty set ($\emptyset$). These two properties are expressed mathematical in Eqn. 2.1.5.

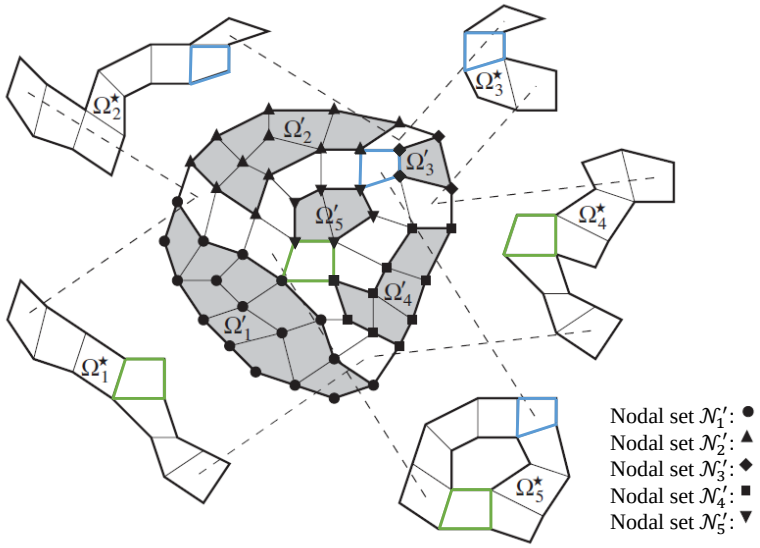

Figure 2.1: Representative decomposition of a global domain Ω into element subdomains Ω_m' (shaded element regions), with corresponding nodal subsets $\mathcal{N}_m'$ as listed in the key, and transition element subdomains Ω_m^* (white element regions). The green and blue outlined elements demonstrate transition elements belonging to multiple transition subdomains (from Ref. [38]: Reprinted with permission from John Wiley and Sons).

$$\mathcal{N} = \bigcup_{m=1}^{n^\Omega} \mathcal{N}_m' \quad \text{and} \quad \mathcal{N}_m' \bigcap \mathcal{N}_n' = \emptyset \quad \forall m \neq n \tag{2.1.5}$$

It is important to understand that each subdomain Ω_m' is comprised of elements exclusively identified as non-enriched or enriched (of a single type: weak, strong, or singular tip), but this distinction is not made here, as these regions are treated in a consistent manner during the domain decomposition. All conjoining non-enriched or enriched elements are collected into a subdomain Ω_m', from which corresponding nodal subset $\mathcal{N}_m'$ is determined. In fact, for the purpose of screening elements to partition the global domain it is only necessary to discern a difference between dissimilar element types. Recognition of the particular class to which an element belongs is only essential when constructing the approximation over its domain, since the corresponding appropriate enriched intrinsic basis must be used in the MLS procedure for generation of the enriched shape functions.

Elements immediately bordering a subdomain Ω_m', shown in white in Figure 2.1, and further illustrated by the cutout element regions, are referred to as transition, or blending, elements. Collectively, the transition elements surrounding subdomain Ω_m' form the neighboring transition subdomain Ω_m^*. Thus given n^Ω distinct

subdomains Ω'_m, in the global domain, i.e. provided $n^{\Omega} \geq 2$, there must exist an equivalent n^{Ω} number of associated transition subdomains Ω^*_m, connecting adjacent subdomains Ω'_n. For transition elements their element node set $\mathcal{N}^{\text{el}}_k, e_k \in \Omega^*_m$ includes nodes from multiple nodal subsets $\mathcal{N}'_n$ with at least one node originating from the nodal subset $\mathcal{N}'_m$. Therefore, transition subdomain nodal subsets $\mathcal{N}^*_m$ will also include nodes from multiple nodal subsets $\mathcal{N}'_n$ as follows.

$$\mathcal{N}^*_m = \bigcup_{e_k \in \Omega^*_m} \mathcal{N}^{\text{el}}_k \quad \{k = 1, \ldots, n^{\text{el}}\} \tag{2.1.6}$$

Lastly, given the n^{Ω} paired subdomains, Ω'_m with Ω^*_m, and nodal subsets, $\mathcal{N}'_m$ with $\mathcal{N}^*_m$, an equal number of n^{Ω} overlapping subdomains and nodal subsets can be declared, based on their associated unions, designated Ω_m and $\mathcal{N}_m$ respectively. Element subdomain Ω_m is the direct union of subdomain Ω'_m with its surrounding transition subdomain Ω^*_m, i.e.

$$\Omega_m = \Omega'_m \bigcup \Omega^*_m \tag{2.1.7}$$

and the nodal subset $\mathcal{N}_m$ is the union of all element nodes belonging to the combined element subdomain Ω_m

$$\mathcal{N}_m = \bigcup_{e_k \in \Omega_m} \mathcal{N}^{\text{el}}_k \quad \{k = 1, \ldots, n^{\text{el}}\} \tag{2.1.8}$$

or similar to Eqn. 2.1.7, $\mathcal{N}_m = \mathcal{N}'_m \bigcup \mathcal{N}^*_m$. Given these expressions it is evident that overlap of these subdomains Ω_m, or nodal subsets $\mathcal{N}_m$, is confined to the regions that have already been identified as transition subdomains Ω^*_m. In final observation from Figure 2.1 and the subdomain definitions introduced it is noted that subdomains Ω'_m neither overlap nor share any boundaries with one another. However, they are connected by the transition regions Ω^*_m that separate them. Also the element subdomains Ω_m contains all elements of the subdomain Ω'_m, therefore $\Omega'_m \subset \Omega_m$, and likewise for the nodal subsets $\mathcal{N}'_m \subset \mathcal{N}_m$.

2.1.2 Domain Decomposition Coupling

In an effort to minimize the computational cost associated with construction and evaluation of the enriched shape functions, the IXFEM is designed to implement the special shape functions only where necessary, hence

terminology of *local enrichment*. This is achieved through the domain decomposition strategy presented in Section 2.1.1, as enrichment of the solution will be confined to specific subdomains Ω'_m that include discontinuities. Those subdomains Ω'_m that are free of discontinuities can be treated with standard FE shape functions, where their ease of use in approximation remains favorable.

From the global domain decomposition differing PUs are selectively built on the overlapping subdomains Ω_m, with corresponding nodal subsets $\mathcal{N}_m$. That is to say the shape functions $\hat{N}_i(\boldsymbol{x})$ defined for all nodes n_i in subset $\mathcal{N}_m$, which exist on subdomain Ω_m, belong to a certain class, non-enriched or enriched. Since the nodal subsets $\mathcal{N}_m$ are overlapping (non-complementary, in that they void the definition provided in Eqn. 2.1.5, their intersections will not yield empty sets) some nodes within $\mathcal{N}_m$ will be used again with another nodal subset $\mathcal{N}_n : n \neq m$ to generate a different PU, thus these nodes will have multiple defined shape functions allotted to them. The nodes for which this occurs are those that makeup the elements in the transition subdomains Ω^*_m, nodal subsets $\mathcal{N}^*_m$. To create an individual shape function for each of these nodes a coupling technique is utilized; this ensures only one resulting shape function form is defined per node for the global domain.

Coupling methods for variable PUs are described in References [10, 49]. Following the recommendation of Ref. [38] the method as discussed in [10] is employed in this study. This technique uses ramp functions $R(\boldsymbol{x})$ to couple the co-existing shape functions by means of a weighted linear superposition, the weight measure being the scalar value of the ramp function at coordinate $\boldsymbol{x}$. In doing so this approach is easily extendable to coupling multiple PUs in a single element [38]. Alternatively, the technique described in Ref. [49] uses a modified MLS approach, but is not as well suited to coupling more than two PUs [38].

Utilizing the coupling technique of Ref. [10] a ramp function $R_m(\boldsymbol{x})$ is defined for each subdomain Ω_m, based on the nodal subset $\mathcal{N}'_m$, refer to Eqn. 2.1.4, as follows

$$R_m(\boldsymbol{x}) = \sum_{n_i \in \mathcal{N}'_m} N_i^{\mathrm{FE}}(\boldsymbol{x}) \quad \forall \boldsymbol{x} \in \Omega_m \tag{2.1.9}$$

where N_i^{FE} are standard FE shape functions, taken as bilinear interpolation functions in this work, having a maximum value of 1 at corresponding node n_i and returning to zero at the function compact support boundary. Within a subdomain Ω'_m, summation of the corresponding ramp function $R_m(\boldsymbol{x})$ is thus constant, with weight value 1. In the associated surrounding transition subdomain Ω^*_m, the ramp function decreases

monotonically from 1 to 0 from the perimeter nodes of $\mathcal{N}'_m$ to the perimeter nodes of $\mathcal{N}_m$ respectfully. Outside of subdomain Ω_m, ramp function $R_m(\boldsymbol{x})$ has constant weight value 0, as no further contributions exist from the weight functions of nodes $\mathcal{N}'_m$, used in defining the ramp function. This behavior of the ramp functions is shown in Figure 2.2, based on the domain decomposition from Figure 2.1.

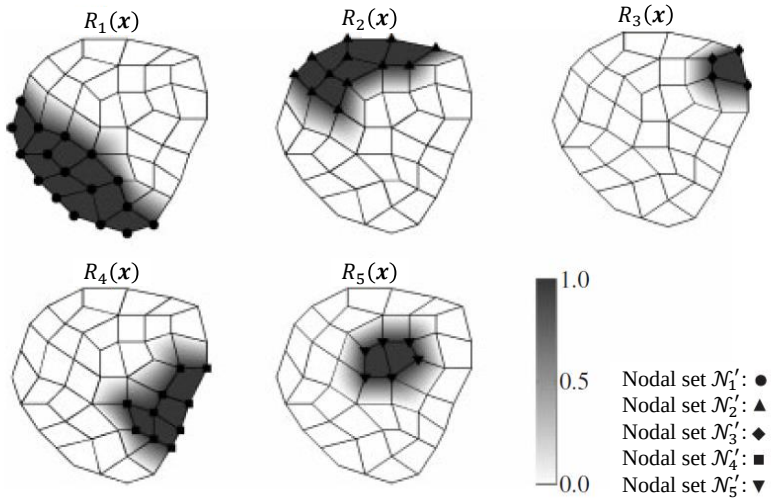

Figure 2.2: Representative ramp functions $R_m(\boldsymbol{x})$ for subdomains Ω_m, based on the global domain decomposition of Figure 2.1 (from Ref. [38]: Reprinted with permission from John Wiley and Sons).

Examining the ramp function weight value contours in Figure 2.2, based on complementary nodal subsets $\mathcal{N}'_m$, it is observable that the sum of the n^Ω ramp functions is unity over the global domain, i.e.

$$\sum_{m=1}^{n^\Omega} R_m(\boldsymbol{x}) = 1, \quad \forall \boldsymbol{x} \in \Omega \tag{2.1.10}$$

with overlap of distinct ramp functions only occurring in the transition subdomains. Using the ramp function of Eqn. 2.1.9, resulting coupled transition shape functions $N_i^{\mathrm{TR}}(\boldsymbol{x})$ are defined over transition subdomains Ω^*_m as the linear combination of the product of overlapping ramp functions $R_n(\boldsymbol{x})$, $n \in \{1, \ldots, n^\Omega\}$, acting as weighting terms, and the multiple defined shape functions $\hat{N}_i^n(\boldsymbol{x})$ existing on corresponding nodal subset $\mathcal{N}^*_m$.

$$N_i^{\mathrm{TR}}(\boldsymbol{x}) = \sum_{m \in J} R_m(\boldsymbol{x}) \cdot \hat{N}_i^m(\boldsymbol{x}), \quad J = \{m = 1, \ldots, n^\Omega : n_i \in \mathcal{N}^*_m\} \tag{2.1.11}$$

This coupling of the PUs allows common terms from the intrinsic bases, to be defined in Section 2.2 in terms of their application within the MLS method, of the shape functions in Eqn. 2.1.11 to be reproduced [38]. For the enriched intrinsic bases of interest to material mechanics, as defined in Section 3.1.2, these common terms will be monomials representative of a linear approximation. Therefore the transition shape functions are at least capable of representing a linear solution over the global domain.

As a final note for numerical implementation, in an element based code, it is only within the transition subdomains Ω_m^* that shape functions belonging to different PUs have to be evaluated. In subdomains Ω_m' only one class of shape functions is evaluated, non-enriched or enriched, based on the appropriate PU for that region. Further discussion on numerical implementation is presented in Section 3.2, with greater detail of certain aspects included in Appendix A.

2.2 Enriched Shaped Function Generation

2.2.1 Moving Least Squares Method

The MLS method is a numerical technique for the continuous local interpolation of a function based on minimizing a "moving" weighted least squares error functional [57, 73]. Ensuring localization of the resulting approximation, the weight function is designed with a compact support and bias towards the region around the point of construction. As the point of evaluation for the MLS fit is arbitrary it can be taken to exist anywhere in the domain giving rise to formulation of a continuous local approximation. The interpolant, as derived using the MLS method, is controlled through the selection of the intrinsic basis vector for the approximation function. Polynomial fits are produced using a strictly monomial basis, while specifically formulated bases can be used to generate fits characteristic of the function components in the intrinsic basis (e.g. to include discontinuities or kinks in the approximation or its derivative) [38]. This key feature makes the MLS method an ideal choice for generating enriched shape functions in the IXFEM.

Founding principles of the MLS method for surface approximation can be found in References [57, 60], whereas summary of the method presented here follows from References [38, 39]. Provided a function $u(\boldsymbol{x})$ existing on an open set $\Omega \in \mathbb{R}^d$, of d-dimensional real space, being sufficiently smooth, i.e. $u(\boldsymbol{x}) \in C^0(\Omega)$, a local approximation function of $u(\boldsymbol{x})$ can be defined around a fixed point $\overline{\boldsymbol{x}} \in \Omega$, existing over $\overline{\Omega}_{\overline{\boldsymbol{x}}}$, as

$$u^h_{\text{local}}(\boldsymbol{x}, \overline{\boldsymbol{x}}) = \boldsymbol{p}^{\mathrm{T}}(\boldsymbol{x})\boldsymbol{a}(\overline{\boldsymbol{x}}) \quad \forall \boldsymbol{x} \in \overline{\Omega}_{\overline{\boldsymbol{x}}} \tag{2.2.1}$$

where column vector $\boldsymbol{p}(\boldsymbol{x})$ prescribes the intrinsic basis to be used in the approximation subspace, denoted by superscript T to be transposed in Eqn. 2.2.1, and column vector $\boldsymbol{a}(\overline{\boldsymbol{x}})$ is a set of unknown coefficients defining the approximation. This is analogous to the general form of a FE approximation function, $u^h(\boldsymbol{x}) = \{\boldsymbol{N}(\boldsymbol{x})\}^{\mathrm{T}}\boldsymbol{u}$. The basis functions $p_j(\boldsymbol{x})$, of $\boldsymbol{p}(\boldsymbol{x})$, perform the same job as the shape functions $N_i(\boldsymbol{x})$, i.e. defining an approximate solution based on an interpolation of determined nodal values. The vector components of $\boldsymbol{p}(\boldsymbol{x})$ are generally taken as monomials when a polynomial approximation of $u(\boldsymbol{x})$ proves adequate. However, in the vicinity of a discontinuity the basis is enriched to include additional function(s) $\tilde{\boldsymbol{p}}^{\text{enr}}(\boldsymbol{x})$, beyond a standard set, typically taken to correspond to the problem dimension and element order, specifically chosen so as to be able to capture the effects of the particular discontinuity. In this work a linear two-dimensional basis, as given by Eqn. 2.2.2, establishes the common terms to which extra functions are added to create appropriate enriched intrinsic bases for modeling discontinuities.

$$\boldsymbol{p}^{\text{lin}}(\boldsymbol{x}) = \{1, x, y\}^{\mathrm{T}} \tag{2.2.2}$$

In evaluation of Eqn. 2.2.2, $\boldsymbol{x} = (x, y)$, such that x and y are the component values of vector coordinate $\boldsymbol{x}$ aligned with the global horizontal and vertical axes respectively. Definitions of the enriched intrinsic bases to model weak, strong, and singular tip discontinuities in the case of linear elastic mechanics are discussed in Section 3.1.2.

To determine the unknown components of vector $\boldsymbol{a}(\overline{\boldsymbol{x}})$ minimization of a weighted least squares discrete L_2-error norm, computed based on Eqn. 2.2.3, of the approximation function variable is sought. Refer to Ref. [73] for an overview comparing the least squares, weighted least squares, and moving least squares methods for generating an approximate interpolant of scattered data.

$$J_{\overline{\boldsymbol{x}}}(\boldsymbol{a}(\overline{\boldsymbol{x}})) = \sum_{i=1}^{r} w_i(\overline{\boldsymbol{x}})[\boldsymbol{p}^{\mathrm{T}}(\boldsymbol{x}_i)\boldsymbol{a}(\overline{\boldsymbol{x}}) - u_i]^2 \tag{2.2.3}$$

Thus an expression linking the coefficients $\boldsymbol{a}(\overline{\boldsymbol{x}})$ to the nodal values $\boldsymbol{u}$ to be determined is found (u_i being the value of $\boldsymbol{u}$ at node n_i). To preserve locality of the approximation the weight functions $w_i(\boldsymbol{x})$ have compact supports $\tilde{\Omega}_i$ centered at node n_i (equivalently coordinate $\boldsymbol{x}_i$). The r nodes n_i that have influence in defining

the L_2-error norm measure are those that exist in the local domain $\overline{\Omega}_{\overline{\boldsymbol{x}}}$ of $u^h_{\text{local}}(\boldsymbol{x}, \overline{\boldsymbol{x}})$, determined as those in the neighborhood of $\overline{\boldsymbol{x}}$ for which $w_i(\overline{\boldsymbol{x}}) \neq 0$, see Figure 2.3 for an example. The four nodes $\boldsymbol{x}_1$, $\boldsymbol{x}_2$, $\boldsymbol{x}_i$, and $\boldsymbol{x}_s$ makeup the list of r nodes in the local domain of $w_{\overline{\boldsymbol{x}}}(\boldsymbol{x})$, as each resides within its compact support $\overline{\Omega}_{\overline{\boldsymbol{x}}}$. As shown for node point $\boldsymbol{x}_s$, this is equivalent to saying node $\overline{x}$ resides in the compact support of each of the r nodes having influence at point $\overline{\boldsymbol{x}}$. For node $\boldsymbol{x}_t$, residing outside of $\overline{\Omega}_{\overline{\boldsymbol{x}}}$, it is demonstrated that its corresponding weight function compact support does not enclose node $\overline{\boldsymbol{x}}$ hence it does not have influence on the local approximation defined at point $\overline{\boldsymbol{x}}$.

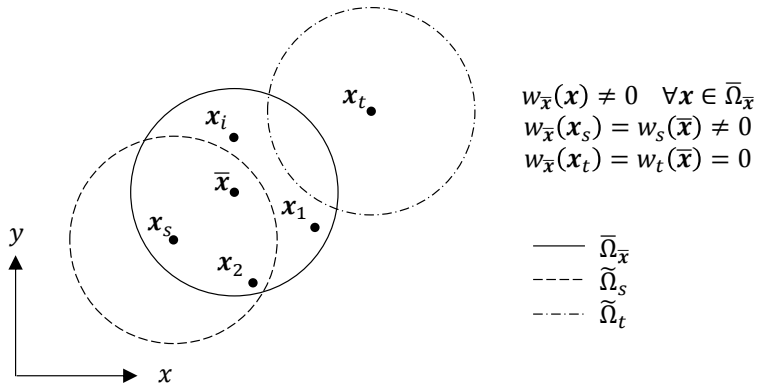

Figure 2.3: Graphical representation of compact support $\overline{\Omega}_{\overline{\boldsymbol{x}}}$ spanned by approximation function u^h_{local} centered at $\overline{\boldsymbol{x}}$. The r nodes within the domain contribute to L_2-error norm measurement based on inclusion in the weight function's $w_{\overline{\boldsymbol{x}}}(\boldsymbol{x})$ local domain.

Definition of these weight functions play a pivotal role in governing the underlying numerical approximation derived from application of the MLS method. Meshless methods are the outcome of utilizing weight functions with mesh-independent supports, typically employing a radius of influence to realize its localization [11], akin to what is demonstrated in Figure 2.3. Consequently the shape functions constructed using the MLS approach in these methods are also mesh-independent. In the IXFEM, however, special mesh-based weight functions, presented in Section 2.2.3, are defined for use in the MLS computation and thus the resulting enriched MLS shape functions are also mesh-dependent. It is vital to distinguish this mesh dependence terminology from that of the standard FEM, where it refers to constraints placed on the mesh geometry directly, i.e. it must conform to all boundary and discontinuity interfaces. In the IXFEM it refers to the fact that the shape functions, and thus the approximation, are built on a mesh, but discontinuity interfaces can exist and past through the mesh geometry arbitrarily,

Evaluation of the L_2-error norm minimum, by differentiation of Eqn. 2.2.3 with respect to $\boldsymbol{a}(\overline{\boldsymbol{x}})$, then

produces the following system of equations,

$$\sum_{i=1}^{r} w_i(\overline{\boldsymbol{x}})\boldsymbol{p}(\boldsymbol{x}_i)\boldsymbol{p}^{\mathrm{T}}(\boldsymbol{x}_i)\boldsymbol{a}(\overline{\boldsymbol{x}}) = \sum_{i=1}^{r} w_i(\overline{\boldsymbol{x}})\boldsymbol{p}(\boldsymbol{x}_i)u_i \tag{2.2.4}$$

which when solved for $\boldsymbol{a}(\overline{\boldsymbol{x}})$, and subsequently substituted into Eqn. 2.2.1 yields an expression for the localized approximation where the only unknowns are the nodal values, u_i.

$$u^h_{\mathrm{local}}(\boldsymbol{x},\overline{\boldsymbol{x}}) = \boldsymbol{p}^{\mathrm{T}}(\boldsymbol{x})\left[\sum_{i=1}^{r} w_i(\overline{\boldsymbol{x}})\boldsymbol{p}(\boldsymbol{x}_i)\boldsymbol{p}^{\mathrm{T}}(\boldsymbol{x}_i)\right]^{-1}\sum_{i=1}^{r} w_i(\overline{\boldsymbol{x}})\boldsymbol{p}(\boldsymbol{x}_i)u_i \tag{2.2.5}$$

The intrinsic basis $\boldsymbol{p}(\boldsymbol{x})$ and weight function $w_i(\boldsymbol{x})$ being selected and defined as appropriate for the discontinuity beforehand. To advance this expression the arbitrarily fixed point $\overline{\boldsymbol{x}}$, around which the local approximation was initially determined, is allowed to move over the entire domain such that $\overline{\boldsymbol{x}} \to \boldsymbol{x}$. Then a weighted least squares interpolant can be constructed and evaluated for any point $\boldsymbol{x}$ in the global domain [73]. In conclusion the continuous local, in effect global, MLS approximation function can be expressed in condensed form as

$$u^h(\boldsymbol{x}) = \boldsymbol{p}^{\mathrm{T}}(\boldsymbol{x})[\mathbf{M}(\boldsymbol{x})]^{-1}\mathbf{B}(\boldsymbol{x})\boldsymbol{u} \tag{2.2.6}$$

with the following definitions:

$$\mathbf{M}(\boldsymbol{x}) = \sum_{k=1}^{r} w_k(\boldsymbol{x})\boldsymbol{p}(\boldsymbol{x}_k)\boldsymbol{p}^{\mathrm{T}}(\boldsymbol{x}_k) \tag{2.2.7}$$

$$\mathbf{B}(\boldsymbol{x}) = [w_1(\boldsymbol{x})\boldsymbol{p}(\boldsymbol{x}_1) \;\; w_2(\boldsymbol{x})\boldsymbol{p}(\boldsymbol{x}_2) \;\; \ldots \;\; w_r(\boldsymbol{x})\boldsymbol{p}(\boldsymbol{x}_r)] \tag{2.2.8}$$

$$\boldsymbol{u} = \{u_1 \;\; u_2 \;\; \ldots \;\; u_r\}^{\mathrm{T}} \tag{2.2.9}$$

Matrices $\mathbf{M}(\boldsymbol{x})$, referred to as the *moment matrix* [11, 41], and $\mathbf{B}(\boldsymbol{x})$ are of size $k \times k$ and $k \times r$ respectively, and column vector $\boldsymbol{u}$ is of dimension k, with k being the number of terms included in the intrinsic basis $\boldsymbol{p}(\boldsymbol{x})$, i.e. $k = \dim(\boldsymbol{p}(\boldsymbol{x}))$.

Repurposing of the MLS approximation function for ease of implementation in the FEM equations follows directly when recalling the MLS method is an interpolation technique. Recognizing Eqn. 2.2.6 as the product

of MLS functions $\{\boldsymbol{p}^{\mathrm{T}}(\boldsymbol{x})[\mathbf{M}(\boldsymbol{x})]^{-1}\mathbf{B}(\boldsymbol{x})\}^{1\times r}$ with nodal data points $\boldsymbol{u}^{r\times 1}$ the approximation can be written succinctly as shown in Eqn. 2.2.10, from which a specific MLS shape function $N_i^{\mathrm{MLS}}(\boldsymbol{x})$ at node n_i can be identified as expressed in Eqn. 2.2.11.

$$u^h(\boldsymbol{x}) = \{\boldsymbol{N}^{\mathrm{MLS}}(\boldsymbol{x})\}^{\mathrm{T}}\boldsymbol{u} \tag{2.2.10}$$

$$N_i^{\mathrm{MLS}}(\boldsymbol{x}) = \boldsymbol{p}^{\mathrm{T}}(\boldsymbol{x})[\mathbf{M}(\boldsymbol{x})]^{-1}w_i(\boldsymbol{x})\boldsymbol{p}(\boldsymbol{x}_i) \tag{2.2.11}$$

A set of r MLS shape functions are generated and contained in $\{\boldsymbol{N}^{\mathrm{MLS}}(\boldsymbol{x})\}$ which build a PU of order n over the d-dimensional domain $\Omega \in \mathbb{R}^d$ [38]. In the scope of an element based code this amounts to evaluating the r enriched MLS shape functions $N_i^{\mathrm{MLS}}(\boldsymbol{x})$ having influence over an enriched element e_k^{enr} at point $\boldsymbol{x}$ when calculating the approximation of $u(\boldsymbol{x})$ within Ω_k^{el}. From the MLS shape function definition, Eqn. 2.2.11, it is noted that the moment matrix must be inverted at every point $\boldsymbol{x}$ of evaluation. The consequence of this implication is the increased computational effort required to process the matrix operation in the numerical scheme. Furthermore, should the MLS shape function derivative need to be computed, as necessary to obtain stress and strain values for a structural mechanics purposed IXFEM, it adds further complexity. Details on the definition of the MLS shape function derivatives are provided in Appendix A Section A.2 for the interested reader.

2.2.2 Intrinsic Enrichment Applied in the MLS Method

From development of the MLS shape function expression, Eqn 2.2.11, through the procedure of Section 2.2.1, it is important to realize that their construction is based exclusively on definition of the intrinsic basis $\boldsymbol{p}(\boldsymbol{x})$ and weight functions $w_i(\boldsymbol{x})$. Information on the interpolation fit to be built is contained within the intrinsic basis, while the weight functions impose continuity and local domain influence restraints. Enriched shape functions are thus achieved by enriching the intrinsic basis to include additional functional components representative of the known discontinuity to be modeled. In other words known analytic solution characteristics of the discontinuity are introduced into the approximation subspace permitting the interpolation to conform to these features. In the absence of discontinuities the intrinsic basis may contain only monomials to build a polynomial approximation of satisfactory degree.

In application of the work in this thesis the two-dimensional linear basis $\boldsymbol{p}^{\mathrm{lin}}(\boldsymbol{x}) = \{1, x, y\}^{\mathrm{T}}$ is of primary

concern. This monomial basis is supplemented with extra functions $\tilde{\boldsymbol{p}}^{\text{enr}}(\boldsymbol{x})$ to design the full enriched intrinsic basis $\boldsymbol{p}^{\text{enr}} = \{\boldsymbol{p}^{\text{lin}}, \tilde{\boldsymbol{p}}^{\text{enr}}\}^{\text{T}}$ specific to a discontinuity type (weak, strong) or a singularity (crack tip). The additional function(s) included in the intrinsic basis for the IXFEM are in fact the same as those added on to the approximation function in the EXFEM [38], refer to Section 1.3. Using the defined MLS shape functions all linear combinations of the functions in the enriched intrinsic basis $\boldsymbol{p}^{\text{enr}}(\boldsymbol{x})$ can be reproduced exactly [38], i.e.

$$\sum_{i=1}^{r} N_i^{\text{MLS}}(\boldsymbol{x})\boldsymbol{p}^{\text{enr}}(\boldsymbol{x}_i) = \boldsymbol{p}^{\text{enr}}(\boldsymbol{x}) \tag{2.2.12}$$

For utilization in the IXFEM, enriched intrinsic bases are designed prior to performing any numerical computations based on knowledge of the discontinuities to be defined in the problem domain or anticipated to emerge[5]. Examples of applied enrichment functions can be found in Ref. [38, 39] for structural mechanics (e.g. distinct material interfaces and crack tips), Ref. [37] for incompressible two-fluid flows, and Ref. [12] for various problems containing arbitrary discontinuities in FEMs (e.g. crack growth and a non-bonded inclusion). The enriched intrinsic bases of interest in this work for weak, strong, and singular tip discontinuities as applicable to solid mechanics model the physical representation of distinct material interfaces, void space interfaces or crack length portions, and crack tips respectively. Expressions for $\boldsymbol{p}^{\text{enr}}(\boldsymbol{x})$ corresponding to each of these discontinuity types are provided in Section 3.1.2.

When using an enriched intrinsic basis $\boldsymbol{p}^{\text{enr}}(\boldsymbol{x})$ in the MLS shape function computation the dimension k of vector $\boldsymbol{p}(\boldsymbol{x})$ is increased. This directly leads to the creation of larger moment matrices $\mathbf{M}(\boldsymbol{x})$, by Eqn. 2.2.7, which must be inverted for all points of evaluation. As discussed in development of the IXFEM, see References [38, 39], ensuring regularity of the moment matrix is a critical responsibility of the weight functions $w_i(\boldsymbol{x})$. Success of the method relies on achieving suitable overlap of the weight functions at any point $\boldsymbol{x} \in \Omega_m$. Stated directly, the necessary condition is that every point $\boldsymbol{x} \in \Omega_m$ must lie in the compact support of at minimum $k = \dim(\mathbf{M}) = \dim(\boldsymbol{p})$ nodes [38, 49], defined mathematical as,

$$\dim\{\boldsymbol{x}_i : w_i(\boldsymbol{x}) \neq 0 \quad \forall n_i \in \mathcal{N}_m\} \geq k = \dim(\mathbf{M}) \quad \forall \boldsymbol{x} \in \Omega_m \tag{2.2.13}$$

where the bracket term lists all points $\boldsymbol{x}_i$, defining coordinate location of nodes n_i, residing within subdomain

[5]For the case of emerging and growing discontinuities, e.g. a crack, initiation and propagation criteria also need to be defined, for instance based on a critical stress value, e.g. hoop stress.

Ω_m, whose weight function has non-zero value at point $\boldsymbol{x}$. To meet this criteria in the framework of the IXFEM specialized mesh-based weight functions $w_i^{\mathrm{S}}(\boldsymbol{x})$ were conceived by Fries and Belytschko, utilizing standard FE shape functions for their definition. Sufficient overlap is guaranteed based on their support domain, which extends beyond the contiguous elements of node n_i, centering the weight function, to include the next neighboring elements. Further details and graphical representation of these specialized weight functions are presented in the following section.

2.2.3 Specialized Weight Functions for Enriched Regions

Along with the intrinsic basis, the weight functions $w_i(\boldsymbol{x})$ in Eqn. 2.2.7 and 2.2.11 play an important role in controlling properties of the MLS shape functions N_i^{MLS}. Primarily, they define the support and continuity of the MLS shape functions as they are equivalent to that of the chosen weight functions, i.e. $\forall n_i \in \mathcal{N}_m,\ N_i^{\mathrm{MLS}}(\boldsymbol{x}) = 0$ where $w_i(\boldsymbol{x}) = 0$ (equivalency of compact support), and $N_i^{\mathrm{MLS}} \in C^s(\Omega)$ if $w_i \in C^s(\Omega)$ (equivalence of continuity), assuming $\boldsymbol{p}(\boldsymbol{x})$ is sufficiently smooth [38]. Additionally given the moment matrix's invertibility requirements, see Eqn. 2.2.13, the weight function supports must provide sufficient overlap to guarantee stable evaluation of the MLS shape functions. To satisfy this criteria the specialized weight function definition proposed in Ref. [38] is used when constructing enriched MLS shape functions.

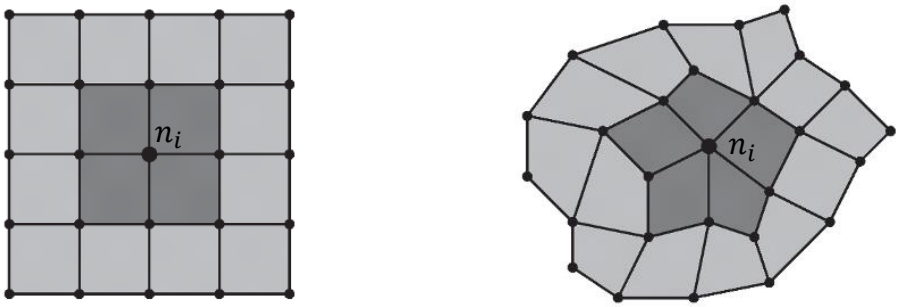

(a) Structured Mesh **(b)** Unstructured Mesh

Figure 2.4: Compact support $\tilde{\Omega}_i^{\mathrm{S}}$ of specialized weight function $w_i^{\mathrm{S}}(\boldsymbol{x})$ indicating neighboring elements (dark grey filling) of center node n_i and next neighboring elements (light grey) filling (from Ref. [38]: Reprinted with permission from John Wiley and Sons).

To work within the mesh based enrichment approach of the IXFEM these specialized weight functions are mesh dependent having compact supports defined by element boundaries. For specialized weight function $w_p^{\mathrm{S}}(\boldsymbol{x})$, centered at node n_p, it's support $\tilde{\Omega}_p^{\mathrm{S}}$ spans the immediate connected elements and their exterior

elements. Representative supports for the case of a structured and unstructured mesh of quadrilateral elements are depicted in Figure 2.4. The extended local support can be understood to encompass two bands of elements; those adjacent to the centering node n_i (first band, dark grey filling in the figure) and their outside neighbors (second band, light grey filling in the figure). To define the specialized weight functions the neighboring node set $\mathcal{N}_m^p$ is first established as the collection of nodes in $\mathcal{N}_m$, excluding (\) node n_p, which belong to the same element(s) as node n_p [38].

$$\mathcal{N}_m^p = \{n_i \in \mathcal{N}_m \setminus n_p : (n_i, n_p) \subset \mathcal{N}_k^{\mathrm{el}}, k = 1, \ldots, n^{\mathrm{el}}\} \tag{2.2.14}$$

Which is then used to express the functional definition of specialized weight function $w_i^{\mathrm{S}}(\boldsymbol{x})$ at node n_p as

$$w_p^{\mathrm{S}}(\boldsymbol{x}) = 2 \cdot N_p^{\mathrm{FE}}(\boldsymbol{x}) + \sum_{n_i \in \mathcal{N}_m^p} N_i^{\mathrm{FE}}(\boldsymbol{x}) \tag{2.2.15}$$

where $N_i^{\mathrm{FE}}(\boldsymbol{x})$ are standard FE shape functions. Rectangular bilinear interpolation functions are considered exclusively in this work, although the formulation of Eqn. 2.2.15 is generic and can be applied to either triangular or quadrilateral elements [39]. The resulting special weight function existing at a node is shown in Figure 2.5, for the support cases of Figure 2.4.

(a) Structured Mesh **(b)** Unstructured Mesh

Figure 2.5: Resulting specialized weight function $w_i^{\mathrm{S}}(\boldsymbol{x})$ at node n_i (from Ref. [38]: Reprinted with permission from John Wiley and Sons).

With a selected intrinsic basis $\boldsymbol{p}(\boldsymbol{x})$ and weight function $w_i(\boldsymbol{x})$ the MLS shape functions N_i^{MLS} are computed according to the procedure of Section 2.2.1. Though it can be shown that standard FE bilinear shape functions will result from the MLS method if a linear basis and bilinear weight function are chosen for $\boldsymbol{p}(\boldsymbol{x})$

and $w_i(\boldsymbol{x})$ respectfully, it is an unnecessary computation in the IXFEM. The polynomial approximations of standard FE shape functions can be derived and implemented directly for triangular or quadrilateral element as shown in various introductory texts to FEMs, e.g. Ref. [82]. It is only for localized regions where discontinuities exist that the MLS shape function procedure is utilized in the IXFEM to construct enriched shape functions.

In summary from Ref. [38, 39], the following properties are held by enriched MLS shape functions constructed by Eqn. 2.2.11 using an enriched intrinsic basis $\boldsymbol{p}^{\text{enr}}(\boldsymbol{x})$ and specialized weight functions $w_i^{\text{S}}(\boldsymbol{x})$:

1. They build a PU in subdomain Ω_m capable of representing all functions included in the enriched intrinsic basis vector $\boldsymbol{p}^{\text{enr}}(\boldsymbol{x})$ exactly. It is the added function terms of $\tilde{\boldsymbol{p}}^{\text{enr}}(\boldsymbol{x})$ in the basis that provide the means for modeling discontinuity interfaces effects in the FE problem solution.

2. Overlap of the special weight functions $w_i^{\text{S}}(\boldsymbol{x})$ guarantee evaluation of the enriched MLS shape functions through stable inversion of the moment matrix $\mathbf{M}(\boldsymbol{x})$, even for enriched intrinsic bases with large dimension k.

3. Their larger supports, compared to standard FE shape functions, increase the computational cost associated with the greater connectivity of an enriched element. For this reason it is most advantageous to only use enriched shape functions in local subdomains as needed to capture the effects of present discontinuities.

4. They are C^0 continuous over their compact support except where functions in the enriched intrinsic basis $\boldsymbol{p}(\boldsymbol{x})$ are discontinuous.

5. Enriched MLS shape functions do not share the Kronecker-delta property of standard FE shape functions, i.e. $N_i^{\text{MLS}}(\boldsymbol{x}_j) \neq \delta_{ij}$. As a result boundary conditions are not easily applied to nodes existing on enriched elements. Special treatment of boundary conditions for such occurrences becomes necessary. This issue is common to meshfree methods, refer to Refernces [11, 41] for various techniques to enforce boundary conditions in such situations.

2.3 Defining Discontinuity Geometry

2.3.1 Level-Set Method

The LSM is a numerical technique for the implicit tracking of moving interfaces and shapes [76, 77]. Its underlying principle relies on representation of such geometric entities as level-set curves or level-set surfaces, in two and three dimensional space respectively, of a higher-dimensional function $\psi(\boldsymbol{x}, t)$ [103]. Advantages of utilizing the LSM include the ability to perform numerical computations involving arbitrary curves and surfaces on a fixed structured grid without the need to parameterize these objects and it's capacity to easily model shapes that undergo topological changes (e.g. shapes dividing in two, initiation and/or growth of new interfaces, or the reverse of these operations). Together these capabilities make the LSM an efficient tool for modeling time-varying discontinuity interfaces within the IXFEM. The text by Sethian [93] demonstrates various applications of the LSM to problems in engineering and applied sciences.

A time dependent discontinuity interface $\Gamma_{\text{disc}}(t) \subset \Omega \in \mathbb{R}^d$ is thus determined as a particular level-set curve (LSC), in two-dimensional space, of the scalar value level-set function (LSF) $\psi(\boldsymbol{x}, t)$ [103]. Taken to be the zero-level of the LSF, the location of the LSC describing the interface at a given time t is denoted by the expression

$$\Gamma_{\text{disc}}(t) = \{\boldsymbol{x} \in \Omega : \psi(\boldsymbol{x}, t) = 0\} \tag{2.3.1}$$

or alternately $\psi(\boldsymbol{x}, t) = 0,\ \forall \boldsymbol{x} \in \Gamma_{\text{disc}}(t)$. The prominent function used to satisfy this property is the signed distance function [38, 103].

$$\psi(\boldsymbol{x}, t) = \pm \min \|\boldsymbol{x} - \boldsymbol{x}_{\Gamma_{\text{disc}}}\|, \quad \forall \boldsymbol{x}_{\Gamma_{\text{disc}}} \in \Gamma_{\text{disc}}(t), \quad \forall \boldsymbol{x} \in \Omega \tag{2.3.2}$$

where $\|\cdot\|$ denotes the Euclidean norm and the sign of the scalar resultant is indicative of the evaluation point's $\boldsymbol{x}$ location in reference to the discontinuity interface. A positive (negative) sign indicates $\boldsymbol{x}$ is outside (inside) the contour defined by $\Gamma_{\text{disc}}(t)$ [103]. This assumes $\Gamma_{\text{disc}}(t)$ is an closed interface (e.g. a circular loop) with an interior and exterior easily defined. For an open interface (e.g. a continuous curve or a crack) the positive side is defined based on the curve's orthogonal normal vector direction, this will be further explained and shown pictorially in Section 3.1.3.

Working with these self-contained functional definitions for arbitrary curves and surfaces removes the conventional FE mesh conformity restraint, i.e. the mesh is no longer required to explicitly form their boundaries. It is for this reason that the domain decomposition of Section 2.1.1 becomes necessary as those elements containing portions of a discontinuity interface, considered to be cut by the curve or surface, will be treated differently than those free of interface segments. The purpose in retaining the FE mesh is then primarily to serve as the foundation for incorporation of the mesh-based enrichment concept of the IXFEM into the FE model. Additionally it is used for approximating the LSF through a FE interpolation as the direct functional expressions are not employed in the IXFEM, as discussed in Section 2.3.2.

Further information explaining and expanding on operation of the LSM can be reviewed in References [76, 77], including an expression for dynamic evolution of a LSF. Additionally an algorithm for the progression of the LSF governing a crack discontinuity can be found in Ref. [96]. In this work two-dimensional static or quasi-static evolution of interfaces are of principal interest, thus dynamic aspects of the LSM are not presented here and the time parameter t will be omitted for brevity going forward. Accordingly for the applications of study in this thesis only one-dimensional LSCs in $\mathbb{R}^2$ are considered.

2.3.2 Discontinuity Approximation by Level-Set Functions

Using the LSM, definition and tracking of the static state or dynamic evolution of discontinuity interfaces is separated from the domain mesh discretization. In doing so explicit representation of these geometries (e.g. boundary of an inhomogeneity or edge of a crack) by the FE mesh is no longer necessary. Characterization of any interface contours is instead achieved by means of LSFs and the zero-level LSCs they define, as described in Section 2.3.1, recall particularly Eqn. 2.3.1. To facilitate implementation of the LSM in the IXFEM it becomes convenient to convert the continuous LSF $\psi(\boldsymbol{x})$ expression to a piece-wise continuous approximate LSF $\psi^h(\boldsymbol{x})$ as follows [103].

$$\psi(\boldsymbol{x}) \approx \psi^h(\boldsymbol{x}) = \sum_i M_i(\boldsymbol{x})\psi_i^n \tag{2.3.3}$$

In which $M_i(\boldsymbol{x})$ are interpolation functions, ψ_i^n are discrete calculated nodal values of the LSF (i.e. $\psi_i^n = \psi(\boldsymbol{x}_i)$), and summation occurs over all nodes n_i in the connectivity of the element e_k containing $\boldsymbol{x}$. With each element e_k having p element nodes its collection of nodal LSF values is indicated by vector $\boldsymbol{\psi}_k^{\mathrm{el}}$ being of dimension p. Taking the interpolation functions $\boldsymbol{M}(\boldsymbol{x})$ as standard FE shape functions, $\boldsymbol{N}^{\mathrm{FE}}(\boldsymbol{x})$, the

LSF approximation follows inline with the underlying approximation principle used in deriving the FEM, i.e. $u(\boldsymbol{x}) \approx u^h(\boldsymbol{x}) = \{\boldsymbol{N}(\boldsymbol{x})\}^{\mathrm{T}}\boldsymbol{u}$ [82]. In essence, the physical geometry of a discontinuity existing in the domain $\Omega \in \mathbb{R}^d$ is described through a FE interpolating functional expression existing exclusively as discrete stored point values. The resulting coordinate location of the zero-level LSC Γ^h_{disc}, defining the interface boundary, calculated based on Eqn. 2.3.4 is thus also an approximation of the real interface position, which improves with mesh refinement [38]. Continuing to use standard bilinear shape functions in this work the corresponding approximate LSC interpolant Γ^h_{disc} is piece-wise linear over a domain composed of four-noded quadrilateral elements.

$$\Gamma^h_{\mathrm{disc}} = \{\boldsymbol{x} \in \Omega : \psi^h(\boldsymbol{x}) = 0\} \tag{2.3.4}$$

Applying the approximate LSF $\psi^h(\boldsymbol{x})$ and LSC Γ^h_{disc} in the IXFEM, discontinuity interfaces are quickly and easily accounted for. Furthermore it greatly reduces computational resources as a FE interpolation approach is used to determine the value of ψ or its derivative ψ' at any point $\boldsymbol{x}$ in the global domain Ω [103]. This becomes an additional benefit when using the LSF as an enriching term in the intrinsic basis $\boldsymbol{p}(\boldsymbol{x})$ to generate enriched shape functions.

3 Description of Computational Model

The computational aspects formalized herein are for application of the intrinsic extended finite element method to plane linear elasticity. Thus far description of the global domain decomposition strategy, enriched MLS shape function computation, and LSM have been universal in regards to their operation within the IXFEM, in that the problem specific considerations for these methodologies and techniques have not been stipulated. These variable factors amount to the screening process used for partitioning of the global domain Ω into subdomains Ω'_m and Ω^*_m plus the subsequent determination of the PU to be built within, definition of the enriched intrinsic basis $\boldsymbol{p}^{\text{enr}}(\boldsymbol{x})$ to be used in the MLS procedure for local enrichment of the shape functions, and definition of the LSF expressions $\psi(\boldsymbol{x})$ for relevant discontinuity interface geometries. Together with selection of a specific class of problem (e.g. solid mechanics, fluid mechanics, heat transfer) to be solved using the IXFEM these parameters of the numerical methods are to be prescribed from knowledge of the problem and discontinuities to be modeled. Of initial interest in this work are the weak and strong discontinuities present in material or solid mechanics, restricted to the scope of plane linear elasticity. With all considerations for the problem model finalized, formulation of the representative numerical system begins from specification of a governing differential equation defining the problem physics. Existing within the conventional FEM framework, development of the underlying mathematics for the IXFEM follow in a straight forward manner to develop the linear system of equations, refereed to herein as the FE model, used in evaluating an approximate solution.

This chapter reviews particulars of the previously described methods and numerical techniques of Chapter 2 in addition to new concepts for implementation of the IXFEM. Together these extended details provide further insight into how this intrinsically enriched FEM is applied to solved problems of plane linear elasticity. The underlying mathematics governing the linear elastic material mechanics to be modeled are presented first in Section 3.1. Subsequent discussion focuses on defining the enriched intrinsic bases for use in the MLS shape function computation and definition of LSFs for specifying geometry through the LSM. Certain aspects for numerical implementation are expanded upon in Section 3.2, starting with development of the governing differential equations weak form to produce the FE model equations. Additional numerical topics include classification of the domain decomposition subdomains for realization of local enrichment plus integration and differentiation of the enriched shape functions.

3.1 Application of the IXFEM to Linear Elastic Mechanics

3.1.1 Governing Equations for Plane Linear Elasticity

For development of the IXFEM particularized to the study of linear elasticity in two-dimensional space we consider a global domain $\Omega \in \mathbb{R}^2$ with external boundary Γ and internal discontinuity boundary Γ_{disc}. Complementary sets Γ_u and Γ_t form the global domain boundary $\Gamma = \Gamma_u \bigcup \Gamma_t$. Global boundary conditions are then applied as follows, displacements $\boldsymbol{u} = \hat{\boldsymbol{u}}$ are prescribed on the Dirichlet boundary Γ_u and tractions $\boldsymbol{t} = \hat{\boldsymbol{t}}$ on the Neumann boundary Γ_t. Internal boundaries are defined using the LSM of Section 2.3.1, and are thus decoupled from the mesh geometry. For weak discontinuities (e.g. distinct material interfaces) continuity of the primary variable is maintained such that $\boldsymbol{u}^+_{\text{disc}} = \boldsymbol{u}^-_{\text{disc}}$. In the case of strong discontinuities (e.g. crack edge or tip) the interface surface is assumed to be traction-free $\hat{\boldsymbol{t}}^+_{\text{disc}} = \hat{\boldsymbol{t}}^-_{\text{disc}} = 0$. Further the discontinuity interfaces can be classified as either closed or open. A closed interface has no ends finishing internal to the domain, therefore the LSC must form a closed loop or finish at the external boundaries. Open interfaces can finish anywhere within the domain, characterized as crack tips in linear elastic material mechanics. Figure 3.1 displays two example cases of a global domain including internal discontinuities defined using the LSM.

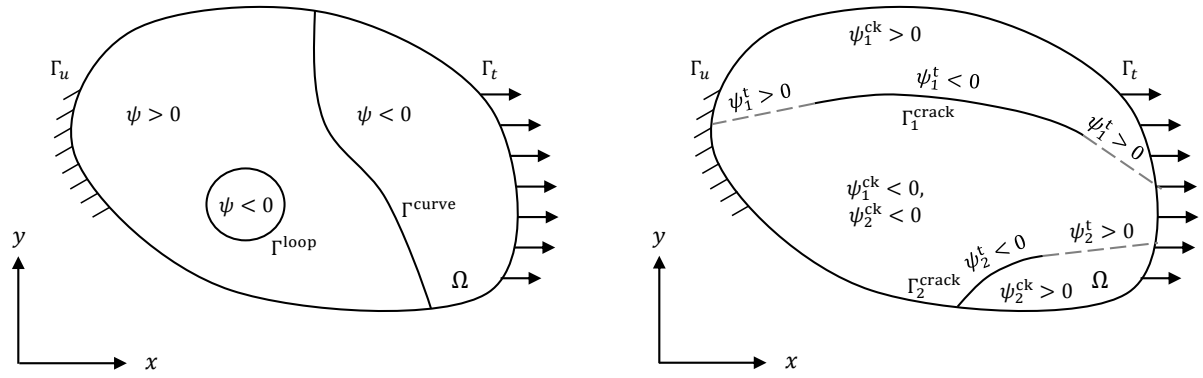

(a) Closed discontinuities (loop, curve) **(b)** Open discontinuities (crack)

Figure 3.1: Example global problem domain Ω containing level-set curves Γ_{disc} defined by level-set functions $\psi(\boldsymbol{x})$.

The comprehensive strong form of the governing differential equation (GDE), also referenced as the equation of motion (EOM), for a linear elastic solid in d-dimensional space, undergoing small displacements and strains under static conditions, expressed in tensor and index notation is [82]

$$\nabla \cdot \boldsymbol{\sigma} + \boldsymbol{f} = 0 \quad \forall \boldsymbol{x} \in \Omega \tag{3.1.1a}$$

$$\sigma_{ji,j} + f_i = 0 \tag{3.1.1b}$$

where notation $(\cdot)_{,j}$ is shorthand for denoting derivative $\partial(\cdot)/\partial x_j$. Vector $\boldsymbol{f}$ defines volumetric prescribed body forces, ∇ is the del operator, and $\boldsymbol{\sigma}$ is the second-order Cauchy stress tensor,

$$\boldsymbol{\sigma} = \mathbf{C} : \boldsymbol{\epsilon} \tag{3.1.2a}$$

$$\sigma_{ij} = C_{ijkl}\epsilon_{kl} \tag{3.1.2b}$$

defined by the above stress-strain (constitutive) relation, with $\mathbf{C}$ representing the fourth-order stiffness tensor, for the generalized Hooke's Law, and $\boldsymbol{\epsilon}$ the infinitesimal (linearized) second-order strain tensor of the displacement vector field $\boldsymbol{u}$,

$$\boldsymbol{\epsilon} = \frac{1}{2}\left(\nabla \boldsymbol{u} + (\nabla \boldsymbol{u})^{\mathrm{T}}\right) \tag{3.1.3a}$$

$$\epsilon_{ij} = \frac{1}{2}\left(u_{j,i} + u_{i,j}\right) \tag{3.1.3b}$$

where superscript T denotes the transpose of the displacement gradient. To return to the simplified two-dimensional problem scenario described previously, and shown in Figure 3.1, Eqn. 3.1.1 is expanded into scalar differential form based on the assumptions of plane linear elasticity, see Ref.[82, chap. 11]. The resulting set of coupled governing partial differential equations (GPDE)s are derived,

$$\frac{\partial \sigma_{xx}}{\partial x} + \frac{\partial \sigma_{xy}}{\partial y} + f_x = 0 \tag{3.1.4a}$$

$$\frac{\partial \sigma_{xy}}{\partial x} + \frac{\partial \sigma_{yy}}{\partial y} + f_y = 0 \tag{3.1.4b}$$

being valid for both plane stress and plane strain problems. Distinction of the plane elasticity condition being realized solely in the constitutive relation, that is the components of tensor $\mathbf{C}$ in Eqn. 3.1.2. Additionally,

based on the stress or strain field assumptions, the tensor quantities that appear in Equations 3.1.1 through 3.1.3 can be reduced to vector and matrix definitions as follows

$$\boldsymbol{\sigma} = \begin{Bmatrix} \sigma_{xx} \\ \sigma_{yy} \\ \sigma_{xy} \end{Bmatrix}, \quad \mathbf{C} = \begin{bmatrix} C_{11} & C_{12} & 0 \\ C_{21} & C_{22} & 0 \\ 0 & 0 & C_{66} \end{bmatrix}, \quad \boldsymbol{\epsilon} = \begin{Bmatrix} \epsilon_{xx} \\ \epsilon_{yy} \\ 2\epsilon_{xy} \end{Bmatrix} \tag{3.1.5}$$

where σ_{ij} and ϵ_{ij} are the components of the stress and stain tensors respectively in the 2D plane of interest (x-y plane in this work) and C_{ij} are the elastic material constants of the domain. Further assuming the linear elastic material is also hyperelastic in combination with the imposed symmetry of the stress and strain tensors, i.e. $\sigma_{ij} = \sigma_{ji}$ and $\epsilon_{ij} = \epsilon_{ji}$ respectively, the stiffness matrix $\mathbf{C}$ is symmetric, $C_{ij} = C_{ji}$ [94]. Then applying material symmetry considerations, the number of independent elastic material constants of the stiffness tensor can be reduced from 21, for the general linear hyperelastic material. In Eqn. 3.1.5 the material is assumed to be transversely isotropic with $\mathbf{C}$ defined for the plane of isotropy, taken as the principal x_1-x_2 material plane in this work. The coefficients C_{ij} are defined in terms of the engineering material properties and constants: elastic (Young's) moduli E_{11} and E_{22}, in plane shear modulus G_{12}, and in plane Poission's ratios ν_{12} and ν_{21}. The subscript number indicates alignment with the principal material directions (x_1, x_2, x_3), taken to coincide with the problem global coordinate axes (x, y, z), where z and x_3 are the out of plane directions, i.e. E_{11} is the elastic modulus in the horizontal x direction. Expressions distinct to the plane stress and plane strain condition for these matrix components can be found in Ref. [82], along with post-processing equations to determine the nonzero through thickness strain or stress for the plane stress and plane strain cases respectively. The body force and displacement vector, $\boldsymbol{f}$ and $\boldsymbol{u}$ correspondingly, simply contain the scalar components aligned with the global planar axes.

$$\boldsymbol{f} = \begin{Bmatrix} f_x \\ f_y \end{Bmatrix}, \quad \boldsymbol{u} = \begin{Bmatrix} u_x \\ u_y \end{Bmatrix} \tag{3.1.6}$$

Lastly the linear infinitesimal strain-displacement relations are given as:

$$\epsilon_{xx} = \frac{\partial u_x}{\partial x}, \quad \epsilon_{yy} = \frac{\partial u_y}{\partial y}, \quad 2\epsilon_{xy} = \frac{\partial u_x}{\partial y} + \frac{\partial u_y}{\partial x} \tag{3.1.7}$$

Using these relations in conjunction with those obtainable through the constitutive relation, $\boldsymbol{\sigma} = \mathbf{C} : \boldsymbol{\epsilon}$,

Eqns. 3.1.4 can be expressed as

$$\frac{\partial}{\partial x}\left(C_{11}\frac{\partial u_x}{\partial x}+C_{12}\frac{\partial u_y}{\partial y}\right)+\frac{\partial}{\partial y}\left[C_{66}\left(\frac{\partial u_x}{\partial y}+\frac{\partial u_y}{\partial x}\right)\right]+f_x=0 \tag{3.1.8a}$$

$$\frac{\partial}{\partial x}\left[C_{66}\left(\frac{\partial u_x}{\partial y}+\frac{\partial u_y}{\partial x}\right)\right]+\frac{\partial}{\partial y}\left(C_{12}\frac{\partial u_x}{\partial x}+C_{22}\frac{\partial u_y}{\partial y}\right)+f_y=0 \tag{3.1.8b}$$

In this representation the coupled GDEs are expressed in terms of only the known material properties and body force components plus the unknown displacement components u_x and u_y, which a FEM approximation can be constructed to solve for, as presented in Section 3.2.1. A post-process calculation of the solved nodal displacements, then yields the strain and stress component values, determined at element Gauss points in the current work. Strains are evaluated first based on the strain-displacement relations of Eqn. 3.1.7, i.e. as single or combination directional derivatives of the displacement fields, requiring the involved differentiation of enriched MLS and transition shape functions in addition to the standard FE shape functions. Once all strain components are known the corresponding stress values at the mesh Gauss points are directly computed through the stress-strain relation, Eqn. 3.1.2. It is lastly noted that Eqn. 3.1.8 holds at all points $\boldsymbol{x}$ in the continuum representation of the problem domain. However, in FE methods a discretized representation of the continuum, i.e. the FE mesh, is used to transfer focus from the infinite number of material points $\boldsymbol{x}$ to a finite number of discrete nodes n_i defining the mesh elements, for solving Eqns. 3.1.8, where this scalability of the EOMs is the primary concept leading to development of the FE approach. Local continuous solutions for each element domain Ω_k^{el} and a single piece-wise continuous solution over the global domain Ω are then approximated using shape functions $\hat{N}_i(\boldsymbol{x})$ to interpolate the solved field variables to any point $\boldsymbol{x}$ in the problem domain.

3.1.2 Enriched Bases for Discontinuity Modeling

Use of an enriched intrinsic basis, vector $\boldsymbol{p}^{\text{enr}}(\boldsymbol{x})$, as introduced in Section 2.2.2, in Eqn. 2.2.11, is the means by which construction of MLS shape functions $N_i^{\text{MLS}}(\boldsymbol{x})$ bring enhancement to the approximate solution. With all bases utilized in this work sharing the two-dimensional linear components $\{1, x, y\}$, it is the added enrichment functions $f_g^{\text{enr}}(\boldsymbol{x})$, in $\tilde{\boldsymbol{p}}^{\text{enr}}(\boldsymbol{x})$, that provide the *intrinsic* ability for specific discontinuity types to be suitably modeled within appropriate elements. These supplementary functions are selected based on previous knowledge of the anticipated response in the primary or secondary variable fields across the

discontinuity interface, to bring the proper behavior into the approximation subspace. For explanation of the enrichment functions used with weak and strong discontinuities the example problem of Figure 3.2 is considered. As shown in Figure 3.2a, this is a one-dimensional bimaterial bar problem with the discontinuity interface existing at its center length $L/2$, as prescribed by LSF $\psi(\boldsymbol{x})$. The discontinuous behavior of the enrichment functions in Figures 3.2b and 3.2c will be explained in reviewing the weak and strong discontinuity enriched intrinsic bases respectively.

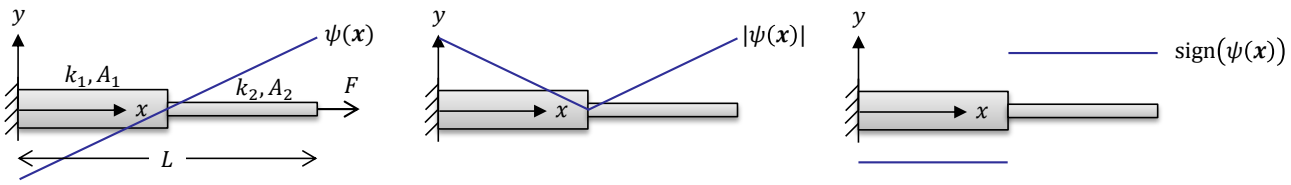

(a) Example problem **(b)** Weak enrichment function **(c)** Strong enrichment function

Figure 3.2: Example problem of a one-dimensional bimaterial bar demonstrating definition of the discontinuity interface with level-set function $\psi(\boldsymbol{x})$ and the weak and strong enrichment functions.

The complete enriched intrinsic bases presented in this section for weak, strong, and singular tip discontinuities are those defined in Ref. [38]. Their corresponding directional derivatives to be used in evaluating the MLS shape function derivatives are provided in Appendix Section A.3. Additionally, illustrations of some resulting enriched shape functions, for two-dimensional quadrilateral element meshes, are depicted in Appendix B for various discontinuity interface examples. Theses figures demonstrate assimilation of the appropriate behavior in the enriched shape function form, as generated using the enriched intrinsic bases presented next, to account for different discontinuity types.

Weak Discontinuities are representative of interfaces across which the primary variable (displacement) is continuous, but its derivatives (strains, evaluated as direct derivative quantities, and stresses, evaluated as derivatives through the constitutive relation to strain) may not be. The Hadamard's compatibility conditions can give an indication to the continuity expected in the strain components, i.e. strain definitions not involving partial derivatives with respect to the normal direction of the weak interface should be continuous, other components are generally discontinuous. Continuity of the stress components are independent of the strains, such that material directions across weak interfaces having discontinuous strains may have continuous stresses, and vice-versa. Distinct material interfaces or shear bands are a common example in solid mechanics where such occurrences exist. The enriched intrinsic basis vector defined in Ref. [38] for use in the MLS

procedure for weak discontinuities is,

$$\boldsymbol{p}_{\mathrm{w}}^{\mathrm{enr}}(\boldsymbol{x}) = \{1, x, y, |\psi(\boldsymbol{x})|\}^{\mathrm{T}} \tag{3.1.9}$$

where the single enrichment function is $f_{\mathrm{w}_1}^{\mathrm{enr}}(\boldsymbol{x}) = |\psi(\boldsymbol{x})|$ (absolute value of the LSF), to be computed using the approximation method discussed in Section 2.3.2. As all vector terms in Eqn. 3.1.9 are continuous functions the resulting enriched MLS shape function computed for a weak discontinuity will likewise be continuous over its compact support, and hence across the discontinuity interface as well. However, by assigning the absolute value of the LSF as the enrichment function, in the intrinsic basis, discontinuities in derivatives of the enriched shape function can be modeled. This behavior is observable in Figure 3.2b, where evaluation of $|\psi(\boldsymbol{x})|$, for the bar problem, shows continuity of the enrichment function at the discontinuity interface location $\boldsymbol{x} = L/2$, but evaluation of its derivative would show a discontinuity at the same location. Through introduction of enrichment function $f_{\mathrm{w}_1}^{\mathrm{enr}}(\boldsymbol{x})$, derivatives of the enriched shape function are able and expected to capture the non-smooth behavior at weak interfaces, as needed to predict the appropriate behavior in the primary variable derivative fields. This will be demonstrated for a bimaterial plate problem considered in Section 4.2 for validation of the weak enrichment basis $\boldsymbol{p}_{\mathrm{w}}^{\mathrm{enr}}(\boldsymbol{x})$.

Strong Discontinuities are representative of interfaces across which the primary variable is discontinuous, and continuity of the secondary variables is dependent on the specific strong discontinuity modeled. Examples where discontinuity of the strains and stresses will exist are across void boundaries and crack segments, in these considerations the apparent continuity of zero stresses through the void space is considered an exception, as free surfaces must be traction free. Slip planes, in plasticity, would be an example where the stress derivatives may retain continuity. Two proposed intrinsic bases are provide in Ref. [38] which can be employed in the MLS procedure for strong discontinuities. The first is given as,

$$\boldsymbol{p}_{\mathrm{s,f}}^{\mathrm{enr}}(\boldsymbol{x}) = \{1, x, y, \mathrm{sign}(\psi(\boldsymbol{x})), |\psi(\boldsymbol{x})|\}^{\mathrm{T}} \tag{3.1.10}$$

and is considered here as the "full-form" enriched intrinsic basis, using two enrichment functions: $f_{\mathrm{s}_1}^{\mathrm{enr}} = \mathrm{sign}(\psi(\boldsymbol{x}))$ (sign function of the LSF) and $f_{\mathrm{s}_2}^{\mathrm{enr}}(\boldsymbol{x}) = |\psi(\boldsymbol{x})|$ (absolute value of the LSF). Examining all vector component terms in Eqn. 3.1.10 it is observed that only the sign function, $\mathrm{sign}(x)$, is non-continuous. This is illustrated in Figure 3.2c, where evaluation of $\mathrm{sign}(\psi(\boldsymbol{x}))$ is shown to be discontinuous at the discontinuity

interface location[6]. Given the discontinuity of enrichment function $f_{s_1}^{enr}(\boldsymbol{x})$ at $x = 0$, and design of the LSF to be zero at the representative discontinuity interface, i.e. $\psi(\boldsymbol{x}) = 0$, $\forall \boldsymbol{x} \in \Gamma_{disc}$, refer to Section 2.3.1, the resulting enriched MLS shape function computed for a strong discontinuity will be discontinuous over its compact support with the change in continuity occurring across interface Γ_{disc}. This directly incorporates the discontinuity into the shape function and subsequently the approximation function. It is relevant to note that in the EXFEM, enrichment for strong discontinuities is realized only using the sign function $\text{sign}(\boldsymbol{x})$ [12, 36], or alternately the Heaveside function $H(\boldsymbol{x})$ [67]. Explanation for the necessary inclusion of the absolute value LSF term $|\psi(\boldsymbol{x})|$ in the IXFEM implementation is further detailed through example for a one-dimensional bimaterial bar problem in Ref. [38]. Essentially it shows the sign function only introduces the jump discontinuity in the approximation, if a kink is also present across the discontinuity the absolute value function must be involved, as in the weak discontinuity basis. The secondary (alternative) intrinsic basis for strong discontinuities proposed in Ref. [38] avoids use of both the sign and absolute value LSF enrichment terms and instead simply uses a linear basis, such that,

$$\boldsymbol{p}_{s,t}^{enr}(\boldsymbol{x}) = \{1, x, y\}^T \tag{3.1.11}$$

in conjunction with truncated supports for the specialized weight functions $w_i^S(\boldsymbol{x})$, of Section 2.2.3, and is hence refereed to as the "truncated" enriched intrinsic basis[7]. Truncation of the compact support is achieved based on the visibility criteria of Ref [75] and is necessary to realize the enriched MLS shape function discontinuity as all vector terms in Eqn. 3.1.11 are continuous. Concisely the visibility criteria states: all points $\boldsymbol{x}$ not in line of sight from node n_i, considering the discontinuity as opaque, are ignored when evaluating the weight function over its local domain $\tilde{\Omega}_i^S$ centered at n_i [38]. In effect, cutting off the weight function along the discontinuity on the side opposite of node n_i, see Figure 3.3 for a demonstration. Consequently the enriched MLS shape function is equivalently truncated as its support is founded on that of the weight function, as mentioned in Section 2.2.3. Such adaptation of local weight function supports is common for treatment of discontinuities in meshless methods [9, 12], and was introduced in a mesh-based context in References [38, 39]. The truncated specialized weight function w_i^{S*} is defined as

[6] It is noted that the strong discontinuity for the example problem is simply used to demonstrate the behavior of the sign(x) enrichment function, it would not represent any discontinuity in a one-dimensional representation of the bimaterial bar.

[7] The advantage of the truncated basis over the full-form should be a lower computational cost given the reduced dimension of $\boldsymbol{p}_{s,t}^{enr}(\boldsymbol{x})$ $(k = 3)$ versus $\boldsymbol{p}_{s,f}^{enr}(\boldsymbol{x})$ $(k = 5)$, as this effects the size of the Moment matrix to be inverted in the MLS shape function computation.

$$w_i^{\mathrm{S}*} = \begin{cases} w_i^{\mathrm{S}}(\boldsymbol{x}) & \text{for } \boldsymbol{x} \text{ visible from } \boldsymbol{x}_n \\ 0 & \text{otherwise} \end{cases} \tag{3.1.12}$$

where $w_i^{\mathrm{S}}(\boldsymbol{x})$ is the specialized weight function defined in Eqn. 2.2.15 and visibility of point $\boldsymbol{x}$ from $\boldsymbol{x}_i$ is determined based on the sign evaluated from product of the discrete LSF values at the two points. Point $\boldsymbol{x}$ is considered visible from $\boldsymbol{x}_i$ if

$$\psi(\boldsymbol{x}) \cdot \psi(\boldsymbol{x}_i) > 0 \tag{3.1.13}$$

Applying this secondary strategy to handle strong discontinuity interfaces it is noted that the overlap of specialized weight functions is diminished for an element cut by a strong discontinuity, see Figure 3.3. However, due to their larger compact supports, adequate overlap is still assured permitting construction of the PU through the MLS computation [39]. Were these supports of equivalent size to standard bilinear FE weight functions, generation of a non-singular moment matrix $\mathbf{M}(\boldsymbol{x})$, by Eqn. 2.2.7, would not be guaranteed, and a PU of equal order to non-enriched elements could not be built [39].

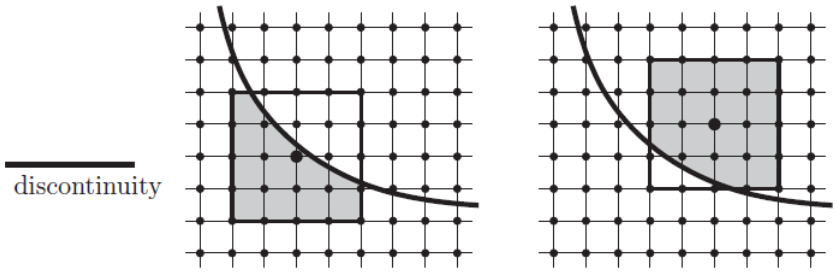

Figure 3.3: Truncated supports of specialized weight function $w_i^{\mathrm{S}}(\boldsymbol{x})$ at select nodes based on a visibility criteria for strong discontinuities (from Ref. [38]: Reprinted with permission from John Wiley and Sons).

Based on the discontinuous behavior of the sign-function, or the modified discontinuous support of the truncated specialized weight function, the enriched MLS shape function computed for a strong discontinuity, and its derivatives, will be discontinuous across the interface. In both approaches the discontinuity is directly incorporated into the final form of the shape function, but different techniques are followed to do so. If applying the full-form basis $\boldsymbol{p}_{\mathrm{s,f}}^{\mathrm{enr}}(\boldsymbol{x})$, the specialized weight function $w_i^{\mathrm{S}}(\boldsymbol{x})$ is used *unmodified* in the MLS method, thus the resultant shape function is defined completely over the full compact support domain $\tilde{\Omega}_i^{\mathrm{S}}(\boldsymbol{x})$. The discontinuity observed in the shape function form itself comes out of the MLS method due to

the addition of the discontinuous sign function in the intrinsic basis. In opposition, if the truncated basis $\boldsymbol{p}^{\text{enr}}_{\text{s,t}}(\boldsymbol{x})$ was applied in the MLS method, in combination with the specialized weight function unmodified, a continuous shape function would result, as all functions in the truncated basis are continuous. To bring the necessary discontinuity into the shape function form the compact support of the specialized weight function is itself truncated at the interface, producing truncated specialized weight function $w_i^{\text{S}*}(\boldsymbol{x})$, thus by extension the shape function is equivalently truncated. This variation in approach is a main point of discussion in Section 4.1 where validation of the strong enrichment bases for a plate with a hole problem shows the full-form basis $\boldsymbol{p}^{\text{enr}}_{\text{s,f}}(\boldsymbol{x})$ providing far superior accuracy compared to the truncated linear basis $\boldsymbol{p}^{\text{enr}}_{\text{s,t}}(\boldsymbol{x})$.

Singular Tip discontinuities are used in the vicinity of open ends of crack interfaces, i.e. the crack tip. The enriched basis vector used in the MLS procedure for crack tip discontinuities is,

$$\boldsymbol{p}^{\text{enr}}_{\text{t}}(\boldsymbol{x}) = \left\{1, x, y, \sqrt{r}\sin\frac{\theta}{2}, \sqrt{r}\sin\frac{\theta}{2}\sin\theta, \sqrt{r}\cos\frac{\theta}{2}, \sqrt{r}\cos\frac{\theta}{2}\sin\theta\right\}^{\text{T}} \tag{3.1.14}$$

where r and θ are the distance and angle of point $\boldsymbol{x}$ respectively, determined in the polar coordinate system based in the tangential direction of the crack tip at $\boldsymbol{x}^t$, as shown in Figure 3.4. The four trigonometric enrichment functions $f^{\text{enr}}_{t_k},\ k = \{1, \ldots, 4\}$, supplementing the linear basis in Eqn. 3.1.14, come from a linear independent basis for the linear elastic asymptotic crack tip solution, refer to Ref. [12].

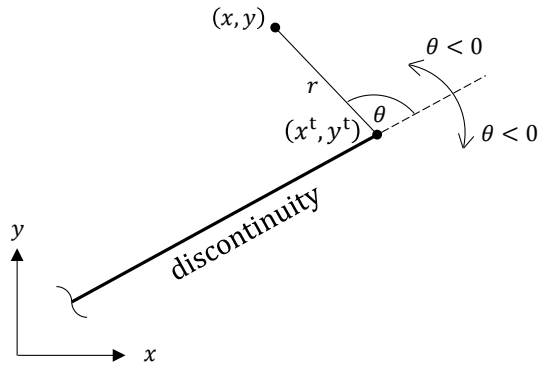

Figure 3.4: Polar coordinate system defined for crack tip (from Ref. [38]: Reprinted with permission from John Wiley and Sons).

Given the allowable range of angle $\theta,\ -\pi \leq \theta \leq \pi$, for point $\boldsymbol{x}$ it is observed that the first enrichment function of Eqn. 3.1.14, $f^{\text{enr}}_{t_1} = \sqrt{r}\sin(\theta/2)$, is discontinuous across the crack opening angle $\theta = \pm\pi$, but

continuous at all other angles radiating from the crack tip $-\pi < \theta < \pi$. The remaining three functions are continuous across the crack face and throughout the surrounding domain. Graphical representation of these four functions can be found in Appendix Section A.3, Figure A.5. With one functional term, in the enriched intrinsic basis, discontinuous over the crack opening the enriched shape functions for a singular tip are able to properly model the continuous and discontinuous behavior surrounding a crack tip.

3.1.3 Level-Set Functions for Discontinuity Modeling

Using the LSM geometric definition of internal discontinuities are prescribed within the global domain Ω independent of the FE mesh. Their interface configuration Γ_{disc} instead determined as the zero-level LSC of the corresponding LSF $\psi(\boldsymbol{x})$. Applying the concept of the signed distance function, Eqn 2.3.2, see Ref. [76, chap. 2] for details, to simple geometries (e.g. circles and straight lines) LSFs specific to such shapes can be derived. Some resulting LSFs, from which LSCs will be obtained, for circular, straight line, and discontinuous tip interfaces are summarized here from References [96, 103]. Expressions for more complex geometries can be considered as shown in Ref. [96] where LSF definitions are provided directly for elliptical and polygonal interfaces.

Circular Interfaces can be used to model the presence of assumed perfectly round inhomogeneities or inclusions in the domain, representative of voids, particulates, or fiber cross-sections. In a global domain Ω containing n^{c} circular discontinuities the ith circular LSF is,

$$\psi_i^{\text{c}}(\boldsymbol{x}) = \|\boldsymbol{x} - \boldsymbol{x}_i^{\text{c}}\| - r_i^{\text{c}} \tag{3.1.15}$$

where $\boldsymbol{x}_i^{\text{c}}$ and r_i^{c} are the center and radius of the ith circular interface $\Gamma_i^{\text{circle}} = \{x : \psi_i^{\text{c}}(\boldsymbol{x}) = 0\}$ respectively, as shown in Figure 3.5a. A unified LSF function is then easily defined as the continuous minimum of the n^{c} circular LSFs,

$$\psi^{\text{c}}(\boldsymbol{x}) = \min_{\substack{\boldsymbol{x}_i^{\text{c}} \in \Omega_i^{\text{c}} \\ i=1,\ldots,n^{\text{c}}}} \{\|\boldsymbol{x} - \boldsymbol{x}_i^{\text{c}}\| - r_i^{\text{c}}\} \tag{3.1.16}$$

where Ω_i^{c} is the domain of the ith circular geometry. Based on Eqn. 3.1.16 it is then feasible to overlap portions of circular LSFs to produce a zero-level LSC describing a more complex discontinuity interface

boundary, e.g. a peanut shape.

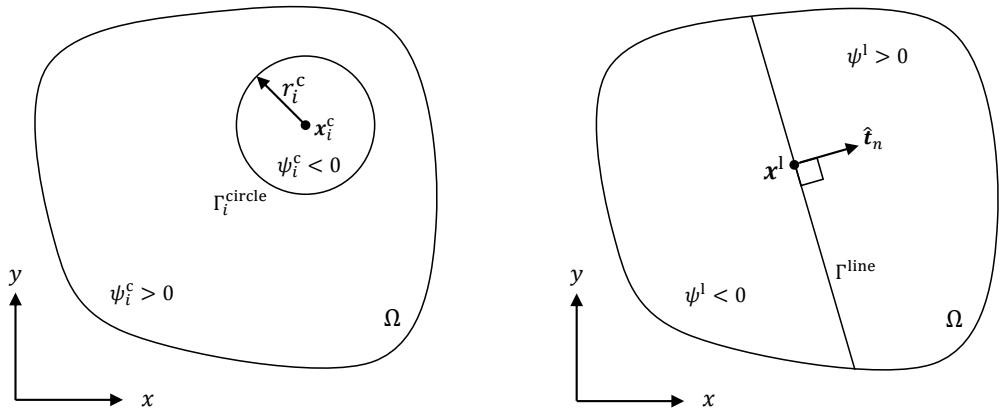

(a) Circular Interface **(b)** Line Interface

Figure 3.5: Geometry parameters for level-set function definition.

Straight Line Interfaces can be used to represent instantaneous material property changes, cutoffs, or as a subdomain deliminator passing through the entire domain. The LSF for a single straight line discontinuity in the global domain Ω is defined by,

$$\psi^{\mathrm{l}}(\boldsymbol{x}) = (\boldsymbol{x} - \boldsymbol{x}^{\mathrm{l}}) \cdot \hat{\boldsymbol{t}}_n \tag{3.1.17}$$

where x^{l} can be taken as any point which lies of the straight line interface $\Gamma^{\mathrm{line}} = \{x : \psi^{\mathrm{l}}(\boldsymbol{x}) = 0\}$, and $\hat{\boldsymbol{t}}_n$ is the orthogonal unit vector to Γ^{line} at point x^{l} pointing in the direction defined as positive with respect to the interface, as shown in Figure 3.5b.

Singular Tips are used to define the point where a discontinuity originates or terminates internal to the global domain, hereafter taken to be the singular (discontinuous) tip of a crack front. For a global domain containing n^{ck} cracks the LSF representing the ith crack running through the global domain Ω is given by $\psi_i^{\mathrm{ck}}(\boldsymbol{x})$. In the case that the crack contour is a straight line $\psi^{\mathrm{ck}}(\boldsymbol{x})$ can be defined using $\psi^{\mathrm{l}}(\boldsymbol{x})$. Although the actual crack is embedded inside the global domain Ω, it is a key observation that the LSF $\psi_i^{\mathrm{ck}}(\boldsymbol{x})$ passes through the entire domain [96]. For this reason it is necessary to prescribe the corresponding ith crack tip LSF as,

$$\psi_i^{\mathrm{t}}(\boldsymbol{x}) = (\boldsymbol{x} - \boldsymbol{x}_i^{\mathrm{t}}) \cdot \hat{\boldsymbol{t}}_t \tag{3.1.18}$$

where x_i^{t} is the location of the ith crack tip and $\hat{\boldsymbol{t}}_t$ is the unit vector tangent to the LSC $\Gamma_i^{\mathrm{crack}}$ at point x_i^{t}, as shown in Figure 3.6a. The design of Eqn. 3.1.18 is such that the zero-level LSC of $\psi_i^{\mathrm{t}}(\boldsymbol{x})$ is orthogonal to $\hat{\boldsymbol{t}}_t$ at the crack tip. With LSFs describing the crack contour and crack tip the interface of the ith crack can be expressed as

$$\Gamma_i^{\mathrm{crack}} = \{x : \psi_i^{\mathrm{ck}}(\boldsymbol{x}) = 0 \text{ and } \psi_i^{\mathrm{t}}(\boldsymbol{x}) \leq 0\} \tag{3.1.19}$$

It should be noted that this determination of the LSC assumes a crack with a single tip (i.e. an edge crack) based on the formulation of Eqn. 3.1.18. For the case of an interior crack, refer to Figure 3.6b, two distinct crack tips t_1 and t_2, each with a defined crack tip LSF $\psi_i^{\mathrm{t}_1}(\boldsymbol{x})$ and $\psi_i^{\mathrm{t}_2}(\boldsymbol{x})$ respectfully, are necessary to enclose the crack LSF $\psi_i^{\mathrm{ck}}(\boldsymbol{x})$ within the global domain. A single crack tip LSF for an interior crack can then be defined by,

$$\psi_i^{\mathrm{t}}(\boldsymbol{x}) = \max_i\{(\boldsymbol{x} - \boldsymbol{x}_i^{\mathrm{t}_1}) \cdot \hat{\boldsymbol{t}}_{t_1}, (\boldsymbol{x} - \boldsymbol{x}_i^{\mathrm{t}_2}) \cdot \hat{\boldsymbol{t}}_{t_2}\} \tag{3.1.20}$$

where the interior crack interface is still evaluated based on Eqn. 3.1.19 using the crack tip LSF as determined by Eqn. 3.1.20. This definition can then be further extend to define a multi-branching crack ψ_i^{ck} with n_i^t crack tips t_l, $l = \{1, \ldots, n_i^t\}$.

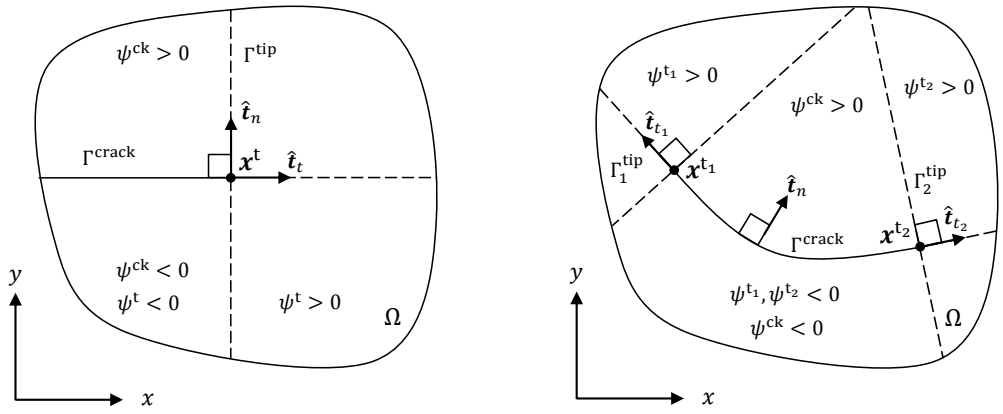

(a) Crack, single tip **(b)** Crack , double tip

Figure 3.6: Geometry parameters for level-set function definition.

3.2 Principles of Numerical Implementation

3.2.1 Finite Element Model

Based in the FE framework, numerical implementation of the IXFEM follows closely to that for the conventional FEM. A solid introduction into the principles for development and implementation of the numerical approximation scheme that is the FEM can be found in the text by Reddy, Ref. [82]. Continuing from the coupled GPDEs presented at the end of Section 3.1.1, Eqn. 3.1.8, the FE model is constructed by first developing their corresponding weak form and then substituting in approximation function expressions for the unknown primary variable functions. The ensuing integral terms are then rearranged to generate a global system of equations, often represented in matrix-vector form, referred to as the FE model in this thesis.

The weak form of the coupled GPDEs are provided by Eqn. 3.2.1, where they are presented without derivation. Detailed discussion of their realization can be found in Ref. [82, chap. 11]. As expressed, the EOMs are defined for an element domain Ω_k^{el} belonging to an element e_k, for which an equivalent globally defined set of EOMs can be analogously determined. In Eqn. 3.2.1 and moving forward it is to be understood that all approximation, shape, and weight functions are defined for an element e_k. For completeness all quantities could be marked with superscript el, but these are omitted for the sake of brevity. Similarly all these functions and elastic material constants C_{ij} could be indexed by k to indicate their element correspondence, but this is likewise omitted to maintain conciseness.

$$0 = \int_{\Omega^{\text{el}}} h^{\text{el}} \left[\frac{\partial w_1}{\partial x} \left(C_{11} \frac{\partial u_x}{\partial x} + C_{12} \frac{\partial u_y}{\partial y} \right) + C_{66} \frac{\partial w_1}{\partial y} \left(\frac{\partial u_x}{\partial y} + \frac{\partial u_y}{\partial x} \right) \right] dA - \int_{\Omega^{\text{el}}} h^{\text{el}} w_1 f_x \, dA - \oint_{\Gamma^{\text{el}}} h^{\text{el}} w_1 t_x \, ds \tag{3.2.1a}$$

$$0 = \int_{\Omega^{\text{el}}} h^{\text{el}} \left[C_{66} \frac{\partial w_2}{\partial x} \left(\frac{\partial u_x}{\partial y} + \frac{\partial u_y}{\partial x} \right) + \frac{\partial w_2}{\partial y} \left(C_{12} \frac{\partial u_x}{\partial x} + C_{22} \frac{\partial u_y}{\partial y} \right) \right] dA - \int_{\Omega^{\text{el}}} h^{\text{el}} w_2 f_y \, dA - \oint_{\Gamma^{\text{el}}} h^{\text{el}} w_2 t_y \, ds \tag{3.2.1b}$$

Displacement functions u_x and u_y are the quantities to be predicted by the FE model. This is accomplished by replacing their continuous representation in the weak form with piece-wise continuous approximation functions u_x^h and u_y^h respectively, this procedure will be further detailed shortly. Weight (test) functions w_1 and w_2 remain from multiplication with the GPDEs in performing the weak form integration. To

maintain consistent approximation between u_x and u_y, equivalency of the weight functions is taken such that $w_1(\boldsymbol{x}) = w_2(\boldsymbol{x}) = w(\boldsymbol{x})$. Later when constructing the FE model, weight function $w(\boldsymbol{x})$ is taken to be correspondent to the shape functions, such that $w_i = \hat{N}_i$, as typically done in FE approximations where the Galerkin method is used. The remaining terms are defined as follows h^{el} is the element thickness, $\boldsymbol{f} = \{f_x, f_y\}$ with f_α the component of a body force, $\boldsymbol{t} = \{t_x, t_y\}$ with t_α the component of an applied traction, $dA = dxdy$, and ds parameterizes the element boundary Γ^{el}. Of interest to solid mechanics problems the primary variables are the displacement components u_i^x and u_i^y evaluated at nodes $n_i, i = \{1, \ldots, n^{\text{nd}}\}$. As such they are carried as the primary degrees of freedom at the nodes. The secondary variables are then recognized as the nodal tractions t_i^x and t_i^y. In further observation of the weak form, only first derivatives of u_x and u_y with respect to x and y are identified. Therefore, the Lagrange family of interpolation functions with at least bilinear interpolation are required [82]. Meeting these requirements is most easily accomplished using either linear triangular or linear quadrilateral elements.

Progressing towards design of the FE model an approximation function is specified to interpolate the primary variable field and substituted into Eqn. 3.2.1. As introduced in Section 1.2, the IXFEM uses an approximation function of the form $u^h(\boldsymbol{x}) = \{\hat{\boldsymbol{N}}(\boldsymbol{x})\}^{\text{T}}\boldsymbol{u}$ containing all necessary enrichment information within the shape functions $\hat{N}_i(\boldsymbol{x})$ themselves. Retaining this formulation for definition of the approximation functions is a major advantage for the IXFEM versus the competing extrinsic enriched FEMs, discussed in Section 1.2, as no additional terms exist in the approximation function, hence no additional unknowns arise in the global system of equations. Moreover given that the approximation function is equivalent to that of the conventional FEM, compare Eqn. 1.2.12 to 1.2.1, the matrix-vector representation of the FE model can be expressed in precisely the same manner without concern of introducing a new coefficient matrix and variable vector into the FE model, as occurs in the EXFEM. Reference [69] and [102] defined comprehensive matrix-vector expressions to handle these new contributions in the FE model, for the case of the EXFEM applied in two- and three-dimensional space respectively. The expressions showcase the complexity involved in numerical implementation of the EXFEM, where the additional unknowns lead to an expansion of the global system of equations. For the IXFEM where enrichment is restricted completely to the specialized shape functions only computational operations directly involving or impacted by evaluation of enriched or transition shape functions need be modified for implementing the intrinsic enrichment scheme in the FEM framework. No conditionally adaptive changes need to be made to the system of equations to bring in the solution enrichment capabilities.

Approximation functions, belonging to an element e_k, for displacement in the x and y direction, identified by u_x^h and u_y^h respectively, are thus expressed as in Eqn. 3.2.2.

$$u_x(\boldsymbol{x}) \approx u_x^h(\boldsymbol{x}) = \sum_{i=1}^{r} \hat{N}_i(\boldsymbol{x}) u_i^x \tag{3.2.2a}$$

$$u_y(\boldsymbol{x}) \approx u_y^h(\boldsymbol{x}) = \sum_{i=1}^{r} \hat{N}_i(\boldsymbol{x}) u_i^y \tag{3.2.2b}$$

Their corresponding approximate directional derivatives are defined as

$$\frac{\partial u_a(\boldsymbol{x})}{\partial a} \approx \frac{\partial u_a^h(\boldsymbol{x})}{\partial a} = \sum_{i=1}^{r} \frac{\partial \hat{N}_i(\boldsymbol{x})}{\partial a} u_i^a \tag{3.2.3}$$

where $a = \{x, y\}$ such that quantities indexed with x associate with the horizontal direction and those indexed with y associate with the vertical direction. In Eqns. 3.2.2 and 3.2.3 $\hat{N}_i(\boldsymbol{x})$ take on standard FE, enriched MLS, or coupled transition shape functions definitions (N_i^{FE}, N_i^{MLS}, and N_i^{TR} correspondingly) as appropriate for an element belonging to a non-enriched, enriched, or transition subdomain respectively. The methodology applied for designation of an element to one of these subdomain types is explained in Section 3.2.2. Coefficients u_i^x and u_i^y are the to-be-determined x and y displacement values of nodes n_i respectively, and r equates to the number of nodes whose shape function $\hat{N}_i(\boldsymbol{x})$ have influence in defining the approximation functions u_x^h and u_y^h for element e_k (for clarity it is noted that r is taken to be implicitly indexed by $k \in \{1, \ldots, n^{\mathrm{el}}\}$, as are all other variables in Eqns. 3.2.2 and 3.2.3). Element displacement approximation functions of Eqn 3.2.2 are thus two-dimensional interpolating functions using the to-be-determined nodal displacement components to define a continuous approximate solution over individual element domains Ω_k^{el}, and a piece-wise continuous approximate solution over the global domain Ω.

In the conventional FEM r is dependent only on the element order, being equal to the number of nodes needed to create shape functions of equivalent degree (e.g. for linear triangular elements $r = 3$, for linear quadrilateral elements $r = 4$, and so on increasing with order of the element approximation function). This sole dependency is the outcome of utilizing standard FE shape function definitions, having a single element "radial" spanning compact support, for the weight and shape functions. Furthermore it can be observed that the r nodes governing the approximation functions for element e_k match the element nodes $\mathcal{N}_k^{\mathrm{el}}$. For non-enriched elements in the IXFEM this single dependency on element order remains true for

prescribing r. However, for enriched or transition elements the number of nodes r impacting definition of the element approximation functions is determined not only from the element order, but also includes nodes beyond the four which define the element boundaries, assuming use of linear quadrilateral elements. These additional nodes of influence result from the extended compact support of the specialized weight functions $w_i^{\mathrm{S}}(\boldsymbol{x})$ used in constructing the enriched MLS shape functions. As the resultant enriched shape functions $N_i^{\mathrm{MLS}}(\boldsymbol{x})$ share the same local support they have a non-zero contribution in all enclosed elements. Referring to Figure 2.4, demonstrating the enlarged support domain, the influence of enriched shape functions over elements immediately surrounding node n_i and their neighboring elements can be anticipated.

For enriched or transition elements in the IXFEM the number of influencing nodes r for element e_k is variable and determined based on overlap of the nearby shape functions compact support over corresponding element domain Ω_k^{el}. Stated conditionally, if the local support of shape function $\hat{N}_i(\boldsymbol{x})$ includes element domain Ω_k^{el} then node n_i is considered an influencing node for element e_k, equivalently the compact support of weight function $w_i(\boldsymbol{x})$ can used to determine the influencing nodes. The collection of r influencing nodes for element e_k is indicated by $\mathcal{N}_k^{\mathrm{inf}} \in (\mathbb{N}^+)^r$. For a structured mesh of rectangular elements the compact support of the special weight function comprises of 25 nodes and 16 elements, refer to Figure 2.4a. Therefore the PU built over an enriched element, taken to be fully enclosed within the global domain, is composed of $r = 16$ unique shape functions. For an enriched element on the domain boundary the number of influencing nodes will be less 16, but no less than 9 for the case of a corner boundary element. This predictable behavior for a structured rectangular mesh is further explored in Appendix Section A.4.

Performing substitution of the approximation functions, Eqn. 3.2.2, into the coupled GPDE weak form, Eqn. 3.2.1 and setting $w_1 = w_2 = w_i$ the ith algebraic equation associated with each weak form expression is acquired. Collecting subsequent integral terms into matrix or vector variables the resulting system of algebraic equations is presented as in Eqn. 3.2.4, i.e. the FE model,

$$\mathbf{K}^{\mathrm{gl}}\mathbf{u}^{\mathrm{gl}} = \mathbf{F}^{\mathrm{gl}} + \mathbf{Q}^{\mathrm{gl}} \tag{3.2.4a}$$

$$\mathbf{K}^{\mathrm{el}}\mathbf{u}^{\mathrm{el}} = \mathbf{F}^{\mathrm{el}} + \mathbf{Q}^{\mathrm{el}} \tag{3.2.4b}$$

or expressed with indexed matrix and vector variables,

$$K_{ij}^{\mathrm{gl}} u_j^{\mathrm{gl}} = F_j^{\mathrm{gl}} + Q_j^{\mathrm{gl}} \tag{3.2.5a}$$

$$K_{ij}^{\mathrm{el}} u_j^{\mathrm{el}} = F_j^{\mathrm{el}} + Q_j^{\mathrm{el}} \tag{3.2.5b}$$

where the superscripts gl and el indicate the FE model is equally valid over the global domain $\Omega^{\mathrm{gl}} \equiv \Omega$ or a single element domain Ω^{el}. In both situations $\mathbf{K}$ represents the stiffness matrix, $\mathbf{u}$ contains the to-be-determined nodal displacements, $\mathbf{F}$ the force vector, and vector $\mathbf{Q}$ contains secondary variable boundary condition contributions. Further details on the FE model equation numerics are provided in Appendix Section A.4, including individual indexed matrix and vector variable definitions based on similar expressions from Ref. [82].

3.2.2 Domain Decomposition

In Section 2.1 a domain decomposition and coupling strategy is presented for an arbitrary global domain Ω containing n^{Ω} distinct element subdomains $\{\Omega'_m, \Omega^*_m, \Omega_m\}$ with corresponding nodal subsets $\{\mathcal{N}'_m, \mathcal{N}^*_m, \mathcal{N}_m\}$. Partitioning of the domain as discussed is done to achieve localized enrichment of the approximation, i.e. to build differing PUs based on enriched or transition shape functions only where needed, and using standard FE shape functions elsewhere. In operation of the IXFEM the non-complementary subdomains Ω'_m are classified as either non-enriched (standard) space Ω^{S} or enriched space Ω^{E}, while the surrounding subdomains Ω^*_m are classified as transition spaces Ω^{T}. If multiple discontinuities are present in the global domain the newly introduced subdomains would be indexed as needed, in moving forward no subscripts will be indicated on these variable for this purpose in the sake of conciseness. It is noted however, that the number of individual enriched and transition subdomains will always be equivalent, but no constraint exists relating the number on non-enriched and enriched subdomains.

Branding of the global domain partitions $\{\Omega'_m, \Omega^*_m\}$ into these sorted subdomains $\{\Omega^{\mathrm{S}}, \Omega^{\mathrm{E}}, \Omega^{\mathrm{T}}\}$ is prerequisite to constructing the varying PUs best suited to fit the desired approximation. In non-enriched areas the PU is built using standard FE shape functions $N_i^{\mathrm{FE}}(\boldsymbol{x})$ as their polynomial approximation is suitable. However, in enriched areas a polynomial approximation is not adequate to accurately predict the material response around the discontinuity. To handle this added complexity the approximation is appropriately enhanced through design of the enriched intrinsic basis $\boldsymbol{p}^{\mathrm{enr}}(\boldsymbol{x})$ used in constructing enriched MLS shape functions

$N_i^{\mathrm{MLS}}(\boldsymbol{x})$, refer to Section 2.2. For transition regions the ramp function $R_m(\boldsymbol{x})$ of Section 2.1.2 is used to couple conflicting PUs, in the overlapping elements of subdomains Ω_m, to create a unified PU built from a linear superposition of standard and enriched shape functions, termed transition shape functions $N_i^{\mathrm{TR}}(\boldsymbol{x})$. These newly labeled subdomains $\{\Omega^{\mathrm{S}}, \Omega^{\mathrm{E}}, \Omega^{\mathrm{T}}\}$ have corresponding nodal subsets $\{\mathcal{N}^{\mathrm{S}}, \mathcal{N}^{\mathrm{E}}, \mathcal{N}^{\mathrm{T}}\}$, from which the n^{Ω} ramp functions, Eqn. 2.1.9, are built based on complementary nodal sets $\mathcal{N}^{\mathrm{S}}$ and $\mathcal{N}^{\mathrm{E}}$, denoted as $R^{\mathrm{S}}(\boldsymbol{x})$ and $R^{\mathrm{E}}(\boldsymbol{x})$ respectively.

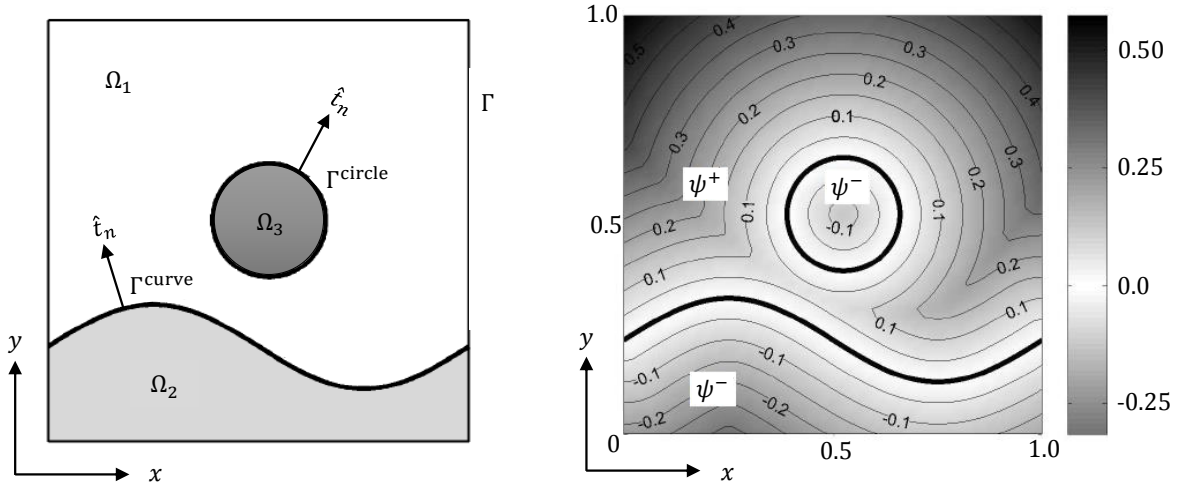

(a) Global domain **(b)** Global LSF contours

Figure 3.7: Example problem global domain composed of three distinct regions Ω_1, Ω_2, and Ω_3 and LSM definition of internal interfaces (from Ref. [37]: Reprinted with permission from John Wiley and Sons).

To explain the process for selection of the elements e_k that make up these subdomains we consider the problem domain shown in Figure 3.7a. The global domain Ω encompasses three distinct regions designated as Ω_1, Ω_2, and Ω_3. Interfaces separating the three regions are defined using the LSM, and a continuous LSF $\psi(\boldsymbol{x})$ for the entire domain is generated. From definition of the interface normal directions the positive and negative spaces of the LSF are set, contours for the resulting global LSF are displayed in Figure 3.7b. Given a problem as in Figure 3.7 classification of the n^{el} elements to specific subdomains is performed sequentially. In this implementation the enriched region(s) Ω^{E} are determined first, followed by the transition region(s) Ω^{T}, the remaining unclassified elements then make up the non-enriched region(s) Ω^{S}.

Assembly of these three subdomain listings is initiated with construction of a preliminary subdomain consisting of all elements containing, i.e. cut by, the discontinuity interface Γ_{disc}. These elements are determined

based on the LSF node values ψ_i^n. With the interface defined as the zero-level LSC, elements cut by its contour will include at least one LSF node value which is positive and one that is negative in their element LSF vector set $\boldsymbol{\psi}_k^{\mathrm{el}}$. Using this property the subdomain Ω^{cut} of elements cut by the discontinuity interface is defined as, [37].

$$\Omega^{\mathrm{cut}} = \bigcup_{k=1}^{n^{\mathrm{el}}} \{\Omega_k^{\mathrm{el}} : \min(\boldsymbol{\psi}_k^{\mathrm{el}}) \cdot \max(\boldsymbol{\psi}_k^{\mathrm{el}}) < 0\} \tag{3.2.6}$$

with corresponding nodal subset $\mathcal{N}^{\mathrm{cut}}$ taken as the union of all nodes on the elements in Ω^{cut}.

$$\mathcal{N}^{\mathrm{cut}} = \bigcup_{e_k \in \Omega^{\mathrm{cut}}} \mathcal{N}_k^{\mathrm{el}}, \quad \{k = 1, \ldots, n^{\mathrm{el}}\} \tag{3.2.7}$$

The resulting cut element subdomain and corresponding nodal subset for the problem of Figure 3.7 is shown in Figure 3.8a. With this preliminary subdomain Ω^{cut} established the standard, enriched and transition subdomains are determined based on the nodal subset $\mathcal{N}^{\mathrm{cut}}$. Subdomains Ω^{S}, Ω^{E}, and Ω^{T} are the union of all element domains Ω_k^{el} for which none, all, or some of their element nodes $\mathcal{N}_k^{\mathrm{el}}$ belong to $\mathcal{N}^{\mathrm{cut}}$ respectively [37]. Expressed mathematically these element groups are defined by Eqn. 3.2.8,

$$\Omega^{\mathrm{S}} = \bigcup_{k=1}^{n^{\mathrm{el}}} \{\Omega_k^{\mathrm{el}} : \mathcal{N}_k^{\mathrm{el}} \cap \mathcal{N}^{\mathrm{cut}} = \emptyset\} \tag{3.2.8a}$$

$$\Omega^{\mathrm{E}} = \bigcup_{k=1}^{n^{\mathrm{el}}} \{\Omega_k^{\mathrm{el}} : \mathcal{N}_k^{\mathrm{el}} \subseteq \mathcal{N}^{\mathrm{cut}}\} \tag{3.2.8b}$$

$$\Omega^{\mathrm{T}} = \bigcup_{k=1}^{n^{\mathrm{el}}} \{\Omega_k^{\mathrm{el}} : \Omega_k^{\mathrm{el}} \notin \Omega^{\mathrm{S}} \text{ and } \Omega_k^{\mathrm{el}} \notin \Omega^{\mathrm{E}}\} \tag{3.2.8c}$$

with the corresponding nodal subsets determined using Eqn. 3.2.9.

$$\mathcal{N}^{\mathrm{S}} = \bigcup_{e_k \in \Omega^{\mathrm{S}}} \mathcal{N}_k^{\mathrm{el}}, \quad \{k = 1, \ldots, n^{\mathrm{el}}\} \tag{3.2.9a}$$

$$\mathcal{N}^{\mathrm{E}} = \bigcup_{e_k \in \Omega^{\mathrm{E}}} \mathcal{N}_k^{\mathrm{el}}, \quad \{k = 1, \ldots, n^{\mathrm{el}}\} \tag{3.2.9b}$$

$$\mathcal{N}^{\mathrm{T}} = \bigcup_{e_k \in \Omega^{\mathrm{T}}} \mathcal{N}_k^{\mathrm{el}}, \quad \{k = 1, \ldots, n^{\mathrm{el}}\} \tag{3.2.9c}$$

As mentioned previously, nodal subsets $\mathcal{N}^{\mathrm{S}}$ and $\mathcal{N}^{\mathrm{E}}$ are complementary of the global nodal set $\mathcal{N}$, such that $\mathcal{N} = \mathcal{N}^{\mathrm{S}} \bigcup \mathcal{N}^{\mathrm{E}}$. Figure 3.8b displays the resulting segregated subdomains for standard, enriched, and transition elements. It should be observed from these definitions that Ω^{E} can contain elements that are not cut by the discontinuity interface, but have all their nodes included in $\mathcal{N}^{\mathrm{cut}}$. Comparing Ω^{cut} in Figure 3.8a to Ω^{E} in Figure 3.8b this outcome is observed for the elements marked with blue crosses, and it can be also be noted that $\Omega^{\mathrm{cut}} \subseteq \Omega^{\mathrm{E}}$.

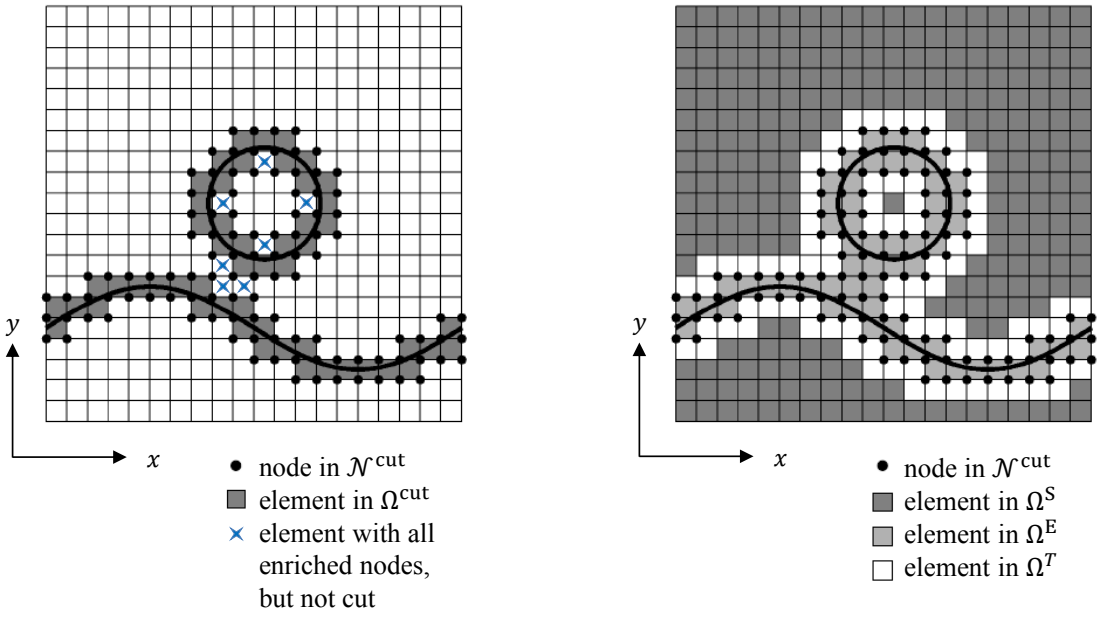

(a) Cut subdomain **(b)** Classified subdomains

Figure 3.8: Example problem global domain decomposition into Ω^{cut} and resulting decomposition to $\{\Omega^{\mathrm{S}}, \Omega^{\mathrm{E}}, \Omega^{\mathrm{T}}\}$ (from Ref. [37]: Reprinted with permission from John Wiley and Sons).

3.2.3 Numerical Integration and Differentiation

Evaluation of the global FE model in Eqn. 3.2.4 for $\mathbf{u}^{\mathrm{gl}}$ equates to generating the global stiffness matrix $\mathbf{K}^{\mathrm{gl}}$ and force vector $\mathbf{F}^{\mathrm{gl}}$ and performing the needed operation(s) to solve the linear system of equations. The component values of theses global system variables are determined through assembly of the n^{el} element stiffness matrices $\mathbf{K}^{\mathrm{el}}$ and force vectors $\mathbf{F}^{\mathrm{el}}$. It is thus within each element e_k that the computations are concentrated for numerical assembly of the FE model, where the element system variable components, i.e. K_{ij}^{el} and F_i^{el}, are determined by integration of the r overlapping shape functions $\hat{N}_i(\boldsymbol{x})$ and their derivatives $\partial\hat{N}_i(\boldsymbol{x})/\partial a,\ a \in \{x, y\}$ having influence over element domain Ω_k^{el}, i.e. defining the approximation function over element e_k. Expressions defining the integral calculations that makeup the element stiffness matrix and force vector are listed in Appendix Section A.4 for completeness.

Recalling as result from the global domain decomposition and subdomain coupling of Section 2.1, a single shape function $\hat{N}_i(\boldsymbol{x})$ is defined at each node n_i of the global domain Ω. For non-enriched subdomains $\Omega'_m = \Omega^{\mathrm{S}}$ the continuous standard bilinear FE shape functions $N_i^{\mathrm{FE}}(\boldsymbol{x})$ ensure continuity of the approximation functions u_x^h and u_y^h, see Eqn. 3.2.2, and their derivatives. Numerical integration of these shape functions and derivatives is aptly handled using an element-wise standard Gauss quadrature implementation, a thorough review of which exists in Ref. [82, chap. 9]. For enriched subdomains $\Omega'_m = \Omega^{\mathrm{E}}$ the approximation enrichment information is incorporated solely into the MLS shape function $N_i^{\mathrm{MLS}}(\boldsymbol{x})$ calculation through the enriched intrinsic basis $\boldsymbol{p}^{\mathrm{enr}}(\boldsymbol{x})$ of Section 2.2, refer to Section 3.1.2 for relevant definitions. The enrichment leads to a strong or weak discontinuity in the approximation functions and/or their derivatives along discontinuity interfaces. At the cost of added complexity for evaluation and integration, these enriched shape function adaptions aptly enhance the approximate solution space to capture the presence of local discontinuities, defined independently of the FE mesh. Examples of enriched shape functions displayed in Appendix B demonstrate the non-continuous behavior these shape functions and/or their derivatives exhibit contributing to their computational burden. Thus to appropriately compute the stiffness matrix for an enriched element integration of the enriched MLS shape functions must be sufficiently accurate to capture their more elaborate functional forms. A decomposition strategy involving subelements for integration will be discussed shortly. In the transition subdomains $\Omega^*_m = \Omega^{\mathrm{T}}$ the coupled shape functions $N_i^{\mathrm{TR}}(\boldsymbol{x})$ have reduced complexity compared to the purely enriched shape functions, as no discontinuity interface cuts through their domain. Consequently their shape functions and derivatives are continuous permitting an element-wise Gauss quadrature approach for integration. However their behavior is expected to be more complex than standard FE shape functions

due to the coupling of standard and enriched shape functions in their formulation, refer to Eqn, 2.1.11. For this reason it is prudent to use a denser Gauss point grid in the numerical computation when compared to non-enriched elements.

With the consideration in mind of the discontinuities adapted into the enriched shape functions, through the enriched intrinsic bases of Section 3.1.2, a viable integration method is presented to handle these intricacies. For an enriched element e_k it is at the discontinuity interface Γ_{disc}, cutting through its domain Ω_k^{el}, that the r enriched shape functions of influence display a jump or kink in their continuity. This sudden change in the shape function behavior cannot be adequately captured by an element-wise Gauss quadrature integration approach. To sufficiently account for these effects the element domain is partitioned into n_k^{se} subelements $e_{k,s}, s = \{1, \dots, n_k^{\text{se}}\}$ with corresponding subdomains $\Omega_{k,s}^{\text{se}}$, such that Eqn. 3.2.10 holds.

$$\Omega_k^{\text{el}} = \bigcup_{s=1}^{n_k^{\text{se}}} \Omega_{k,s}^{\text{se}} \tag{3.2.10}$$

Within each subelement integration by Gauss quadrature is again permissible with the portion of the shape function existing over its domain being smooth and continuous, as the jump or kink in the enriched shape functions will occur between the subelement boundaries. Evaluation of the numerical integration by Gauss quadrature as a discrete summation of weighted values at the element Gauss points expressed by Eqn. 3.2.11, is now realized as a summation over the subelements individual integration approximations. Computed as a discrete sum of weighted values at the subelement Gauss points, see Eqn. 3.2.12.

$$\int_{\Omega_k^{\text{el}}} F(\xi, \eta)\, d\xi d\eta \approx \sum_{I=1}^{M} \sum_{J=1}^{N} F(\xi_I, \eta_J) W_I W_J \tag{3.2.11}$$

$$\int_{\Omega_k^{\text{el}}} F(\xi, \eta)\, d\xi d\eta = \sum_{s=1}^{n_k^{\text{se}}} \int_{\Omega_{k,s}^{\text{se}}} F(\xi, \eta)\, d\xi d\eta \approx \sum_{s=1}^{n_k^{\text{se}}} \sum_{I=1}^{M} \sum_{J=1}^{N} F(\xi_I, \eta_J) W_I W_J \tag{3.2.12}$$

In these expressions $F(\xi, \eta)$ is a function of two variables ξ and η, similar to the shape and weight functions $\hat{N}_i(\boldsymbol{x})$ and $w_i(\boldsymbol{x})$ where $\boldsymbol{x} = (x, y)$. The summation limits M and N denote the number of Gauss points in the ξ and η directions respectively, (ξ_I, η_J) define their coordinate location, with W_I and W_J defining their corresponding Gauss weight. It is thus by selection of the number of Gauss points $M \times N$, used in the integration scheme, that the numerical accuracy is controlled, as higher degree polynomial behavior will be captured with a denser Gauss point configuration. For enriched elements local 5×5 Gauss point grids are

used in each subelement to ensure sufficient capture of the enriched shape function form. For non-enriched and transition elements local Gauss point grids of 2×2 and 5×5 are used in the complete element respectively. The higher number of Gauss points for transition elements is done to safeguard against the complexity that predominantly enriched transition elements might exhibit, i.e. those for which three nodes are considered enriched and only one is considered non-enriched.

The element domain decomposition, into subelements, on which the modified integration approximation is determined, is based on the discontinuity interface path taken through the element. Taken to fit a given arrangement type of the three shown in Figure 3.9.

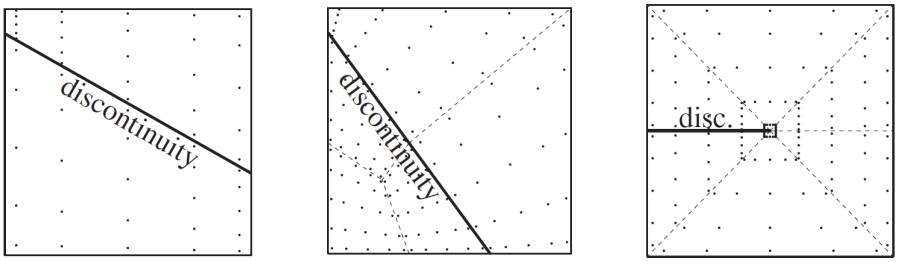

(a) Side-side split element **(b)** Corner split element **(c)** Crack tip split element

Figure 3.9: Sub-discretization of enriched element for Gauss quadrature integration into quadrilateral or triangular subelements (from Ref. [38]: Reprinted with permission from John Wiley and Sons).

When the discontinuity passes completely through the element the division of Figure 3.9a or 3.9b is realized depending if opposite sides or adjacent sides of the element are crossed respectively. In these cases the element division is designed to produce quadrilateral subelements, though a triangular division as presented in References [12, 67] is equally feasible. In instance(s) where a crack tip is contained within the element a triangular partitioning is applied using an isoparametric mapping of rectangular elements to concentrate Gauss points around the crack tip, as shown in Figure 3.9c. This "nearly polar" integration concept was introduced by Laborde et al. [56] to bring the local behavior of the crack tip solution into appropriate consideration, while minimizing otherwise needed refinement of the element decomposition or Gauss point configuration, to obtain good accuracy. In short, the tactic ensures the crack tip singular behavior dominated by $1/\sqrt{r}$ is effectively integrated [38]. Radial arrangement of the Gauss points within the triangular elements is achieved by mapping a reference quadrilateral element into a triangle, where two nodes of the reference element are coincident in the mapped domain Ω, as demonstrated in Figure 3.10. By specifying this particular triangular subelement node as that located directly at the crack tip the Gauss points are clustered within

its vicinity as desired.

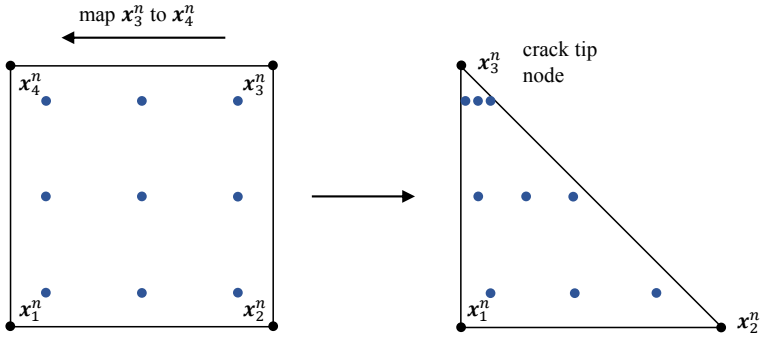

Figure 3.10: Gauss point configuration transformation from master quadrilateral element to master triangular element for "polar" integration around crack tip, demonstrated for a 3×3 Gauss point grid.

In differentiating the approximation functions for post-processing of the displacement field to obtain strain and stress values the same methodology is followed as for the integration. Shape functions existing over non-enriched or transition element domains Ω_k^{el} are sufficiently smooth and continuous to permit an element-wise differentiation approach. Whereas for enriched elements the jump or kink in the enriched shape functions will translate to discontinuities in their derivatives. Thus the subelement decomposition is again used to divide the differentiation over their corresponding domains $\Omega_{k,s}^{\text{se}}$. In all cases the numerical derivatives are realized based on the approximation function derivative, refer to Eqn. 3.2.3, where evaluation occurs for the shape function derivatives at the element or subelement Gauss points. Definitions of the standard FE, enriched MLS, and coupled transition shape function derivatives can be found in Appendix Section A.2.

Temporary coordinate locations for defining the subelement vertices and edges are evaluated from intersection of the approximate LSC Γ_{disc}^h with the element edges. These calculations are carried out using simple relations based on the LSF node values ψ_i^n and knowledge of the zero-level LSC representation of a discontinuity interface, or are taken from predetermine quantities (e.g. the crack tip coordinate $\boldsymbol{x}_t$). Further details and expressions for these calculations are presented in Appendix Section A.1. It is worthwhile to realize their role is only *temporary* because they are purely used to define subelement divisions of enriched elements for integration and differentiation of the shape functions. They have no permanent role in defining any interface geometry. All relevant information descriptive of a discontinuity interface Γ_{disc}^h is stored in the associated LSF approximation $\psi^h(\boldsymbol{x})$.

4 Results and Discussion

In the present chapter results determined using a developed IXFEM code, based on the principles discussed and developed through Chapters 2 and 3, are presented for a series of study cases against analytic and FEM solutions to demonstrate the capacity of the IXFEM as an effective numerical tool for the analysis of composite material systems. Beginning with comparisons against known analytic solutions for simple problems containing a single strong or weak discontinuity, the validity of the strong and weak enriched intrinsic bases are established for their intended design in modeling corresponding discontinuities. In conjunction with these tests a FEM code is also verified, to be used subsequently for comparison of calculated effective material properties for an idealized nanocomposite of interest, based on a representative volume element (RVE). These results are additionally compared against an analytic solution as determined using the composite cylinder method (CCM) taken from Ref. [47]. In culmination the efficiency of the IXFEM, as a mesh independent approximating method, is used to evaluate a series of enlarged RVE's, in which the idealized composite filler distribution constraint has been removed and in a RVE with an evolving microstructure in time.

All problems considered are analyzed in the two-dimensional domain applying appropriate plane elasticity assumptions, and utilize meshes composed of bilinear quadrilateral elements. Meshes used with the IXFEM are further arranged as purely rectangular elements, to take advantage of the predictable nature of such structured meshes when building the local enriched approximation functions, reference Appendix Section A.4 for more details. As applicable to the analysis the material response, evaluated in terms of nodal displacements plus Gauss point stress and strain values, are presented in qualitative and quantitative comparison, through visual inspection of the primary and secondary variable fields and error norm differentials respectively. For the validation cases the error measures are determined in the context of error convergence results with respect to the analytic solution, whereas in later analysis, when analytic solution fields are no longer available, the error difference is taken with respect to the FEM solution. The two error measures accounted in these studies are the L_2 and energy norm as defined in Eqn. 4.0.1 and 4.0.2 respectively,

$$\|\boldsymbol{u} - \boldsymbol{u}^h\|_{L_2} = \left(\int_\Omega (\boldsymbol{u} - \boldsymbol{u}^h)^{\mathrm{T}} (\boldsymbol{u} - \boldsymbol{u}^h) \, d\Omega \right)^{1/2} \tag{4.0.1}$$

$$\|\boldsymbol{u} - \boldsymbol{u}^h\|_{E} = \left(\int_\Omega (\boldsymbol{\epsilon} - \boldsymbol{\epsilon}^h)^{\mathrm{T}} (\boldsymbol{\epsilon} - \boldsymbol{\epsilon}^h) \, d\Omega \right)^{1/2} \tag{4.0.2}$$

where $\boldsymbol{u}$ and $\boldsymbol{\epsilon}$ represent the displacement and strain of the analytic solution respectively, while superscript h denotes the corresponding approximate numerical solution. Normalization of these two error norm measures is achieved by division with the analytic norm values, i.e. $\|\boldsymbol{u}-\boldsymbol{u}^h\|_{L_2}/\|\boldsymbol{u}\|_{L_2}$ and $\|\boldsymbol{u}-\boldsymbol{u}^h\|_E/\|\boldsymbol{u}\|_E$.

4.1 Strong Discontinuity - Plate with a Hole

The first validation case considered is that of an infinite plate with a circular hole (a strong discontinuity in the IXFEM) at its center under an applied uniform uniaxial tension in the vertical direction. Following the process outlined in Ref. [53] for deriving the analytic solution of a double filled plate, under equivalent boundary conditions, by means of the Airy stress function, the solution for the comparatively simplified problem in consideration (plate with a hole) was found by extension. In order to properly compare results obtainable from the FEM and IXFEM implementations, against this known analytic solution, a matching plate problem of finite dimension was devised for the numerical simulations. Illustrated in Figure 4.1, the finite plate model is composed of physical domain Ω_1, indicated as the shaded region, and void domain Ω_2. Using the relevant dimensional parameters identified in the figure the computational solutions were determined for a plate of unit height $h = 1\text{m}$ having width to height ratio $w/h = \sqrt{3}/2$ and hole radius to height ratio $r/h = 0.15$. Additional specified problem variables include the plate material, selected as isotropic aluminum 1199 (99% pure aluminum) with Elastic modulus $E = 70\text{GPa}$ and Poisson's ratio $\nu = 0.35$ [27], plus the applied tension in the form of uniform uniaxial traction $\boldsymbol{t}^\infty = t_y^\infty = 10\text{GPa}$ on the top and bottom edge of the infinite plate. The plate is analyzed under plane stress assumptions.

For application with the FEM only domain Ω_1, representing the physical continuum of the aluminum plate, is meshed. Domain Ω_2, being unmeshed, is then implicitly recognized as internally void space, within corresponding strong discontinuity boundary Γ_2, signifying presence of the center hole geometry. In contrast, for the IXFEM the entire problem domain union $\Omega = \Omega_1 \bigcup \Omega_2$ is meshed, without regard to internal discontinuity interface Γ_2. Presence of the strong discontinuity is instead defined using the LSM, as described in Section 2.3.1, where direct characterization is achieved using a circular LSF $\psi^{\text{c}}(\boldsymbol{x})$, prescribing a zero-level LSC Γ^{circle} being coincident with the boundary of domain Ω_2. See Figure 4.2 for comparison of such described meshes used in the FE analyses, where the LSC in the IXFEM is drawn overtop the mesh. A subsequent decomposition of the domain will determine which elements are cut by the discontinuity and group elements into non-enriched Ω^{S}, enriched Ω^{E} and transition Ω^{T} subdomains accordingly for evaluation,

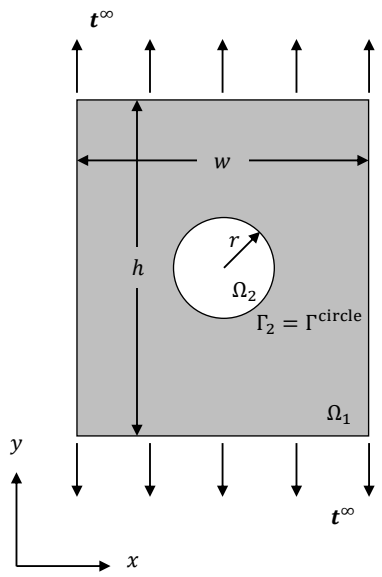

Figure 4.1: Representation of boundary conditions, distinct domains, and defining dimension parameters for plate with a hole problem.

as shown in Figure 4.3b given the Level-set of Figure 4.3a. As the hole is a strong discontinuity, primary variables (displacements) are to be discontinuous across interface Γ_2, the full-form enriched intrinsic basis for strong discontinuities $\boldsymbol{p}_{\text{s,f}}^{\text{enr}}(\boldsymbol{x})$, Eqn. 3.1.10, is used in the MLS shape function calculations to appropriately enhance the approximation space. Furthermore, to properly model the effects of the hole as void space the material properties of elements and subelements residing within Ω_2 are set to zero (to avoid singular matrices initially encountered in the numerical solution routine, the material properties are actually set to extremely small values, e.g. $< 10^{-10}$).

To couple the to-be-determined approximate solution of the finite plate with a hole in tension to the analytic solution, of the corresponding infinite plate, nodal displacements for all boundary nodes of the FE meshes were evaluated using the analytic (Airy stress function) solution and applied as Dirichlet (essential) boundary conditions in both FE computations. This assures comparison of results based on consistent loading cases. The resultant displacement, strain, and stress fields, as evaluated from the standard FEM and IXFEM implementation are presented next in comparison to the analytic solution. These results were computed based on meshes of 4592 elements for the FEM and 4140 elements for the IXFEM. In both cases equivalent baseline element sizes were used to seed (generate) the boundary element configuration (number of elements on boundary width×number of elements on boundary height), such that the simulations performed with

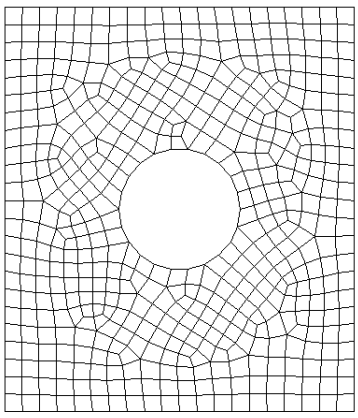

(a) Example conforming mesh for FEM

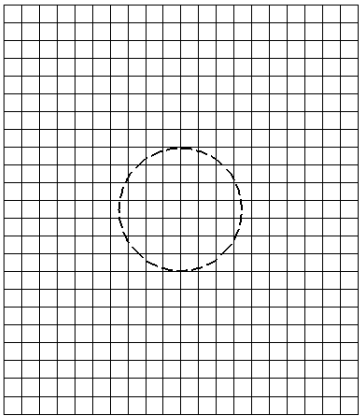

(b) Example structured mesh for IXFEM

Figure 4.2: Comparison of a conforming mesh required with the standard FEM and a structured mesh used with the IXFEM to model the plate with a hole problem, in subfigure b the discontinuity interface boundary is overlaid for reference

both numerical methods had the same essential boundary conditions imposed from the Airy stress function. However, whereas prevalent variability of element size occurs in generating the conforming mesh, around hole domain Ω_2, to be used with the FEM, the structured mesh permissible with the IXFEM is able to uniformly best meet the prescribed baseline element size, as shown by the example meshes of Figure 4.2a and 4.2b accordingly. This difference in number of mesh elements, ~10% less for the IXFEM compared to the FEM, is thus a consequence of the mesh dependency associated with the standard FEM, i.e. that all discontinuity interfaces must be directly defined by the mesh geometry.

Contour plots for the plate with a hole problem are shown in Figures 4.4 through 4.9, displaying in comparison displacement fields (u_x, u_y), corresponding strain fields (ϵ_{xx}, ϵ_{yy}), and stress fields (σ_{xx}, σ_{yy}), where subscripts x and y denote quantities aligned with the horizontal and vertical direction respectively. In all cases, from initial visual inspection, there is good agreement between the analytic solution and the FEM and IXFEM approximations, for all primary and secondary variables in the physical domain Ω_1, with both the magnitude and bulk field response of the plotted solution fields showing qualitatively equivalent behavior. An error norm difference for both approximations will be discussed following analyses of the contour plots. Recalling the mesh geometries used with the FEM and IXFEM analysis, refer to Figure 4.2, the reason domain Ω_2, representing the circular hole, is directly evident in the FEM plots, as void space, while in the IXFEM plots this same region is filled can be explained. For the FEM the computational mesh resides exclusively within domain Ω_1, thus evaluated nodal displacements plus Gauss point stresses and strains will

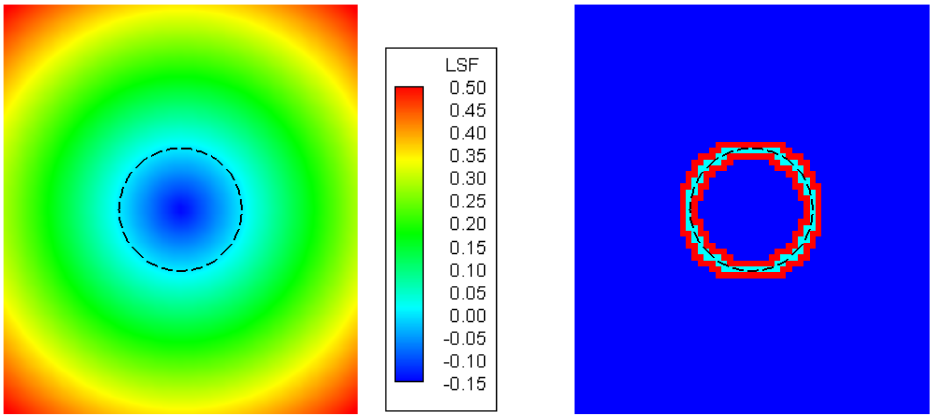

(a) Level-set contour **(b)** Domain decomposition

Figure 4.3: Level-set definition of circular hole in plate and corresponding domain decomposition, blue regions indicate non-enriched subdomains Ω^{S}, light blue enriched subdomains Ω^{E}, and red transition subdomains Ω^{T}. The discontinuity interface boundary is overlaid for reference.

also only be determined at points internal to or on the boundary mesh. Stated otherwise, since the mesh for the FEM does not extend into domain Ω_2 no assessable points exists at which the field variables can be calculated. However, for the IXFEM the computational mesh covers the problem domain union Ω such that the nodes and Gauss points residing on elements enclosed in the discontinuity domain Ω_2 will have calculated displacement plus strain and stress values from solution of the FE model and post-processing of the displacement derivatives respectively.

It is of primary interest to note for the IXFEM results shown in subfigure c of Figures 4.4 through 4.7 (u_x, u_y, ϵ_{xx}, ϵ_{yy}), in addition with ϵ_{xy}, not shown here, that the displacements and strains have non-zero, and in the case of the strains also non-uniform, value within the strong discontinuity domain Ω_2. As will be discussed following comparison of the field variable plots this irregular behavior is resultant from application of the full-formed enriched intrinsic basis $\boldsymbol{p}^{\mathrm{enr}}_{\mathrm{s,f}}(\boldsymbol{x})$, in the enriched shape function computations. Thus in the subsequent qualitative comparison analysis the as determined results for the discontinuity domain will be precluded from discussion. Before reviewing each individual set of responses (displacement, strain, and stress) it is noted that the IXFEM stress contours, Figures 4.8c and 4.9c, do not display similar behavior, instead having constant value zero within the confines of the strong circular discontinuity. This is expected as the material properties, and thus the elastic material constants C_{ij} in Eqn. 3.1.5, are defined as zero for void domain Ω_2, thus the post-processed stresses determined through the constitutive relation Eqn. 3.1.2 are guaranteed to be zero, as should be for void space. Displacement fields (u_x, u_y), Figures 4.4 and 4.5

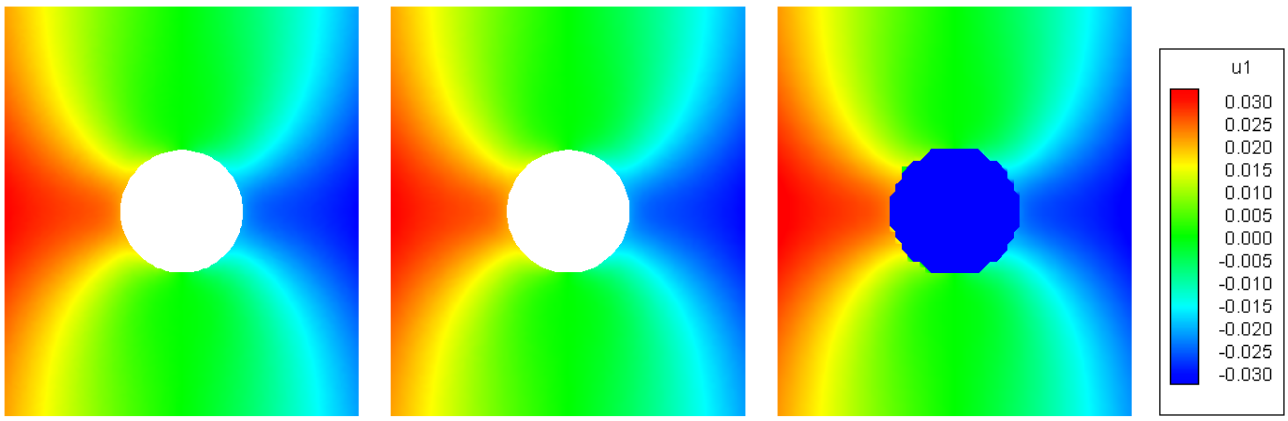

(a) Analytic, u_x (m) **(b)** FEM, u_x (m) **(c)** IXFEM, u_x (m)

Figure 4.4: Comparison of u_x displacement field from analytic, FEM, and IXFEM (using full-form enriched intrinsic basis, Eqn. 3.1.10) solution for plate with a hole problem.

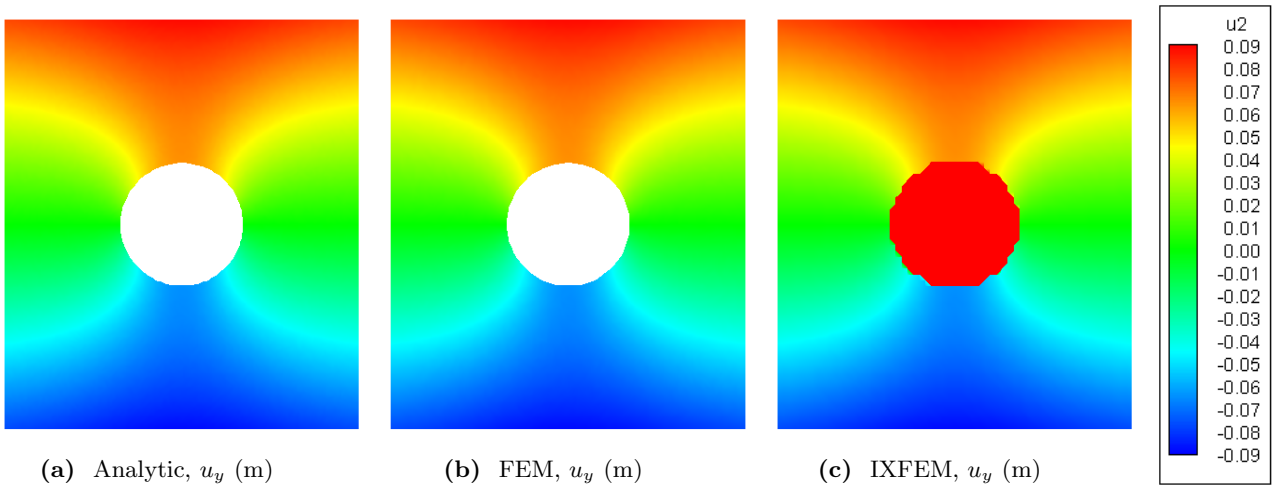

(a) Analytic, u_y (m) **(b)** FEM, u_y (m) **(c)** IXFEM, u_y (m)

Figure 4.5: Comparison of u_y displacement field from analytic, FEM, and IXFEM (using full-form enriched intrinsic basis, Eqn. 3.1.10) solution for plate with a hole problem.

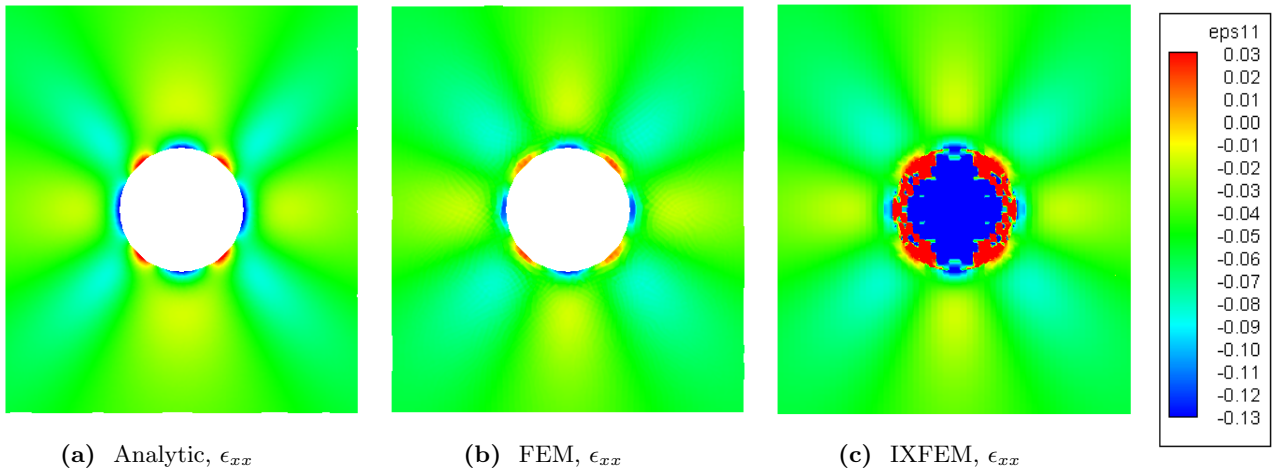

(a) Analytic, ϵ_{xx} **(b)** FEM, ϵ_{xx} **(c)** IXFEM, ϵ_{xx}

Figure 4.6: Comparison of ϵ_{xx} strain field from analytic, FEM, and IXFEM (using full-form enriched intrinsic basis, Eqn. 3.1.10) solution for plate with a hole problem.

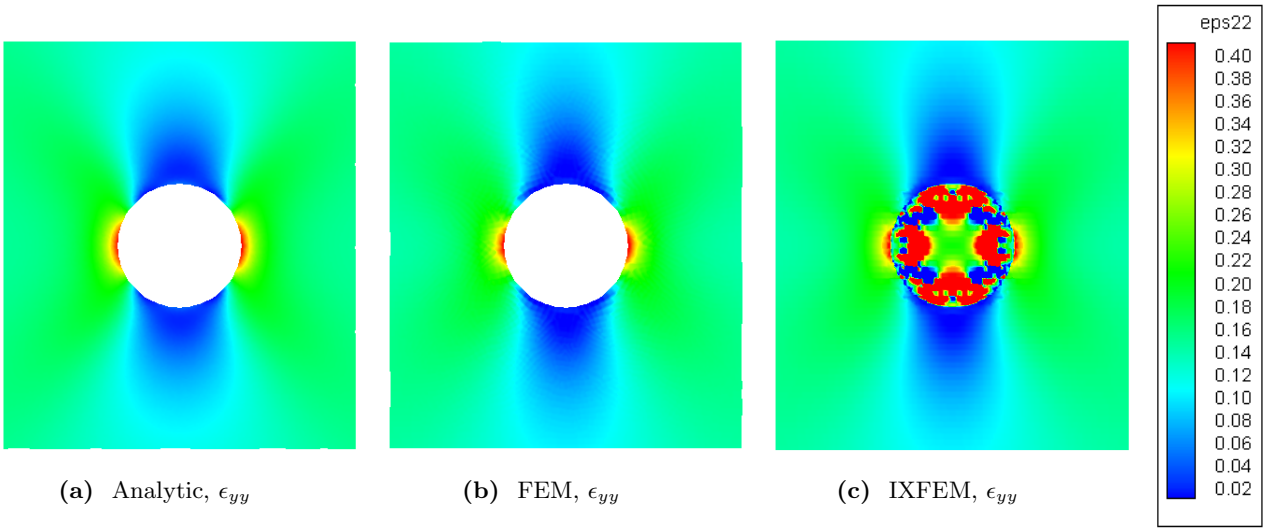

(a) Analytic, ϵ_{yy} **(b)** FEM, ϵ_{yy} **(c)** IXFEM, ϵ_{yy}

Figure 4.7: Comparison of ϵ_{yy} strain field from analytic, FEM, and IXFEM (using full-form enriched intrinsic basis, Eqn. 3.1.10) solution for plate with a hole problem.

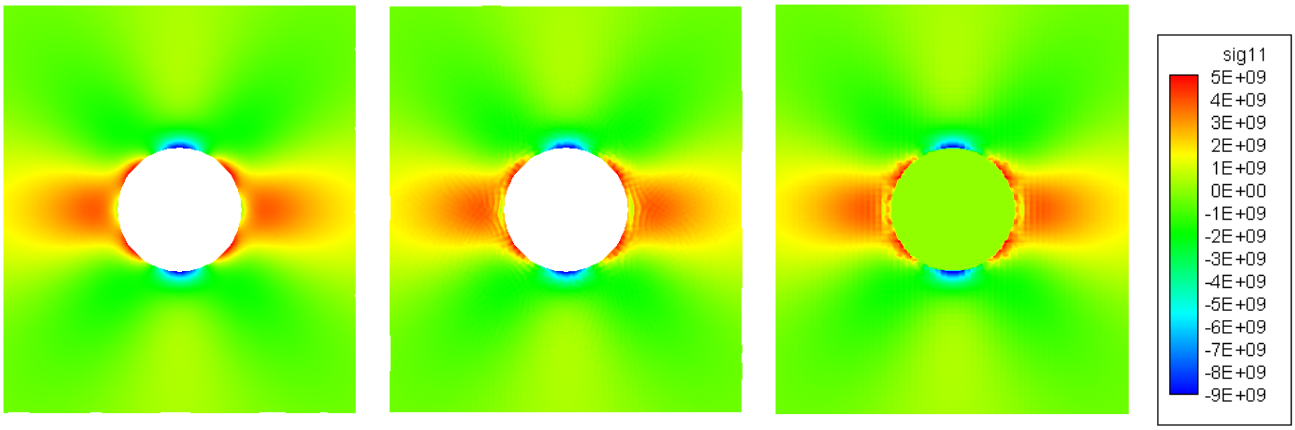

(a) Analytic, σ_{xx} (Pa) **(b)** FEM, σ_{xx} (Pa) **(c)** IXFEM, σ_{xx} (Pa)

Figure 4.8: Comparison of σ_{xx} stress field from analytic, FEM, and IXFEM (using full-form enriched intrinsic basis, Eqn. 3.1.10) solution for plate with a hole problem.

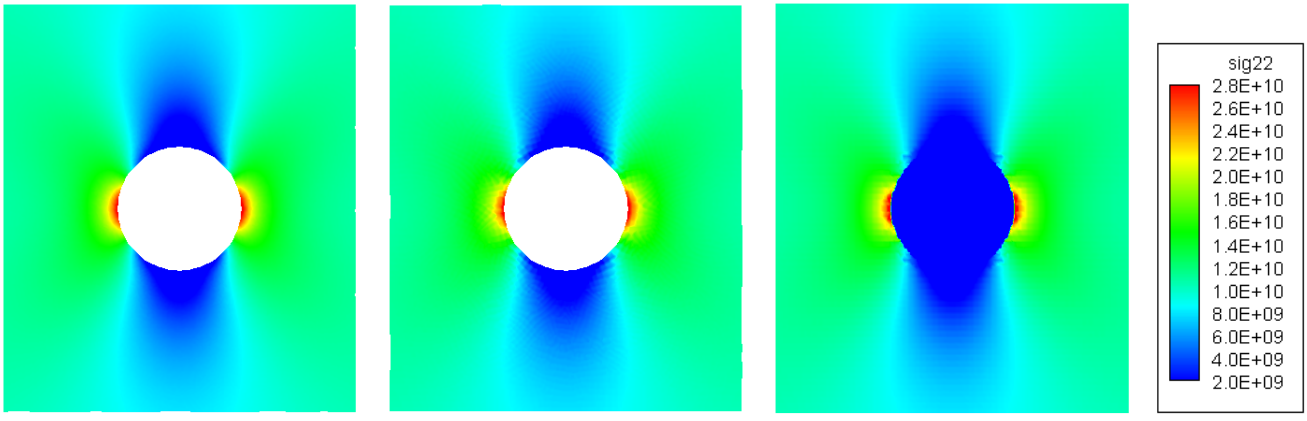

(a) Analytic, σ_{yy} (Pa) **(b)** FEM, σ_{yy} (Pa) **(c)** IXFEM, σ_{yy} (Pa)

Figure 4.9: Comparison of σ_{yy} stress field from analytic, FEM, and IXFEM (using full-form enriched intrinsic basis, Eqn. 3.1.10) solution for plate with a hole problem.

respectively, display highly uniform response in the physical domain Ω_1 and are nearly indistinguishable from visual examination alone. Examining strain fields (ϵ_{xx}, ϵ_{yy}), in Figures 4.6 and 4.7, determined from differentiation of displacement fields (u_x, u_y) in the (x, y) direction respectively, inaccuracies are more easily identifiable. Minor, though perceptible, deficiencies are most evident at the opposing horizontal, vertical, and cross-diagonal quadrant points edging the strong discontinuity boundary Γ_2, discernible by loss in fidelity and smoothness in the FE approximations. This particular inaccuracy is most prominent at the horizontal quadrant points in the ϵ_{xx} strain field were both the FEM and IXFEM results indicate a smaller strain concentration region than that seen in the derived analytic solution. Additional deviations from the analytic solution are observed in the strain banding, where the computational results display reduced thickness and increased extension through the vertical centerline band in both the ϵ_{xx} and ϵ_{yy} contours, as well as increased thickness along the oblique bands in strain field ϵ_{xx}. Stress fields (σ_{xx}, σ_{yy}), shown in Figures 4.8 and 4.9 respectively, exhibit minor losses in smoothness while otherwise capturing the field response magnitude and shape to a high degree of consistency. Overall the bulk strain and stress field responses are well predicted by both FE methods, and demonstrates the capacity of the full-form basis $\boldsymbol{p}^{\text{enr}}_{\text{s,f}}(\boldsymbol{x})$, applied in the IXFEM, to enrich the approximation space to appropriately model the presence of a strong discontinuity.

Returning to the strong discontinuity domain, it is not entirely unexpected for the IXFEM to evaluate non-zero nodal displacements, and thus non-zero strains, within the meshed void domain Ω_2. Given that the discontinuity boundary Γ_2 undergoes deformation, clearly captured by the IXFEM, as demonstrated in Figures 4.4c and 4.5c, it might seem logical for that deformation to "propagate" smoothly through the discontinuity domain mesh to the plate center. Nonetheless, this is not the behavior captured by the IXFEM. Instead the results display behavior more suggestive of an unconstrained fictitious rigid body translation, as indicated from comparing the well behaved response throughout physical domain Ω_1 to the isolated large deformations of void domain Ω_2. From tabulated output actual nodal displacements at nodes $\mathcal{N}_2^{\text{disc}}$, internal to domain Ω_2, are found to be orders of magnitude larger than those at nodes $\mathcal{N}_1^{\text{phys}}$, of domain Ω_1, having maximum absolute value displacement components recorded as high as $|u^{\max}_{x,\text{disc}}| > 1300$m and $|u^{\max}_{y,\text{disc}}| > 3600$m. The corresponding strain fields for the discontinuity domain likewise have evaluated maximum values at orders of magnitude higher than in the physical domain, as they are derived from the displacements, with $|\epsilon^{\max}_{xx,\text{disc}}| > 2$ and $|\epsilon^{\max}_{yy,\text{disc}}| > 5$. In any case, as shown by Figures 4.4 through 4.7, the irregular behavior for the discontinuity domain has negligible, if any, impact on the approximate solution determined in the physical domain, this is further confirmed with the error convergence results discussed at

the end of the section.

As mentioned earlier it is the use of the full-from enriched basis $\boldsymbol{p}_{\mathrm{s,f}}^{\mathrm{enr}}(\boldsymbol{x})$, in the MLS shape function computation that is attributed with causing the usually large displacements for subdomains internal to strong discontinuity interfaces. To be discussed, by comparison with the truncated enriched basis $\boldsymbol{p}_{\mathrm{s,t}}^{\mathrm{enr}}(\boldsymbol{x})$, this "instability" seen for void space deformations results when not directly enforcing the strong discontinuity in the underlying continuity of the enriched shape function. Recalling the point made in Section 3.1.2, the two enriched bases defined for modeling strong discontinuities implement different approaches in the MLS computation for incorporating the proper discontinuous behavior in the shape function form. Whereas the full-form basis uses the inclusion of the sign function in the intrinsic basis, the truncated basis is designed to work with a truncated version of the specialized weight function $w_i^{S*}(\boldsymbol{x})$, Eqn. 3.1.12, having a modified compact support based on the visibility criteria of Ref. [75]. In both approaches the strong discontinuity is explicitly assimilated into the enriched shape function form as a "zeroing" (or flattening) of the shape function across the discontinuity interface, it is in this execution that the two intrinsic bases differ. With the full-form basis, the sign function brings in the discontinuity at the interface but does not ensure a strict zero evaluation in the portion of the enriched element that would be considered internal to the discontinuity from the visibility criteria. In this section of the element the enriched shape function evaluates to near zero quantities. This is in opposition to the truncated basis, using truncated weight function $w_i^{\mathrm{S}*}(\boldsymbol{x})$ the discontinuity is directly enforced by extension of the continuity of the weight function to the enriched shape function, as discussed in Section 2.2.3, i.e. $N_i^{\mathrm{MLS}}(\boldsymbol{x}) = 0$ where $w_i^{S*}(\boldsymbol{x}) = 0$. Since the element region truncated corresponds to that internal to the discontinuity the shape function was no value over this portion, thus it evaluates precisely to zero. These marginal differences in evaluation of the shape function lead to different contributions from the enriched approximation functions formed and integrated during assembly of the global FE model, and impacts the "stability" of void domain deformations.

Application of the truncated basis $\boldsymbol{p}_{\mathrm{s,t}}^{\mathrm{enr}}(\boldsymbol{x})$ in evaluation of the validation problem (plate with a hole) lead to stable displacements, strains, and stresses within the void domain Ω_2. In these cases the displacements, and thus the strains, at nodes, and Gauss points, internal to the strong circular discontinuity Γ^{circle} evaluated to value zero in the IXFEM approximation. The cause of this "cutoff" behavior can be traced back to the operation of the truncated basis, and receives further detailed discussion in Appendix Section A.3. Stresses were zero as well for the same reason discussed previously, i.e. material properties of the void domain are set to zero thus no non-zero stresses are calculated in the post-processing. Given this reasonable behavior in

the void domain it was unexpected to find the solution field in the physical domain Ω_1 to be almost entirely inaccurate, except near the problem boundaries where essential boundary conditions are imposed. Contour plots of the field variables are not provided, but error norm comparisons with the analytic solution gave differences are far off as 40% and 70% in the L_2 and energy norm respectively with marginal improvement with mesh refinement as shown in the error convergence results presented subsequently. In an additional study of the validation problem the full-form basis $\boldsymbol{p}^{\text{enr}}_{\text{s,f}}(\boldsymbol{x})$ was paired with the truncated specialized weight function, in what is considered a full-form with truncation basis $\boldsymbol{p}^{\text{enr}}_{\text{s,ft}}(\boldsymbol{x})$, to investigate if the cause of the error seen with the truncated basis lies within the intrinsic basis or the truncated weight function. Results obtained with this basis compared much more favorably to the analytic solution, and are shown in Figure 4.10. As with the truncated basis, zero valued displacements and strains result for the void domain reaffirming the truncated weight function inherently act to stabilize the otherwise observed fictitiously large void space deformations. Additional comparison to the IXFEM results, using the full-form basis, in Figures 4.4-4.9 also display fair agreement, though noticeable loss in smoothness of the approximation near the discontinuity interface is visible. The error norm measures show this discrepancy as added inaccuracy with the full-form with truncation basis over the full-form basis.

To further study the various enriched bases applied in modeling a strong discontinuity in the IXFEM, the validation problem was run for a series of four meshes with increasing h-refinement (element count) to obtain a measure of the error convergence rate with each basis (full-form $\boldsymbol{p}^{\text{enr}}_{\text{s,f}}(\boldsymbol{x})$, full-form with truncation $\boldsymbol{p}^{\text{enr}}_{\text{s,ft}}(\boldsymbol{x})$, and truncated $\boldsymbol{p}^{\text{enr}}_{\text{s,t}}(\boldsymbol{x})$). For a point of comparison the convergence rate was also determined for the FEM. Details of the four meshes used with the FEM and IXFEM are provide in tables of Appendix C, in terms of number of nodes n^{nd}, number of elements n^{el}, and the boundary element configuration $n^{\text{el}}_{\text{width}} \times n^{\text{el}}_{\text{height}}$. For each mesh case the Airy stress function was used to evaluate the analytic nodal displacements and Gauss point strains for use in the L_2 and energy norm measures, Eqn. 4.0.1 and 4.0.2 respectively. When computing the norms for the IXFEM approximations only the values at nodes and Gauss points residing in the physical domain Ω_1 were considered, as those in void domain Ω_2 are in a sense "fictitious" having been shown to be controllable through selection of the enrichment basis. The convergence rate results are shown in Figure 4.11 as curves of percent error in the norms, with respect to the analytic solution, versus baseline element size h on log-log axes.

Initial inspection of Figure 4.11a reveals linear decreasing trends for the L_2 norms of the FEM and IXFEM results, when using the full-form or full-form with truncation bases, as should be expected. In the case of

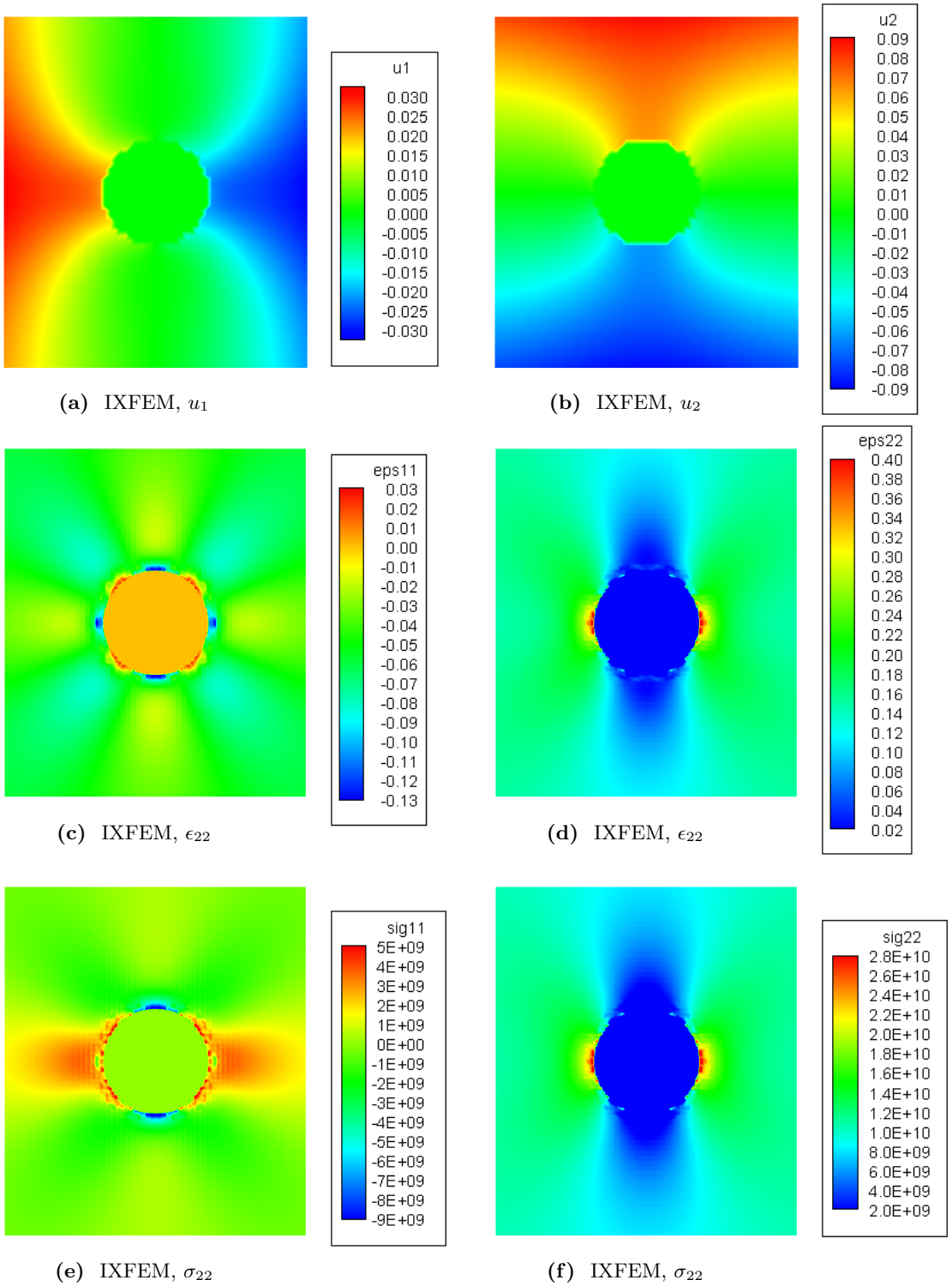

(a) IXFEM, u_1 **(b)** IXFEM, u_2

(c) IXFEM, ϵ_{22} **(d)** IXFEM, ϵ_{22}

(e) IXFEM, σ_{22} **(f)** IXFEM, σ_{22}

Figure 4.10: Displacement, strain, and stress field solutions from the IXFEM (using full-form enriched intrinsic basis, Eqn. 3.1.10 in combination with truncated specialized weight function, Eqn. 3.1.12) for plate with a hole problem demonstrating zeroed variable fields in the strong discontinuity domain.

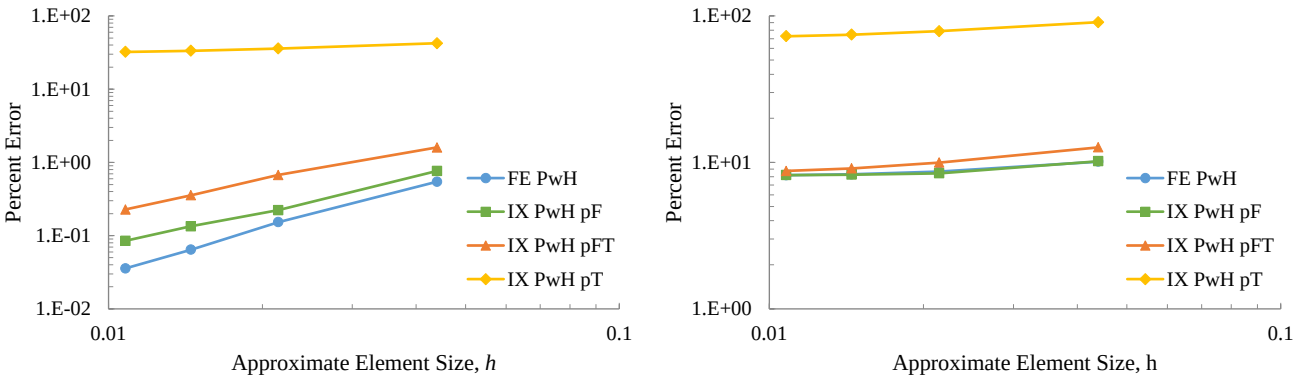

(a) L_2 norm **(b)** Energy norm

Figure 4.11: Error norm convergence results for strong discontinuity validation problem (Plate with a hole, PwH). As listed in the plot legend abbreviations are defined as follows: FE - FEM, IX - IXFEM, pF - full-form basis $\boldsymbol{p}^{\text{enr}}_{\text{s,f}}(\boldsymbol{x})$, pFT-full-form basis with truncation $\boldsymbol{p}^{\text{enr}}_{\text{s,ft}}(\boldsymbol{x})$, pT-truncated basis $\boldsymbol{p}^{\text{enr}}_{\text{s,t}}(\boldsymbol{x})$

the truncated basis in the IXFEM the results show significant deviation from the analytic solution with only nominal improvement as the mesh element size is decreased. In the energy norm results of Figure 4.11b all cases including the FEM show minimal change in the error with decreases in element size. From both figures the full-form basis $\boldsymbol{p}^{\text{enr}}_{\text{s,f}}(\boldsymbol{x})$ performs best in terms of rate of convergence and magnitude of error. Investigation into the large error for the cases using the truncated basis found the enriched shapes constructed through the MLS method to be different in form to those generated with the full-form basis, it is suspected this is the leading cause for the dramatic error differential.

4.2 Weak Discontinuity - Plate with an Inhomogeneity

The second validation case considered is that of an infinite plate with a circular inhomogeneity (a weak discontinuity in the IXFEM) at its center under an applied uniform uniaxial tension in the vertical direction. Again following the outline in Ref. [53], the analytic solution of the problem in consideration (plate with an inhomogeneity) was found. Likewise as in Section 4.1, numerical results determined from the FEM and IXFEM codes were computed on a matching plate problem of finite dimension for comparison to the analytic solution. The finite plate model for this problems is taken to be of the same dimensions as provided for the validation problem of Section 4.1 and displayed in Figure 4.1, except in this case domain Ω_2 is that of the inhomogeneity and has non-zero material property definitions. In connection with the CNT-polymer

nanocomposite system to be analyzed subsequently, the material properties for the two distinct domains (phases) of the composite plate are taken to be that of the nanocomposite matrix material (EPON 862, $E = 3.07$GPa, $\nu = 0.03$) for surrounding domain Ω_1 and that of an effective transversely isotropic SWCNT ($E_{22} = 346$GPa, $\nu_{12} = 0.38$) for filler domain Ω_2, where Material directions (x_1,x_2) align with global axes (x,y) respectively. These material properties match those determined in Ref. [88] in using the CCM to derive effective properties for an effective transversely isotropic SWCNT based on material properties of a isotropic hallow SWCNT. The applied traction is also changed to $\boldsymbol{t}^{\infty} = t_y^{\infty} = 100$MPa on the top and bottom edge of the infinite plate, and a switch to plane strain assumptions is made as the out of plane fiber direction is much larger than the in plane dimensions.

As discussed previously the FEM requires a mesh defined over the entire physical problem domain, constrained to explicitly represent all global boundaries and internal discontinuity interfaces, whereas the IXFEM is designed to work with an arbitrary mesh existing over the entire problem domain, including any void spaces. Thus for application with the FEM both domains Ω_1 and Ω_2, representative of the composite matrix and filler material respectively, will contain mesh elements with the bimaterial interface Γ_2 defined by conforming element boundaries. For the IXFEM the entire problem domain $\Omega = \Omega_1 \bigcup \Omega_2$ is meshed as well using rectangular elements, again without regard for internal interface Γ_2. See Figure 4.12 for comparison of these described meshes. One advantage of the IXFEM over the conventional FEM becomes evident as the same structured mesh shown in Figure 4.2b, for the plate with a hole problem, along with the same circular LSF $\psi^{\mathrm{c}}(\boldsymbol{x})$ can be used *unmodified* for decomposition and solution of the plate with an inhomogeneity problem (keeping in mind that the same global domain geometry is used in both validation problems). The difference in discontinuity type is entirely resolved by using a different enriched intrinsic basis $\boldsymbol{p}^{\mathrm{enr}}(\boldsymbol{x})$ in the MLS shape function computations. Specifically as the material interface is a weak discontinuity, secondary variables (strain and stress) are expected to show degrees of discontinuity across interface Γ_2, the enriched intrinsic basis $\boldsymbol{p}_w^{\mathrm{enr}}(\boldsymbol{x})$, Eqn. 3.1.9, is applied in the MLS method.

Along the same lines as in Section 4.1, the to-be-determined approximate solution for the finite composite plate in tension is coupled to the corresponding analytic solution through the evaluated mesh boundary node displacements from the Airy stress function and applied as essential boundary conditions in the FE codes. Resulting primary and secondary variable fields are presented next in comparison to the analytic solution. These results were computed on a mesh of 5078 elements and the same 4140 element mesh of the previous section for the FEM and IXFEM respectively. As before equivalent baseline element sizes were used to

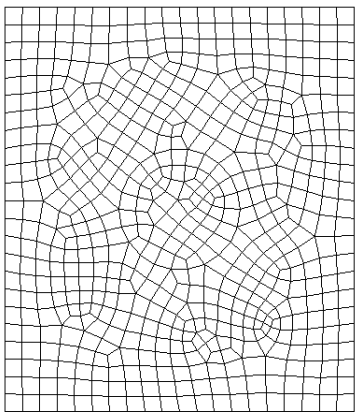

(a) Example conforming mesh for FEM

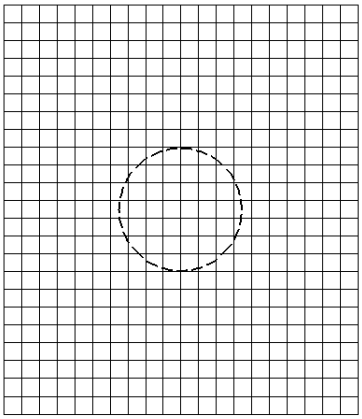

(b) Example structured mesh for IXFEM

Figure 4.12: Comparison of a conforming mesh required with the standard FEM and a structured mesh used with the IXFEM to model the plate with an inhomogeneity problem, in subfigure b the discontinuity interface boundary is overlaid for reference

generate the boundary element configuration from which the internal mesh configuration was determined. Therefore the same argument given previously, in regards to the problem geometry based mesh dependency associated with the FEM, stands for explaining the difference in number of mesh elements, ~18% less for the IXFEM compared to the FEM mesh.

Contour plots displaying displacement fields (u_x, u_y) plus corresponding strain and stress fields (ϵ_{xx}, ϵ_{yy}, σ_{xx}, σ_{yy}) are shown in Figures 4.13 through 4.18 for the plate with a inhomogeneity problem. For all cases, except stress fields σ_{xx} and σ_{yy} determined from the IXFEM, Figures 4.17c and 4.18c respectively, there is good agreement between the analytic solution and the FEM and IXFEM approximations, based on initial qualitative inspection of the magnitude and bulk field response of the plotted variables. The inconsistencies observed in the two stress contours, plus σ_{xy} not displayed here, will be shown to have marginal impact on overall error with increasing mesh refinement based on an error norm difference. Furthermore based on recent analysis of similar discrepancies in mesh-embedded methods [2, 86] one conceivable explanation for the source of the error is identified.

Immediately from displacement fields (u_x, u_y) and strain fields (ϵ_{xx}, ϵ_{yy}), shown in Figures 4.13 through 4.16, it is observed that the intrinsic enriched basis $\boldsymbol{p}_w^{\text{enr}}(\boldsymbol{x})$ fully supports the prediction of discontinuities in primary variable derivatives where appropriate while preserving a smooth continuous approximation of the primary variables. As with the plate with a hole problem, the displacement fields determined using the FEM and IXFEM are highly uniform and virtually indistinguishable from the analytic solution based on visual

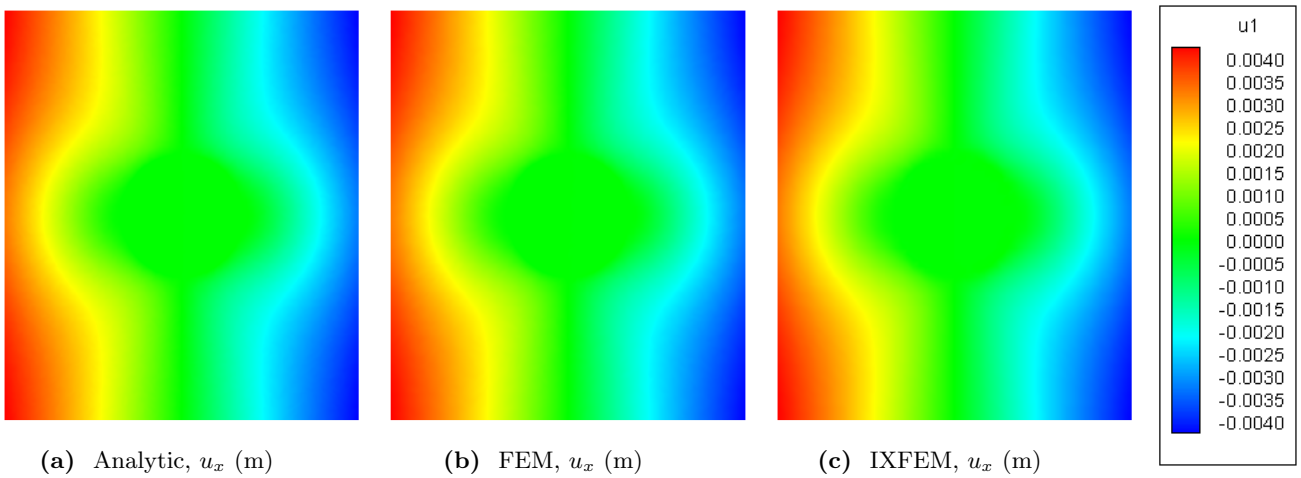

(a) Analytic, u_x (m) **(b)** FEM, u_x (m) **(c)** IXFEM, u_x (m)

Figure 4.13: Comparison of u_x displacement field from analytic, FEM, and IXFEM solution for plate with a in homogeneity problem.

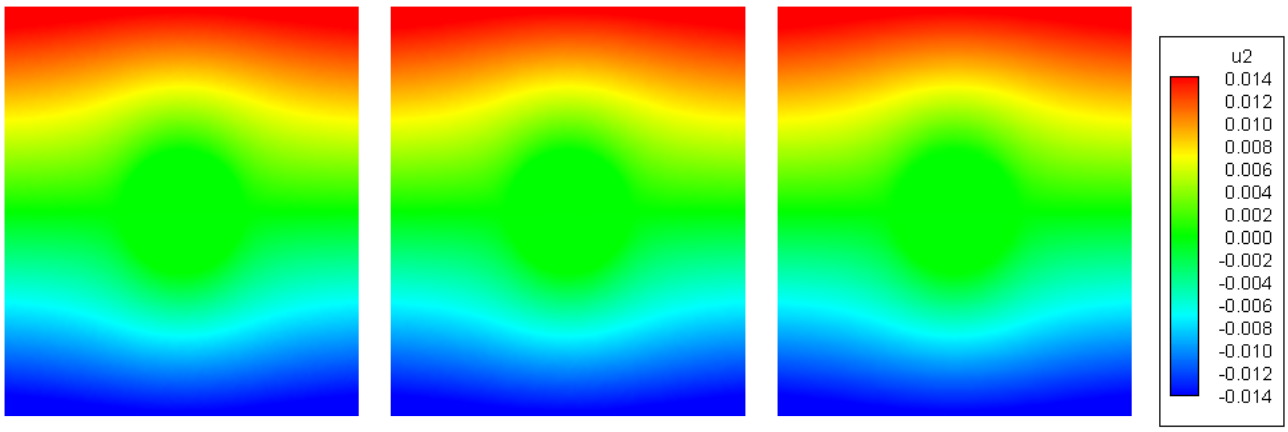

(a) Analytic, u_y (m) **(b)** FEM, u_y (m) **(c)** IXFEM, u_y (m)

Figure 4.14: Comparison of u_y displacement field from analytic, FEM, and IXFEM solution for plate with a inhomogeneity problem.

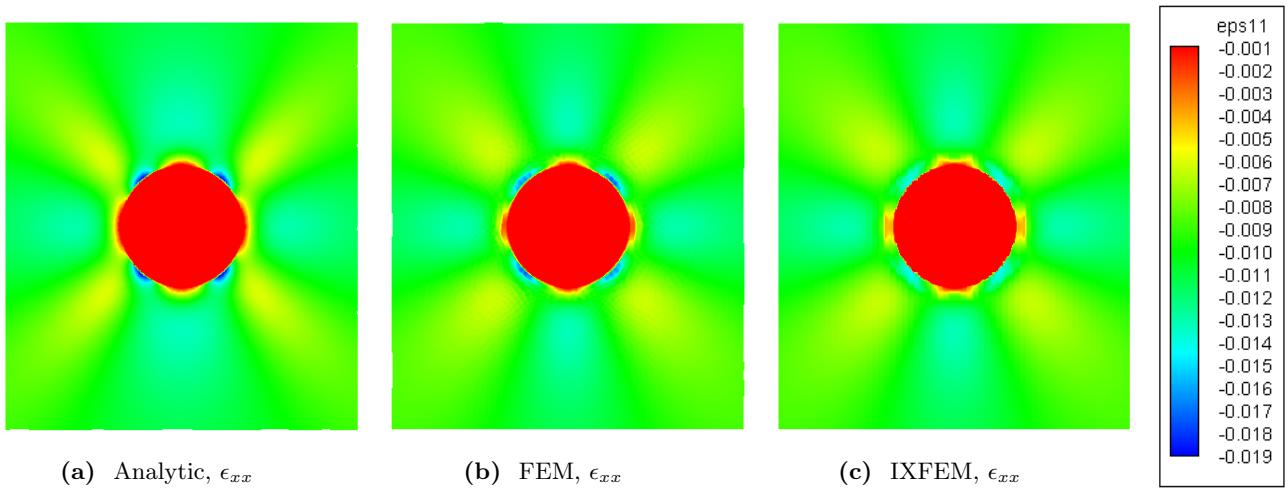

(a) Analytic, ϵ_{xx} **(b)** FEM, ϵ_{xx} **(c)** IXFEM, ϵ_{xx}

Figure 4.15: Comparison of ϵ_{xx} strain field from analytic, FEM, and IXFEM solution for plate with a inhomogeneity problem.

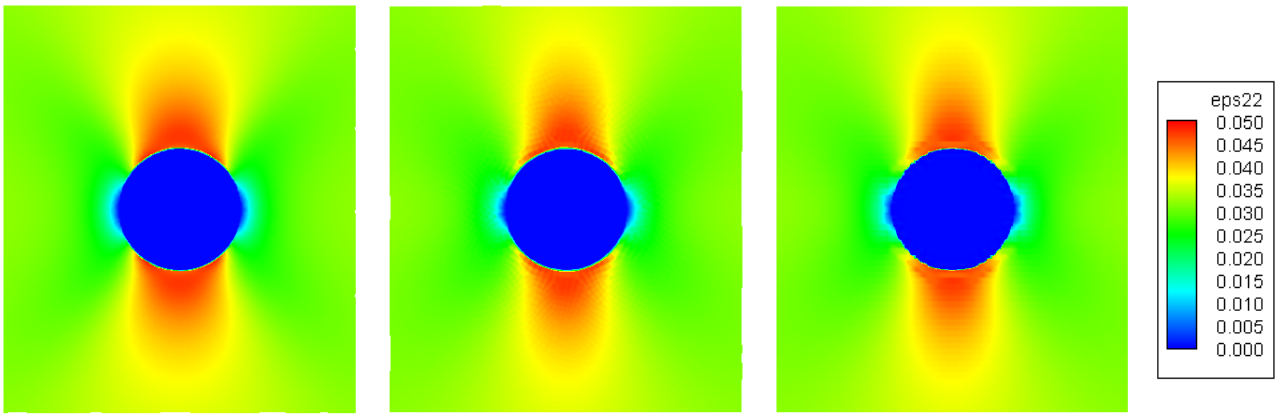

(a) Analytic, ϵ_{yy} **(b)** FEM, ϵ_{yy} **(c)** IXFEM, ϵ_{yy}

Figure 4.16: Comparison of ϵ_{yy} strain field from analytic, FEM, and IXFEM solution for plate with a inhomogeneity problem.

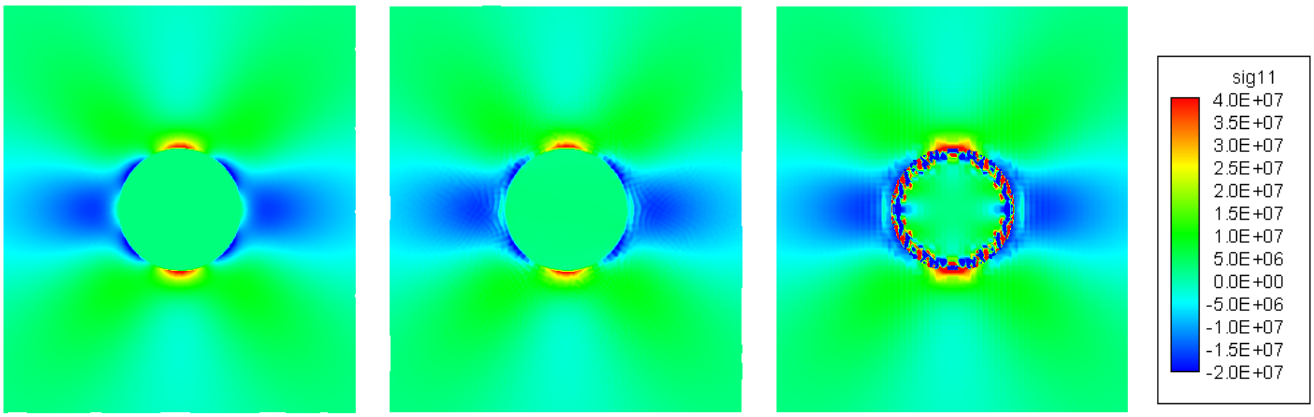

(a) Analytic, σ_{xx} (Pa) **(b)** FEM, σ_{xx} (Pa) **(c)** IXFEM, σ_{xx} (Pa)

Figure 4.17: Comparison of σ_{xx} stress field from analytic, FEM, and IXFEM solution for plate with a inhomogeneity problem.

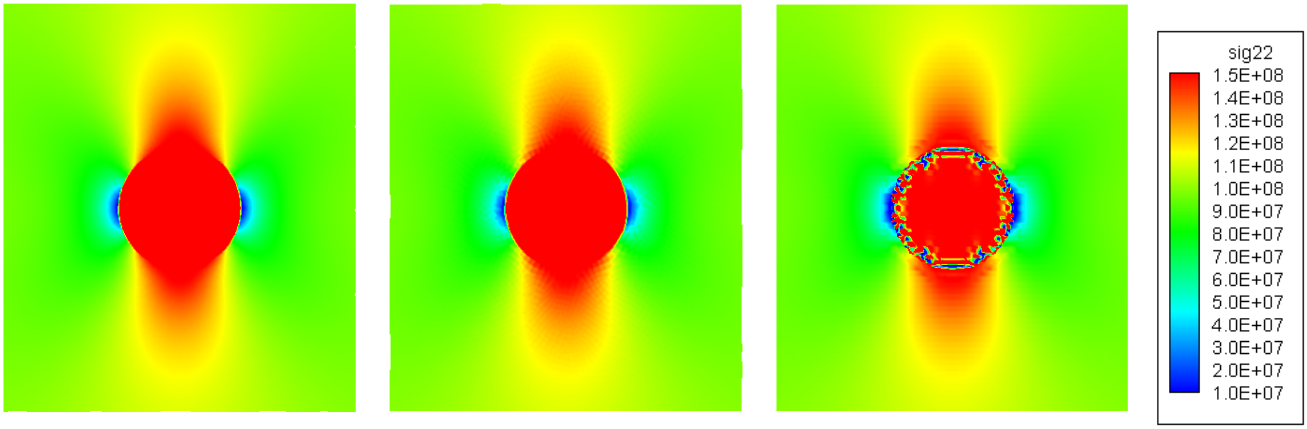

(a) Analytic, σ_{yy} (Pa) **(b)** FEM, σ_{yy} (Pa) **(c)** IXFEM, σ_{yy} (Pa)

Figure 4.18: Comparison of σ_{yy} stress field from analytic, FEM, and IXFEM solution for plate with a inhomogeneity problem.

inspection alone. Examination of the analytic strain fields, Figures 4.15a and 4.16a, demonstrate continuity of strain component ϵ_{xx} in material directions x_1 and x_2 and continuity of strain component ϵ_{yy} in material direction x_1 across the weak discontinuity interface Γ_2 (where x_1 coincides with the horizontal x direction, and x_2 coincides with the vertical y direction). Remaining material cross directions x_{12} plus x_2 and x_{12} display discontinuous behavior across the bimaterial interface for strain fields ϵ_{xx} and ϵ_{yy} respectively. This same behavior is observed for the FEM and IXFEM approximations as desired, but show minor, though noticeable, losses in fidelity and smoothness at the horizontal and vertical opposing quadrant points outside the circular filler material. Further nuances in variation can be observed in the strain banding, where the numerical results show diminished thickness and extension along the vertical centerline band for both ϵ_{xx} and ϵ_{yy}, and increased thickness for the oblique bands in strain field ϵ_{xx}. Additionally the IXFEM shows particular loss of accuracy at the concentrated cross-diagonal quadrant points of the filler in strain field ϵ_{xx}. Overall the bulk strain field response is well predicted by both FE methods, and demonstrates for the enriched basis $\boldsymbol{p}_{\mathrm{w}}^{\mathrm{enr}}(\boldsymbol{x})$, applied in the IXFEM, that even though discontinuities of primary variables derivatives can be sufficiently captured, the inherent operation of $\boldsymbol{p}_{\mathrm{w}}^{\mathrm{enr}}(\boldsymbol{x})$ only models such response where is physical.

In observation of the compared σ_{xx} and σ_{yy} stress field solutions, Figures 4.17 and 4.18 respectively, a systematic error residing in the current implementation of the IXFEM is immediately visible, existing at the bimaterial interface. Close inspection reveals that the discrepancy is exclusively contained internal to discontinuity boundary Γ_2, and is mainly concentrated in the innermost layer of enriched element subelements and transition elements. A survey of recent literature found similar issues in the context of *instabilities of interface tractions* in works utilizing the XFEM [7, 51, 85] and overlapping finite element, or embedded mesh, methods [2, 86]. Typical strategies pursued to stabilize the constraints on these embedded surfaces include penalty methods, Lagrange multipliers [7, 51], and more recently Nitsche's method [2, 85, 86]. Of interest to the work presented here is the issue encountered for material interfaces with high ratios of elastic properties, as these were show in [2, 58, 86] to exhibit mesh (or stress) locking, producing similar inconsistencies in stress results as shown for the composite plate. Figure 4.19 shows an example problem of Ref. [86] demonstrating the mesh locking effect on the computed stress field. The problem geometry and material characterization is depicted in Figure 4.19a. Without any special treatment inconsistencies are shown to occur internal to interfaces of higher elastic properties than the surrounding medium, as shown in Figure 4.19b. Given this resemblance in results to Figures 4.17c and 4.18c it is proposed that same phenomenon occurs in the vicinity

of enriched elements and is responsible for the error observed with the IXFEM. In the work of Sanders et al. a weighted Nitsche's method was employed to resolve this issue, the result is shown in Figure 4.19c.

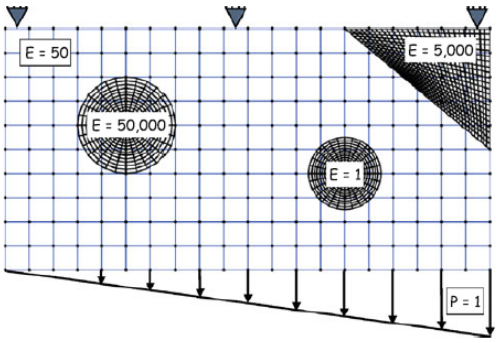

(a) Multiple inhomogeneity mesh embedded problem

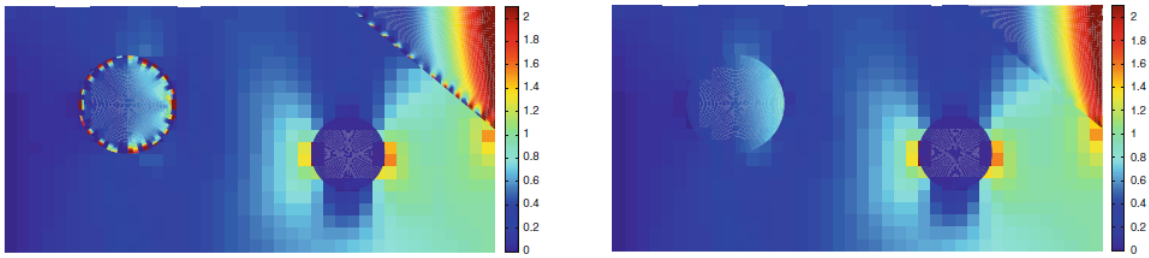

(b) Standard mortar solution

(c) Weighted Nitsche solution

Figure 4.19: Stress contour σ_{yy} for multimaterial plate with three regions of local inhomogeneities demonstrating inconsistencies in stress results at bimaterial interfaces due to mesh locking and resolution of the error with a weighted Nitsche's method (from Ref. [86]: Reprinted with permission from Springer).

Besides the interior boundary of the weak discontinuity, where the systematic inconsistencies in the stress field results, as determined from the IXFEM are localized, the remaining stress field response appears to be negligibly influenced by the mesh locking issue plaguing the material interface. Excluding this region both FE methods perform well in predicting the overall bulk stress response when comparing to the analytic solution. Continuity of stress components σ_{xx} and σ_{yy}, across the material interface Γ_2, are shown to exist in material directions x_1 and x_2 respectively, from Figures 4.17a and 4.18a. The remaining material cross directions displaying discontinuous behavior across the weak discontinuity for both stress fields. Ignoring the established discrepancy in the IXFEM results, the same behavior is observed from both FE approximations, with the FEM solution showing marginal loss of smoothness while the IXFEM displays slightly greater variation in smoothness and magnitude of response. Additionally with the IXFEM the opposing vertical and opposing horizontal quadrant points of the circular filler show larger regions of stress concentration in the

σ_{xx} and σ_{xx} fields respectively. Comparison of stress field σ_{yy} in Figure 4.18 to strain field ϵ_{yy} in Figure 4.16 clearly displays the independence of the stress components continuity to that of the strains. Whereas stress σ_{yy} is continuous in material direction x_2 and discontinuous in x_1 when crossing the material interface strain ϵ_{yy} shows the opposite response.

As done for the strong discontinuity validation problem, an error norm convergence analysis was completed for the weak validation problem. Results were again obtained for both the FEM and IXFEM based on a series of four meshes. Details of the mesh configurations can be found in Appendix C, where it is indicated that the same meshes as used with the plate with a hole problem are use with the plate with a inhomogeneity problem in the IXFEM analysis. The convergence rate results are shown in Figure 4.20, as curves of percent error in the error norms versus the baseline element size h.

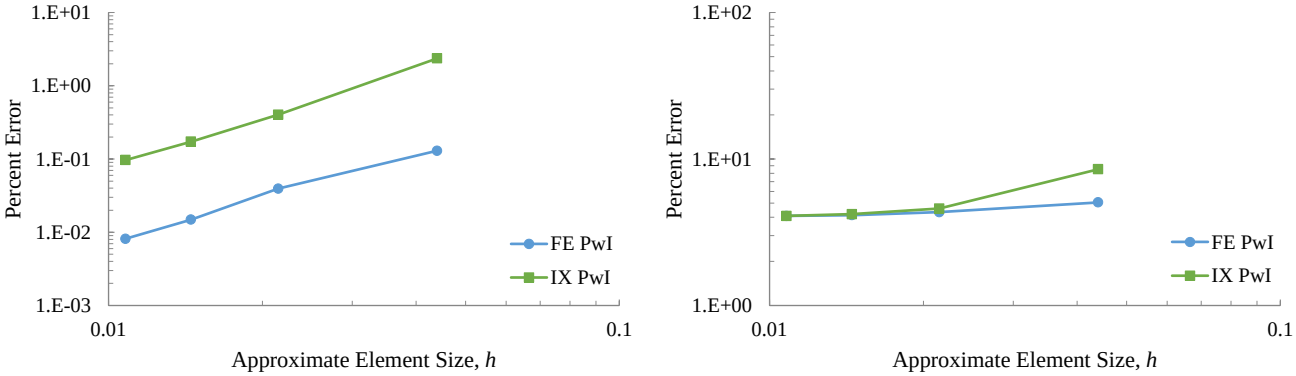

(a) L_2 norm **(b)** Energy norm

Figure 4.20: Error norm convergence results for weak discontinuity validation problem (Plate with a inhomogeneity, PwI). As listed in the plot legend abbreviations are defined as follows: FE - FEM, IX - IXFEM.

From inspection of the L_2 norm in Figure 4.20a there is near equivalent rate of convergence for the IXFEM approximation compared to the FEM, particularly for the three finer meshes. In the energy norm plots of Figure 4.20b there is little change seen in either FE method with a decrease in mesh element size, with the exception of the transition from the most coarse mesh for the IXFEM to the second mesh case. Review of the field variable plots for these two meshes revealed a far higher concentration in the strain field inconsistencies for the coarsest mesh, attributed to the low number of elements existing around the discontinuity to be used as enriched or transition elements. The mesh locking phenomenon is consequently considered to be more influential in introducing greater error into the approximation at low counts of enriched elements for a

discontinuity interface.

4.3 Computational Characterization of a Well-Dispersed Aligned Composite

Having demonstrated the ability of the IXFEM to accurately model the presence of a weak discontinuity, in the previous section, the remainder of the chapter is focused on modeling CNT-polymer nanocomposite RVEs, including multiple weak discontinuities. In this section the IXFEM will be applied for the computational characterization of a nanocomposite system, through evaluation of its effective elastic material properties, corresponding to a nano-filler configuration of well-dispersed aligned CNTs embedded in an epoxy matrix. Comparison of the results obtained using the IXFEM against those from a standard FEM and an analytic CCM model gives confidence that the IXFEM can be used for expanded RVE cases in which the well-dispersed assumption is removed. To model the well-dispersed CNT configuration the nanoscale geometry is modeled as a periodic hexagonal array of fibers, as displayed in Figure 4.21, confirmed to produce transversely isotropic effective properties [1, 34].

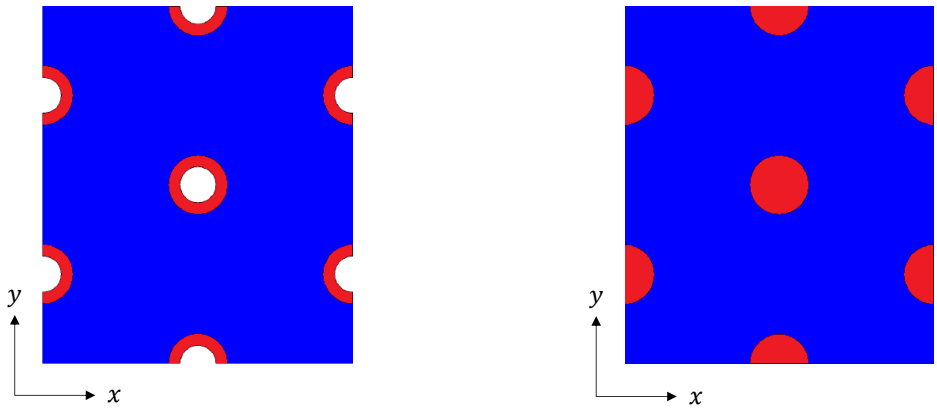

(a) Hallow CNT fiber **(b)** Effective solid CNT fiber

Figure 4.21: Comparison of hallow and solid fiber representation of CNTs in a nanoscale RVE characterizing a well dispersed aligned CNT-polymer nanocomposite. Show for a 10% volume fraction of CNT.

Based on Figure 4.21 there are two continuum approaches for modeling CNTs in a FEM. The first, shown in Figure 4.21a, uses isotropic hallow fibers, consistent with the observation of CNTs as rolled sheets of graphite (i.e. graphene) [84]. In the second, shown in Figure 4.21b, CNTs are represented as transversely isotropic solid fibers, where their effective properties are identified using a CCM, as done in Ref. [88]. In the present work the effective solid fibers are used, to defer the intricacies of working with embedded LSFs,

wherein a strong discontinuity interface would be defined within a weak discontinuity interface. Given the literature demonstrating near equivalent results when comparing modeling approaches [47, 95], studies using an effective high-stiffness solid representation are considered satisfactory for a preliminary proof on concept. The matrix material is that of a homogeneous compliant epoxy polymer (EPON 828) [87]. As the analysis performed in this work examines the nanocomposite response in the two-dimensional plane of isotropy, for consideration in a plane elasticity model both materials can be consider isotropic. Furthermore in this analysis all materials are defined as linear elastic isotropic in the plane. Relevant material properties and dimensions for both CNT representations plus the epoxy polymer matrix are listed in Table 4.1, where material directions (x_1, x_2, x_3) are taken to coincide with the problem global coordinate axes (x, y, z), where z and x_3 are the out of plane directions.

Table 4.1: Table of elastic material properties for epoxy matrix, isotropic hollow CNTs, and transversely isotropic effective CNT nanofiber.

EPON 828 [87]		Isotropic Hollow CNT [84]	
E	3.07 GPa	E	1100 GPa
ν	0.30	ν	0.14
		Inner Radius	0.51 nm
		Outer Radius	0.85 nm
Transversely Isotropic Effective CNT [47]			
$\tilde{E}_{33}$	704 GPa	$\tilde{G}_{31}$	227.04 GPa
$\tilde{E}_{11}$	345.54 GPa	$\tilde{G}_{12}$	125.52 GPa
$\tilde{\nu}_{31}$	0.14	Outer Radius	0.85 nm

For computational analysis of the CNT-polymer nanocomposite, RVEs were created for several different volume fractions of CNTs, ranging from $V_f^{\text{CNT}} = 0.1$ to 0.8 in increments of 0.1. Dimensions of the individual RVE can be determined based on the Eqns. 4.3.1 - 4.3.3, where r is the outer radius of the fiber and l is the distance between the center of one CNT and the center of one of the nearest neighboring CNTs, as illustrated in Figure 4.22. As demonstrated in Figure 4.22 the fiber radius is taken as fixed such that when changing the CNT volume fraction it is only the inter-fiber distance l that correspondingly changes, impacting the overall width W and height H of the RVE.

$$V_f^{\text{CNT}} = \frac{\pi r^2}{l^2 \cos(\theta)}, \quad \theta = 30^\circ \tag{4.3.1}$$

$$H = l + 2l\sin(\theta) = 2l \tag{4.3.2}$$

$$W = 2l\cos(\theta) \tag{4.3.3}$$

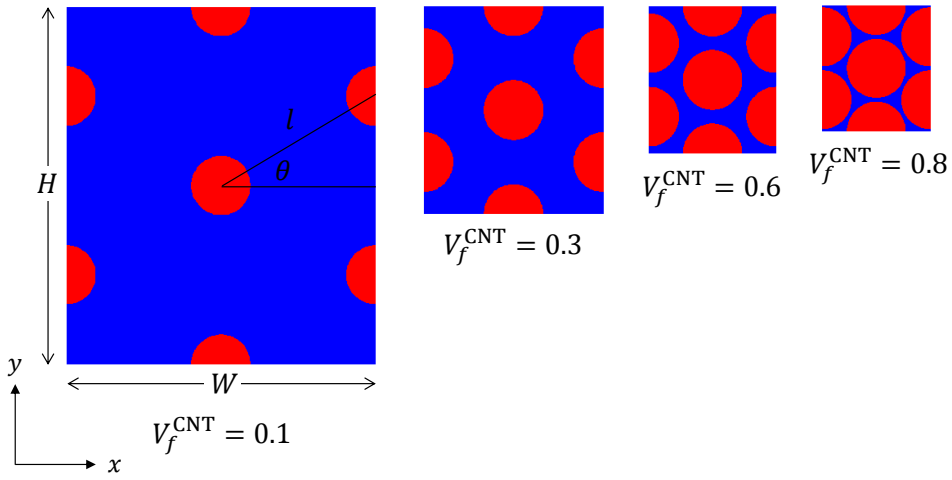

Figure 4.22: Representative volume elements for well-dispersed hexagonally packed CNT-polymer nanocomposite at several volume fractions.

As done in the previous two sections discontinuity interface conforming meshes, in this case explicitly defining the fiber boundaries, are generated for use with the FEM while structured meshes of rectangular elements are generated for use with the IXFEM, where the fiber boundaries are defined through the LSM. Individual circular LSFs $\psi_i^c(\boldsymbol{x})$ are prescribed for each CNT fiber based on a center location $\boldsymbol{x}_i^c$ and radial distance r_i^c, the unified LSF $\psi^c(\boldsymbol{x})$ for the problem domain is then determine using Eqn. 3.1.16. Corresponding global resultant LSF contours for the four RVEs shown in Figure 4.22 are displayed in Figure 4.23. A consistent contour legend is used at each volume fraction to further illustrate that the CNTs are of fixed radius and only their inter-spacing l changes with volume fraction.

For each volume fraction equivalent baseline element sizes were used in generating the mesh such that for all RVEs the CNTs would be defined by a near identical number of elements. For the highest volume fraction case, $V_f^{\text{CNT}} = 0.8$, an unexpected issue was encountered in the IXFEM as distinct enriched regions came into contact, this error will be further discussed when presenting the effective material property results. Details for the eight meshes used with the FEM and IXFEM are provided in Appendix C. For the two-dimensional FEA of the CNT-polymer nanocomposite, plane strain assumptions are applied consistent with the large aspect ratio of CNTs [84].

To evaluate the effective in plane elastic material properties of the nanocomposite system a series of average strain states, where only one strain component is non-zero, are applied to the RVEs under periodic boundary conditions. The material system response, in terms of the displacement, strain, and stress fields, is then

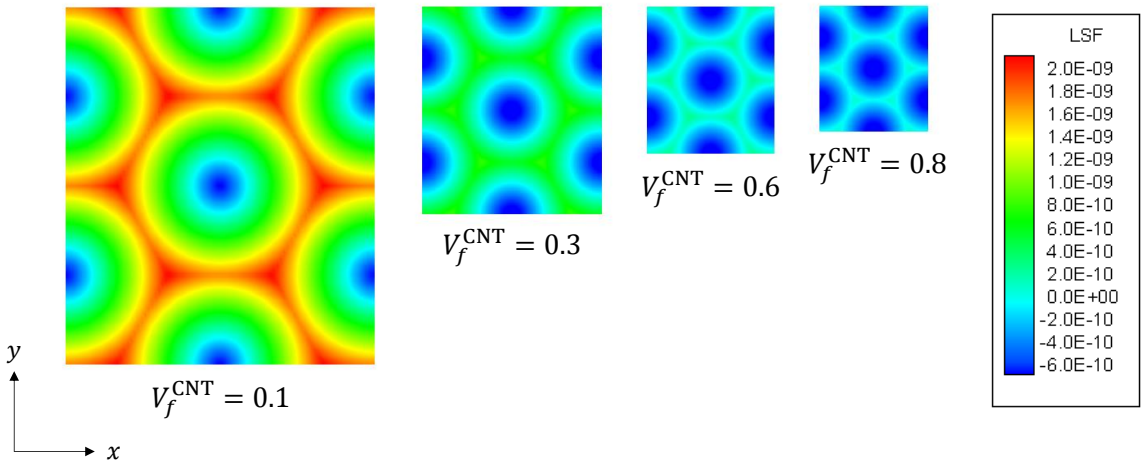

Figure 4.23: Representative volume elements for well-dispersed hexagonally packed CNT-polymer nanocomposite, displaying level-set function contours defining CNT locations for use with the IXFEM, at several volume fractions.

numerically solved using the developed FEM and IXFEM codes. Volume averaged strains $\bar{\epsilon}_{ij}$ and stresses $\bar{\sigma}_{ij}$ are then calculated as a post-processing step and used to populate the effective global "homogeneous" material constitutive relation,

$$\begin{Bmatrix} \bar{\sigma}_{xx} \\ \bar{\sigma}_{yy} \\ \bar{\sigma}_{xy} \end{Bmatrix} = \begin{bmatrix} C_{11} & C_{12} & 0 \\ C_{21} & C_{22} & 0 \\ 0 & 0 & C_{66} \end{bmatrix} \begin{Bmatrix} \bar{\epsilon}_{xx} \\ \bar{\epsilon}_{yy} \\ 2\bar{\epsilon}_{xy} \end{Bmatrix} \tag{4.3.4}$$

where the material is assumed to be orthotropic linear elastic, for the purpose of capturing the well-dispersed and subsequent randomly dispersed cases. Given that only one component of the volume average strain is non-zero the corresponding column of the effective stiffness matrix is determined by dividing the volume average stress component by the applied volume average strain component [47]. Once the effective stiffness is fully computed it can be inverted to attain the effective compliance from which the effective elastic moduli and Poisson's ratios can be calculated based on the plane strain expressions provided in Ref. [82, chap. 11]. To determine the three distinct in-plane material properties (E_{22}, G_{12}, ν_{12}) three sets of periodic boundary conditions are applied to each RVE. Periodic boundary conditions in this case are representative of translational periodicity in the x and y directions, simulating an infinite medium under an applied far-field displacement control. A complete description for the implementation of periodic boundary conditions for a

more general three-dimensional RVE can be found in Ref. [47], the extension to the further simplified case of two-dimensions is straight forward.

Numerical results for the transverse elastic material properties of the FE representation of the well-disperse RVE cases are shown in Figure 4.24, as determined from the FEM and IXFEM approximations. For comparison, analytic results determined using a CCM model are also shown on the plots [47, 88]. From Figure 4.24a, displaying the effective transverse elastic modulus E_{22}^{eff}, good agreement between both FEMs and the CCM solution is visible for fiber volume fractions below 70%. Above 70% the FEM approximation begins to show slight deviation, while the IXFEM shows a significant increase in error. A percent difference in the effective transverse elastic modulus with respect to the CCM solution is found to be of the order of 7% and 60% for the FEM and IXFEM respectively at a CNT volume fraction of 80%. Deviations in the FEM solution are due to the use of the solid effective fiber representation in the FEA, as shown in Ref. [47] at higher volume fractions the effective fiber leads to greater inaccuracy in the predicted effective properties compared to a hallow fiber representation in the FEA. The source of error in the IXFEM is the contact of enriched element domains used in modeling two separate CNT boundaries. To be shown subsequently this leads to localized deterioration of the strain field approximation across these contacting regions and a significant distortion of the bulk stress field solution. The effective transverse shear modulus G_{12}^{eff}, shown in Figure 4.24b, displays similar behavior in its trends as the effective elastic modulus. At low volume fractions each FE method shows favorable comparison, while at higher volume fraction the same issues as discussed previously are at fault for the increasing divergence in the predicted effective shear modulus. In-plane effective Poisson's ratio ν_{12}^{eff}, shown in Figure 4.24c, also shows similar behavior in the predicted effective property. At volume fractions of CNTs below 60% agreement between the computational methods and analytic solution is good, however above 60% the computational determined effective Poisson's ratio deviates in trend from the analytic solution and increasing error in results are observed. This departure of the computational solution from the analytic is again attributed to the use of the effective fibers in the FEA. The results of Ref. [47] show the hallow representation as performing better in this aspect as well, and points to the inadequate modeling of the zero stiffness hallow region of the CNTs, which have greater influence on the effective transverse material properties at high fiber volume fractions.

Examining the global domain decomposition of the RVEs along with the associated stress and strain field contours the role of contacting enriched element domains Ω^{E}, due to coarse enough meshes at high fiber volume fractions, leading to the error in the effective material property calculations is readily identified.

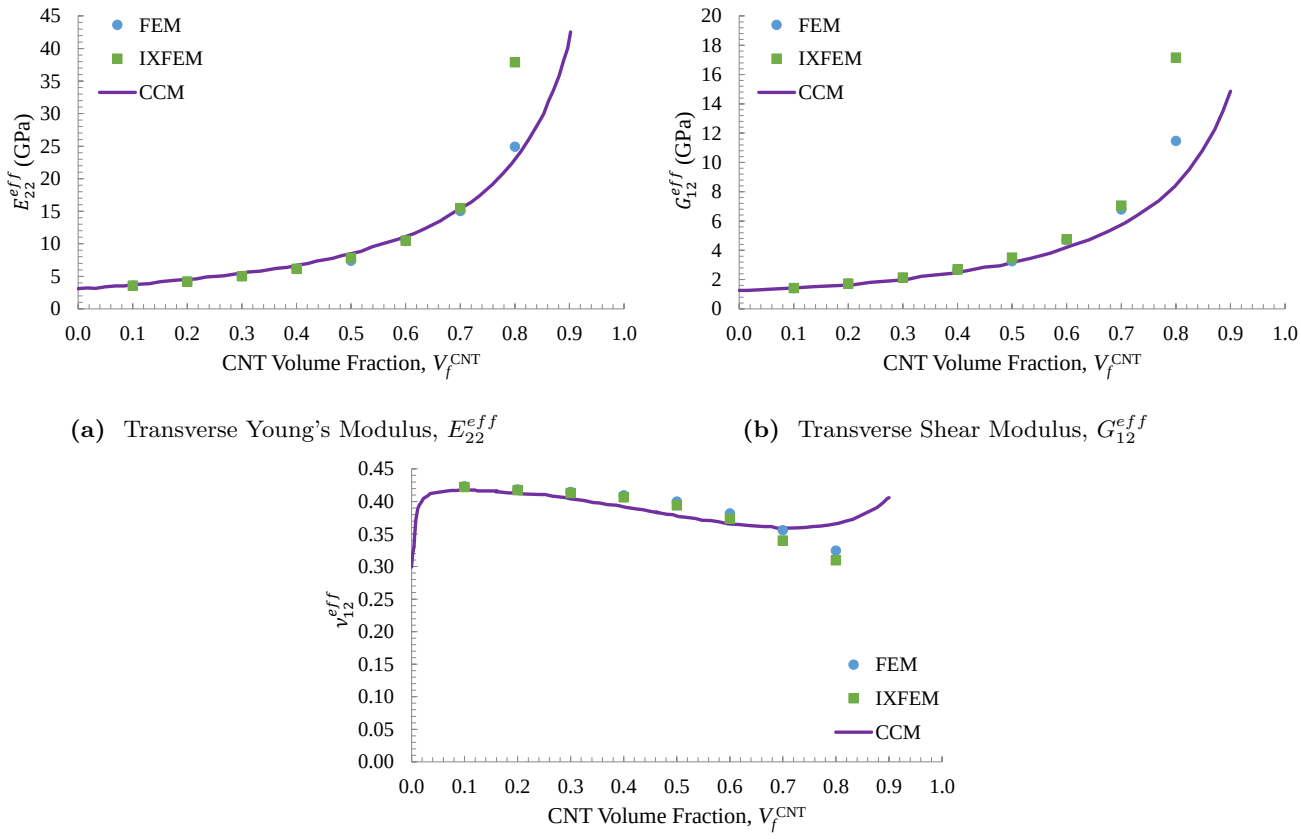

(a) Transverse Young's Modulus, E_{22}^{eff}

(b) Transverse Shear Modulus, G_{12}^{eff}

(c) Transverse Poission's Ratio, ν_{12}^{eff}

Figure 4.24: Comparison of effective material property results computed using the FEM and the IXFEM to an analytic CCM model [88, 47] for assumed well-dispersed CNT-polymer nanocomposite RVEs.

Figure 4.25 displays the domain decomposition of several RVEs, used with the IXFEM, at various volume fractions. Given the baseline element size selected when generating the meshes, RVEs with fiber volume fractions below 60% have "complete transitions" between distinct enriched subdomains. A complete transition is taken here to mean any path connecting two enriched regions (Ω_m^{E}, Ω_n^{E}) will pass through their corresponding distinct surrounding transition subdomains (Ω_m^{T}, Ω_n^{T}) and a non-enriched subdomain Ω_p^{S} between them. This level of separation is clearly evident in Figure 4.25a for at a volume fraction of 30%, and extends to lower volume fractions as the separation distance between fibers increases, as shown previously in Figure 4.22. With increasing volume fraction this definition of separation continues to exist for the RVE until the fiber volume fraction reaches nearly 60%, when distinct transition subdomains between neighboring enriched subdomains begin to make contact. Barely discernible in Figure 4.25b where contact occurs over a

single node between each CNT pair, full contact among neighboring transition subdomain elements is visible in Figure 4.25c at a volume fraction of 70%. Given the comparable minor deviation seen in the calculated effective properties when using the IXFEM or FEM with $V_f^{\text{CNT}} = 0.7$, the contact of distinct transition subdomains is not considered to be a major contributor of error in the IXFEM. With continuing increase in the fiber volume fraction the contacting transition regions transform into contacting regions of enriched elements, as shown in Figure 4.25d. As will be shown next these locations are major sources of error in the computational approximation of the IXFEM.

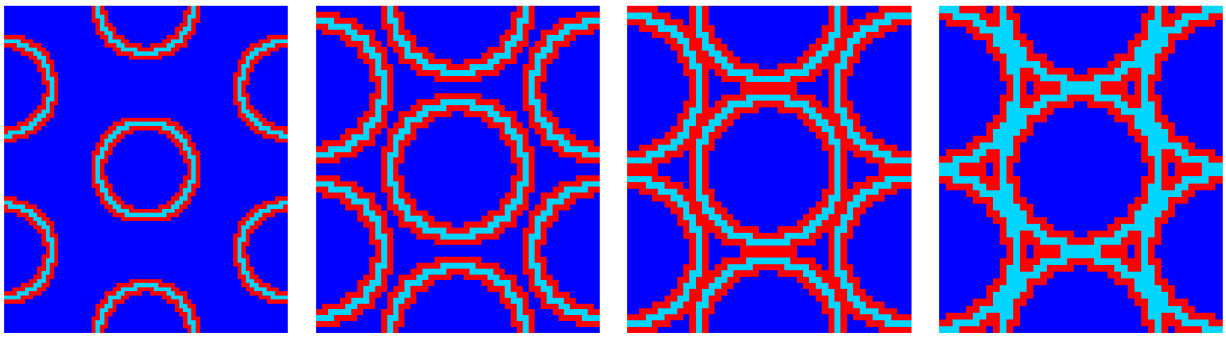

(a) $V_f^{\text{CNT}} = 0.3$ **(b)** $V_f^{\text{CNT}} = 0.6$ **(c)** $V_f^{\text{CNT}} = 0.7$ **(d)** $V_f^{\text{CNT}} = 0.8$

Figure 4.25: Global domain decomposition of hexagonally packed CNT RVEs, showing percolation of enriched element domains at V_f^{CNT}. Blue regions indicate non-enriched subdomains Ω^{S}, light blue enriched subdomains Ω^{E}, and red transition subdomains Ω^{T}.

Stress field contour plots for the well dispersed CNT-polymer nanocomposite RVE at volume fractions of 30% and 80% ($V_f^{\text{CNT}} = 0.3$, $V_f^{\text{CNT}} = 0.8$) are shown in Figures 4.26 and 4.27 respectively, with corresponding strain field shown for the $V_f^{\text{CNT}} = 0.8$ case in Figure 4.28. In all cases the material response is due to an applied 1% average normal strain $\bar{\epsilon}_{yy}$ with periodic boundary conditions imposed on all external boundaries. Comparison of stress field σ_{yy} in Figures 4.26a and 4.26b demonstrates good overall agreement between the IXFEM and FEM approximation in the bulk material response. The same discrepancies as discussed in Section 4.2 are visible internal to the weak discontinuity interfaces, but given the results displayed in Figure 4.24 appear to have negligible impact on the effective material property calculations. Strain field contour plots, not provided here, from both FEMs also show good agreement. Similar equivalence in the stress and strain field behavior is observed for all remaining volume fractions of RVEs except in the case when $V_f^{\text{CNT}} = 0.8$. Comparing the domain decomposition for this RVE, shown in Figure 4.25d, to the ϵ_{yy} strain field computed by the IXFEM, Figure 4.28b, to that for the FEM, Figure 4.28a, the IXFEM strain field shows local deterioration in the approximation in areas where enriched elements of separate subdomains are

in direct contact, i.e. in the matrix material domain along centerlines connecting neighboring fiber centers. The remaining portion of the strain field displays favorable agreement between the IXFEM and the FEM, particularly in the high-stiffness fiber domains. This is in contrast to the stress field approximations which shows wide-spread distortion throughout the fiber domains and in the contacting enriched element regions, though regions of the compliant matrix were cross-contamination of enriched elements does not occur still show adequate capture of the material response. This further indicates the contact of enriched elements as the central source of error in the enriched approximation of the IXFEM. Equivalent response in the shear stress and strain, σ_{xy} and ϵ_{xy} respectively, for the RVEs under an applied 1% average shear strain $\bar{\epsilon}_{xy}$ can be seen in Figures 4.29 through 4.31. Again, as demonstrated for the case with $V_f^{\text{CNT}} = 0.3$, volume fractions without contacting enriched elements display good agreement when comparing solutions of the IXFEM and FEM, but once enriched elements of different subdomains begin to share element boundaries the accuracy of the IXFEM declines rapidly.

To further compare consistency between the IXFEM approximation to that of the FEM, a percent differences of the L_2 and energy norm measures for each volume fraction RVE were calculated. As the solutions were determined on different meshes a pointwise error norm measures cannot be evaluated, as was done for the two validation problems where an analytic solution existed, instead a percent difference in the global norm measures is preformed based on Eqns. 4.3.5 and 4.3.6.

$$L_2^{\text{diff}} = \frac{\|\boldsymbol{u}_{\text{FE}}^h\|_{L_2} - \|\boldsymbol{u}_{\text{IXFE}}^h\|_{L_2}}{\|\boldsymbol{u}_{\text{FE}}^h\|_{L_2}} \tag{4.3.5}$$

$$E^{\text{diff}} = \frac{\|\boldsymbol{\epsilon}_{\text{FE}}^h\|_E - \|\boldsymbol{\epsilon}_{\text{IXFE}}^h\|_E}{\|\boldsymbol{\epsilon}_{\text{FE}}^h\|_E} \tag{4.3.6}$$

Results for the L_2 and energy norm percent differences are shown in Figures 4.32a and 4.32b respectively, as data points of percent difference on a log scale versus the RVE fiber volume fraction. The legend entries, labeled as effective material properties, indicate the norm percent differences were calculated based on the displacement and strain solution fields for each average strain state applied in order to determine the corresponding effective material property. Initial inspection of Figure 4.32a reveals good agreement between the IXFEM and FEM approximation as percent differences in the L_2 norm measure remain well below 0.1% for nearly all effective property calculations when the fiber volume fraction is below 80%. It is noted that at $V_f^{\text{CNT}} = 0.5$ their is a spike in the percent difference value, but it remains below 1%. No easily

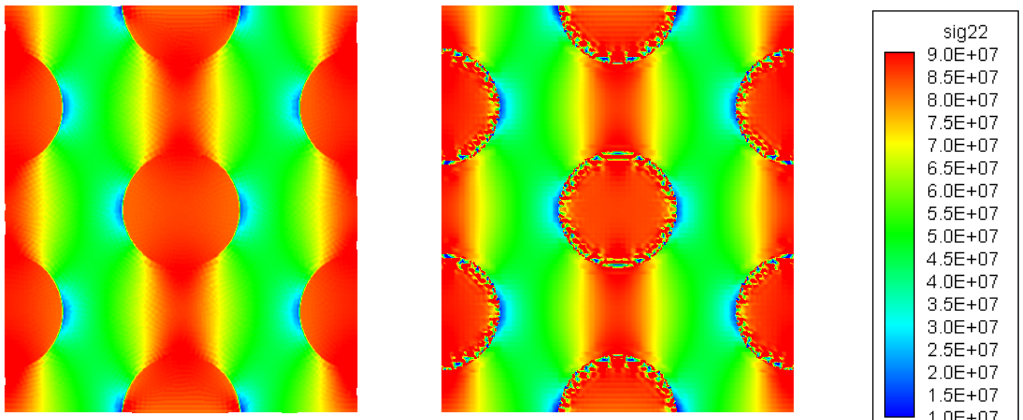

(a) FEM, σ_{yy} (Pa) **(b)** IXFEM, σ_{yy} (Pa)

Figure 4.26: Comparison of σ_{yy} stress field from FEM and IXFEM solution for RVE with $V_f^{\text{CNT}} = 0.3$ due to applied 1% average strain $\bar{\epsilon}_{yy}$.

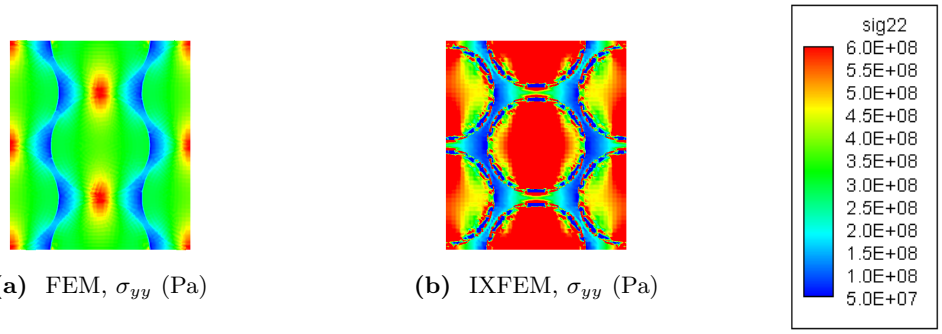

(a) FEM, σ_{yy} (Pa) **(b)** IXFEM, σ_{yy} (Pa)

Figure 4.27: Comparison of σ_{yy} stress field from FEM and IXFEM solution for RVE with $V_f^{\text{CNT}} = 0.8$ due to applied 1% average strain $\bar{\epsilon}_{yy}$.

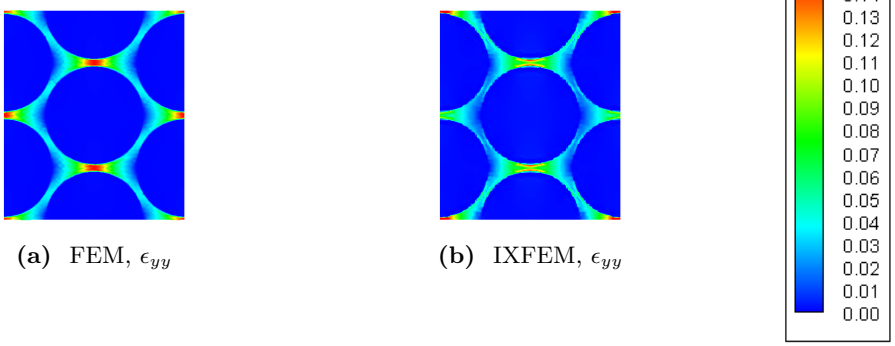

(a) FEM, ϵ_{yy} **(b)** IXFEM, ϵ_{yy}

Figure 4.28: Comparison of ϵ_{yy} strain field from FEM and IXFEM solution for RVE with $V_f^{\text{CNT}} = 0.3$ due to applied 1% average strain $\bar{\epsilon}_{yy}$.

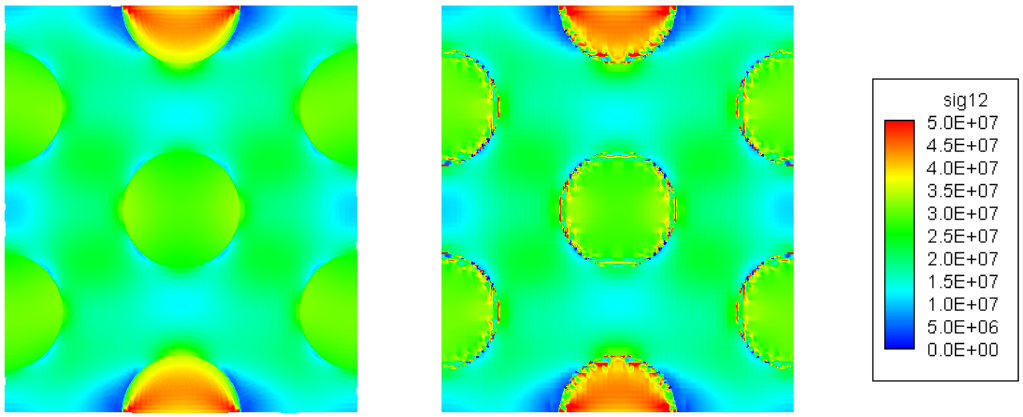

(a) FEM, σ_{xy} (Pa) **(b)** IXFEM, σ_{xy} (Pa)

Figure 4.29: Comparison of σ_{xy} stress field from FEM and IXFEM solution for RVE with $V_f^{\text{CNT}} = 0.3$ due to applied 1% average shear strain $\bar{\epsilon}_{xy}$.

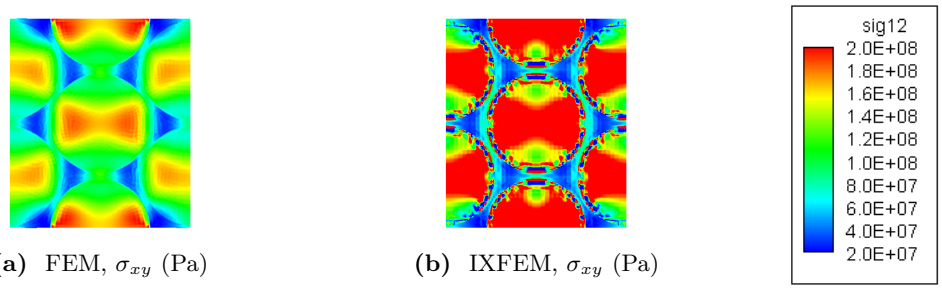

(a) FEM, σ_{xy} (Pa) **(b)** IXFEM, σ_{xy} (Pa)

Figure 4.30: Comparison of σ_{xy} stress field from FEM and IXFEM solution for RVE with $V_f^{\text{CNT}} = 0.8$ due to applied 1% average shear strain $\bar{\epsilon}_{xy}$.

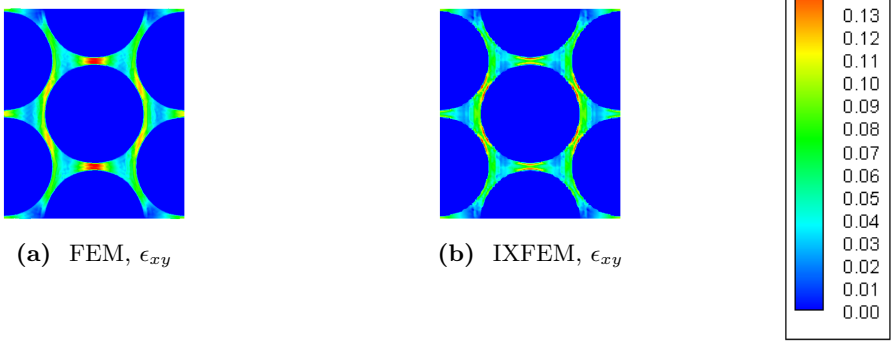

(a) FEM, ϵ_{xy} **(b)** IXFEM, ϵ_{xy}

Figure 4.31: Comparison of ϵ_{xy} strain field from FEM and IXFEM solution for RVE with $V_f^{\text{CNT}} = 0.3$ due to applied 1% average shear strain $\bar{\epsilon}_{xy}$.

identifiable source of error could be found leading to this anomaly in otherwise relatively consistent results; it is suspected the root cause lies in the input data more so than an error arsing out of the evaluation. A large increase in the percent difference (~10%) is seen when $V_f^{\text{CNT}} = 0.8$, this coincides with the increase in error seen in the effective material property calculations, and is due to the same reasons as discussed when presenting the stress and strain field contours, i.e. the contact of enriched elements for separate subdomains. Percent difference in the energy norm measure, visible in Figure 4.32b, displays a linear relationship on the semilog plot, indicative of an exponential relation for the strain field accuracy with the inter-fiber spacing distance l. At low volume fractions there is good agreement between the IXFEM and FEM approximation as before, with percent difference values remaining below 0.1% for all effective property calculations when the fiber volume fraction is less than 50%. The spike at $V_f^{\text{CNT}} = 0.5$ is visible again, in this case an outcome of the deviation in the displacement field impacting the gradient (strain) field. Up to volume fractions of 70% the percent difference in the energy norm doesn't surpass more than a few percent, and approaches higher single digit differences at $V_f^{\text{CNT}} = 0.8$. Reviewing the strain fields for the 80% volume fraction RVE in Figures 4.28 and 4.31, this difference is caused by the localized degradation of approximation in those regions where distinct enriched subdomains begin to share element boundaries as the remainder to problem domain demonstrates qualitatively good comparison. As shown by the corresponding stress fields in Figures 4.27 and 4.30 the error in the approximation most significant emerges in the stress field[8].

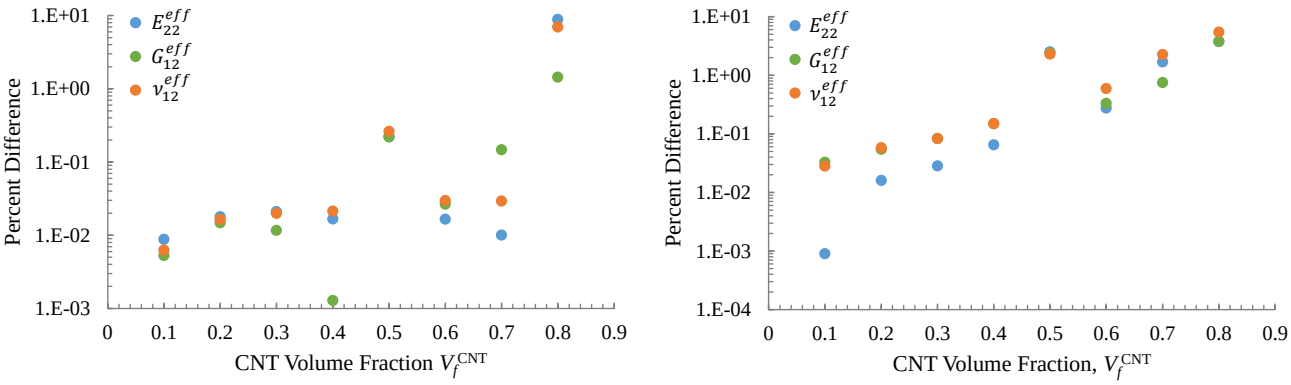

(a) L_2 norm **(b)** Energy norm

Figure 4.32: Error norm difference between FEM and IXFEM results for well-dispersed CNT-polymer nanocomposite RVE results. Differences are given based on displacement and strain fields for three periodic boundary condition cases to determined effective transverse materiel properties.

[8]Given the high elastic material properties of the effective CNT it is likely that the minimal error observed in the strain fields is exasperated through the constitutive relation in calculating the stress fields, leading to the large inaccuracies demonstrated.

Two solutions to work out the error observed and shown to occur when enriched elements of distinct subdomains come into contact are immediately recognized to exist. The first is the simplest, to refine the mesh to such degree that separate enriched subdomains no longer share any element boundaries with each another, as determined during the domain decomposition. In consequence to this fix the computational cost will be directly increased, as a mesh with an enlarged number of degrees of freedom must be solved for the same problem. This is particularly true for the approach taken in this work where structured meshes are used, as mesh refinement would have to be uniform across the entire problem domain. Thus, regions containing largely non-enriched elements (e.g. those far enough inside or outside the fiber boundaries for the hexagonally packed RVE problem) would be refined beyond what is necessary to obtain an good approximation. If instead a unstructured mesh was used, selective regions with close proximity to discontinuity interfaces could be locally refined. However this would bring explicit problem geometry considerations back into the mesh generation process, reintroducing a pre-processing form of mesh dependency into the evaluation, which the XFEM is intended to remove. The second approach would be mathematical in design, to propose an augmented enriched basis or an appropriate blending technique to use in cross-contacting elements of enriched subdomains.

4.4 Computational Characterization of a Randomly Aligned Composite

In the present section a similar study as completed in the previous, in terms of calculating effective material properties of a CNT-polymer nanocomposite, is performed for enlarged RVE cases in which the well-dispersed assumption of fibers is removed. Given the ability of the IXFEM to work very simply with various internal discontinuity configurations, based on their definition through the LSM, a series of ten CNT fiber distributions are considered at two volume fractions ($V_f^{\mathrm{CNT}} = 0.1$ and $V_f^{\mathrm{CNT}} = 0.3$), and two filler counts ($n^{\mathrm{CNT}} = 50$ and $n^{\mathrm{CNT}} = 100$). The intent of this study is to illustrate the benefit of working with a mesh independent FEM when investigating potential geometry dependence on material characterization. In this instance, consider the number of distributions (10) and RVE parameters, volume fraction (2) plus filler count (2), varied in this assessment. If the FEM is applied for executing the computational simulations the 40 fiber distributions are required to be represented by conforming meshes, each explicitly defining the CNT fibers for one distinct configuration. This would entail the geometric modeling and meshing of 3000 fiber locations in total for the 40 RVE cases in a preliminary process, prior to performing any numerical analysis. In contrast, if the IXFEM is applied for executing the computations only 4 standardized meshes are required to be created in

this same preliminary process, each being infinitely reusable for evaluation of a RVE fiber distribution of select volume fraction and filler count. The distinct filler configuration is instead provide as a separate input of listed fiber center locations and corresponding radius values, which are used to define the multiple LSFs representative of the fibers.

Filler distributions for the 40 RVEs of the study are determined based on a random generation with some favoring towards clustering of fibers, consistent with observation of CNTs to form bundles due to interatomic van der Waals forces [112, 113]. In all cases square RVEs, of dimension $W \times W$, are created based on Eqn. 4.4.1, with the CNT fibers contained whole within the domain of the RVE. Two demonstrative RVEs are shown in Figure 4.33, of $V_f^{\text{CNT}} = 0.1$ and $V_f^{\text{CNT}} = 0.3$ where $n^{\text{CNT}} = 50$ in both cases. Refer to Appendix C for examples of the larger RVEs with $n^{\text{CNT}} = 100$, and for illustrations of the global domain decomposition.

$$V_f^{\text{CNT}} = \frac{n^{\text{CNT}} \pi r^2}{W^2} \tag{4.4.1}$$

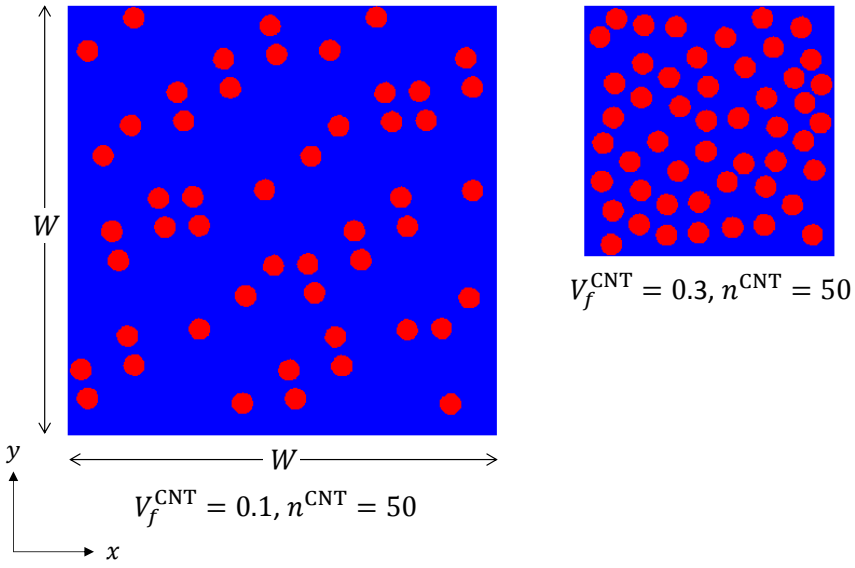

Figure 4.33: Representative volume element for randomly aligned CNT-polymer nanocomposite at two volume fractions of study.

Discernible in the 10% volume fraction RVE, of Figure 4.33, are localized concentrations of fibers, illustrative of the clustering or bundling of CNTs. In the 30% volume fraction RVE specific bundles are not as directly perceptible as the global fiber arrangements quickly becomes more uniform, in terms of fiber proximity,

with increasing volume fraction. As done for the well-dispersed RVE models, the CNT fiber locations are prescribed through the LSM. Thus, as described before, enabling a single structured mesh to be used for the analysis of each internal fiber arrangement variation of a RVE, belonging to a given volume fraction and filler count case. Corresponding global LSF contours for the two RVEs in Figure 4.33 are shown in Figure 4.34, using the same contour layers as in Figure 4.23 for the well-dispersed RVEs. This reiterates the uniformity in fiber size used in the CNT-polymer nanocomposite representation, and given the contour cutoff in effect for the RVE of $V_f^{\text{CNT}} = 0.1$ it further demonstrates the variance in the expanse of matrix material existing between fibers at low volume fractions while also emphasizing the ease in recognizing CNT bundles at these same low volume fractions.

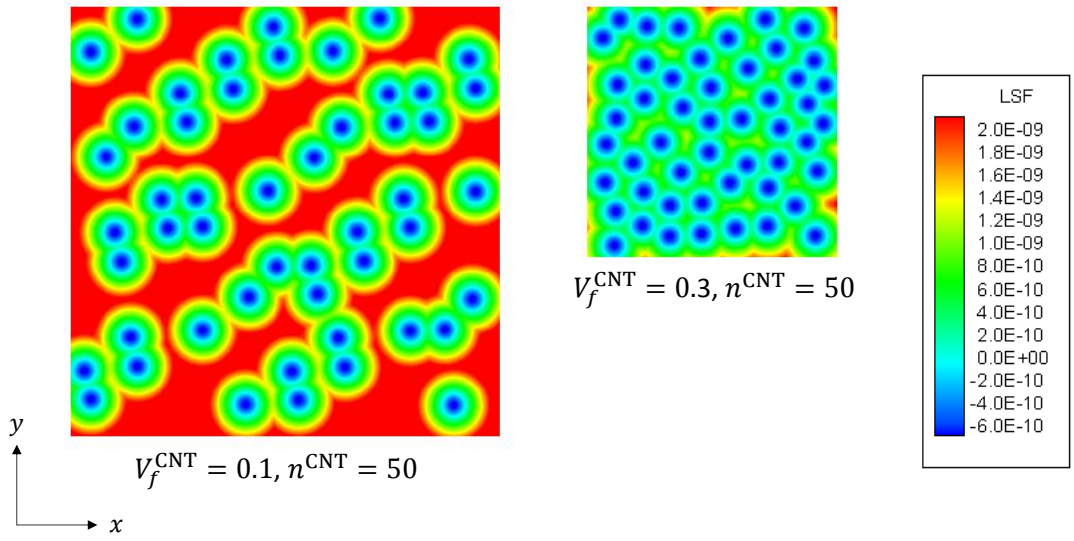

Figure 4.34: Representative volume fraction for randomly aligned CNT-polymer nanocomposite at two volume fractions of study, displaying level-set function contours defining CNT locations for use with the IXFEM.

To reduce the computational cost associated with evaluating these enlarged RVE cases, coarser meshes are utilized compared to those of the well-dispersed cases. Inspection of the global domain decompositions revealed these meshes to produce regions of contacting enriched elements where the fibers are in close proximity, i.e. mostly in the bundles. However, these regions are not as expansive as shown for the Hexagonal RVE of $V_f^{\text{CNT}} = 0.8$, refer to Figure 4.25d, largely due to the lower fiber volume fractions. A simple analysis varying the baseline mesh size found that with the permitted minimal inter-spacing of fibers (measured center to center, and set as 2.25 times the fiber radius) and the scale of the RVEs investigated a sufficiently refined mesh, to eliminate all cross-contamination of enriched subdomains, would have required number of

degrees of freedom on the order of 10^6, which was beyond the scope of analysis. Details on the four meshes used with the IXFEM are provided in a table of Appendix C.

Effective material properties are calculated in the same manner as before, using a series of average applied strain states with periodic boundary conditions applied on all boundaries. However, with deviation from the well-dispersed (transversely isotropic) hexagonal fiber configuration the in-plane isotropic assumption is no longer reasonable. Thus in these cases the complete set of in-plane effective material properties (E_{11}^{eff}, E_{22}^{eff}, ν_{12}^{eff}, ν_{21}^{eff}, G_{12}^{eff}) of the CNT-polymer nanocomposite RVE are determined, using two additional average strain states along with those implemented in Section 4.3. Numerical results of the effective transverse elastic material properties are provided in Tables 4.2a and 4.2b, for the randomly dispersed aligned fiber RVEs at volume fractions of 10% and 30% respectively. The tables list average values for the effective material properties (determined based on ten fiber distribution cases), standard deviation in their averages, and a percent difference taken with respect to the effective material property value determined for the corresponding well-dispersed fiber RVE, as determined for the randomly dispersed RVEs with CNT filler counts of $n^{\text{CNT}} = 50$ and $n^{\text{CNT}} = 100$.

Table 4.2: Table of effective transverse elastic material properties and standard deviation as determined for series of randomly aligned CNT-polymer nanocomposite RVEs.

(a) At fiber volume fraction, $V_f^{\text{CNT}} = 0.1$.

	RRVE: $n^{\text{CNT}} = 50$			RRVE: $n^{\text{CNT}} = 100$		
Property	Average Value (GPa)	Standard Deviation	Variation with Clustering (%)	Average Value (GPa)	Standard Deviation	Variation with Clustering (%)
E_{11}^{eff}	3.640	±0.015	1.681	3.788	±0.037	5.842
E_{22}^{eff}	3.648	±0.027	1.947	3.640	±0.004	1.744
ν_{12}^{eff}	0.416	±0.003	1.769	0.422	±0.002	0.293
ν_{21}^{eff}	0.417	±0.002	1.889	0.404	±0.003	4.926
G_{12}^{eff}	1.394	±0.006	1.721	1.401	±0.004	1.203

(b) At fiber volume fraction, $V_f^{\text{CNT}} = 0.3$.

	RRVE: $n^{\text{CNT}} = 50$			RRVE: $n^{\text{CNT}} = 100$		
Property	Average Value (GPa)	Standard Deviation	Variation with Clustering (%)	Average Value (GPa)	Standard Deviation	Variation with Clustering (%)
E_{11}^{eff}	5.680	±0.040	12.843	5.789	±0.068	15.018
E_{22}^{eff}	5.649	±0.066	12.036	5.987	±0.225	18.737
ν_{12}^{eff}	0.384	±0.005	7.434	0.370	±0.014	10.691
ν_{21}^{eff}	0.386	±0.005	8.068	0.380	±0.005	9.381
G_{12}^{eff}	2.196	±0.029	3.572	2.226	±0.029	4.989

Initial examination of the tabulated average effective material property results in Table 4.2 indicates the random fiber arrangements remain nearly isotropic in the transverse plane, with only marginal variation with distribution changes as indicated by the small standard deviations. This is largely a consequence of the applied periodic boundary conditions, which assume a repeating RVE configuration in the plane of analysis. Percent differences in the bi-direction paired elastic properties (i.e. E_{11}^{eff} and E_{22}^{eff} plus ν_{12}^{eff} and ν_{21}^{eff}) show variation no greater than 1% at both volume fractions with the lower count of fillers in the RVE, $n^{\text{CNT}} = 50$, at the higher filler count, $n^{\text{CNT}} = 100$, these differences range between 2.5-4.5% for both volume fractions. Differences between the corresponding effective material properties when changing the filler count likewise shows little variance, with almost all deviations remaining within 5%. These disparities seen with the filler count are largely an artifact of the fiber distribution configurations used in the RVEs. Inspection of the numerous fiber arrangements, as created using the random generator routine, revealed a partiality to alignment of the CNT fiber bundles in specific material directions, as visible in figures provide in Appendix C. This was more evident in the low volume fraction cases of 10%, where the greater expanse of matrix material permitted such clustering behavior to be developed with lesser issue. Such bias is most prevalent in the cases of $V_f^{\text{CNT}} = 0.1$ and $n^{\text{CNT}} = 100$ and shows through its effective transverse elastic moduli which have the largest variance between E_{11}^{eff} and E_{22}^{eff}. At the higher volume fraction cases of 30%, the increased confinement of the RVE dimensions produce fiber arrangements with less identifiable consistencies in alignment, though greater variance is again seen with a higher filler count. Overall the material characterization appears unaffected by the increase in filler count, suggesting modeling a 50 count fiber distribution is sufficient to represent a random alignment for a CNT-polymer nanocomposite. Extension of the analysis to smaller filler count cases could prove if a 50 fiber distribution is even more than necessary.

The largest changes observed in this study are with variation in the effective material properties of the randomly aligned RVEs compared to the well-dispersed RVEs, particularly at higher volume fractions. For the 10% volume fraction cases variation with random disbursement and clustering is mostly well below 5% in all effective properties, matching well with the computational results presented in Ref. [47] for clustered RVEs of equivalent volume fraction and no interphase effects considered but with a much lower filler count. Noticeable are higher discrepancies between the effective elastic moduli E_{11}^{eff} and E_{22}^{eff} plus Poisson's ratios ν_{12}^{eff} and ν_{21}^{eff} for the cases of $V_f^{\text{CNT}} = 0.1$ and $n^{\text{CNT}} = 100$, compared to the cases of $V_f^{\text{CNT}} = 0.1$ and $n^{\text{CNT}} = 50$, this is due to the preferential alignment of CNT clusters in the material x_1 direction for the largest RVEs cases. In the higher volume fraction cases of 30% considerably larger variations are observed

in the effective material properties, typically near or above 10%. The greater influence of clustering effects on the transverse effective elastic moduli with increasing volume fractions can be examined through the associated stress fields. Figure 4.35 shows the transverse stress field contour plots for two aligned randomly dispersed RVEs of $V_f^{\text{CNT}} = 0.1$ and $V_f^{\text{CNT}} = 0.3$, both with $n^{\text{CNT}} = 50$, in comparison to their corresponding well-dispersed hexagonally packed RVE cases. Stress fields for the enlarge RVEs with $n^{\text{CNT}} = 100$ displayed similar results and are thus not provided here, for the same reason these plots only show the σ_{yy} stress field, i.e. the σ_{xx} results were practically identical. In both randomly dispersed RVEs there is visible stress banding and interaction between CNTs of near proximity, with regions or particularly close fibers (fiber clusters) demonstrating slightly increased stress states in their surrounding vicinity. For the 10% volume fraction RVEs such regions are relatively sparse, as visiblie in Figure 4.35b, hence only a minimal increase in observed effective transverse moduli occurs. In contrast for the 30% volume fraction RVE, of Figure 4.35d. there is considerably greater concentration of clustered CNTs leading to a higher influence on the effective material properties. Examination of the global domain decomposition did reveal more extensive contacting of enriched element subdomains for cases of $V_f^{\text{CNT}} = 0.3$ versus $V_f^{\text{CNT}} = 0.1$, it is likely that this introduces error in the effective property calculations leading to the larger variations, though given the qualitatively correct response it is suggested that this error contribution is not as significant as observed for the well-dispersed case of $V_f^{\text{CNT}} = 0.8$. Further studies with higher refined meshes could indicate the severity the contacting enriched subdomains play in calculating effective material properties.

4.5 Computational Characterization of an Evolving Composite

The final case study leverages the mesh independent operation of the IXFEM to investigate how the effective material properties of a CNT-polymer nanocomposite change under simulation of an evolving nanostructure. In this analysis the mechanism for modifying the nanostructure is gravity during the curing cycle of an nanocomposite manufacturing process. Starting with a RVE containing a random disbursement of CNT fibers in matrix material, a fabricated reduced gravity acceleration law is applied to the CNTs to let them settle to the bottom boundary of the problem domain over time[9]. It is noted that the acceleration applied to the CNTs is selected to produce a complete settling time of several hours, but is otherwise not based on any experimental observations or data. Such a rate is also selected to allow a quasi-static evaluation of the material structure evolution, in which inertial mass considerations can be neglected. At each time-step, incremented in hours,

[9] A reduced gravity acceleration is used to consider drag effects that slow down the settling of the CNTs.

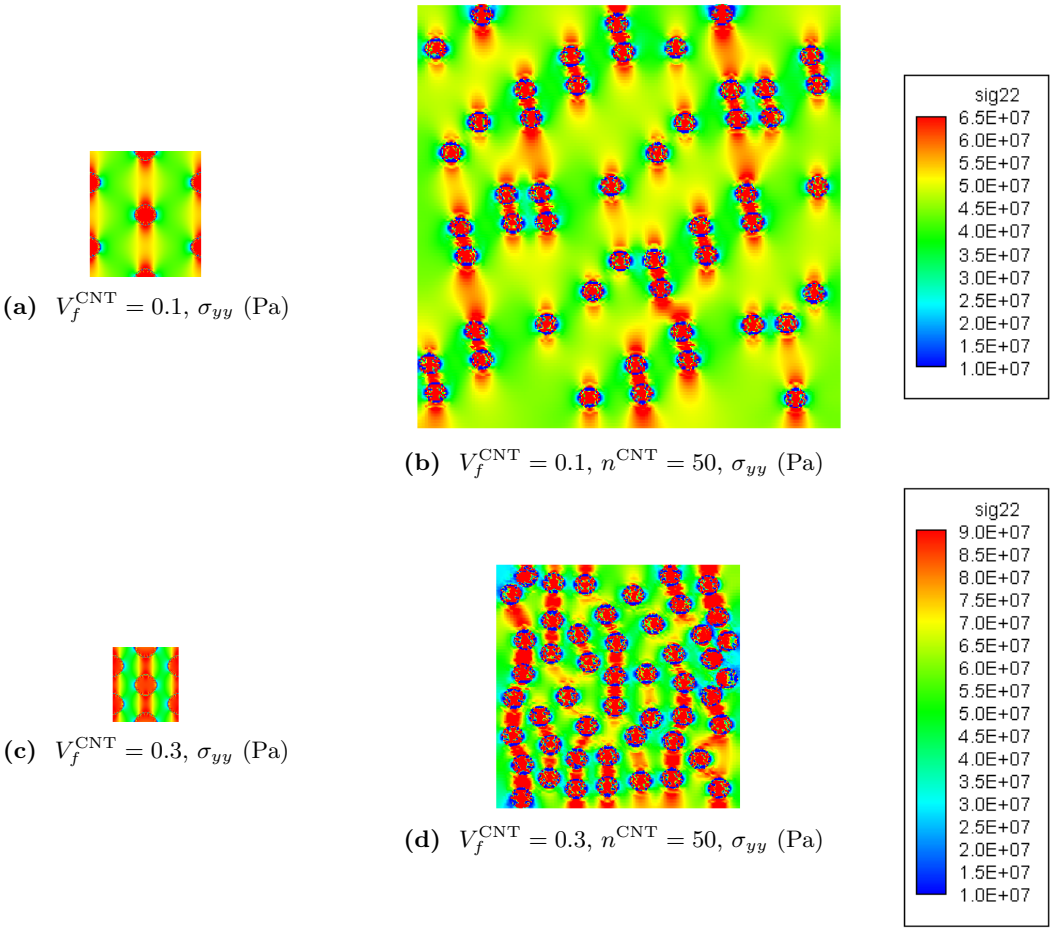

(a) $V_f^{\text{CNT}} = 0.1$, σ_{yy} (Pa)

(b) $V_f^{\text{CNT}} = 0.1$, $n^{\text{CNT}} = 50$, σ_{yy} (Pa)

(c) $V_f^{\text{CNT}} = 0.3$, σ_{yy} (Pa)

(d) $V_f^{\text{CNT}} = 0.3$, $n^{\text{CNT}} = 50$, σ_{yy} (Pa)

Figure 4.35: Comparison of σ_{yy} stress field in 10% and 30% volume faction randomly dispersed RVEs due to applied 1% average strain $\bar{\epsilon}_{yy}$.

the center positions of the CNT fibers are first updated based on the acceleration evolution law and simple interaction criteria, e.g. no interpenetration or direct contact between CNTs. New fiber locations are used to redefine the n^{CNT} circular LSFs, establishing an evolving fiber arrangement. Decomposition of the domain into non-enriched, enriched, and transition subdomains for constructing the FE model using standard FE, enriched MLS, and coupled transition shape functions as appropriate follows naturally to develop a quasi-static IXFEM. As in Section 4.4 the complete set of in-plane effective material properties are calculated, using average applied strains and periodic boundary conditions, with the expectation that the effective transverse isotropic material system will be replaced by an effective orthotropic material system.

Evolution of the RVE nanostructure under the reduced gravitational acceleration is shown in Figure 4.36. Figure 4.36a is the initial configuration and corresponds to one of the random RVE cases of $V_f^{\text{CNT}} = 0.1$ and

$n^{\text{CNT}} = 50$ of Section 4.4. Based on the timeline presented through the figures there is little change in the material structure within the first time-step. Noticeable accumulation of CNTs begins in the second time-step, visible in Figure 4.36c, with their alignment along the bottom boundary and becomes further evident with increases in time elapsed. Simultaneously with the nanostructure evolution the effective isotropic plane symmetry weakens as the fibers collect together in settling and leave a bulk portion of the matrix material largely void of filler material.

Evolution of the effective transverse elastic moduli E_{11}^{eff} and E_{22}^{eff} with time under the settling of the CNT fibers is shown in Figure 4.37. Negligible change is observed in the first two time-steps for the effective moduli compared to the initial configuration. Based on the corresponding distribution of Figures 4.36b and 4.36c this is not unexpected, as the nanostructure of the composite experiences little alteration particularly within the first time-step. Starting with the third time-step ($t = 3$hours) a significant number of CNTs have settled to formed a near continuous band of transverse fibers of close enough proximity to begin to influence the effective transverse moduli. The change is marginal for both elastic moduli, but it is more observable in E_{11}^{eff} (~8.5% increase for E_{11}^{eff} versus ~2% increase for E_{22}^{eff} from their respective initial values). Given that the continuity of the CNTs is aligning with the material x_1 direction it should be anticipated that material properties along this principal axis are quicker to experience influence under the transforming nanostructure, and of greater effect. With the formation of a full band of CNT fibers at time-step four ($t = 4$hours), as visible in Figure 4.36e, a significant increase in effective transverse modulus E_{11}^{eff} occurs (~40% increase from initial value), while effective transverse modulus E_{22}^{eff} undergoes a more subtle increase (~8% increase from initial value). A near consistent increase in the elastic moduli follows with the formation of a second band of fully continuous transverse CNT fibers (and a near complete third band as well), increasing E_{11}^{eff} by ~73% and E_{22}^{eff} by ~13% from their initial values. Based on these observations there appears to be a linear relationship between the effective transverse elastic moduli and number of full formed in-plane CNT fiber rows, at least for low volume fractions. Effective shear modulus G_{12}^{eff} demonstrated no significant changes in value or trend in behavior as the nanocomposite structure changed. Effective Poisson's ratios ν_{12}^{eff} and ν_{21}^{eff} both underwent minor decreases in value due to the total problem evolution, ~1.5% and ~5.5% respectively. The trend in ν_{12}^{eff} matched the elastic moduli, only starting to decrease after the third time-step when a full band of CNTs had formed on the bottom boundary. In contrast, ν_{21}^{eff} underwent a parabolic decrease with evolution of the nanostructure. This difference in behavior is suspected to arise due to the development of two separate regions within the nanocomposite: the high-stiffness region at the bottom of the RVE, where

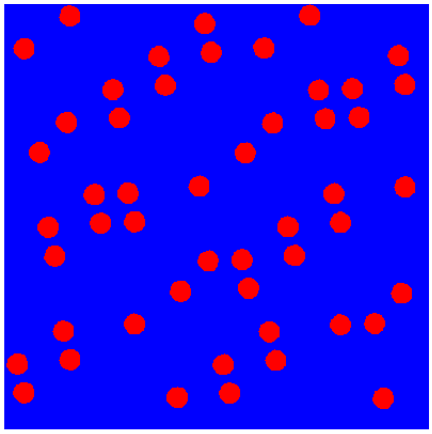

(a) $t = t_0$, initial configuration

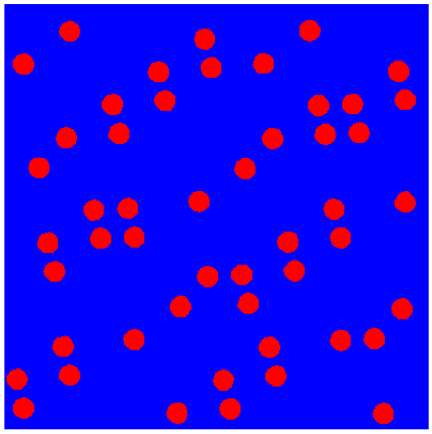

(b) $t = 1$hour

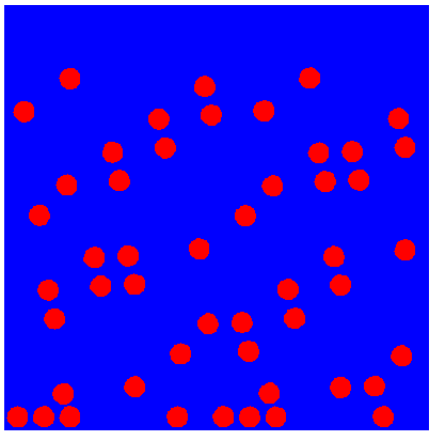

(c) $t = 2$hours

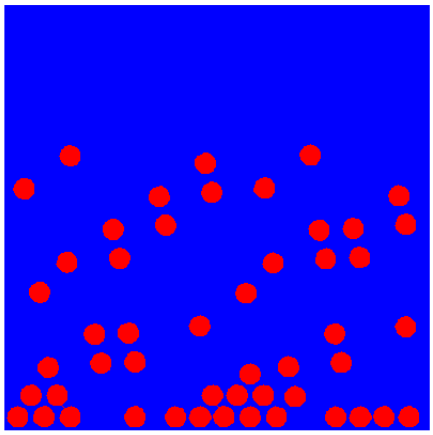

(d) $t = 3$hours

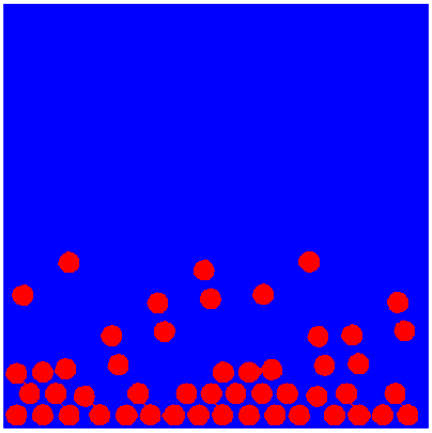

(e) $t = 4$hours

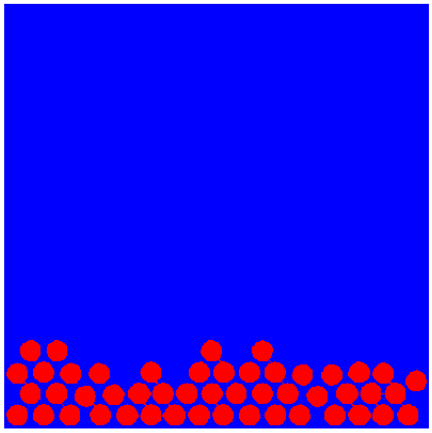

(f) $t = 5$hours

Figure 4.36: Simulated evolution of settling CNT fibers in an epoxy matrix under an applied reduced gravitational acceleration.

the CNTs collectively gather, and the remaining large compliant portion of pure matrix above.

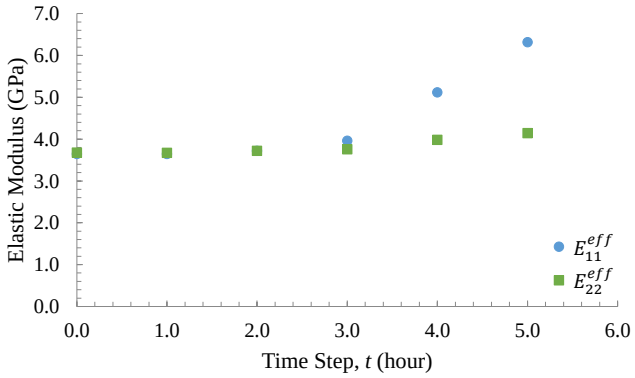

Figure 4.37: Change in effective transverse elastic modulus E_{11}^{eff} and E_{22}^{eff} with evolution of a settling CNT fiber distribution.

The increase in effective transverse moduli in response to the settling of CNTs can be understood by examining alterations in the σ_{xx} and σ_{yy} stress distributions with time. Transverse stress field contour plots for the randomly dispersed RVE of Figure 4.36 are shown in Figure 4.38 for three time-steps (t_1, t_3, and t_5) showing the evolving CNT-polymer nanocomposite RVE stress state response to average applied strains of 1% in the material x_1 and x_2 direction, according displayed in the first and second column of subfigures. Comparison of the σ_{xx} and σ_{yy} stress field at time-step t_1 in Figures 4.38a and 4.38b respectively to the σ_{yy} stress field of Figure 4.35b, corresponding to the initial configuration, shows negligible difference with the marginal settling of fibers during the first time-step. Consistent stress banding behavior is seen in both the σ_{xx} and σ_{yy} stress fields with equivalent average stresses existing throughout the fibers and matrix material for either loading case. At the third time-step, Figures 4.38c and 4.38d, similarity in the bulk field response breaks down, particularly at the top and bottom portions of the RVE. Visible in the σ_{xx} stress field the top third section of the RVE, consisting of pure matrix material, supports the same ~40MPa stress state as the matrix material separating the fibers in the middle third section. This is in contrast to that seen for the σ_{yy} stress field, where the pure matrix portion of the RVE experiences an approximate 25% increase in the stress state as the high-stiffness fibers have settled out of the region, leaving the matrix material unaided in supporting the loading case. Differences in stress state behavior are also visible in the bottom third of the RVE. In the σ_{xx} stress field, growing alignment of the CNTs into a full transverse band, aligned with the loading direction, contributes to an increased stress state in the CNTs and surrounding matrix material as result of the interactions between the fibers in close proximity. This increase in the stress state indicates the load is

in majority being transfer through the high-stiffness region of collecting fibers permitting the pure matrix material to sustain its low stress state. In opposition, in the σ_{yy} stress field the gathering of CNTs along the bottom edge does not significantly assist in supporting the applied loading in the x_2 direction as continuous bands of high-stiffness are deteriorating. In the middle third portion, the CNT-polymer nanocomposite maintains a well-dispersed region of CNTs and the stress state response is similar between loading cases and to previous time-steps. With the complete settling of all fibers at the final time-step, Figures 4.38e and 4.38f, the variations discussed previously become further evident. The RVE structure after this duration is divided into two portions: a high-stiffness region of nearly three complete rows of transversely banded CNTs composing the bottom quarter of the RVE, and a compliant pure matrix region composing the top three-quarters of the RVE. Shown in the σ_{xx} stress field the CNT bands support a continuous high stress state above that of the well-dispersed arrangement hence giving rise to the 73% increase seen in E_{11}^{eff} in Figure 4.37. As before the pure matrix region experiences no contributing change in its stress state. In the σ_{yy} stress field, high stress regions are localized within the effective CNTs with no appreciable transfer occurring through the surrounding matrix material. The increasing pure matrix portion that remains continues to support a near consistent 25% increase in its stress state, over the well-dispersed initial configuration. This separation of the load bearing is responsible for the by comparison smaller increase in E_{22}^{eff}, of 13% with the evolving nanostructure.

Together with the previous two sections this explorative evaluation in computing the effective elastic material properties of a CNT-polymer nanocomposite, demonstrate where the benefits of an mesh independent FEM are most advantageous for replacing the standard FEM for computational micromechanics analysis. Removing the mesh explicit definition of discontinuity interfaces, it was shown that high numbers of filler agents in a composite material RVE and evolving composite micro- or nanostructures can easily and directly be considered in a FE framework. Based on the investigations performed in this work it is perceivable how extension of the IXFEM to coupled mechanics problems for nanocomposites would provide an major advantage in studying multifunctional behavior in more complex settings then currently undertaken using the standard FEM.

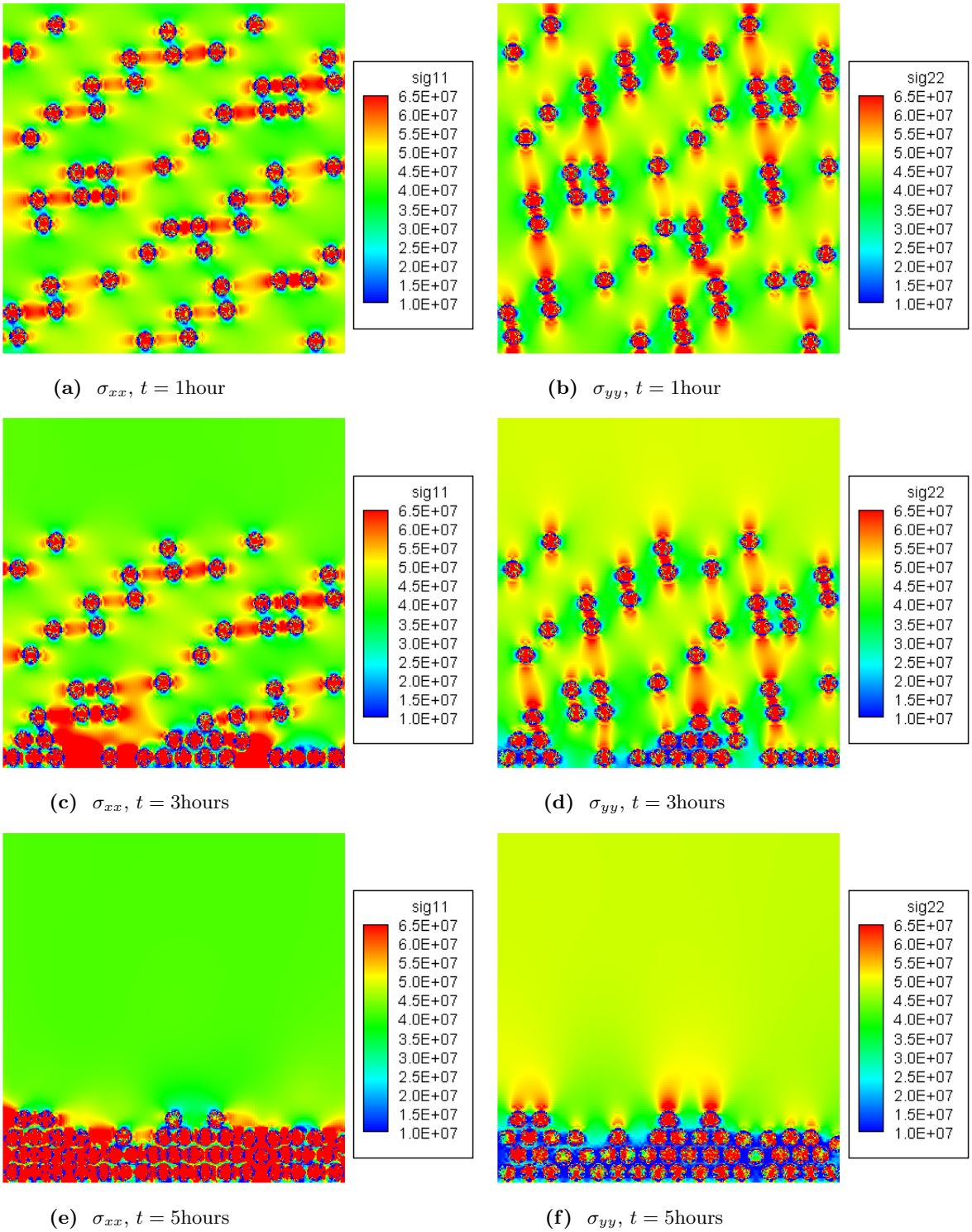

(a) σ_{xx}, $t = 1$hour **(b)** σ_{yy}, $t = 1$hour

(c) σ_{xx}, $t = 3$hours **(d)** σ_{yy}, $t = 3$hours

(e) σ_{xx}, $t = 5$hours **(f)** σ_{yy}, $t = 5$hours

Figure 4.38: Change in σ_{xx} and σ_{yy} stress field due to applied 1% normal strain $\bar{\epsilon}_{xx}$ and $\bar{\epsilon}_{yy}$ respectively with evolution of settling CNT fiber distribution.

5 Conclusions

The IXFEM has been applied as a numerical tool for the computational analysis of plane linear elastic material mechanics problems to demonstrate its capabilities and efficiency in comparison to the standard FEM, with particular focus on composite RVEs. Developed by Fries and Belytschko [38, 39], the IXFEM is a mesh independent approximating FEM which applies a local intrinsic enrichment strategy to build specialized shape functions to account for the presence of anticipated discontinuities in solution of a boundary value problem. A variant of the standard XFEM (i.e. the EXFEM), the IXFEM is distinguished by its intrinsic (versus extrinsic) enrichment approach for modifying the approximation function, for the purpose of modeling discontinuity interface effects separate from the FE mesh discretization. Opposed to supplementing the standard polynomial approximation function of the FEM with the addition of appropriate enrichment functions, as done in extrinsically enriched FEMs, the enrichment functions are directly included in the approximation subspace to generate enhanced shape functions that explicitly exhibit discontinuous behavior in their functional form or their gradient. With these inherent shape function properties involved in the approximation function the expected discontinuous response of primary or secondary variable fields across strong or weak discontinuity interfaces respectively can be captured without the introduction of additional unknowns in the FE model.

Resultant of the intrinsic enrichment process, two unique advantages make the IXFEM particularly appealing for the analysis of composite materials as proposed in this thesis, when compared with extrinsically enriched FEMs. First is its direct enrichment of the shape functions, as this circumvents the introduction of additional unknowns, or extra degrees of freedom, in the approximation. In typical micromechanics analysis composite materials are studied through a RVE characterizing relevant dimensional and composition arrangement information. If considering large RVE cases with multiple filler agents, modeled as weak bimaterail discontinuity interfaces, as done in this work, maintaining the number of unknowns as low as possible is preferential in sustaining a consistent computational cost associated with solving the FE model. Second is its approximation function formulation, which for general purposes can be considered unmodified from that of the standard FEM, as all enrichment information is completely contained within the shape function forms themselves. This is a significant factor for developing an IXFEM coded versus an EXFEM code as only the shape function and derivative evaluation routines in a standard FEM code need to be adapted to evaluate enriched MLS shape functions in the IXFEM, while the EXFEM must deal with similar issues in

evaluating enriched approximation functions it must also contend with the adaptive expansion of the FE model to bring in the additional unknowns.

Comparison of results obtained using the IXFEM to those of a standard FEM and analytic solutions for common validation problems (plate with a hole and plate with a inhomogeneity) demonstrate the ability of the full-form strong discontinuity and the weak discontinuity enriched intrinsic bases to model domain void and bimaterial interfaces respectively. Results from the IXFEM are in good agreement with corresponding analytic solutions, showing high degrees of qualitative accuracy in the displacement, strain, and stress fields. Notable observations in the results include the fictitious displacement values seen for void domains when using the full-form strong basis, and the systematic error existing internal to weak discontinuities, where large ratios in the material properties exist. Comparing solutions determined using the full-form basis $\boldsymbol{p}_{\mathrm{s,f}}^{\mathrm{enr}}(\boldsymbol{x})$ against those determined using the truncated basis $\boldsymbol{p}_{\mathrm{s,t}}^{\mathrm{enr}}(\boldsymbol{x})$ and a full-form basis with truncation $\boldsymbol{p}_{\mathrm{s,ft}}^{\mathrm{enr}}(\boldsymbol{x})$, indicate the full-form basis as having the greatest accuracy, based on a quantitative measure of the error norms against the analytic solution. Truncation of the strongly enriched shape functions is demonstrated to stabilize the void domain deformation, but at the cost of increased error for the full-form basis with truncation and widespread inaccuracy with the truncated basis. Based on similar findings in current literature the error observed at the bimaterial interfaces is proposed to result from local mesh locking at the discontinuity interface. For both validation problems error norm measures against the analytic solution show anticipated trends for the L_2 norm, i.e. a linear decrease on a log-log plot of percent error versus element size, while the energy norm was found to quickly converge to a percent difference of 8% and 3% for the strong and weak discontinuity validation problems respectively.

Extension of the IXFEM to study CNT-polymer nanocomposities is readily achieved using multiple LSFs to define each fiber location in the RVE. The IXFEM, along with a FEM, are used to analyze a series of average strain state loading conditions with periodic boundary conditions applied to evaluate effective elastic material properties of the nanocomposite for a series of volume fractions. Both methods compare favorable to each other and to an analytic solution determined using a composite cylinder method model for fiber volume fractions below 60%. An unexpected issue was found to occur with the IXFEM where distinct subdomains of enriched elements come into contact. In these regions the strain field approximation of the IXFEM is found to deteriorate in comparison to the bulk field response elsewhere. Though the strain field only shows localized inaccuracies, the resulting stress field shows significant inaccuracy throughout the problem domain. Two conceivable solutions were proposed to work around this issue. Percent differences in

the global norm measures between the IXFEM and FEM show minimal variance, less than 1%, at volume fractions below 60%, in both the L_2 and energy norm. Greater differences are again observed when separate enriched subdomains share element boundaries.

Enlarged RVEs are also studied for a series of randomly aligned fiber distributions as a preliminary showcase of the IXFEM to quickly and easily work with variable internal geometries of discontinuities. In line with other studies it is shown that clustering alone has minimal impact on the effective martial properties at low volume fractions, $V_f^{\mathrm{CNT}} = 0.1$, of a CNT-polymer nanocomposite. Larger deviations compared to the well-dispersed assumption are seen for increased fiber volume fractions of $V_f^{\mathrm{CNT}} = 0.3$. A secondary analysis implementing the mesh independent operation of the IXFEM simulates an evolving nanostructure for a CNT-polymer nanocomposite during the curing cycle of the manufacturing process and examines its effect on effective material properties with time. A rudimentary evolution law was applied which updated the level-set representation of the fiber distribution in time to perform a quasi-static analysis of settling CNTs. The analysis showed a transition from an effectively transversely isotropic material to a potential effectively orthotropic material as the CNTs formed continuous transverse bands. Together these explorative evaluations in computing effective elastic material properties of large scale RVEs or evolving composite microstructures demonstrate when the benefits of an mesh independent FEM are most advantageous in replacing the standard FEM for computational micromechanics analysis.

Overall the IXFEM is shown to be a promising substitute for the standard FEM when performing computational micromechanics. Major benefits gained with switching to the mesh independent FEM include the ability to quickly consider variable and evolving internal geometries and the reduction in the pre-processing work to develop suitable meshes on which the evaluation is executed. This thesis demonstrated a number of these benefits, and contributed to the advancing numerical techniques available for the efficient computational modeling of composite materials. Based on the investigations performed in this work it is perceivable how extension of the IXFEM to coupled mechanics problems for nanocomposites would provide an major advantage in studying multifunctional behavior in more complex settings then currently undertaken using the standard FEM.

6 Future Challenges

To further demonstrate utility of the IXFEM, for modeling and characterizing composite material systems, the computational method can readily be adapted to perform or assist in a number of studies. This thesis work was completed with the intent to introduce a mesh independent FEM, specifically the IXFEM, as an efficient substitute for the standard FEM, typically used in computational micromechanics analysis, when researching the influence of variations in the composite filler material configuration (particularly at high filler counts) or an evolving microstructure on the effective material properties. Having shown the IXFEM to perform with comparable accuracy to the FEM, in modeling the mechanical response (displacement, strain, and stress) of a material system with internal strong or weak discontinuities without an explicit definition of their interface(s) through the FE mesh, gives confidence it can be readily modified for application to coupled physics problems, to model the multifunctional response of nanocomposites. To do so requires definition of a new GDE expressing the additional problem physics, e.g. electrostatic equations if investigating multifunctional effects on the effective conductivity or piezoresistivity of CNT-polymer nanocomposites, and criteria governing the new considerations, e.g. probability of electron hopping or tunneling resistance for the same electrostatic problem. In such studies advantages of the IXFEM can assist in examining the changes incurred in the conducting pathways more readily when varying the degree of clustering or other configuration parameters. Furthermore the LSM, already used to define discontinuity interfaces, may facilitate calculation of inter-fiber distances as necessary for evaluating the tunneling resistance.

Additional areas open for near immediate exploration using the IXFEM include microstructural changes of more complex behavior. Interaction effects in, or as consequence of, growing networks of the filler material can easily be evaluated with development of accurate representative evolution laws. These might consider such phenomenon as merging, splitting, growing, shrinking, or realignment of discontinuities as appropriate. Damage effects can also be included in more advanced models through utilization of applicable enrichment functions, e.g. the crack tip enrichment basis discussed in this work. With the incorporation of an initiation and propagation criteria evolving, merging, and branching cracks can be simulated in the material response through tracking of separate LSFs. Cohesive zone damage modeling has been utilized in the EXFEM, extension to the IXFEM should follow similarly, and could be used to permit debonding at weak bimaterial discontinuity interfaces in composite materials. Development of a three-dimensional IXFEM, through likely more burdensome in defining the analogous specialized weight function and handling of the increased number

of influencing nodes for an enriched element, would allow out of plane effective material properties to be directly calculated through computational characterization techniques.

Together with these more straightforward extensions of the IXFEM for numerical analysis of composite materials there are also opportunities to advance the capabilities of the IXFEM, and mesh independent FEMs in general. Prevalent at the weak discontinuity interfaces, discrepancies in the stress contours, proposed to occur in response to mesh locking, have been resolved in other FEMs using penalty approaches with Lagrange multipliers or a Nitsche's method. Applying such strategies in the IXFEM should follow naturally to solve the issue. A more unique problem to identify and fix is the deterioration in the approximation shown to occur in contacting regions of distinct enriched subdomains. Thorough review of mesh sizing can indicate if the issue arises only when enriched elements of one subdomain are directly sharing a element edge with other enriched elements of a separate subdomain, or if the issue arises even if an enriched element (due to all its nodes being considered enriched) divides the two subdomains, Figure 6.1 illustrates the difference in these two scenarios. An progressive solution to this problem requires development of augment enriched bases or advanced blending techniques to model multiple discontinuity interfaces within the compact support of a single enriched shape function. Further extension of this concept could allow multiple discontinuities to exist within an single enriched element as might be necessary to predict accurate crack growth in a composite material.

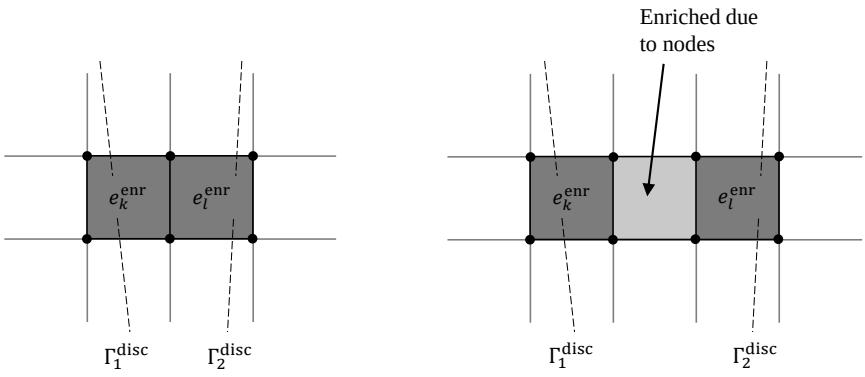

(a) Direct contact **(b)** Indirect contact

Figure 6.1: Demonstration of contacting enriched elements from distinct enriched subdomains.

Another unique opportunity to expand the capabilities of the mesh independent FEMs is development of a hierarchical LSM strategy to define discontinuities within other discontinuities. To the author's knowledge

such interest has not been pursued in development or application of enriched FEMs. Such a technique would allow the CNT-polymer nanocomposite to be modeled using the hallow fiber representation of Figure 4.21a (i.e. a strong discontinuity inside a weak discontinuity). Moreover as it should be developed to allow multiple layering, an interphase region between the matrix material and the filler material could easily be introduced into the model as well. Given the proximity of such interfaces in an CNT-polymer nanocomposite it would likely require resolving the contacting enriched element issue first. Considerations to defining ranked LSFs in one approach might use non-zero LSC descriptions of the discontinuity interfaces. Use of the zero-level LSC certainly facilities the computational aspects, but is otherwise arbitrary. A final area of additional study proposed is a quantified computational cost comparison of the EXFEM versus the IXFEM. Based on the added costs in either implantation, extra unknowns in the EXFEM or evaluation of the enriched shape functions in the IXFEM, a theoretical assessment can be devised based on the number of floating point operations that need to completed with either method and can be linked to numerical evaluation runtimes.

Future work will look to solve and implement a number of these challenges to develop a mesh independent IXFEM which is capable of predicting a host of multifunctional behaviors while supporting the representation of more complex composite RVE geometries.

References

[1] JD Achenbach and H Zhu. Effect of interphases on micro and macromechanical behavior of hexagonal-array fiber composites. *Journal of Applied Mechanics*, 57(4):956–963, 1990.

[2] Chandrasekhar Annavarapu, Martin Hautefeuille, and John Dolbow. A robust Nitsches formulation for interface problems. *Computer Methods in Applied Mechanics and Engineering*, 225-228:44–54, June 2012.

[3] Pedro M. A. Areias and Ted Belytschko. Analysis of three-dimensional crack initiation and propagation using the extended finite element method. *International Journal for Numerical Methods in Engineering*, 63(5):760–788, June 2005.

[4] Ivo Babuška. The partition of unity method. *International Journal for Numerical Methods in Engineering*, 40(July 1995):727–758, 1997.

[5] Ivo Babuška, Uday Banerjee, and John E. Osborn. Survey of meshless and generalized finite element methods: A unified approach. *Acta Numerica*, 12(July 2003):1–125, May 2003.

[6] E. Béchet, H. Minnebo, N. Moës, and B. Burgardt. Improved implementation and robustness study of the x-fem for stress analysis around cracks. *International Journal for Numerical Methods in Engineering*, 64(8):1033–1056, 2005.

[7] Éric Béchet, Nicolas Moës, and Barbara Wohlmuth. A stable lagrange multiplier space for stiff interface conditions within the extended finite element method. *International Journal for Numerical Methods in Engineering*, 78(8):931–954, 2009.

[8] Ted Belytschko and T Black. ELASTIC CRACK GROWTH IN FINITE ELEMENTS WITH MINIMAL REMESHING. *International Journal for Numerical Methods in Engineering*, 45(July 1998): 601–620, 1999.

[9] Ted Belytschko, Y. Y. Lu, and L Gu. Element-Free Galerkin methods. *International Journal for Numerical Methods in Engineering*, 37:229–256, 1994.

[10] Ted Belytschko, D Organ, and Y Krongauz. A coupled finite element-element-free Galerkin method. *Computational Mechanics*, 17(3):186–195, 1995.

[11] Ted Belytschko, Y Krongauz, and D Organ. Meshless methods: an overview and recent developments. *Computer Methods in Applied Mechanics and Engineering*, 139(1-4):3–47, 1996.

[12] Ted Belytschko, Nicolas Moës, S Usui, and Parimi. Arbitrary discontinuities in finite elements. *International Journal for Numerical Methods in Engineering*, 50(August 2000):993–1013, 2001.

[13] Ted Belytschko, Robert Gracie, and Giulio Ventura. A review of extended/generalized finite element methods for material modeling. *Modelling and Simulation in Materials Science and Engineering*, 17 (4):043001, June 2009.

[14] T.N. Bittencourt, P.A. Wawrzynek, A.R. Ingraffea, and J.L. Sousa. Quasi-automatic simulation of crack propagation for 2d {LEFM} problems. *Engineering Fracture Mechanics*, 55(2):321–334, 1996.

[15] René de Borst, Miguel A. Gutiérrez, Garth N. Wells, Joris J. C. Remmers, and Harm Askes. Cohesive-zone models, higher-order continuum theories and reliability methods for computational failure analysis. *International Journal for Numerical Methods in Engineering*, 60(1):289–315, 2004.

[16] P.O. Bouchard, F. Bay, and Y. Chastel. Numerical modelling of crack propagation: automatic remeshing and comparison of different criteria. *Computer Methods in Applied Mechanics and Engineering*, 192(35-36):3887–3908, 2003.

[17] O Breuer and Uttandaraman Sundararaj. Big returns from small fibers: a review of polymer/carbon nanotube composites. *Polymer composites*, 25(6):630–645, 2004.

[18] É. Budyn, G. Zi, N. Mos, and T. Belytschko. A method for multiple crack growth in brittle materials without remeshing. *International Journal for Numerical Methods in Engineering*, 61(10):1741–1770, 2004.

[19] Elie Chahine, Patrick Laborde, and Yves Renard. A quasi-optimal convergence result for fracture mechanics with {XFEM}. *Comptes Rendus Mathematique*, 342(7):527–532, 2006.

[20] Adarsh K. Chaurasia and Gary D. Seidel. Computational micromechanics analysis of electron hopping induced conductive paths and associated macroscale piezoresistive response in carbon nanotube-polymer nanocomposites. *Journal of Intelligent Material Systems and Structures*, January 2014.

[21] Adarsh K. Chaurasia, Xiang Ren, and Gary D. Seidel. Computational micromechanics analysis of electron hopping and interfacial damage induced piezoresistive response in carbon nanotube-polymer nanocomposites. *Smart Materials and Structures*, 23(7):075023, July 2014.

[22] Jack Chessa and Ted Belytschko. An enriched finite element method and level sets for axisymmetric two-phase flow with surface tension. *International Journal for Numerical Methods in Engineering*, 58 (13):2041–2064, 2003.

[23] Jack Chessa and Ted Belytschko. Arbitrary discontinuities in space–time finite elements by level sets and x-fem. *International Journal for Numerical Methods in Engineering*, 61(15):2595–2614, 2004.

[24] Jack Chessa and Ted Belytschko. A local space–time discontinuous finite element method. *Computer Methods in Applied Mechanics and Engineering*, 195(13):1325–1343, 2006.

[25] Jack Chessa, Patrick Smolinski, and Ted Belytschko. The extended finite element method (xfem) for solidification problems. *International Journal for Numerical Methods in Engineering*, 53(8):1959–1977, 2002.

[26] Jack Chessa, Hongwu Wang, and Ted Belytschko. On the construction of blending elements for local partition of unity enriched finite elements. *International Journal for Numerical Methods in Engineering*, 57(7):1015–1038, June 2003.

[27] MatWeb LLC Material Property Data. Aluminum al. `http://www.matweb.com/`, 2014. Accessed 2014-03-15.

[28] Christophe Daux, Nicolas Moës, John Dolbow, Natarajan Sukumar, and Ted Belytschko. Arbitrary branched and intersecting cracks with the extended finite element method. *Int. J. Numer. Meth. Engng*, 48(September 1999):1741–1760, 2000.

[29] René de Borst, Joris J.C. Remmers, and Alan Needleman. Mesh-independent discrete numerical representations of cohesive-zone models. *Engineering Fracture Mechanics*, 73(2):160–177, 2006.

[30] John Dolbow. *An extended finite element method with discontinuous enrichment for applied mechanics.* Phd dissertation, Northwestern University, 1999.

[31] John Dolbow, Nicolas Moës, and Ted Belytschko. Discontinuous enrichment in finite elements with a partition of unity method. *Finite elements in analysis and design*, 36:235–260, 2000.

[32] John Dolbow, Nicolas Moës, and Ted Belytschko. An extended finite element method for modeling crack growth with frictional contact. *Computer Methods in Applied Mechanics and Engineering*, 190: 6825–6846, 2001.

[33] C.Armando Duarte and J.Tinsley Oden. An h-p adaptive method using clouds. *Computer methods in applied mechanics and ...*, 139(1-4):237–262, December 1996.

[34] G Dvorak and J Teply. Plasticity today: Modeling, methods and applications. *Elsevier*, page 625, 1985.

[35] H.L. Ewalds and R.J.H. Wanhill. *Fracture Mechanics*. Edward Arnold, 1984.

[36] TP Fries. A corrected XFEM approximation without problems in blending elements. *International Journal for Numerical Methods in Engineering*, 75(November 2007):503–532, 2008.

[37] TP Fries. The Intrinsic XFEM for Two-Fluid Flows. *International Journal for Numerical Methods in Fluids*, 60(August 2008):437–471, 2009.

[38] TP Fries and Ted Belytschko. The intrinsic XFEM: a method for arbitrary discontinuities without additional unknowns. *International Journal for Numerical Methods in Engineering*, 68(May):1358–1385, 2006.

[39] TP Fries and Ted Belytschko. New Shape Functions for Arbitrary Discontinuities without Additional Unknowns. *Meshfree Methods for Partial Differential Equations III*, 2007.

[40] TP Fries and Ted Belytschko. The extended/generalized finite element method: an overview of the method and its applications. *International Journal for Numerical Methods in Engineering*, (October 2009):1–6, 2010.

[41] TP Fries and HG Matthies. Classification and Overview of Meshfree Methods. *Scientific Computing, Informatikbericht*, 2003.

[42] Thomas C. Gasser and Gerhard A. Holzapfel. Modeling 3d crack propagation in unreinforced concrete using {PUFEM}. *Computer Methods in Applied Mechanics and Engineering*, 194:2859–2896, 2005.

[43] Robert Gracie, Giulio Ventura, and Ted Belytschko. A new fast finite element method for dislocations based on interior discontinuities. *International Journal for Numerical Methods in Engineering*, 69(2): 423–441, 2007.

[44] Robert Gracie, Jay Oswald, and Ted Belytschko. On a new extended finite element method for dislocations: Core enrichment and nonlinear formulation. *Journal of the Mechanics and Physics of Solids*, 56(1):200–214, 2008.

[45] Robert Gracie, Hongwu Wang, and Ted Belytschko. Blending in the extended finite element method by discontinuous galerkin and assumed strain methods. *International Journal for Numerical Methods in Engineering*, 74(11):1645–1669, 2008.

[46] A. Gravouil, Nicolas Moës, and Ted Belytschko. Non-planar 3D crack growth by the extended finite element and level sets: Part II: Level set update. *International Journal for Numerical Methods in Engineering*, 53(11):2569–2586, April 2002.

[47] Daniel C. Hammerand, Gary D. Seidel, and Dimitris C. Lagoudas. Computational Micromechanics of Clustering and Interphase Effects in Carbon Nanotube Composites. *Mechanics of Advanced Materials and Structures*, 14(4):277–294, April 2007.

[48] Anita Hansbo and Peter Hansbo. A finite element method for the simulation of strong and weak discontinuities in solid mechanics. *Computer Methods in Applied Mechanics and Engineering*, 193 (33-35):3523–3540, August 2004.

[49] Antonio Huerta and S Fernandez Mendez. Enrichment and coupling of the finite element and meshless methods. *International Journal for Numerical Methods in Engineering*, 48(July 1999):1615–1636, 1999.

[50] E. V. Iarve. Mesh independent modelling of cracks by using higher order shape functions. *International Journal for Numerical Methods in Engineering*, 56(6):869–882, February 2003.

[51] H. Ji and J. E. Dolbow. On strategies for enforcing interfacial constraints and evaluating jump conditions with the extended finite element method. *International Journal for Numerical Methods in Engineering*, 61(14):2508–2535, 2004.

[52] H. Ji, D. Chopp, and J. E. Dolbow. A hybrid extended finite element/level set method for modeling phase transformations. *International Journal for Numerical Methods in Engineering*, 54(8):1209–1233, 2002.

[53] Nat Kasayapanand. Exact solution of double filled hole of an infinite plate. *J. Mech. Mater. Struct*, 3 (February):365–373, 2008.

[54] Frank K Ko, Sakina Khan, Ashraf Ali, Yury Gogotsi, Nevin Naguib, Guoliang Yang, Christopher Li, Hideo Shimoda, Otto Zhou, Michael J Bronikowski, et al. Structure and properties of carbon nanotube reinforced nanocomposites. In *Proceedings of the 43rd Structures, Structural Dynamics and Materials Conference*, volume 3, pages 1779–1787, 2002.

[55] Y. Krongauz and T. Belytschko. Efg approximation with discontinuous derivatives. *International Journal for Numerical Methods in Engineering*, 41(7):1215–1233, 1998.

[56] Patrick Laborde, Julien Pommier, Yves Renard, and Michel Salaün. High-order extended finite element method for cracked domains. *International Journal for Numerical Methods in Engineering*, 64(3):354–381, September 2005. ISSN 0029-5981.

[57] P. Lancaster and K. Salkauskas. Surfaces Generated by Moving Least Squares Methods. *Mathematics of Computation*, 37(155):141–158, July 1981.

[58] Tod A. Laursen, Michael A. Puso, and Jessica Sanders. Mortar contact formulations for deformabledeformable contact: Past contributions and new extensions for enriched and embedded interface formulations. *Computer Methods in Applied Mechanics and Engineering*, 205-208(0):3–15, 2012.

[59] G. Legrain, N. Mos, and E. Verron. Robust and direct evaluation of j2 in linear elastic fracture mechanics with the x-fem. *International Journal for Numerical Methods in Engineering*, 76(10):1471–1488, 2008.

[60] Wing-Kam Liu, Shaofan Li, and Ted Belytschko. Moving least-square reproducing kernel methods (I) Methodology and convergence. *Computer Methods in Applied Mechanics and Engineering*, 143(1-2): 113–154, April 1997.

[61] X. Y. Liu, Q. Z. Xiao, and B. L. Karihaloo. XFEM for direct evaluation of mixed mode SIFs in homogeneous and bi-materials. *International Journal for Numerical Methods in Engineering*, 59(8): 1103–1118, February 2004.

[62] Yu Liu, S Murakami, and Y Kanagawa. Mesh-dependence and stress singularity in finite element analysis of creep crack growth by continuum damage mechanics approach. *European journal of mechanics. A. Solids*, 13(3):395–418, 1994.

[63] Stefan Loehnert and Ted Belytschko. A multiscale projection method for macro/microcrack simulations. *International Journal for Numerical Methods in Engineering*, 71(12):1466–1482, 2007.

[64] J.M. Melenk and Ivo Babuška. The partition of unity finite element method: Basic theory and applications. *Computer Methods in Applied Mechanics and Engineering*, 139:289–314, 1996.

[65] R. Merle and J. Dolbow. Solving thermal and phase change problems with the extended finite element method. *Computational Mechanics*, 28(5):339–350, 2002.

[66] Nicolas Moës and Ted Belytschko. Extended finite element method for cohesive crack growth. *Engineering fracture mechanics*, 69:813–833, 2002.

[67] Nicolas Moës, John Dolbow, and Ted Belytschko. A finite element method for crack growth without remeshing. *Int. J. Numer. Meth. Engng*, 150(February):131–150, 1999.

[68] Nicolas Moës, A. Gravouil, and Ted Belytschko. Non-planar 3D crack growth by the extended finite element and level sets: Part I: Mechanical model. *International Journal for Numerical Methods in Engineering*, 53(11):2549–2568, April 2002.

[69] Soheil Mohammadi. *Extended Fintie Element Method*. Blackwell, 2008.

[70] Hashem M. Mourad, John Dolbow, and Isaac Harari. A bubble-stabilized finite element method for dirichlet constraints on embedded interfaces. *International Journal for Numerical Methods in Engineering*, 69(4):772–793, 2007.

[71] S Murakami and Y Liu. Mesh-dependence in local approach to creep fracture. *International Journal of Damage Mechanics*, 4(3):230–250, 1995.

[72] Toshio Nagashima, Youhei Omoto, and Shuichi Tani. Stress intensity factor analysis of interface cracks using x-fem. *International Journal for Numerical Methods in Engineering*, 56(8):1151–1173, 2003.

[73] Andrew Nealen. An As-Short-As-Possible Introduction to the Least Squares, Weighted Least Squares and Moving Least Squares Methods for Scattered Data Approximation and Interpolation. Technical Report 1, 2004.

[74] James Njuguna and Krzysztof Pielichowski. Polymer nanocomposites for aerospace applications: fabrication. *Advanced Engineering Materials*, 6(4):193–203, 2004.

[75] D Organ, M Fleming, T Terry, and Ted Belytschko. Continuous meshless approximations for nonconvex bodies by diffraction and transparency. *Computational Mechanics*, 18(3):225–235, 1996.

[76] Stanley. Osher and R. Fedkiw. *Level Set Methods and Dynamic Implicit Surfaces*. Applied Mathematical Sciences. Springer, 2003.

[77] Stanley Osher and James A Sethian. Fronts propagating with curvature-dependent speed: Algorithms based on Hamilton-Jacobi formulations. *Journal of Computational Physics*, 79(1):12–49, November 1988.

[78] Jay Oswald, Robert Gracie, Roopam Khare, and Ted Belytschko. An extended finite element method for dislocations in complex geometries: Thin films and nanotubes. *Computer Methods in Applied Mechanics and Engineering*, 198:1872–1886, 2009.

[79] Cheol Park, Zoubeida Ounaies, Kent A Watson, Kristin Pawlowski, Sharon E Lowther, John W Connell, Emilie J Siochi, Joycelyn S Harrison, and Terry L St Clair. Polymer-single wall carbon nanotube composites for potential spacecraft applications. In *MRS Proceedings*, volume 706, pages Z3–30. Cambridge Univ Press, 2001.

[80] J.P. Pereira and C.A. Duarte. Extraction of stress intensity factors from generalized finite element solutions. *Engineering Analysis with Boundary Elements*, 29(4):397–413, 2005.

[81] J.N. Reddy. *An Introduction to Nonlinear Finite Element Analysis*. Oxford University Press, 2004.

[82] J.N. Reddy. *An Introduction to the Finite Element Method, 3rd ed.* Engineering Series. McGraw-Hill Education, 2005.

[83] Xiang Ren and Gary D. Seidel. Computational micromechanics modeling of inherent piezoresistivity in carbon nanotube-polymer nanocomposites. *Journal of Intelligent Material Systems and Structures*, 24(12):1459–1483, January 2013.

[84] Riichiro Saito, Gene Dresselhaus, Mildred S Dresselhaus, et al. *Physical properties of carbon nanotubes*, volume 4. World Scientific, 1998.

[85] Jessica D. Sanders, John E. Dolbow, and Tod A. Laursen. On methods for stabilizing constraints over enriched interfaces in elasticity. *International Journal for Numerical Methods in Engineering*, 78(9): 1009–1036, 2009.

[86] Jessica D. Sanders, Tod A. Laursen, and Michael A. Puso. A Nitsche embedded mesh method. *Computational Mechanics*, 49(2):243–257, September 2011.

[87] L. S. Schadler, S. C. Giannaris, and P. M. Ajayan. Load transfer in carbon nanotube epoxy composites. *Applied Physics Letters*, 73(26):3842–3844, 1998.

[88] Gary D. Seidel and Dimitris C. Lagoudas. Micromechanical analysis of the effective elastic properties of carbon nanotube reinforced composites. *Mechanics of Materials*, 38(8-10):884–907, August 2006.

[89] Gary D. Seidel and Dimitris C. Lagoudas. A Micromechanics Model for the Thermal Conductivity of Nanotube-Polymer Nanocomposites. *Journal of Applied Mechanics*, 75(4):041025, 2008.

[90] Gary D. Seidel and Dimitris C. Lagoudas. A Micromechanics Model for the Electrical Conductivity of Nanotube-Polymer Nanocomposites. *Journal of Composite Materials*, 43(9):917–941, April 2009.

[91] JA Sethian. A fast marching level set method for monotonically advancing fronts. *Proceedings of the National Academy of Science*, 93(4):1591–5, February 1996.

[92] JA Sethian. Fast marching methods. *SIAM review*, 41(2):199–235, 1999.

[93] James Albert Sethian. *Level set methods and fast marching methods: evolving interfaces in computational geometry, fluid mechanics, computer vision, and materials science*, volume 3. Cambridge university press, 1999.

[94] William S Slaughter. *The Linearized Theory of Elasticity*. Birkhäuser Boston, 2002.

[95] Skylar N. Stephens. *Analytical and Computational Micromechanics Analysis of the Effects of Interphase Regions , Bundling , and Orientation on the Effective Coefficient of Thermal Expansion of Carbon Nanotube-Polymer Nanocomposites*. Master's thesis, Virginia Tech, 2013.

[96] M Stolarska, D. L. Chopp, Nicolas Moës, and Ted Belytschko. Modelling crack growth by level sets in the extended finite element method. *Int. J. Numer. Meth. Engng*, 51(January 2000):943–960, 2001.

[97] T Strouboulis, Ivo Babuška, and K Copps. The design and analysis of the generalized finite element method. *Computer Methods in Applied Mechanics and Engineering*, 181:43–69, 2000.

[98] T Strouboulis, K Copps, and Ivo Babuška. The generalized finite element method: an example of its implementation and illustration of its performance. *... Journal for Numerical Methods ...*, 47(May 1999):1401–1417, 2000.

[99] T Strouboulis, K Copps, and Ivo Babuška. The generalized finite element method. *Computer Methods in Applied Mechanics and Engineering*, 190:4081–4193, 2001.

[100] N. Sukumar, D.L. Chopp, and B. Moran. Extended finite element method and fast marching method for three-dimensional fatigue crack propagation. *Engineering Fracture Mechanics*, 70(1):29–48, 2003.

[101] N. Sukumar, Z. Y. Huang, J.-H. Prévost, and Z. Suo. Partition of unity enrichment for bimaterial interface cracks. *International Journal for Numerical Methods in Engineering*, 59(8):1075–1102, February 2004.

[102] Natarajan Sukumar, Nicolas Moës, B Moran, and Ted Belytschko. Extended finite element method for three-dimensional crack modelling. *International Journal for Numerical Methods in Engineering*, 48(November 1999):1549–1570, 2000.

[103] Natarajan Sukumar, D. L. Chopp, Nicolas Moës, and Ted Belytschko. Modeling holes and inclusions by level sets in the extended finite-element method. *Computer Methods in Applied Mechanics and Engineering*, 190(46-47):6183–6200, 2001.

[104] PK Valavala and GM Odegard. Modeling techniques for determination of mechanical properties of polymer nanocomposites. *Rev. Adv. Mater. Sci*, 9:34–44, 2005.

[105] G. Ventura, B. Moran, and T. Belytschko. Dislocations by partition of unity. *International Journal for Numerical Methods in Engineering*, 62(11):1463–1487, 2005.

[106] Giulio Ventura, Robert Gracie, and Ted Belytschko. Fast integration and weight function blending in the extended finite element method. *International Journal for Numerical Methods in Engineering*, 77 (1):1–29, 2009.

[107] G. N. Wells and L. J. Sluys. A new method for modelling cohesive cracks using finite elements. *International Journal for Numerical Methods in Engineering*, 50(12):2667–2682, 2001.

[108] Q. Z. Xiao, B. L. Karihaloo, and X. Y. Liu. Incremental-secant modulus iteration scheme and stress recovery for simulating cracking process in quasi-brittle materials using xfem. *International Journal for Numerical Methods in Engineering*, 69(12):2606–2635, 2007.

[109] P.D Zavattieri and H.D Espinosa. Grain level analysis of crack initiation and propagation in brittle materials. *Acta Materialia*, 49(20):4291–4311, 2001.

[110] QH Zeng, AB Yu, and GQ Lu. Multiscale modeling and simulation of polymer nanocomposites. *Progress in Polymer Science*, 33(2):191–269, 2008.

[111] F. Zhou and J. F. Molinari. Dynamic crack propagation with cohesive elements: a methodology to address mesh dependency. *International Journal for Numerical Methods in Engineering*, 59(1):1–24, 2004.

[112] Jiang Zhu, JongDae Kim, Haiqing Peng, John L Margrave, Valery N Khabashesku, and Enrique V Barrera. Improving the dispersion and integration of single-walled carbon nanotubes in epoxy composites through functionalization. *Nano Letters*, 3(8):1107–1113, 2003.

[113] Jiang Zhu, Haiqing Peng, Fernando Rodriguez-Macias, John L Margrave, Valery N Khabashesku, Ashraf M Imam, Karen Lozano, and Enrique V Barrera. Reinforcing epoxy polymer composites through covalent integration of functionalized nanotubes. *Advanced Functional Materials*, 14(7):643–648, 2004.

[114] Goangseup Zi and Ted Belytschko. New crack-tip elements for xfem and applications to cohesive cracks. *International Journal for Numerical Methods in Engineering*, 57(15):2221–2240, 2003.

[115] Goangseup Zi, Jeong-Hoon Song, Elisa Budyn, Sang-Ho Lee, and Ted Belytschko. A method for growing multiple cracks without remeshing and its application to fatigue crack growth. *Modelling and Simulation in Materials Science and Engineering*, 12(5):901, 2004.

Appendix A IXFEM Details for Numerical Implementation

Appendix A is intended to provide the interested reader more insight into details of numerical implementation for the IXFEM. The underlying methodologies and numerical methods utilized in extending the FEM for localized enrichment are discussed in Chapter 2 whereas presentation of the approach particularized to solid mechanics occurs in Chapter 3. It is in the later that the intrinsic enrichment concept is integrated into the conventional FEM for numerical evaluation. As this appendix only covers select details for numerical implementation it is not meant to be considered an all encompassing or self-contained explanation of the IXFEM. Thus, it is presumed the reader already has a fundamental understanding of the IXFEM and its operation based on the previously mentioned thesis chapters. Additionally it is assumed the reader has a general knowledge of the FEM and its application. As such, no details will be provided herein on developing either concept. For readers seeking more information on the FEM the introductory text of Reddy [82] is suggested. Readers looking for the introductory development work of the IXFEM are referred to the papers of Fries and Belytschko, References [38, 39].

A.1 Domain Decomposition

Global Domain

As indicated in Section 3.2.2 designation of elements to non-enriched (standard), enriched, or transition subdomains (Ω^{S}, Ω^{E}, and Ω^{T} correspondingly) is determined exclusively based on the nodal set $\mathcal{N}^{\mathrm{cut}}$ belonging to the initially determined cut element subdomain Ω^{cut}. Then following the rules of Eqn. 3.2.8 the global domain Ω is decomposed to non-enriched, enriched, and transition subdomains, the cut subdomain Ω^{cut} being redeclared to the enriched subdomain Ω^{E} in this process, refer to Figure 3.8. Together with the global domain decomposition, in which all elements are classified into specific subdomains, for the purpose of achieving and managing localized enrichment of the solution approximation, a global nodal set decomposition is performed, classifying all nodes into subsets for subsequent identification of the shape function type having influence over an element. To this end global node set $\mathcal{N}$ is separated into non-complementary nodal subsets, $\mathcal{N}^{\mathrm{FE}}$ and $\mathcal{N}^{\mathrm{MLS}}$, based on the following unions of predetermined nodal subsets,

$$\mathcal{N}^{\mathrm{FE}} = \mathcal{N}^{\mathrm{S}} \bigcup \mathcal{N}^{\mathrm{T}} \tag{A.1.1a}$$

$$\mathcal{N}^{\mathrm{MLS}} = \mathcal{N}^{\mathrm{E}} \bigcup \mathcal{N}^{\mathrm{T}} \tag{A.1.1b}$$

which can be thought to exist over corresponding subdomains.

$$\Omega^{\mathrm{FE}} = \Omega^{\mathrm{S}} \bigcup \Omega^{\mathrm{T}} \tag{A.1.2a}$$

$$\Omega^{\mathrm{MLS}} = \Omega^{\mathrm{E}} \bigcup \Omega^{\mathrm{T}} \tag{A.1.2b}$$

Resultant nodal subsets $\mathcal{N}^{\mathrm{FE}}$ and $\mathcal{N}^{\mathrm{MLS}}$ are depicted in Figure A.1, based on the same example problem used in Section 3.2.2 for presenting the subdomain classification methodology. Given the definitions of Eqn. A.1.1, the three nodal subsets defined in Eqn. 3.2.9 ($\mathcal{N}^{\mathrm{S}}$, $\mathcal{N}^{\mathrm{E}}$, and $\mathcal{N}^{\mathrm{T}}$) are not used directly for identifying what shape function type is generated at a node. Using these new nodal subsets, $\mathcal{N}^{\mathrm{FE}}$ and $\mathcal{N}^{\mathrm{MLS}}$, all nodes are considered belonging to either the alternate non-enriched (standard) space Ω^{FE}, where standard FE shape functions are used for the solution approximation, the alternate enriched space Ω^{MLS}, where enriched MLS shape functions are used in the approximation, or both for the case of nodes on transition elements. Based on these two retained nodal subsets all determinations on what type of shape function $\hat{N}_i(\boldsymbol{x})$ will be generated at node n_i are made, e.g. non-enriched N_i^{FE}, enriched N_i^{MLS}, or transition N_i^{TR}. It is important to note that a distinct subset of transition nodes $\mathcal{N}^{\mathrm{T}}$ is not needed for this. However such a subset can be easily reevaluated using Eqn. A.1.3, as it equates to the intersection of nodal subsets $\mathcal{N}^{\mathrm{FE}}$ and $\mathcal{N}^{\mathrm{MLS}}$.

$$\mathcal{N}^{\mathrm{T}} = \mathcal{N}^{\mathrm{FE}} \bigcap \mathcal{N}^{\mathrm{MLS}} \tag{A.1.3}$$

Revisiting the example problem of Section 3.2.2, reference Figure 3.7, the utility of nodal subsets $\mathcal{N}^{\mathrm{FE}}$ and $\mathcal{N}^{\mathrm{MLS}}$ for prescribing node shape function types, particularly for defining transition shape functions, is discussed. In performing the global domain decomposition (i.e. when assigning elements e_k to appropriate subdomain: Ω^{S}, Ω^{E}, or Ω^{T}) the element nodes $\mathcal{N}_k^{\mathrm{el}}$ belonging to elements in subdomains Ω^{S} or Ω^{E}, are explicitly tagged as being non-enriched or enriched and included in $\mathcal{N}^{\mathrm{FE}}$ or $\mathcal{N}^{\mathrm{MLS}}$ respectively. However, the same cannot be done for the nodes that exist in $\mathcal{N}^{\mathrm{T}}$ because they are simultaneously categorized as

either $\mathcal{N}^{\mathrm{S}}$ or $\mathcal{N}^{\mathrm{E}}$, with these identities taking precedence, and thus have already been classified accordingly. Referring back to the definition of transition subdomains, provide in Section 2.1.1: transition subdomains are composed of elements whose element nodes set $\mathcal{N}_k^{\mathrm{el}}$ have some nodes belonging to non-enriched subdomain Ω^{S} and some nodes belonging to enriched subdomain Ω^{E}, implied this same realization. Element nodes belonging to transition elements are thus not explicitly recognized as transition nodes. Whereas, non-enriched and enriched elements have all their element nodes correspondingly tagged, transition elements are recognized as having multiple distinct nodal enrichment tags at their nodes. It is then pertinent to differentiate between the element node set $\mathcal{N}_k^{\mathrm{el}}$ of transition element e_k, which includes nodes shared between $\mathcal{N}_k^{\mathrm{S}}$ and $\mathcal{N}_k^{\mathrm{T}}$ plus $\mathcal{N}_k^{\mathrm{E}}$ and $\mathcal{N}_k^{\mathrm{T}}$, and the overlap of nodal subsets $\mathcal{N}_k^{\mathrm{FE}}$ and $\mathcal{N}_k^{\mathrm{MLS}}$, which include the complete element node set $\mathcal{N}_k^{\mathrm{el}}$ of e_k regardless of its individual node identities. This is observable comparing Figure A.1a and A.1b, where the transition elements are distinguished from those in either Ω^{S} or Ω^{E}, but are shown to have all their element nodes included in both $\mathcal{N}^{\mathrm{FE}}$ and $\mathcal{N}^{\mathrm{MLS}}$.

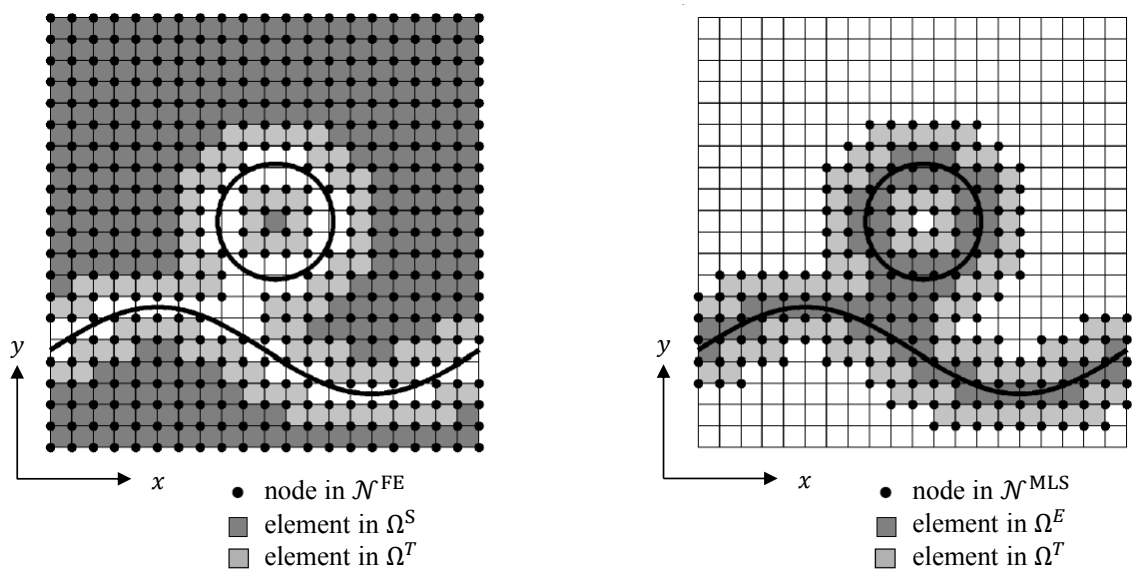

(a) Non-enriched subdomain **(b)** Enriched subdomain

Figure A.1: Example problem global domain decomposition into overlapping nodal subsets $\mathcal{N}^{\mathrm{FE}}$ and $\mathcal{N}^{\mathrm{MLS}}$ (from Ref. [37]: Reprinted with permission from John Wiley and Sons).

In observation of Figure A.1 and recalling the discussion in Section 3.2.1, pertaining to dependence on the nodes of influence $\mathcal{N}_k^{\mathrm{inf}}$ for definition of approximation functions u_x^h and u_y^h, Eqn. 3.2.2, for element e_k, the purpose of constructing nodal subsets $\mathcal{N}_k^{\mathrm{FE}}$ and $\mathcal{N}_k^{\mathrm{MLS}}$ is presented. For an element e_k in non-enriched

subdomain Ω^{S} or enriched subdomain Ω^{E}, its list of influencing nodes $\mathcal{N}_k^{\mathrm{inf}}$ will reside exclusively in nodal subset $\mathcal{N}^{\mathrm{FE}}$ or $\mathcal{N}^{\mathrm{MLS}}$ respectively, facilitating their identification. Combination of the transition subdomain nodal subset $\mathcal{N}^{\mathrm{T}}$ with $\mathcal{N}^{\mathrm{S}}$ and $\mathcal{N}^{\mathrm{E}}$ is more essential in forming $\mathcal{N}^{\mathrm{MLS}}$, as the increased number of influencing nodes participating in the approximation function definition, for enriched elements, come from beyond just the enriched element nodal subset $\mathcal{N}^{\mathrm{E}}$. Explanation of this expanded set of influencing nodes is covered in detail in Appendix Section A.4. For transition elements, recognized as those with non-uniform node tags, two listings of nodes of influence are determined, one from $\mathcal{N}^{\mathrm{FE}}$, denoted as $\mathcal{N}_k^{\mathrm{inf,S}}$, the another from $\mathcal{N}^{\mathrm{MLS}}$, denoted as $\mathcal{N}_k^{\mathrm{inf,E}}$. The element node set $\mathcal{N}_k^{\mathrm{el}}$ being coincident to both sets, such that $\mathcal{N}_k^{\mathrm{el}} = \mathcal{N}_k^{\mathrm{inf,S}} \bigcap \mathcal{N}_k^{\mathrm{inf,E}}$. Knowing transition shape functions $N_i^{\mathrm{TR}}(\boldsymbol{x})$, Eqn. 2.1.11, are generated from a weighted superposition of standard FE and enriched MLS shape functions, from the discussion in Section 2.1.2, it is to be expected that their construction will be dependent on nodes which simultaneously support standard FE and enriched MLS shape functions. The distinction of nodes in $\mathcal{N}_k^{\mathrm{el}}$, i.e. belonging to either $\mathcal{N}^{\mathrm{S}}$ or $\mathcal{N}^{\mathrm{E}}$, is only used to properly define corresponding ramp function $R^{\mathrm{S}}(\boldsymbol{x})$ or $R^{\mathrm{E}}(\boldsymbol{x})$ respectively, refer to Eqn. 2.1.9. Applying all this information the transition shape functions are generated, coupling non-enriched subdomains to enriched subdomains and ensuring continuity of the global solution approximation.

Element Domain

Revisiting the element decomposition strategy, presented in Section 3.2.3, an equation for evaluation of the temporary supplementing node coordinates is given. As discussed for an enriched element its domain Ω_k^{el} is decomposed into subelement domains $\Omega_{k,s}^{\mathrm{se}}$, for the purpose of integrating and differentiating the enriched MLS shape functions in order to build the FE model and post-process the primary variable field respectively. The subelement nodes are thus computed only when needed and retained solely for the purpose of defining the subelement connectivity needed to complete these calculations. Knowing the discontinuity interface Γ_{disc} is represented by the approximate zero-level LSC, $\Gamma_{\mathrm{disc}}^h = \boldsymbol{x} : \psi^h(\boldsymbol{x}) = 0$, of the approximate LSF of Eqn. 2.3.3, interpolated from nodal values ψ_i^n, the discontinuity intersection coordinate $\boldsymbol{x}_s^\Gamma$ along element edge $\mathrm{eg}_s, s \in \{1, \ldots, n^{\mathrm{eg}}\}$, where n^{eg} is the number of element edges, is readily calculated based on a straight line fit between the LSF nodal values of the two element nodes defining edge eg_s, denoted by $\psi_s^h(\boldsymbol{x})$. Using known element node coordinates $\boldsymbol{x}_i^n$ and LSF node values ψ_i^n the discontinuity intersection coordinate is determined as the location on an element edge where the LSF line interpolant has zero value, $\boldsymbol{x}_s^\Gamma = \{\boldsymbol{x} \in \Omega : \psi_s^h(\boldsymbol{x}) = 0\}$. Equation A.1.4 gives an explicit expression for evaluating this coordinate location, where the relevant geometric definitions are provided by Figure A.2.

$$\boldsymbol{x}_s^{\Gamma} = \boldsymbol{x}_1^{\mathrm{eg}_s} + \eta^{\mathrm{eg}_s}(\boldsymbol{x}_2^{\mathrm{eg}_s} - \boldsymbol{x}_1^{\mathrm{eg}_s}) \tag{A.1.4a}$$

$$\eta^{\mathrm{eg}_s} = -\frac{\psi_1^{\mathrm{eg}_s}}{\psi_2^{\mathrm{eg}_s} - \psi_1^{\mathrm{eg}_s}} \tag{A.1.4b}$$

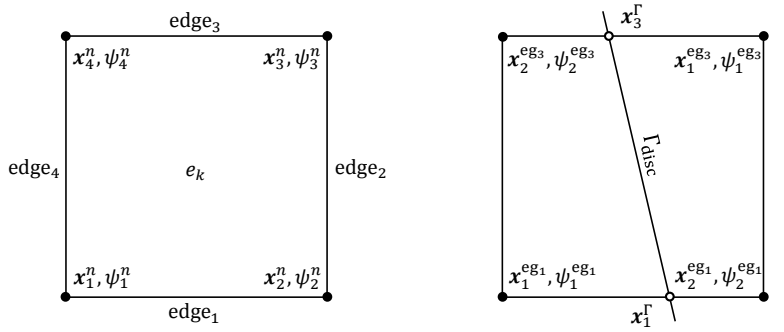

(a) Master element definitions **(b)** Example cut element

Figure A.2: Respective definition of element node coordinates and nodal LSF value.

As mentioned in Section 3.2.3 the element partitioning scheme is based on the path discontinuity interface Γ_{disc} takes through the element domain Ω_k^{el}. Three subelement divisions were identified to occur: side-side split, corner split, and crack tip split leading to element decompositions of two, five, and six subelements respectively. Figure A.3 portrays the three scenarios illustrating where the extra subelement nodes would be found, given the discontinuity interface path taken through the element domain.

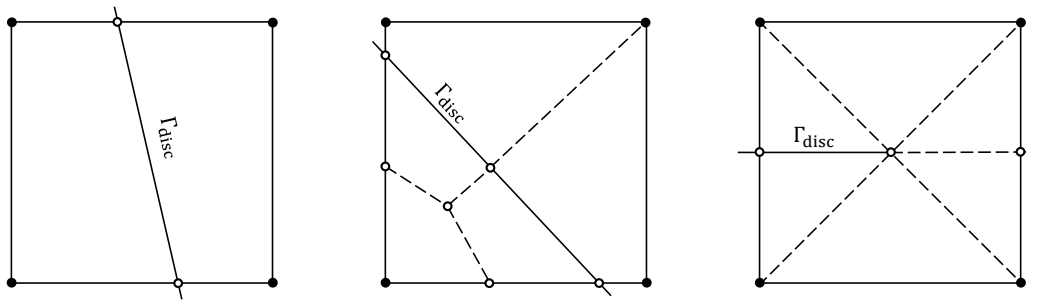

(a) Side-side split, $n^{\mathrm{se}} = 2$ **(b)** Corner split, $n^{\mathrm{se}} = 5$ **(c)** Crack tip split, $n^{\mathrm{se}} = 6$

Initial element nodes: ● Added subelemnt nodes: ○

Figure A.3: Sub-discretization of enriched elements depending on path of discontinuity interface Γ_{disc} running through element domain. Solid lines are element and discontinuity boundaries and dashed lines are added subelement boundaries, as needed.

In the case of a discontinuity interface cutting through opposing horizontal or vertical element sides a

decomposition of the form shown in Figure A.3a results. Given that the division results in two quadrilateral subelements no further decomposition processing is needed. The two extra subelement nodes are taken directly as the discontinuity interface intersection points on the element boundary, splitting its domain, and are calculated based on the previously described methodology of Eqn. A.1.4. For the case of a discontinuity interface cutting through an element corner as in Figure A.3b the element is split into a triangular and pentagonal region, which are further partitioned into 3 and 2 quadrilateral subelements respectively. The two discontinuity interface points are evaluated as in the previous case, whereas the four additional coordinates are simply determined as the bisection points of the triangular sides and its centroid. In the case of the crack tip including element of Figure A.3c the element is partitioned into six triangular subelements. Their boundaries determined by partitioning the element to the four node corners from the crack tip location, and along the crack discontinuity plus its extension through the element. The crack intersection point is computed using the method already mentioned and recalling that the crack LSF $\psi^{\text{ck}}(\boldsymbol{x})$ extends through the entire domain Ω the crack extension intersection point is found equivalently. The crack tip location $\boldsymbol{x}_t$ is known from the LSF definition, refer to Eqn 3.1.18.

A.2 Shape Functions and Derivatives

As presented in Section 3.2.1, the shape (interpolation) functions $\hat{N}_i(\boldsymbol{x})$ compose the displacement component approximation functions u_x^h and u_y^h, Eqn. 3.2.2, used in deriving the FE model, Eqn. 3.2.4. Based on the global domain decomposition strategy, of Section 2.1.1, different shape functions are used in building PUs over distinct subdomains Ω_m. Subdomains free of discontinuities are modeled with standard FE shape functions N_i^{FE} while those containing the discontinuity interface Γ_{disc} are modeled using the enriched MLS shape functions N_i^{MLS}. Transition subdomains, linking these two regions, use coupled shape functions N_i^{TR} to ensure continuity of the approximation. Their functional expressions are summarized here in conjunction with their derivatives for use in evaluating the linear system of equations, i.e. the FE model Eqn. 3.2.4, presented in Section 3.2.1.

Standard FE shape functions are used in non-enriched (standard) subdomains $\Omega'_m = \Omega^S$. Expressions for various FE shape functions based on spatial dimension, functional order, and element shape can be found in Ref. [82]. The standard FE shape functions of interest in this work are the two-dimensional bilinear interpolation functions defined for the master quadrilateral element, shown in Figure A.4, as

$$N_i^{\mathrm{FE}}(\boldsymbol{x}) = \frac{1}{4}\,(1 + x\; x_i)\,(1 + y\; y_i) \tag{A.2.1}$$

where (x_i, y_i) denotes the ith node coordinates. The standard FE shape function derivatives of Eqn. A.2.1 are defined by

$$\frac{\partial N_i^{\mathrm{FE}}(\boldsymbol{x})}{\partial a} = \frac{1}{4}\frac{\partial}{\partial a}\left((1 + x\; x_i)\,(1 + y\; y_i)\right) \tag{A.2.2}$$

taking $a \in \{x, y\}$ to denote derivatives taken with respect to either global variable direction x (horizontal) or y (vertical).

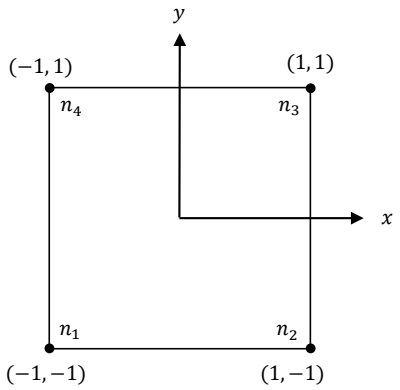

Figure A.4: Master quadrilateral element node numbers.

Enriched MLS shape functions are used in enriched subdomains $\Omega'_m = \Omega^E$. Recalling Eqn. 2.2.11 the MLS shape function at node n_i is expressed by

$$N_i^{\mathrm{MLS}}(\boldsymbol{x}) = \boldsymbol{p}^{\mathrm{T}}(\boldsymbol{x})[\mathbf{M}(\boldsymbol{x})]^{-1} w_i(\boldsymbol{x})\boldsymbol{p}(\boldsymbol{x}_i) \tag{A.2.3}$$

with

$$\mathbf{M}(\boldsymbol{x}) = \sum_{k=1}^{r} w_k(\boldsymbol{x})\boldsymbol{p}(\boldsymbol{x}_k)\boldsymbol{p}^{\mathrm{T}}(\boldsymbol{x}_k) \tag{A.2.4}$$

where $\boldsymbol{p}(\boldsymbol{x})$ is the intrinsic basis defining the approximation space, $\mathbf{M}(\boldsymbol{x})$ is the moment matrix, and $w_i(\boldsymbol{x})$ is

a weight function with compact support. The computational cost associated with evaluation of the enriched MLS shape function being directly tied to dimension k of the enriched intrinsic basis $\boldsymbol{p}^{\text{enr}}(\boldsymbol{x})$, as it dictates the size of the moment matrix based on Eqn. A.2.4. Summation for the moment matrix occurs over the r influencing nodes $\mathcal{N}_k^{\text{inf}}$ whose enriched MLS shape function have non-zero value over element e_k, containing $\boldsymbol{x}$ and a portion of a discontinuity interface Γ_{disc} ($r = 16$ for the case of a structured rectangular mesh, see Section 3.2.1). Given the invertability requirements of the moment matrix, recall the point of discussion in Section 2.2.2 and Eqn. 2.2.13, specialized weight functions $w_i^{\text{S}}(\boldsymbol{x})$, defined in Eqn. A.2.5, were designed by Fries and Belytschko [38] to ensure stability of the computation, refer to Section 2.2.3 for details.

$$w_p^{\text{S}}(\boldsymbol{x}) = 2 \cdot N_p^{\text{FE}}(\boldsymbol{x}) + \sum_{n_i \in \mathcal{N}_m^p} N_i^{\text{FE}}(\boldsymbol{x}) \tag{A.2.5}$$

These mesh-based weight functions have extended local supports including elements contiguous to node n_p, centering the weight function, and the next neighboring nodes providing sufficient overlap for guaranteed invertability, even for the truncated supports used in the enriched MLS procedure for strong discontinuities discussed in Section 3.1.2. With $\boldsymbol{p}(\boldsymbol{x})$, $\mathbf{M}(\boldsymbol{x})$, and $w_i(\boldsymbol{x})$ being functions of $\boldsymbol{x}$ after applying a triple product rule the Enriched MLS shape function derivative of Eqn. A.2.3 is defined as

$$\frac{\partial N_i^{\text{MLS}}(\boldsymbol{x})}{\partial a} = \left[\frac{\partial \boldsymbol{p}^{\text{T}}(\boldsymbol{x})}{\partial a} [\mathbf{M}(\boldsymbol{x})]^{-1} w_i(\boldsymbol{x}) + \boldsymbol{p}^{\text{T}}(\boldsymbol{x}) \frac{\partial [\mathbf{M}(\boldsymbol{x})]^{-1}}{\partial a} w_i(\boldsymbol{x}) + \boldsymbol{p}^{\text{T}}(\boldsymbol{x}) [\mathbf{M}(\boldsymbol{x})]^{-1} \frac{\partial w_i(\boldsymbol{x})}{\partial a} \right] \boldsymbol{p}(\boldsymbol{x}_i) \tag{A.2.6}$$

where the intrinsic basis derivatives are as defined in Section A.3 for weak, strong, and discontinuous tip discontinuities. Differentiation of the moment matrix inverse is realized using the identity property of the inverse matrix, i.e. $\mathbf{M}(\boldsymbol{x})[\mathbf{M}(\boldsymbol{x})]^{-1} = \boldsymbol{I}$. Applying the product rule the result obtained is

$$\frac{\partial [\mathbf{M}(\boldsymbol{x})]^{-1}}{\partial a} = [\mathbf{M}(\boldsymbol{x})]^{-1} \left[-\frac{\partial \mathbf{M}(\boldsymbol{x})}{\partial a} [\mathbf{M}(\boldsymbol{x})]^{-1} \right] \tag{A.2.7}$$

where the moment matrix derivative is simply the derivative of the summation terms in Eqn. A.2.4 given as

$$\frac{\partial \mathbf{M}(\boldsymbol{x})}{\partial a} = \sum_{k=1}^{r} \frac{\partial w_k(\boldsymbol{x})}{\partial a} \boldsymbol{p}(\boldsymbol{x}_k) \boldsymbol{p}^{\text{T}}(\boldsymbol{x}_k) \tag{A.2.8}$$

and the specialized weight function derivative is similarly obtained.

$$\frac{\partial w_p^{\mathrm{S}}(\boldsymbol{x})}{\partial a} = 2 \cdot \frac{\partial N_p^{\mathrm{FE}}(\boldsymbol{x})}{\partial a} + \sum_{n_i \in \mathcal{N}_m^p} \frac{\partial N_i^{\mathrm{FE}}(\boldsymbol{x})}{\partial a} \tag{A.2.9}$$

Coupled Transition shape functions are used in transition subdomains $\Omega_m^* = \Omega^T$. Recalling Eqn. 2.1.11 the transition shape function at node n_i is expressed by

$$N_i^{\mathrm{TR}}(\boldsymbol{x}) = \sum_{m \in J} R_m(\boldsymbol{x}) \cdot \hat{N}_i^m(\boldsymbol{x}), \quad J = \{m = 1, \ldots, n^{\Omega} : i \in \mathcal{N}_m^*\} \tag{A.2.10}$$

where $\hat{N}_i^m(\boldsymbol{x})$ are either standard or enriched MLS shape functions and $R_m(\boldsymbol{x})$ are the ramp functions discussed in Section 2.1.2 for coupling the coexisting shape functions at node n_i through a linear superposition. The ramp function for subdomain Ω_m determined as the summation of standard FE shape functions for corresponding nodes $\mathcal{N}'_m$.

$$R_m(\boldsymbol{x}) = \sum_{n_i \in \mathcal{N}'_m} N_i^{\mathrm{FE}}(\boldsymbol{x}) \quad \forall \boldsymbol{x} \in \Omega_l \tag{A.2.11}$$

With $R_m(\boldsymbol{x})$ and $\hat{N}_i^m(\boldsymbol{x})$ being functions of $\boldsymbol{x}$ after applying the product rule the transition shape function derivative of Eqn. A.2.10 is defined as

$$\frac{\partial N_i^{\mathrm{TR}}(\boldsymbol{x})}{\partial a} = \sum_{m \in J} \left[\frac{\partial R_m(\boldsymbol{x})}{\partial a} \cdot \hat{N}_i^m(\boldsymbol{x}) + R_m(\boldsymbol{x}) \cdot \frac{\partial \hat{N}_i^m(\boldsymbol{x})}{\partial a} \right] \tag{A.2.12}$$

where the shape function derivatives are calculated using either Eqn. A.2.2 or A.2.6 and the ramp function derivative is simply determined as the summation of standard FE shape function derivatives.

$$\frac{\partial R_m(\boldsymbol{x})}{\partial a} = \sum_{n_i \in \mathcal{N}'_m} \frac{\partial N_i^{\mathrm{FE}}(\boldsymbol{x})}{\partial a} \quad \forall \boldsymbol{x} \in \Omega_l \tag{A.2.13}$$

A.3 Enriched Intrinsic Bases

As discussed in Section 2.2.2 the intrinsic basis $\boldsymbol{p}(\boldsymbol{x})$ contains the functional terms making up the approximation space on which the MLS interpolant is built. Enriched MLS shape functions $N_i^{\mathrm{MLS}}(\boldsymbol{x})$ are thus the result of utilizing enriched intrinsic bases $\boldsymbol{p}^{\mathrm{enr}}(\boldsymbol{x})$ in their construction, where the supplementary components

$\tilde{\boldsymbol{p}}^{\text{enr}}(\boldsymbol{x})$ have been specifically chosen to accommodate certain discontinuity types. Vector definitions of the enriched bases used in this work were first presented in Section 3.1.2 for weak, strong, and discontinuous tip discontinuities. Their functional expressions are repeated here in conjunction with their directional derivatives, particularized to constrained geometry in the x-y plane, for use in evaluating the MLS shape functions and their derivatives, as presented in Appendix Section A.2.

Weak Discontinuities are descriptive of interfaces across which the primary variable is continuous but its derivatives may not be. Recalling Eqn. 3.1.9 the enriched intrinsic basis vector used in the MLS procedure for such interfaces is

$$\boldsymbol{p}_{\text{w}}^{\text{enr}}(\boldsymbol{x}) = \{1, x, y, |\psi(\boldsymbol{x})|\}^{\text{T}} \tag{A.3.1}$$

where $|\cdot|$ denotes the absolute value and $\psi(\boldsymbol{x})$ is the LSF, approximated using the approached defined in Section 2.3.2, i.e. a FE approximation of the form

$$\psi(\boldsymbol{x}) \approx \psi^h(\boldsymbol{x}) = \sum_i M_i(\boldsymbol{x})\psi_i^n \tag{A.3.2}$$

where $M_i(\boldsymbol{x})$ are interpolation functions and ψ_i^n are discrete calculated nodal values of the LSF $\psi_i^n = \psi(\boldsymbol{x}_i)$. The enriched basis vector derivatives of Eqn. A.3.1 are then defined as

$$\frac{\partial \boldsymbol{p}_{\text{w}}^{\text{enr}}(\boldsymbol{x})}{\partial x} = \left\{0, 1, 0, \text{sign}(\psi(\boldsymbol{x}))\frac{\partial \psi(\boldsymbol{x})}{\partial x}\right\}^{\text{T}} \tag{A.3.3a}$$

$$\frac{\partial \boldsymbol{p}_{\text{w}}^{\text{enr}}(\boldsymbol{x})}{\partial y} = \left\{0, 0, 1, \text{sign}(\psi(\boldsymbol{x}))\frac{\partial \psi(\boldsymbol{x})}{\partial y}\right\}^{\text{T}} \tag{A.3.3b}$$

where the LSF derivative is approximated in the same manner, again using a FE approximation, following inline with the principle used in the FEM, i.e. $u'(\boldsymbol{x}) \approx u^{h'}(\boldsymbol{x}) = \{\boldsymbol{N}'(\boldsymbol{x})\}^{\text{T}}\boldsymbol{u}$

$$\frac{\partial \psi(\boldsymbol{x})}{\partial a} \approx \frac{\partial \psi^h(\boldsymbol{x})}{\partial a} = \sum_i \frac{\partial M_i(\boldsymbol{x})}{\partial a}\psi_i^n \tag{A.3.4}$$

Strong Discontinuities are descriptive of interfaces across which the primary variable is discontinuous. Recalling Eqn. 3.1.10 and 3.1.11 two intrinsic basis vectors can be used in the MLS procedure for such

interfaces. As the truncated basis can be considered a special case of the full-form basis only its functional form and derivatives are reviewed here, though expressions for the truncated basis can be easily obtained by simply disregarding the extra vector terms supplementing the initial linear polynomial basis $\{1, x, y\}$ in the following expressions. The full-form enriched intrinsic basis is defined as

$$\boldsymbol{p}_{\mathrm{s,f}}^{\mathrm{enr}}(\boldsymbol{x}) = \{1, x, y, \mathrm{sign}(\psi(\boldsymbol{x})), |\psi(\boldsymbol{x})|\}^{\mathrm{T}} \tag{A.3.5}$$

where $\mathrm{sign}(\cdot)$ and $|\cdot|$ denote the sign and absolute value function respectively. Evaluation of the LSF $\psi(\boldsymbol{x})$ for these enrichment terms is carried out in the same manner as for the weak discontinuity, using Eqn. A.3.2. The enriched basis vector derivatives of Eqn. A.3.5 are then defined as

$$\frac{\partial \boldsymbol{p}_{\mathrm{s,f}}^{\mathrm{enr}}(\boldsymbol{x})}{\partial x} = \left\{0, 1, 0, 0, \mathrm{sign}(\psi(\boldsymbol{x}))\frac{\partial \psi(\boldsymbol{x})}{\partial x}\right\}^{\mathrm{T}} \tag{A.3.6a}$$

$$\frac{\partial \boldsymbol{p}_{\mathrm{s,f}}^{\mathrm{enr}}(\boldsymbol{x})}{\partial y} = \left\{0, 0, 1, 0, \mathrm{sign}(\psi(\boldsymbol{x}))\frac{\partial \psi(\boldsymbol{x})}{\partial y}\right\}^{\mathrm{T}} \tag{A.3.6b}$$

If considering the truncated basis, it is important to recall the truncated specialized weight function $w_i^{\mathrm{S}*}(\boldsymbol{x})$, as defined in Eqn. A.3.7, is used to realize the discontinuity,

$$w_i^{\mathrm{S}*} = \begin{cases} w_i^{\mathrm{S}}(\boldsymbol{x}) & \text{for } \boldsymbol{x} \text{ visible from } \boldsymbol{x}_n \\ 0 & \text{instead} \end{cases} \tag{A.3.7}$$

where $w_i^{\mathrm{S}}(\boldsymbol{x})$ is the specialized weight function, refer to Eqn. A.2.5, and point $\boldsymbol{x}$ is considered visible from $\boldsymbol{x}_i$ if $\psi(\boldsymbol{x}) \cdot \psi(\boldsymbol{x}_i) > 0$.

Recalling the observation made in Section 4.1, that the truncated weight function inherently acts to stabilize the fictitious displacements of void domains represented as strong discontinuities, the following discussion expounds upon why it occurs. As will be explained, when using the truncated specialized weight function, primary degrees of freedom, i.e. global nodal displacements u_i^x and u_i^y, corresponding to nodes n_i, of global nodal set $\mathcal{N}$, internal to strong discontinuities are not associated through any local approximation function to the global approximate solution determined, as all entries in the global stiffness matrix corespondent to such nodes will have value zero. In essence this allows the displacement value at these nodes to take

any arbitrary value while still satisfying the GDE, Eqn. 3.1.1. To generalize this discussion to both closed discontinuity types, e.g. loops and continuous curves refer to Figure 3.1a, "internal" is taken to imply $\psi < 0$, refer to Section 3.1.3 for definition of LSFs expressions $\psi(\boldsymbol{x})$ and the conventions adhered to for defining positive and negative regions for specific LSFs. Recalling the discussion in Section 3.1.2, the truncated weight functions use a visibility criteria, Eqn. 3.1.13, to cutoff the compact support of the special weight function $w_i^{\mathrm{S}}(\boldsymbol{x})$ along strong discontinuity interfaces [38], see Figure 3.3 for a demonstration. Thus for an enriched element e_k, having been cut by a strong discontinuity LSC Γ_{disc}, its influencing nodes list $\mathcal{N}_k^{\mathrm{inf}}$ will contain r nodes n_j existing on either side of the discontinuity. However, when it comes time to build the local approximation function $u^h(\boldsymbol{x})$, Eqns 3.2.2, over element e_k only the enriched shape functions $N_j^{\mathrm{MLS}}(\boldsymbol{x})$, centered at nodes n_j, which reside on the same side of the discontinuity interface Γ_{disc} as point $\boldsymbol{x}$ contribute influence. Shape functions originating from nodes on the opposing side will be truncated at the discontinuity interface, and thus have constant value zero on the side of $\boldsymbol{x}$. To identify this effect on the outcome first consider the portion, subelement(s), of enriched element e_k internal to a strong discontinuity domain, the local approximation function would have influence only from those nodes in $\mathcal{N}_k^{\mathrm{inf}}$ that reside inside of the discontinuity LSC Γ_{disc}. This portion of the influencing nodes are then initially associated to their corresponding global nodal displacements u_j^x and u_j^y, by definition through the approximation function. However, when completing the numerical integration to populate element stiffness matrix $\mathbf{K}^{\mathrm{el}}$, leading to assembly of the global stiffness matrix and the FE model, multiplication with the elastic material constants C_{ij} occurs, for a strong discontinuity representative of void space these are evaluated to zero, based on definition of the material properties to zero, thus the node to primary variable association is negated. Now considering the portion of element e_k external to a strong discontinuity ($\psi > 0$), the local approximation function is defined only from the nodes in $\mathcal{N}_k^{\mathrm{inf}}$ that reside outside of the discontinuity LSC, hence an association is not even initially made between nodes internal to the discontinuity and their corresponding global nodal displacements. Further considering transition and non-enriched elements that reside completely within the strong discontinuity domain, initial node to displacement associations will be made from definition of the local approximation function, but they will likewise be negated during the numerical integration, as observed for internal subelements of enriched elements. From this rationalization it becomes evident that all primary variable quantities corresponding to nodes n_i, of $\mathcal{N}$, internal to a closed strong discontinuities have no involvement in defining any local approximations. Therefore, they also have no influence on the global approximation determined by the IXFEM, existing over the physical domain, e.g. domain Ω_1 for the validation problem considered in Section 4.1 (Ω_2 being considered void domain). As a result the unassociated

global nodal displacements, u_i^x and u_i^y, are unrestrained in the global system of equations. Evaluated displacements of zero value for nodes n_i, within strong discontinuities, thus result as an inherent outcome of utilizing truncated specialized weight functions in the enriched MLS shape function computations for strong discontinuities, as no specific code logic is implemented to do so. This was discussed and shown for the validation problem of Section 4.1, where the truncated basis $\boldsymbol{p}_{\mathrm{s,t}}^{\mathrm{enr}}(\boldsymbol{x})$ and the full-form basis with truncation $\boldsymbol{p}_{\mathrm{s,ft}}^{\mathrm{enr}}(\boldsymbol{x})$ were applied in analysis along with the full-form basis $\boldsymbol{p}_{\mathrm{s,f}}^{\mathrm{enr}}(\boldsymbol{x})$ for their comparison in a error convergence study.

Discontinuous Tips are descriptive of interface origin or termination points internal to the global domain. Used exclusively in this work to define the singular tip of a crack front. Recalling Eqn. 3.1.14 the enriched basis vector used in the MLS procedure for such interfaces is

$$\boldsymbol{p}_{\mathrm{t}}^{\mathrm{enr}}(\boldsymbol{x}) = \left\{1, x, y, \sqrt{r}\sin\frac{\theta}{2}, \sqrt{r}\sin\frac{\theta}{2}\sin\theta, \sqrt{r}\cos\frac{\theta}{2}, \sqrt{r}\cos\frac{\theta}{2}\sin\theta\right\}^{\mathrm{T}} \tag{A.3.8}$$

where r and θ are the distance and angle of the point $\boldsymbol{x}$ respectively, determined in the polar coordinate system as shown in Figure 3.4 and calculated using the following expressions

$$\sqrt{r} = ((x - x_t)^2 + (y - y_t)^2)^{1/4} \tag{A.3.9}$$

$$\theta = \arctan(y - y_t, x - x_t) \tag{A.3.10}$$

where (x_t, y_t) defines the crack tip location. Figure A.5 displays the four trigonometric enrichment functions $f_{t_k}^{\mathrm{enr}},\ k = \{1, \ldots, 4\}$, in Eqn. A.3.8, where the discontinuity is evident in $f_{t_1}^{\mathrm{enr}}$. Recognizing r and θ as functions of x and y and applying the chain rule the enriched basis vector derivatives of Eqn. A.3.8 are then defined as

$$\frac{\partial \boldsymbol{p}_{\mathrm{d}}^{\mathrm{enr}}(\boldsymbol{x})}{\partial x} = \Bigg\{0, 1, 0, \sqrt{r_x}\sin\frac{\theta}{2} + \frac{1}{2}\sqrt{r}\cos\frac{\theta}{2}\,\theta_x, \sqrt{r_x}\sin\frac{\theta}{2}\sin\theta + \frac{1}{2}\sqrt{r}\cos\frac{\theta}{2}\sin\theta\,\theta_x + \sqrt{x}\sin\frac{\theta}{2}\cos\theta\,\theta_x,$$
$$\sqrt{r_x}\cos\frac{\theta}{2} - \frac{1}{2}\sqrt{r}\sin\frac{\theta}{2}\theta_x, \sqrt{r_x}\cos\frac{\theta}{2}\sin\theta - \frac{1}{2}\sqrt{r}\sin\frac{\theta}{2}\sin\theta\,\theta_x + \sqrt{x}\cos\frac{\theta}{2}\cos\theta\,\theta_x\Bigg\}^{\mathrm{T}} \tag{A.3.11a}$$

$$\frac{\partial \boldsymbol{p}_{\mathrm{t}}^{\mathrm{enr}}(\boldsymbol{x})}{\partial y} = \Bigg\{0, 0, 1, \sqrt{r_y}\sin\frac{\theta}{2} + \frac{1}{2}\sqrt{r}\cos\frac{\theta}{2}\,\theta_y, \sqrt{r_y}\sin\frac{\theta}{2}\sin\theta + \frac{1}{2}\sqrt{r}\cos\frac{\theta}{2}\sin\theta\,\theta_y + \sqrt{x}\sin\frac{\theta}{2}\cos\theta\,\theta_y,$$
$$\sqrt{r_y}\cos\frac{\theta}{2} - \frac{1}{2}\sqrt{r}\sin\frac{\theta}{2}\theta_y, \sqrt{r_y}\cos\frac{\theta}{2}\sin\theta - \frac{1}{2}\sqrt{r}\sin\frac{\theta}{2}\sin\theta\,\theta_y + \sqrt{x}\cos\frac{\theta}{2}\cos\theta\,\theta_y\Bigg\}^{\mathrm{T}} \tag{A.3.11b}$$

where $\sqrt{r_x}$, $\sqrt{r_y}$, θ_x, and θ_y are derivative quantities determined from Eqns. A.3.9 and A.3.10 as listed below.

$$\sqrt{r_x} = \frac{\partial\sqrt{r}}{\partial x} = \frac{x - x_t}{2((x-x_t)^2 + (y-y_t)^2)^{3/4}} \tag{A.3.12a}$$

$$\sqrt{r_y} = \frac{\partial\sqrt{r}}{\partial y} = \frac{y - y_t}{2((x-x_t)^2 + (y-y_t)^2)^{3/4}} \tag{A.3.12b}$$

$$\theta_x = \frac{\partial\theta}{\partial x} = \frac{y_t - y}{(x-x_t)^2 + (y-y_t)^2} \tag{A.3.12c}$$

$$\theta_y = \frac{\partial\theta}{\partial y} = \frac{x - x_t}{(x-x_t)^2 + (y-y_t)^2} \tag{A.3.12d}$$

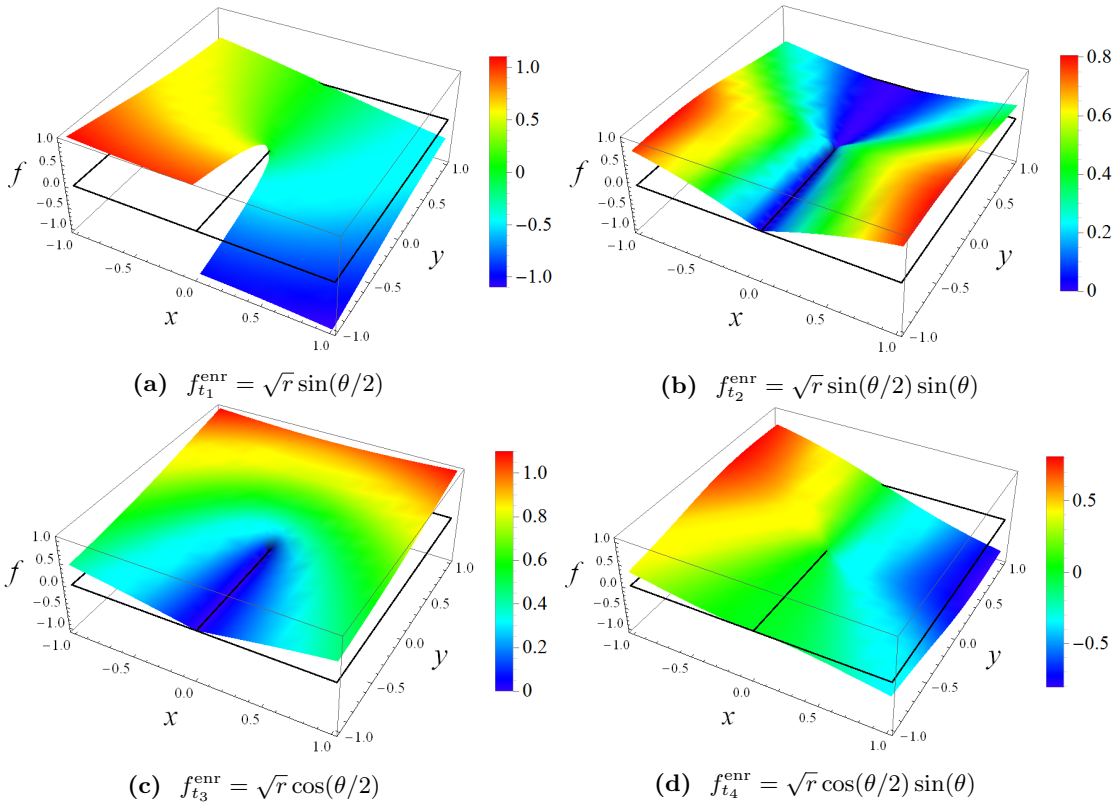

(a) $f_{t_1}^{\text{enr}} = \sqrt{r}\sin(\theta/2)$ **(b)** $f_{t_2}^{\text{enr}} = \sqrt{r}\sin(\theta/2)\sin(\theta)$

(c) $f_{t_3}^{\text{enr}} = \sqrt{r}\cos(\theta/2)$ **(d)** $f_{t_4}^{\text{enr}} = \sqrt{r}\cos(\theta/2)\sin(\theta)$

Figure A.5: Enrichment functions $f_{t_k}^{\text{enr}}$, $k = \{1, \ldots, 4\}$ for a crack tip in linear elastic fracture mechanics.

A.4 Finite Element Model

Approximation Function

Revisiting the discussion point, in Section 3.2.1, pertaining to the variability in number of additional influencing nodes used to define the approximation function over an enriched element e_k, the extended compact support of special weight function $w_i^{\text{S}}(\boldsymbol{x})$ for realizing these nodes is discussed. Recall the displacement approximation functions $u_a^h(\boldsymbol{x})$, Eqn. 3.2.2, are expressed as product summations of shape functions $\hat{N}_i(\boldsymbol{x})$ and nodal displacement values u_i^a, as restated by Eqn. A.4.1.

$$u_a(\boldsymbol{x}) \approx u_a^h(\boldsymbol{x}) = \sum_{i=1}^{r} N_i(\boldsymbol{x}) u_i^a \tag{A.4.1}$$

The number of shape functions, i.e. the number of influencing nodes included in $\mathcal{N}_k^{\text{inf}}$, utilized to define the local approximate solution is indicated by r. Nodes n_i populating $\mathcal{N}_k^{\text{inf}}$ being determined based on whether

their corresponding shape functions, or equivalently their weight functions, have non-zero value over element domain Ω_k^{el}. Alternatively, element e_k is under the influence of node n_i if it is contained within the weight function compact support $\tilde{\Omega}_i$, as weight and shape functions are non-zero over their support domain. To examine how the compact support of weight functions disclose information identifying nodes as being of influence (or not) for an element, example cases are presented. Before previewing the outcome surrounding an enriched element, the principle is applied to a non-enriched element to showcase their single dependency on element order from using standard FE shape functions as weight functions.

For a two-dimensional linear quadrilateral element the minimum number of influencing nodes permissible is $r = 4$ and corresponds to the case of a non-enriched element as shown in Figure A.6. Consider for explanation the non-enriched element, identified as e_k^{ner}, in the structured square element mesh of Figure A.6a. The local support $\tilde{\Omega}_i$ of weight function $w_i(\boldsymbol{x})$ existing at the element's lower left node is indicated by the dark grey shading. As demonstrated in the figure the weight function, defined as a bilinear FE shape function $w_i = N_i^{\text{FE}}$, spans the four elements contiguous to node n_i. Thus based on the coverage of $w_i(\boldsymbol{x})$, node n_i would be identified as an influencing node for the four elements within its local support boundary, i.e. the four shaded elements in Figure A.6a. To visualize the compact support overlap defining the r influencing nodes for element e_k^{ner} first envision a second weight function $w_j(\boldsymbol{x})$ centered at the element's top right node. Its support likewise spans four adjacent elements to node n_j, as indicated by the dashed lines. Further visualizing the compact support of the remaining two element nodes and the surrounding nodes it becomes apparent that only the four distinct nodes defining the geometry of element e_k^{ner} contribute to $\mathcal{N}_k^{\text{inf}}$. Thus for a non-enriched element $\mathcal{N}_k^{\text{inf}} = \mathcal{N}_k^{\text{el}}$, recalling $\mathcal{N}_k^{\text{el}}$ as denoting the element nodes of element e_k, this end result is depicted by Figure A.6b.

(a) Compact support overlap of $w_i(\boldsymbol{x})$ **(b)** Non-enriched element influencing nodes

Figure A.6: Demonstration, on a structured rectangular mesh, of the compact support $\tilde{\Omega}_i$ overlap of standard weight functions $w_i(\boldsymbol{x})$ leading to influence of 4 standard FE shape functions N_i^{FE} on an non-enriched element e_k^{ner} (dark grey filling in (b)).

A similar analysis, now conducted, for an enriched element reveals an increased number of nodes having influence over the element domain. This leads directly to the higher number of terms used in the approximation function for these elements relative to those which are non-enriched. As will be shown, the additional nodes stem from the extended compact support of the specialized weight function, defined in Section 2.2.3, used in generating enriched MLS shape functions. Consider for discussion the enriched element, identified as e_k^{enr}, in the structured square element mesh of Figure A.7a. The local support $\tilde{\Omega}_i^{\text{S}}$ of specialized weight function $w_i^{\text{S}}(\boldsymbol{x})$ centered at the element's lower left node is indicated by the surrounding shaded elements. Signified by the shading contrast in the figure, as done in Figure 2.4, the extended support spans the four elements contiguous to node n_i (dark grey shading) and their additional 12 neighboring elements (light grey shading). Thus given the coverage of $w_i^{\text{S}}(\boldsymbol{x})$, node n_i would contribute in the local approximation functions of the 16 elements within its support domain. To perceive the compact support overlap for element e_k^{enr} first envision a second specialized weight function $w_j^{\text{S}}(\boldsymbol{x})$ existing at the element's top right node. Its support likewise spans the 16 elements encompassing node n_j, denoted by the dashed lines. Imagining the compact support for the remaining two element nodes and the additional surrounding nodes it is evident that 16 distinct nodes, four of which define element e_k^{enr}, contribute to $\mathcal{N}_k^{\text{inf}}$. The 12 supplementary influencing nodes are indicated in Figure A.7b by unfilled circular icons whereas the four common influencing nodes, common with a non-enriched element, are indicated by filled circular icons.

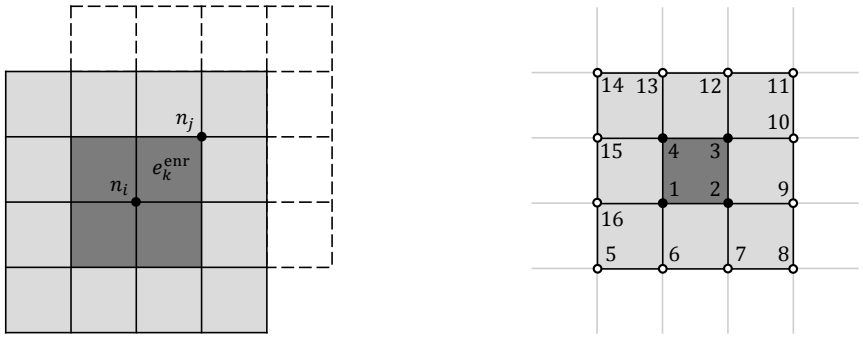

(a) Compact support overlap of $w_i^{\text{S}}(\boldsymbol{x})$ **(b)** Enriched element influencing nodes

Figure A.7: Demonstration, on structured rectangular mesh, of the compact support Ω_i^{S} overlap of specialized weight functions $w_i^{\text{S}}(\boldsymbol{x})$ leading to influence of 16 enriched MLS shape functions N_i^{MLS} over an enriched element e_k^{enr} (dark grey filling in (b)).

Repeating the same analysis, considering a unstructured mesh of quadrilateral elements the result will be the same for a non-enriched element, $r = 4$. A consequence of the single element radial extending support of standard bilinear shape functions. However, for enriched elements variability in the number of influencing

nodes r should be expected. Foremost because the mesh irregularity does not establish an orderly repeating pattern as seen with a structured mesh. Therefore no consistent number of surrounding elements exist, preventing establishment of a set number of influencing nodes. Comparing the compact support $\tilde{\Omega}_i^{\mathrm{S}}$ of the special weight function in Figure 2.5a to that in Figure 2.5b provides one realization for justification as the depicted local supports of $w_i^{\mathrm{S}}(\boldsymbol{x})$, in the two figures, span over 16 and 18 elements respectively for this example. Acknowledging this unsystematic element arrangement, configurations are conceivable leading to enriched elements with more or less than 16 influencing nodes contributing in the element approximation functions.

In the demonstrative examples, element e_k^{ner} or e_k^{enr} was assumed to preside internal to the domain such that it was completely surrounded by elements, leading itself to generation of a full set of influencing nodes $\mathcal{N}_k^{\mathrm{inf}}$. Foreseeable cause for incomplete sets in both a structured or unstructured mesh will arise within proximity of global domain boundaries. This issue is only relevant to enriched elements, as for non-enriched elements the element nodes exclusively influence the approximation, where nodes beyond the element set $\mathcal{N}_k^{\mathrm{el}}$ factor in. Again in a structured mesh the alignment permits predictable configurations to exist. For example an enriched element along a straight edge and at a corner would have $r = 12$ and $r = 9$ influencing nodes respectively, in an unstructured mesh such definitive arguments cannot be stated. In either case recalling the moment matrix inversion criteria, Eqn. 2.2.13, discussed in Section 2.2.2, sufficient overlap is still maintained due to the enlarged compact support of the special weight function to insure invertability in evaluation of the enriched shape functions, Eqn. 2.2.11, and thus the approximation functions.

FE Model Matrix and Vector Definitions

The concise form of the FE model equation is derived and presented at the end of Section 3.2.1. Restated below by Eqn. A.4.2, it is composed of the stiffness matrix $\mathbf{K}$, the to-be-determined primary variable vector $\mathbf{u}$, force vector $\mathbf{F}$, and secondary variable boundary condition vector $\mathbf{Q}$. Though the FE model equation is valid over both the global domain Ω and element domain Ω_k^{el} for consideration here, where the intent is to explicitly demonstrate how the elemental system of equations is generated for assembly into the global system, it is best to keep an element domain in mind for the formulation.

$$\mathbf{K}\mathbf{u} = \mathbf{F} + \mathbf{Q} \tag{A.4.2}$$

Considering the two degrees of freedom existing at each node, x and y displacement, u_x and u_y corre-

spondingly, the FE model of Eqn. A.4.2 can be expanded to delineate between these two variable sets as follows.

$$\begin{bmatrix} \mathbf{K}^{11} & \mathbf{K}^{12} \\ \mathbf{K}^{21} & \mathbf{K}^{22} \end{bmatrix} \begin{Bmatrix} \mathbf{u}_x \\ \mathbf{u}_y \end{Bmatrix} = \begin{Bmatrix} \mathbf{F}^1 \\ \mathbf{F}^2 \end{Bmatrix} + \begin{Bmatrix} \mathbf{Q}^1 \\ \mathbf{Q}^2 \end{Bmatrix} \tag{A.4.3}$$

All variable divisions retain the same terminology as before, having just been separated for expressing the alternate formulation of the FE model. Each of these variables, $\mathbf{K}^{ab}$, $\mathbf{F}^{a}$, and $\mathbf{Q}^{ab}$, where $\{a, b = 1, 2\}$, in turn is generated through a coefficient-matrix product sum or a single coefficient-vector product. These expressions are listed in Eqn. A.4.4, provided for the individual matrix and vector components, i.e. the subscript entries.

$$\mathrm{K}_{ij}^{11} = h\left(C_{11}\mathrm{S}_{ij}^{11} + C_{66}\mathrm{S}_{ij}^{22}\right) \tag{A.4.4a}$$

$$\mathrm{K}_{ij}^{12} = \mathrm{K}_{ji}^{21} = h\left(C_{12}\mathrm{S}_{ij}^{12} + C_{66}\mathrm{S}_{ij}^{21}\right) \tag{A.4.4b}$$

$$\mathrm{K}_{ij}^{22} = h\left(C_{66}\mathrm{S}_{ij}^{11} + C_{22}\mathrm{S}_{ij}^{22}\right) \tag{A.4.4c}$$

$$\mathrm{F}_{i}^{1} = hf_x\mathrm{F}_{i}^{0} \tag{A.4.4d}$$

$$\mathrm{F}_{i}^{2} = hf_y\mathrm{F}_{i}^{0} \tag{A.4.4e}$$

$$\mathrm{Q}_{i}^{1} = ht_x\mathrm{Q}_{i}^{0} \tag{A.4.4f}$$

$$\mathrm{Q}_{i}^{2} = ht_y\mathrm{Q}_{i}^{0} \tag{A.4.4g}$$

Coefficients C_{ij} are the stiffness tensor components, refer to Eqn. 3.1.5, f_a are body force function components, t_a are external applied traction components (secondary variable boundary conditions, and h is the prescribed domain thickness. The components of matrices $\mathbf{S}^{\alpha\beta}, \{\alpha, \beta = 0, 1, 2\}$ and vectors $\mathbf{F}^0$ and $\mathbf{Q}^0$ are evaluated based on area or line integrals, of weight functions w_i, shape functions $\hat{N}_i$, their derivatives, or their multiples, over the element domain Ω_k^{el} or along the element boundary Γ_k^{el} respectively. Definitions for these variable components are expressed in Eqn. A.4.5,

$$\mathrm{S}_{ij}^{\alpha\beta} = \int_{\Omega^{\mathrm{el}}} w_{i,\alpha} \hat{N}_{j,\beta} \, dA \tag{A.4.5a}$$

$$\mathrm{F}_{i}^{0} = \int_{\Omega^{\mathrm{el}}} w_i \, dA \tag{A.4.5b}$$

$$\mathrm{Q}_{i}^{0} = \oint_{\Gamma^{\mathrm{el}}} w_i \, ds \tag{A.4.5c}$$

where $dA = dxdy$, and the integrand terms are defined as follows $\xi_{k,\gamma} \equiv \partial \xi_k / \partial \boldsymbol{x}_\gamma$; $\xi_{k,0} = \xi_k$ where ξ is taken as either the weight function w_i or shape function $\hat{N}_i$. Recall that the Galerkin method is utilized in this work therefore the weight functions in these expressions are taken as corresponding shape functions, such that $w_{i,\alpha} = \hat{N}_{i,\alpha}$. From these equations the increased connectivity on an enriched element in the global system of equations is identifiable. Take the enriched element of Figure A.7, having a total of $r = 16$ influencing nodes, for consideration. Those influencing nodes correspond directly to the shape functions used in defining the approximation function over the element, which are then integrated for constructing $\mathbf{K}^{\mathrm{el}}$, $\mathbf{F}^{\mathrm{el}}$, and $\mathbf{Q}^{\mathrm{el}}$, through the process laid out in this section. Therefore 16 distinct shape functions would be integrated in Eqns. A.4.5 giving rise to matrices and vectors of dimension 16×16 and 16×1 respectively. Moving through the process the matrices and vectors in Eqn. A.4.4 are of the same dimensions, but the element system of Eqn. A.4.3 expands to a matrix of size 32×32 with vectors of size 32×1. Compared to a non-enriched element, where $r = 4$, the element system matrix is of size 8×8 with vectors of size 8×1.

Appendix B Example LSFs and Enriched MLS Shape Functions

Appendix B is designed to provide validation of the enriched MLS shape function forms constructed using the MLS procedure of Section 2.2.1. It is also the intent of this work to provide the reader interested in reproducing such results some comparative cases and input for doing so. Illustrations of the enriched shape functions are given over a 4×4 square element discretization of a two-dimensional square domain. This amounts to the extended compact support of the specialized weight functions $w_i^{\mathrm{S}}(\boldsymbol{x})$, and thus the enriched MLS shape functions N_i^{MLS} local support, as seen for a structured rectangular FE mesh as used in this work, refer to the explanation in Appendix Section A.4. In generating the enriched shape functions, shown next, the square domain has boundaries $\{x, y\} \in [-1, 1]$. Within this domain a discontinuity interface Γ_{disc} is defined using the LSM of Section 2.3.1, i.e. through definition of a LSF $\psi(\boldsymbol{x})$ and determination of its zero-level LSC. Where the LSF is approximated using the approach discussed in Section 2.3.2 for the domain decomposition and shape function evaluation, thus the LSC is also an approximation.

The example LSFs and resulting enriched shape functions provided are for a weak and strong circular interface, a weak and strong straight line interface, and a crack tip discontinuity. Refer to Section 3.1.2 for definition of the enriched intrinsic bases $\boldsymbol{p}^{\mathrm{enr}}(\boldsymbol{x})$ for such discontinuities, and Section 3.1.3 for definition of the LSFs for such interfaces. For each case plots depicting the true LSF and LSC (ψ and Γ respectively), the approximated LSF and LSC (ψ^h and Γ^h respectively), and the corresponding enriched MLS shape function centered at $\boldsymbol{x} = (0, 0)$ are provided.

Weak Circular Discontinuity

Using the LSF of Eqn. 3.1.15, $\psi^{\mathrm{c}}(\boldsymbol{x})$, a circular LSC, interface Γ^{circle}, centered at point x^{c} and with radius r^{c} is defined. For this example the selected values are $x^{\mathrm{c}} = (0, 0)$ and $r^{\mathrm{c}} = 0.75$. Figure B.1 displays the resulting LSF and LSC plus their approximation.

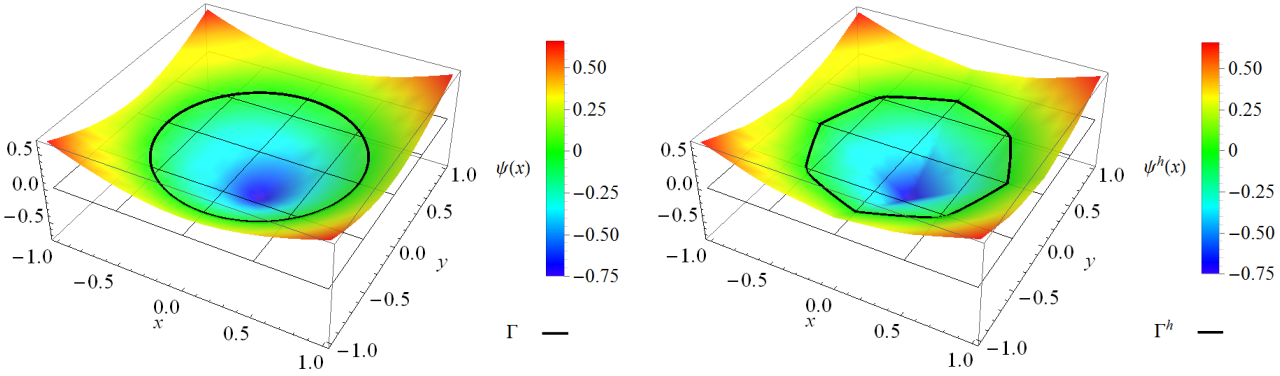

(a) Level-set function **(b)** Level-set approximation

Figure B.1: Level-set definition of circular interface Γ^{circle}.

From Figure B.1a it is shown that the LSF has positive value for all points $\boldsymbol{x}$ outside the interface and negative value inside as designed, refer to Figure 3.5a. The LSC is also shown to be perfectly round for the functional definition. Comparing to Figure B.1b it is visible that the approximate LSC determined from the approximate LSF is modeled as a piece-wise linear polygon. This figure also helps to illustrate that with a higher fidelity mesh the approximation would improve as a larger number of piece-wise linear edges would represent the circular interface. The resulting enriched MLS shape function calculated with the enriched intrinsic basis of Eqn. A.3.1 and the specialized weight function of Eqn. A.2.5 for this weak circular discontinuity is shown in Figure B.2.

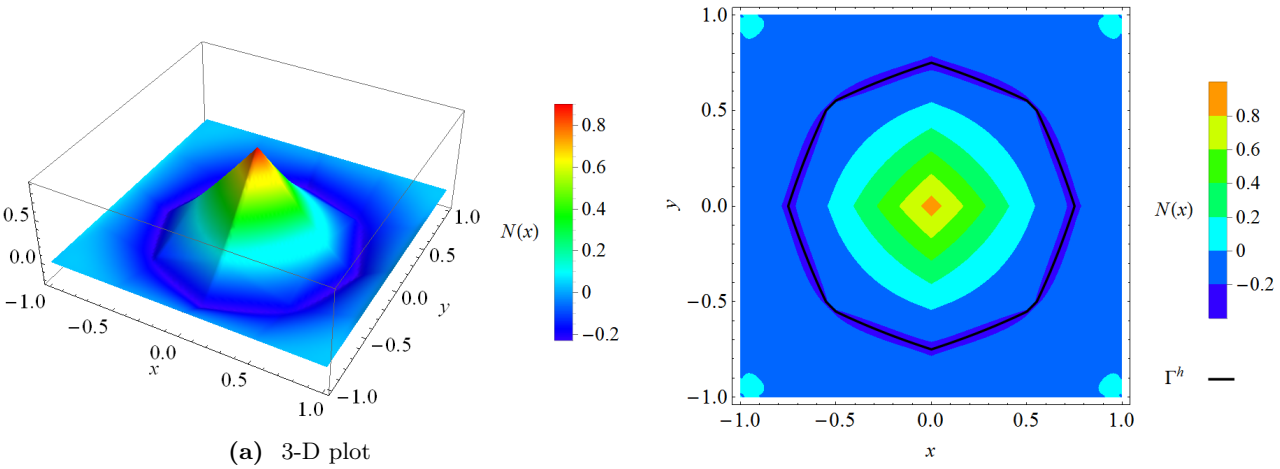

(a) 3-D plot **(b)** Contour plot

Figure B.2: Enriched MLS shape function: weak circular discontinuity.

From this figure it is visible that the shape function is continuous over the entire domain but experiences a sudden change in its directional derivatives $\partial/\partial x$ and $\partial/\partial y$ at the discontinuity interface. This will ensure continuity of the primary variable(s) while introducing discontinuity in the secondary variable(s) as needed. These intrinsic shape function properties provide the means for weak discontinuity interfaces to be properly modeled.

Strong Circular Discontinuity

Using the same circular discontinuity as for the weak interface, the LSF and LSC plus their approximations will be the same as shown in Figure B.1. The resulting enriched MLS shape function calculated with the full-form enriched intrinsic basis of Eqn. A.3.5 for this strong circular discontinuity is shown in Figure B.3. For clarity, and to enforce the notion of direct incorporation of the discontinuity into the shape function form, the near zero values determined for the enclosed discontinuous region are cutoff in this representation, similar to what would occur if using the truncated specialized weight function of Eqn. A.3.7

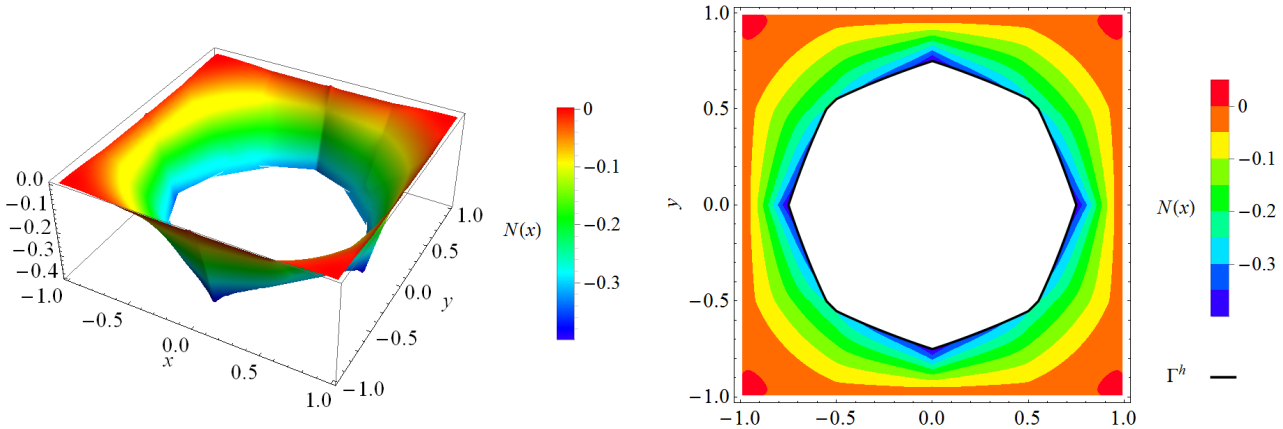

(a) 3-D plot

(b) Contour plot

Figure B.3: Enriched MLS shape function: strong circular discontinuity.

From this figure it is visible that the shape function discontinuity occurs at the interface boundary. All points $\boldsymbol{x}$ interior to this region, those for which the level-set value is negative $\psi(\boldsymbol{x}) < 0$, have near-zero value $N_i(\boldsymbol{x}) \ll 1$, and thus have negligible influence during the shape function and derivative integration when constructing the element stiffness matrix for assembly in the global stiffness matrix. This behavior will introduce discontinuity in the primary and secondary variable(s) fields. These intrinsic shape function properties provide the means for strong discontinuity interfaces to be properly modeled.

Weak Line Discontinuity

Using the LSF of Eqn. 3.1.17, $\psi^{\mathrm{l}}(\boldsymbol{x})$, a straight line LSC, interface Γ^{line}, running through point x^{l} with an orthogonal unit vector $\hat{\boldsymbol{t}}_n$ is defined. For this example the selected values are $x^{\mathrm{l}} = (0, 0)$ and $\hat{\boldsymbol{t}}_n = \{1, 1\}$. Figure B.1 displays the resulting LSF and LSC plus their approximation.

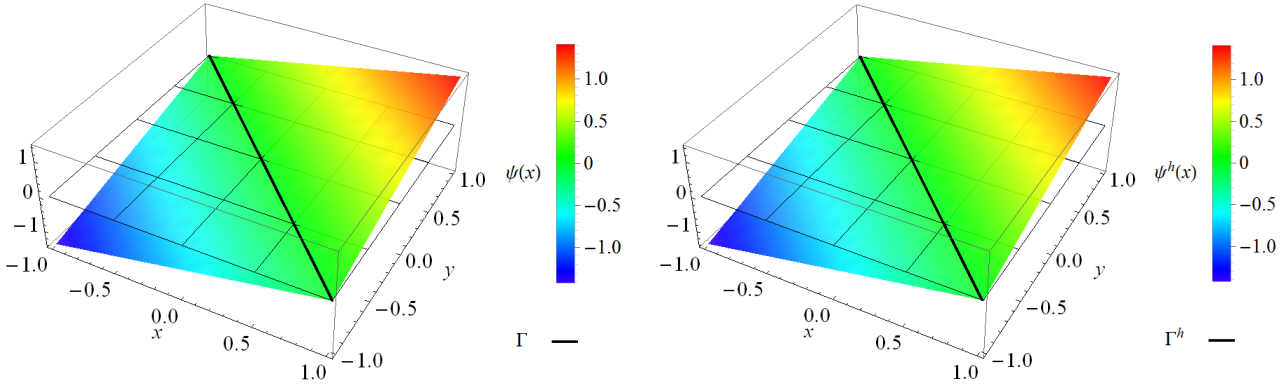

(a) Level-set function **(b)** Level-set approximation

Figure B.4: Level-set definition of straight line interface Γ^{line}.

From Figure B.4a it is shown that the LSF has positive value for all points $\boldsymbol{x}$ on the positive side as indicated by the direction of the orthogonal unit vector and negative value on the opposite side as designed, refer to Figure 3.5b. Comparing the true LSC to its approximate in Figure B.4b it is visible that straight line interfaces can be exactly modeled with a discrete FE approximation of the form in Eqn. A.3.2. Thus a high fidelity mesh is not essential for accurate representation of straight line discontinuity geometries as is the case for curved discontinuities. The resulting enriched MLS shape function calculated with the enriched intrinsic basis of Eqn. A.3.1 and the specialized weight function of Eqn. A.2.5 for this weak line discontinuity is shown in Figure B.5.

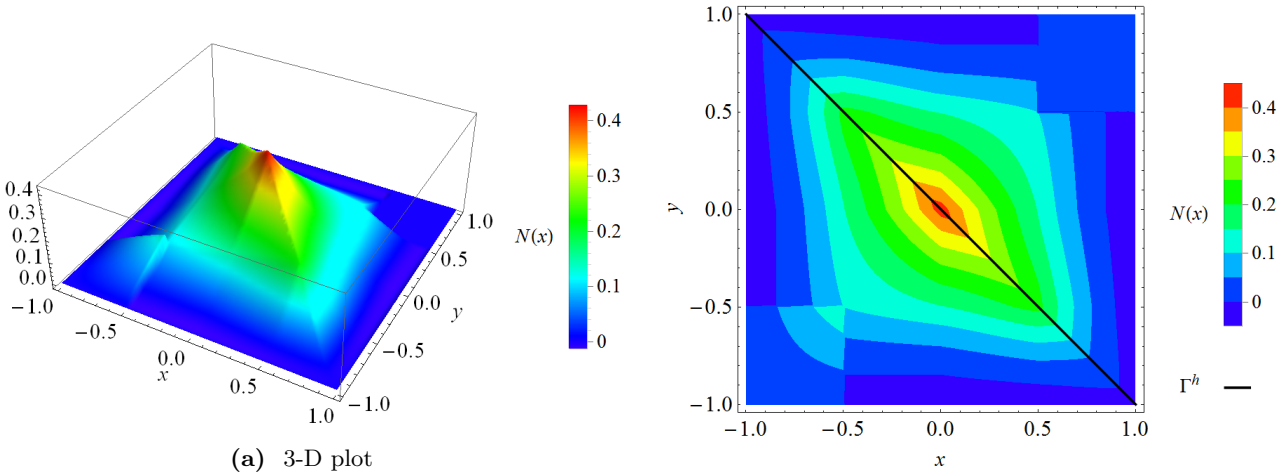

(a) 3-D plot

(b) Contour plot

Figure B.5: Enriched MLS shape function: weak line discontinuity.

From this figure it is visible that the shape function is continuous over the entire domain but experiences a sudden change in its directional derivatives $\partial/\partial x$ and $\partial/\partial y$ at the discontinuity interface. Again demonstrating the ensured continuity of the primary variable(s) while introducing discontinuity in the secondary variable(s), meeting the properties needed to properly model weak discontinuity interfaces.

Strong Line Discontinuity

Using the same straight line discontinuity as for the weak interface, the LSF and LSC plus their approximations will be the same as shown in Figure B.4. The resulting enriched MLS shape function calculated with the full-form enriched intrinsic basis of Eqn. A.3.5 for this strong line discontinuity is shown in Figure B.6. Again the near-zero values seen on the discontinuous side have been removed for clarity.

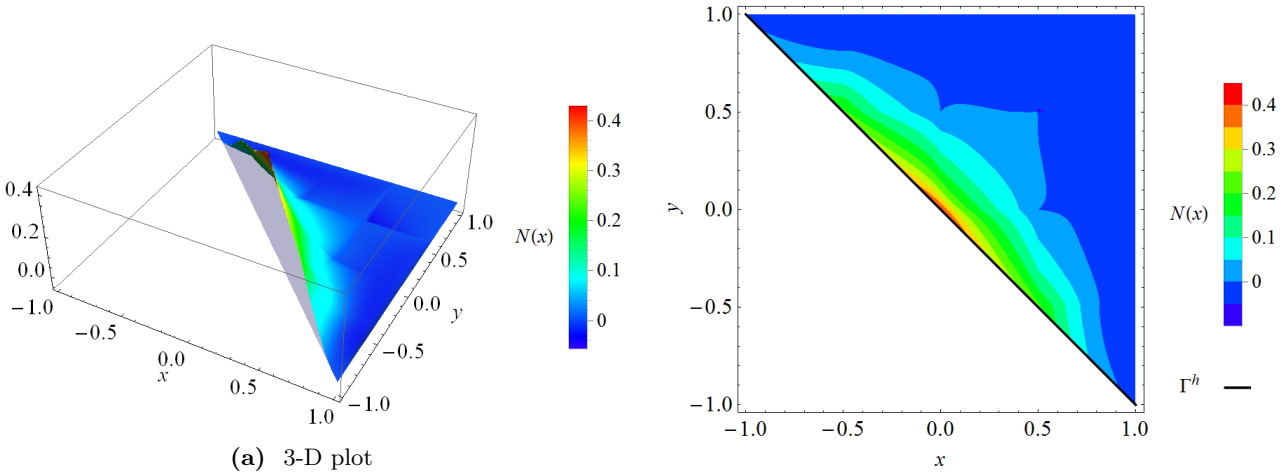

(a) 3-D plot

(b) Contour plot

Figure B.6: Enriched MLS shape function: strong line discontinuity.

From this figure it is visible that the shape function is discontinuous at the interface boundary. All points $\boldsymbol{x}$ opposite to the positive defining interface unit normal $\hat{\boldsymbol{t}}_n$, refer to Figure 3.5b, those for which the level-set value is negative $\psi(\boldsymbol{x}) < 0$, have near-zero value $N_i(\boldsymbol{x}) \ll 1$, and thus have negligible influence during the shape function and derivative integration when constructing the element stiffness matrix for assembly in the global system. Again this demonstrates the incorporation of the discontinuity in the primary and secondary variable(s) fields, meeting the properties needed to properly model strong discontinuity interfaces.

Discontinuous Tip

Using the LSF of Eqn. 3.1.17, $\psi^{\mathrm{l}}(\boldsymbol{x})$, and of Eqn. 3.1.18, $\psi^{\mathrm{t}}(\boldsymbol{x})$, a straight crack LSC, Γ^{crack}, running through point x^{l} with orthogonal unit vector $\hat{\boldsymbol{t}}_n$ and crack tip LSC, Γ^{tip}, at point x^{t} with tangent unit vector $\hat{\boldsymbol{t}}_t$ to Γ^{crack} is defined, refer to Figure 3.6a. For this example the selected values are $x^{\mathrm{l}} = x^{\mathrm{t}} = (0, 0)$, $\hat{\boldsymbol{t}}_n = \{-1, 1\}$, and $\hat{\boldsymbol{t}}_t = \{1, 1\}$. Figure B.7 displays the resulting LSFs and LSCs.

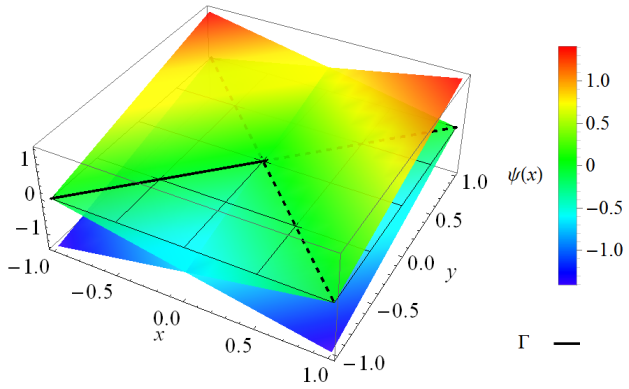

Figure B.7: Level-set definition of crack Γ^{crack} and crack tip Γ^{tip}.

As straight line interfaces are exactly modeled by the level-set approximation method the approximate LSFs and LSCs plot would be the same as Figure B.7 and is thus not included. In this figure the solid line indicates the crack edge and tip. The dashed lines indicate the extension of the line defining the crack and the crack tip normal curve. The resulting enriched MLS shape function calculated with the enriched intrinsic basis of Eqn. A.3.8 and the specialized weight function of Eqn. A.2.5 for this discontinuous tip discontinuity is shown in Figure B.8.

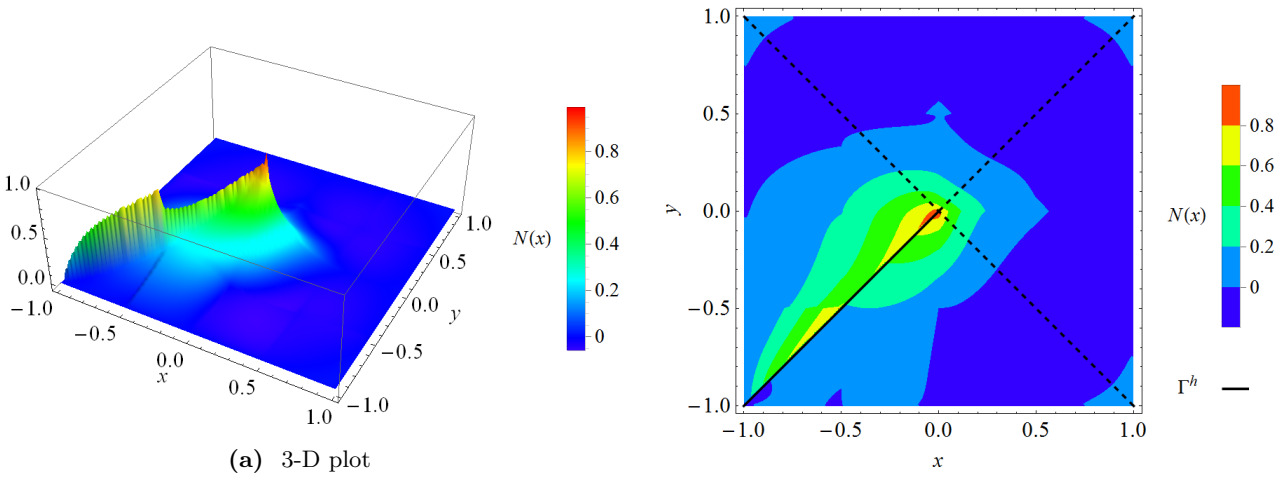

(a) 3-D plot

(b) Contour plot

Figure B.8: Enriched MLS shape function: discontinuous tip.

From this figure it is visible that the shape function is continuous over the entire domain except where the crack interface is defined, here the shape function is discontinuous. This behavior is a result of the crack tip enrichment functions as shown in Figure A.5, particular function $f_{t_1}^{\text{enr}}$ which is itself discontinuous across the

crack tip. Together this ensures continuity of the primary and secondary variable(s) fields surrounding the crack tip but not necessarily across the crack interface. These intrinsic shape function properties provide the means for discontinuous tips to be properly modeled.

Appendix C Problem Input Details

Appendix C is provided to supply further details on the FE meshes utilized in obtaining the results presented in Chapter 4, and provides one example figure of the enlarged RVEs used in Section 4.4 for each volume fraction and filler count case with its corresponding global decomposition. It is also the objective of this information to make available, to the reader interested in reproducing the results, some input information in regards to the problem geometry and mesh discretization. What follows are tables, listing common mesh characteristics (e.g. number of nodes, and number of elements), plus figures, illustrating the mesh structure, descriptive of the overall meshes used to represent the problem domains for analysis with the FEM or the IXFEM. Given that rectangular structured meshes were used exclusively for processing in the IXFEM, for this work, distinction of the presented meshes, based on the figures, for application with either method is easily identifiable from the mesh form. This is particularly evident when comparing the meshes in Figures C.1 and C.2 to those in Figure C.3. Whereas a mesh used with the conventional FEM must explicitly represent all geometric features of the problem (i.e. the circular hole in Figure C.1 or the circular inhomogeneity in Figure C.2), the IXFEM is designed to allow use of a regularized mesh unconstrained to match internal geometric features, instead using the LSM, of Section 2.3.1, to define internal discontinuity interfaces.

All meshes used in this work, and shown next, were created with the assistance of the commercial FE software Abaqus/CAE v6.13. Using the CAD and mesh generation tools of Abaqus the problem domain, and internal features for the FEM cases, were modeled with the software package and discretized using the built-in mesh controls. This generated the list of FE mesh node coordinates and element connectivity which were then output and processed using a MATLAB script for creating the input file to be used with the FEM and IXFEM codes developed as part of this research.

Table C.1: Global characteristics of the four meshes used with the FEM for analysis of the plate with a hole problem.

Mesh	Border Element Configuration*	Number of Nodes, n^{nd}	Number of Elements, n^{el}
1	20×23	560	506
2	40×47	2092	1983
3	60×69	4754	4592
4	80×93	8545	8328

*(width×height)

Table C.2: Global characteristics of the four meshes used with the FEM for analysis of the plate with a inhomogeneity problem.

Mesh	Border Element Configuration*	Number of Nodes, n^{nd}	Number of Elements, n^{el}
1	20×23	582	626
2	40×47	2283	2195
3	60×69	5208	5078
4	80×93	9322	9148

*(width×height)

Table C.3: Global characteristics of the four meshes used with the IXFEM for analysis of the plate with a hole and plate with a inhomogeneity problem.

Mesh	Border Element Configuration*	Number of Nodes, n^{nd}	Number of Elements, n^{el}
1	20×23	504	460
2	40×47	1968	1880
3	60×69	4270	4140
4	80×93	7614	7440

*(width×height)

Table C.4: Global characteristics of the problem domain and meshes used with the FEM and IXFEM for analysis of the well-dispersed (hexagonally packed) CNT-polymer nanocomposite RVEs.

		FEM Meshes		IXFEM Meshes	
Mesh	CNT Volume Fraction (%)	Number of Nodes, n^{nd}	Number of Elements, n^{el}	Number of Nodes, n^{nd}	Number of Elements, n^{el}
1	10	11356	11164	9270	9078
2	20	8022	7862	6450	6290
3	30	7099	6950	5520	5372
4	40	5355	5226	4140	4012
5	50	4219	4104	3348	3233
6	60	3622	3520	2793	2688
7	70	3168	3069	2438	2340
8	80	2878	2785	2107	2016

Table C.5: Global characteristics of the problem domain and meshes used with the IXFEM for analysis of the randomly distributed CNT nanocomposite RVEs.

Mesh	CNT Volume Fraction (%)	Number of CNTs, n^{CNT}	Number of Nodes, n^{nd}	Number of Elements, n^{el}
1	10	50	18496	18225
2	10	100	36864	36481
3	30	50	6241	6084
4	30	100	12321	12100

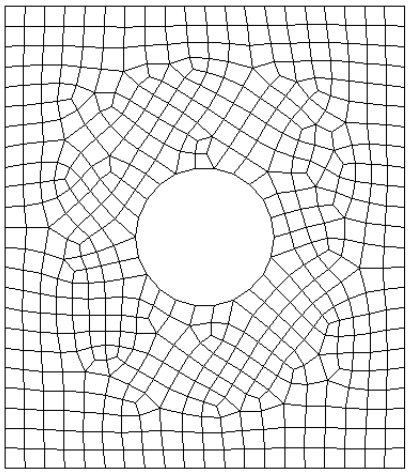

(a) Mesh 1

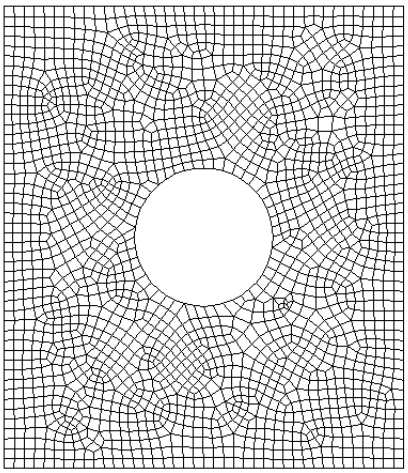

(b) Mesh 2

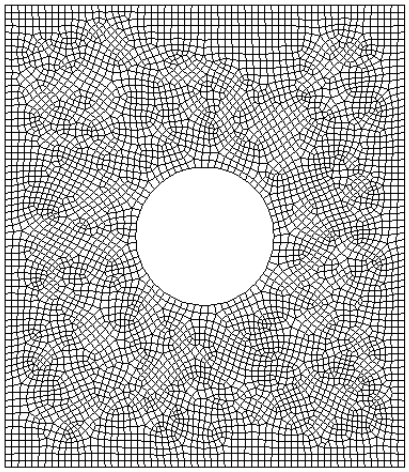

(c) Mesh 3

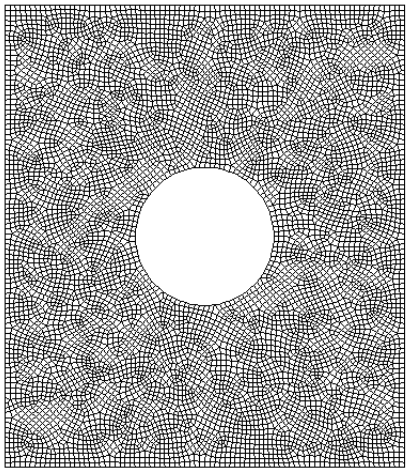

(d) Mesh 4

Figure C.1: Global domain meshes used with the FEM for analysis of plate with a hole problem, demonstrating increasing mesh fineness with decreasing element size.

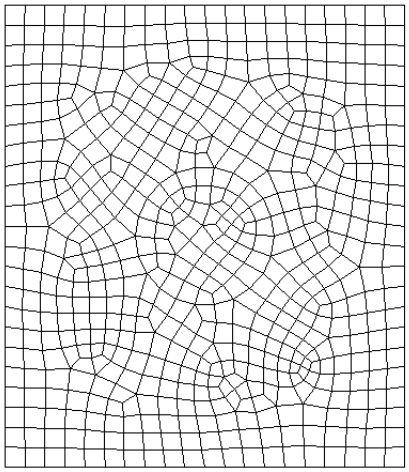

(a) Mesh 1

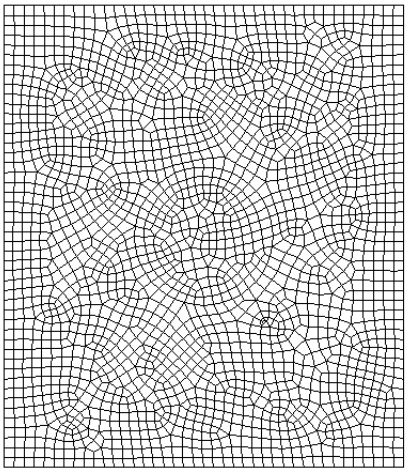

(b) Mesh 2

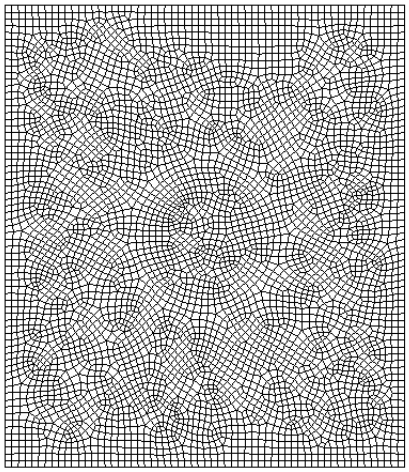

(c) Mesh 3

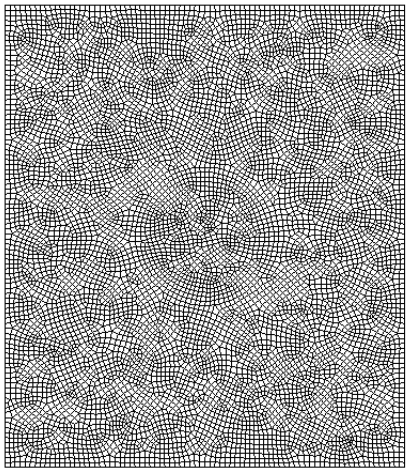

(d) Mesh 4

Figure C.2: Global domain meshes used with the FEM for analysis of plate with a inhomogeneity problem, demonstrating increasing mesh fineness with decreasing element size.

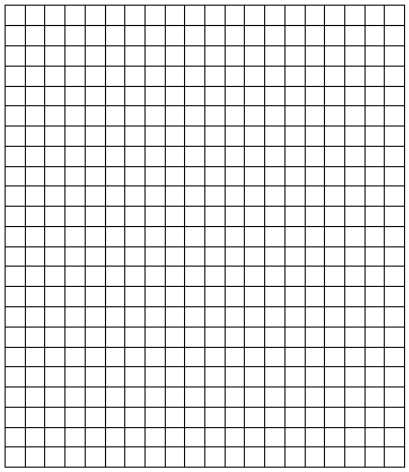

(a) Mesh 1

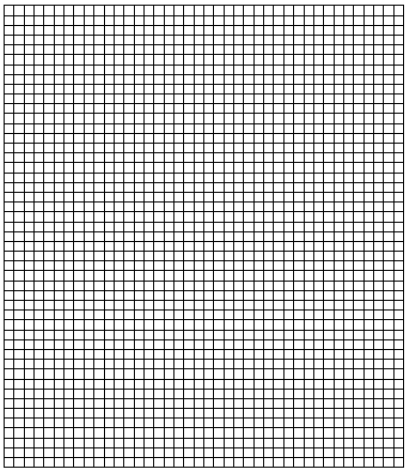

(b) Mesh 2

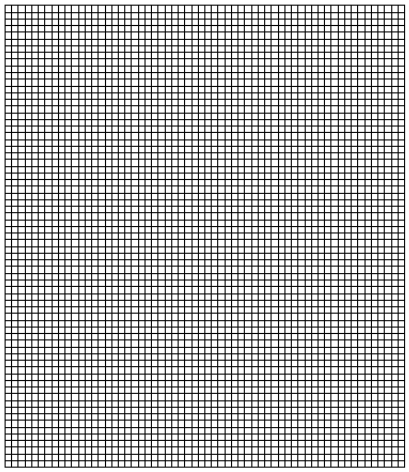

(c) Mesh 3

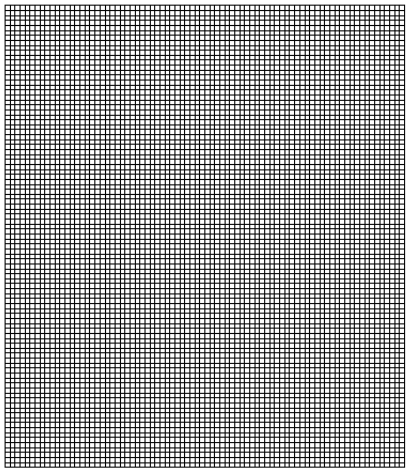

(d) Mesh 4

Figure C.3: Global domain meshes used with the IXFEM for analysis of plate with a hole problem and plate with a inhomogeneity problem, demonstrating increasing mesh fineness with decreasing element size.

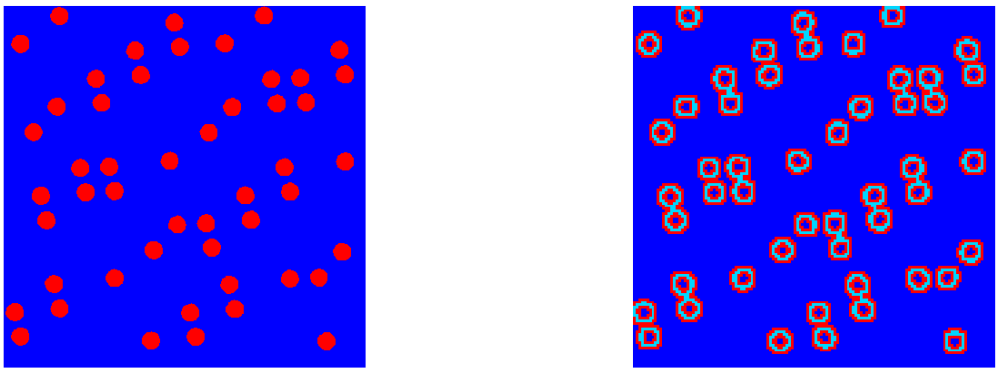

(a) Random disbursement of CNTs **(b)** Global domain decomposition

Figure C.4: Representative volume element for randomly aligned CNT-polymer nanocomposite of $V_f^{\mathrm{CNT}} = 0.1$ and $n^{\mathrm{CNT}} = 50$. In decomposition: blue regions indicate non-enriched subdomains Ω^{S}, light blue enriched subdomains Ω^{E}, and red transition subdomains Ω^{T}

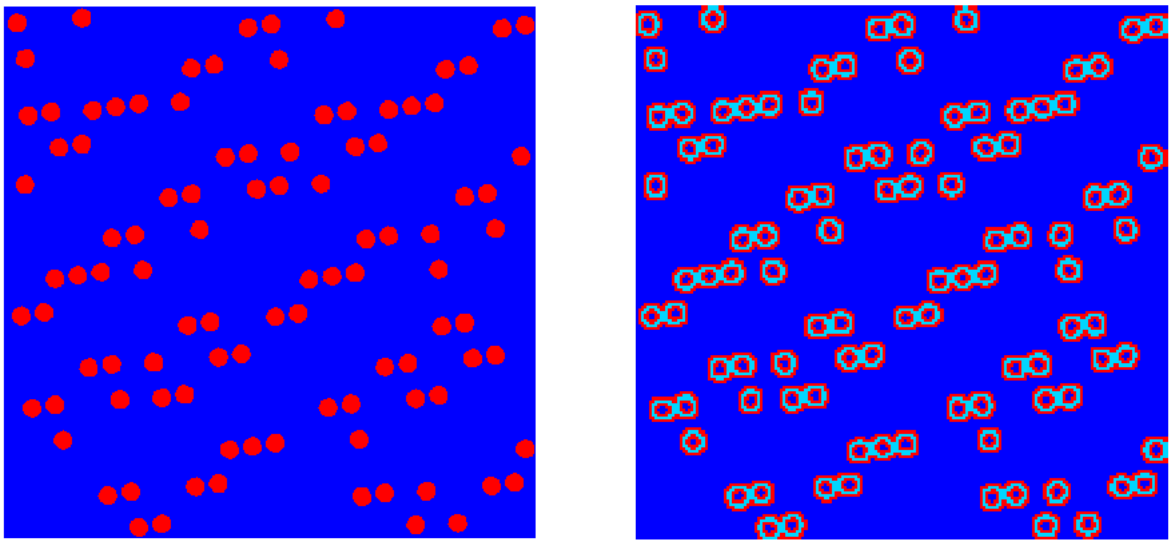

(a) Random disbursement of CNTs **(b)** Global domain decomposition

Figure C.5: Representative volume element for randomly aligned CNT-polymer nanocomposite of $V_f^{\mathrm{CNT}} = 0.1$ and $n^{\mathrm{CNT}} = 100$. In decomposition: blue regions indicate non-enriched subdomains Ω^{S}, light blue enriched subdomains Ω^{E}, and red transition subdomains Ω^{T}

(a) Random disbursement of CNTs **(b)** Global domain decomposition

Figure C.6: Representative volume element for randomly aligned CNT-polymer nanocomposite of $V_f^{\mathrm{CNT}} = 0.3$ and $n^{\mathrm{CNT}} = 50$. In decomposition: blue regions indicate non-enriched subdomains Ω^{S}, light blue enriched subdomains Ω^{E}, and red transition subdomains Ω^{T}

(a) Random disbursement of CNTs **(b)** Global domain decomposition

Figure C.7: Representative volume element for randomly aligned CNT-polymer nanocomposite of $V_f^{\mathrm{CNT}} = 0.3$ and $n^{\mathrm{CNT}} = 100$. In decomposition: blue regions indicate non-enriched subdomains Ω^{S}, light blue enriched subdomains Ω^{E}, and red transition subdomains Ω^{T}